Dissertation
submitted to the
Combined Faculties of the Natural Sciences and Mathematics
of the Ruperto-Carola-University of Heidelberg, Germany,
for the degree of
Doctor of Natural Sciences

Put forward by
Paul Maurice Mollière
born in Frankfurt am Main, Germany
Oral examination: July 12th, 2017

Modeling of Exoplanet Atmospheres

REFEREES:

PROF. DR. THOMAS HENNING
PD DR. SABINE REFFERT

Abstract
Spectrally characterizing exoplanet atmospheres will be one of the fastest moving astronomical disciplines in the years to come. Especially the upcoming *James Webb Space Telescope* (*JWST*) will provide spectral measurements from the near- to mid-infrared of unprecedented precision. With other next generation instruments on the horizon, it is crucial to possess the tools necessary for interpretating observations. To this end I wrote the *petitCODE*, which solves for the self-consistent atmospheric structures of exoplanets, assuming chemical and radiative-convective equilibrium. The code includes scattering, and models clouds. The code outputs the planet's observable emission and transmission spectra. In addition, I constructed a spectral retrieval code, which derives the full posterior probability distribution of atmospheric parameters from observations. I used *petitCODE* to systematically study the atmospheres of hot jupiters and found, e.g., that their structures depend strongly on the type of their host stars. Moreover, I found that C/O ratios around unity can lead to atmospheric inversions. Next, I produced synthetic observations of prime exoplanet targets for *JWST*, and studied how well we will be able to distinguish various atmospheric scenarios. Finally, I verified the implementation of my retrieval code using mock *JWST* observations.

Zusammenfassung
Durch Nutzung zukünftiger Teleskope wird die spektrale Charakterisierung von Exoplanetenatmosphären in den kommenden Jahren große Fortschritte machen. Grade das *James-Webb-Weltraumteleskop* (*JWST*) wird uns präzise Messungen im Nah- und Mittinfraroten erlauben. Es ist daher wichtig rechtzeitig über Methoden zu verfügen um solche Beobachtungen zu interpretieren. Aus diesem Grund habe ich das Programm *petitCODE* geschrieben, welches die Strukturen von Exoplanetenatmosphären selbstkonsistent berechnet, indem es die Annahme von Atmosphären im radiativ-konvektiven und chemischen Gleichgewicht macht. Die Berechnungen beinhalten Photonenstreuung, wofür auch Wolken behandelt werden. Das Ergebnis solcher Berechnungen sind die Emissions- und Transmissionsspektren der Atmosphären. Darüberhinaus habe ich einen Retrieval-Code geschrieben, welcher die Wahrscheinlichkeitsverteilung der Atmosphärenparameter aus Beobachtungsdaten abschätzt. Meine erste Anwendung von *petitCODE* war eine systematische Studie sogenannter "Hot Jupiter"-Atmosphären, bei der ich, unter anderem, herausfand, dass die Struktur der Atmosphären stark vom Spektraltyp ihres Sterns abhängt. Zusätzlich fand ich heraus, dass C/O-Verhältnisse mit einem Wert von ungefähr eins Temperaturinversionen hervorrufen können. Ich untersuchte außerdem wie Beobachtungen mit *JWST* verschiedene atmosphärische Zusammensetzungen unterscheiden können. Abschließend verifizierte ich meinen Retrieval-Code indem ich synthetische Beobachtungen mit *JWST* nutzte.

Für meine Eltern.

Contents

1 Introduction

This PhD thesis is concerned with the study of exoplanet atmospheres and their spectra and describes how I build the numerical tools for simulating such atmospheres. As we will see in this introduction, the study of atmospheres touches upon many other aspects of the science of exoplanets, such as their formation and internal structure. To prepare concepts of the following chapters, this introduction is intended to give an overview over the current field of exoplanet science, exoplanet detection, formation paradigms, observational techniques, observational characterization and which open questions are left to answer in the future. This chapter ends with the thesis outline. Many of the concepts important for exoplanet atmospheres have been developed from the study of Solar System planets, hence I will start with a summary of the Solar System exploration below.

1.1 The history of atmospheric characterization in the Solar System

The planets of our Solar System have been the subject of study for thousands of years, shaping mankind's understanding of the universe, and our place in it. Scrutinizing the planets' motions in the sky has given rise to Copernicus' heliocentric interpretation of our *Solar* System, and enabled Johannes Kepler to postulate the laws describing the movements of the planets in the gravitational field of the Sun. Finally, as one of the very first applications of Newton's laws, Kepler's laws were derived in Newton's book *'Philosophiae Naturalis Principia Mathematica'*, and can thus be regarded as giving rise to the fundaments of modern physics. In this way, investigating the Solar System planets, and their motions, can be viewed as one of the most important scientific studies to have ever been carried out.

However, while being fundamental to modern-day physics, little was known about the nature of the Solar System planets (and their atmospheres) for the majority of the time they were being studied. It was only with the advent of the first telescopes that the planets attracted further attention and were viewed as more than just point masses.

1.1.1 The terrestrial planets

One of the earliest planets to be characterized in greater detail, apart from Earth, was Mars. While it was believed that Mars could be harboring intelligent life for quite some time, with geological features and optical illusions mistaken for the notorious *'Mars Channels'*, mordern

astronomy could dispel this misconception rather quickly: Using multi-wavelength observations of Mars in the optical by Wright (1925), it was possible for Menzel (1926) to show that Mars indeed possesses a scattering atmosphere, with an upper limit on the surface pressure of 0.06 bars, which is roughly 10 times larger than the true value. In comparison to Earth, which has a surface pressure of ∼1 bar, this corresponds to a very thin atmosphere. By 1947 infrared observations of Mars by Gerard Kuiper at the McDonald Observatory indicated that its atmosphere was consisting mostly of CO_2. Given this knowledge of a thin CO_2 atmosphere it was possible to estimate Mars' surface temperature and it was found it was too cold to have liquid water on its surface. This picture of an arid, freezing planet with a low pressure atmosphere was confirmed by the first Mars flyby of a space probe, *Mariner 4*, in 1965, that analyzed the attenuation of the space probe's radio signal through the atmosphere of Mars just before and after the passage of the probe behind Mars (Kliore et al. 1965). This finding made use of the signal's transmission through the atmosphere of Mars, quite similar in principle to modern-day transmission spectroscopy of exoplanets (see Section 1.4.1). In 1976 *Viking 1* was the first probe to successfully land on Mars, proving all the remotely inferred properties of Mars and its atmosphere beyond doubt, and indicating a surface temperature of only 241 K (Nier et al. 1976). Mars has since been visited by a multitude of orbiters, landers, and even rovers, and there are plans for the first visits by astronauts sometime in the 2020s or 2030s.

Given its apparent brightness in the sky it is no wonder that also Venus was studied in detail as soon as the first telescopes became available. The existence of the atmosphere of Venus was known since 1761, when Mikhail Lomonosov observed Venus as it transited across the Sun (Lomonosov 1762). Just before the planet became fully superimposed on the solar disk Lomonosov could observe a ring of light tracing the spherical shape of Venus even in regions not yet covering the Sun: the atmosphere was diffracting the light of the sun around the planet. We therefore see that current techniques such as transmission spectroscopy take root in Venus transit observations carried out some 250 years ago. In the beginning this thick, cloudy atmosphere of Venus made a more detailed study difficult, however. Similar to Mars, it was first assumed that Venus could be habitable, owing to the planet's Earth-like size (0.95 $R_\oplus$) and its comparable distance to the sun (0.72 AU). Early temperature estimates, based on infrared (IR) radiometric measurements, indicated that Venus had a surface temperature of ∼250 K (Pettit & Nicholson 1955), which prompted attempts to explain Venus high reflectivity with water clouds (Menzel & Whipple 1955). In contrast to the IR results of Venus' atmosphere were the microwave measurements by Mayer et al. (1958), which they correctly identified as thermal emission, and which corresponded to a much hotter temperature of $\gtrsim$600 K. Mayer et al. (1958) further correctly pointed out that the previous measurements in the IR were merely tracing the cooler part of the atmosphere, just above the clouds of Venus, and should therefore not be mistaken with the planet's surface temperature. At this point it was still unknown where this radio emission was stemming from, whether it was from the hot surface of the planet or whether it originated from locations higher up in the atmosphere. An important piece of this puzzle was delivered by Carl Sagan in 1960, when he recognized that a thick greenhouse atmosphere (consisting of CO_2

and possibly water) could lead to such high temperatures (Sagan 1960). He further correctly pointed out that the hot temperatures, and consequently the absence of liquid water, would not allow for a removal of CO_2 from the atmosphere, in contrast to the situation on Earth (Sagan 1962). Having sparked planetary scientists' interests, 36 space probes visited or flew by Venus in the 60s, 70s, and 80s of the past century, about half of them successful, including multiple landings of the Soviet *Venera* probes. These probes helped to refine a picture of a planet with a thick, almost pure CO_2 greenhouse atmosphere. We now know that Venus' surface temperature is 730 K, and its surface pressure is 92 bar, with the clouds consisting mostly of sulphur dioxide and sulphuric acid. The reason for the absence of water, and a CO_2 atmosphere this massive, is theorized to have been caused by a runaway greenhouse process (Kombayashi 1967; Ingersoll 1969); in this scenario the oceans of a water-rich planet start being evaporated by the insolation, and the corresponding increase in atmospheric opacity, due to the steam, leads to a further temperature increase on the planet. Consequently, more water gets evaporated in a self-amplifying manner until all oceans have been put into the steam atmosphere. High-energy solar radiation will then break down the water at the top of the atmosphere, preferentially removing the less massive hydrogen atoms, which are lost to space. Thus only oxygen is retained, which reacts with the rocky surface of the planet to form CO_2.

The study of Mars and Venus has taught planetary scientists some valuable lessons. For example, the distance and size may not always be the most important properties of a planet when wanting to assess its surface conditions. For Mars the atmosphere is not thick enough to heat the planet significantly when compared to the temperature which are expected without an atmosphere. The radiation observed as coming from the planet can be used to study its surface conditions quite easily. For Venus the situation is completely different. Here the atmosphere strongly affects the surface conditions of the planet. In addition, it was learned that the effect of optical depth[1] has to be taken into account when trying to infer the conditions on a planetary surface and within the atmosphere: First IR temperature estimates were merely probing the highest atmospheric layers and it was not certain in the beginning whether the microwave signals measured on Venus correspond to the planet's surface or higher atmospheric regions. Studying multi-wavelength observations of planetary atmospheres often means studying different altitudes, and therefore different physical conditions.

1.1.2 The gas and ice giants

Shining brightly in the sky like Venus or Mars, Jupiter was likewise an obvious target for study, and was looked upon with the first telescopes by Galileo in the early 1600s. The noticeable change in the patterns on the apparent surface of this planet was the first evidence for this planet to have an atmosphere, and the fact that this planet really is gaseous,

[1] The optical depth measures distances in units of photon mean free paths, see Equation 1.7. If an atmosphere is 'optically thick' this means that its spatial extent is much larger than a photon mean free path, and that photons cannot easily escape from the atmosphere.

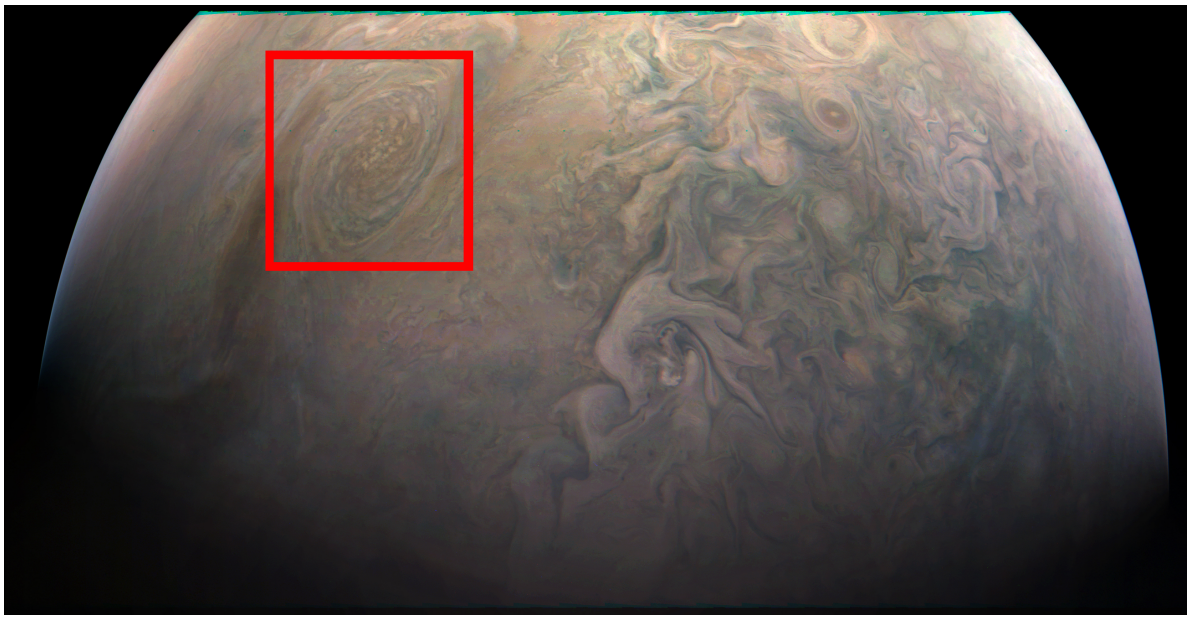

FIGURE 1.1: Picture of Jupiter taken on December 11, 2016 by the *JunoCam* instrument on the *Juno* spacecraft. This shot was taken during a close flyby, at a distance of 16,000 km (0.22 Jupiter radii) to Jupiter's surface. The anticyclonic storm called *'Little Red Spot'* is visible in the upper left, and marked by the red box.
Image credit: NASA/JPL-Caltech/SwRI/MSSS/Gerald Eichstaedt/John Rogers

rather than rocky, was already alluded to when Cassini found that Jupiter exhibited a distinct oblateness due to its fast rotation in the 1660s.[2] Another, not atmosphere-related, observation from these early-day studies was that the orbits of the Jovian moons seemed to occur later than predicted when Jupiter was further away from Earth, which was correctly inferred by Cassini and Ole Rømer to be due to the finite speed of light (Bobis & Lequeux 2008). In the beginning of the 20th century the first IR spectra obtained for Jupiter and the other gas and ice planets started to shed light on the planets' atmospheric composition. The presence of ammonia and methane on Jupiter and Saturn was identified by Dunham (1933), detecting two key molecules present in gas planet atmospheres at low temperatures (Jupiter has an effective temperature of 125 K, see, e.g. Fortney et al. 2011, and the references therein). Radio observations led to the discovery of Jupiter being a bright radio source (Burke & Franklin 1955; Franklin & Burke 1956), and it is now known that this signal originates from Jupiter's radiation belts, rather than the thermal radio emission of this planet. In order to measure Jupiter's thermal radio emission NASA's *Juno* probe, currently in orbit around Jupiter, dives under these belts during its pericenter passage, and may allow to detect the thermal radio emission of water in Jupiter's atmosphere. A picture of *JunoCam*, the probe's visible-light camera, is shown in Figure 1.1. It shows a sample of the dynamical patterns occurring in the atmosphere of Jupiter, among it the *'Little Red Spot'*, which is an anticyclonic storm in the planet's southern hemisphere.[3]

Both Jupiter and Saturn have been visited by space probes repeatedly, with the beginning made by the *Pioneer 10* (Jupiter) and *11* (Jupiter and Saturn) spacecrafts in the early 1970s.

[2] http://www-history.mcs.st-andrews.ac.uk/Biographies/Cassini.html

[3] Anticyclonic cells are regions of high central pressure which, due to the Coriolis force, rotate counterclockwise on Jupiter's southern hemisphere.

Among other instruments, the *Pioneer* spacecrafts were equipped with UV photometers as well as IR radiometers which allowed to measure the amount of hydrogen and helium in the gas giant's atmospheres as well as obtaining the cloud temperatures and total planetary luminosities. It was found that both these planets, while being hydrogen-dominated, have sub-solar helium abundances in their atmospheres, which is attributed to the rainout of helium droplets in Jupiter and more notably Saturn (Stevenson & Salpeter 1977). The next suite of space probes sent to Jupiter and Saturn were the famous *Voyager 1* and *2* probes, which provided the public with stunning photographs of the outer Solar System planets in the end of the 70s and 80s. Both probes contained an exciting array of instruments which were, for example, used to detect the planets' radio emission, as well as measuring the vertical atmospheric temperature structure of the gas and ice giants using infrared, and radio occultation measurements (Lindal et al. 1985, 1987; Lindal 1992). After having studied Saturn's moon Titan, which had made a passage of Saturn's south pole necessary, *Voyager 1* left the ecliptic of the Solar System, whereas *Voyager 2* continued on within the ecliptic to become the first and only space probe to ever visit Uranus and Neptune. One more mission truly valuable for the Jupiter exploration was the *Galileo* probe. Launched from aboard the Space Shuttle *Atlantis* in 1989, the *Galileo* space craft also carried an atmospheric entry probe that was separated from the main space craft 5 months prior to arrival on Jupiter. When it arrived, the *Galileo* entry probe entered the Jovian at atmosphere with a velocity of 47 km/s, burning away its 80 kg ablative heat shield in the process.[4] Suspended from a parachute, the probe then began its decent into Jupiter's atmosphere, and measured the atmospheric temperature and composition for 58 minutes. The probe delivered valuable information on the planet's temperature structure, as well as on its abundances, and it was found that Jupiter was 3-fold enriched in heavy elements when compared to the sun (Niemann et al. 1998; Wong et al. 2004). The same measurements found water to be depleted with respect to all other species by a factor of 10, and it is assumed that the entry probe, by chance, fell into a so-called hot spot region of dry, downwelling gas. As stated above, the *Juno* mission will try to fill in this gap in our knowledge by measuring the deep atmospheric water abundance in the radio wavelengths.

As mentioned before, *Voyager 2* went on to study the ice giants Uranus and Neptune after its encounter with Saturn and is the only space probe to have visited these two planets. Augmented by remote telescope observations from Earth, the *Voyager 2* data paint a picture of two extremely cold planets with atmospheric temperatures as low as 45 K. The atmospheres are significantly enriched in metals, by up to a factor of 80, when compared to the sun (Tyler et al. 1986; Sromovsky et al. 2011; Karkoschka & Tomasko 2011). The mass and radius values for both planets, as well as their gravitational moments measured by the *Voyager 2* flybys indicate that their outer gaseous envelopes make up only ∼10 % of their total masses, with the rest consisting of an ice mantle and rocky core, hidden underneath the atmosphere (Podolak et al. 1995, 2000).

Before ending this summary, I want to at least quickly mention Saturn's moon Titan. This

[4] https://web.archive.org/web/20060929185050/http://spaceprojects.arc.nasa.gov/Space_Projects/galileo_probe/htmls/Heat_Shield.html

moon is about 1.5 times the radius and only 1.8 times the mass of Earth's moon, yet it has a thick (1.4 bar) nitrogen atmosphere (Niemann et al. 2005), containing gaseous methane, (most-likely hydrocarbon) hazes (Waite et al. 2007), and lakes of liquid methane and ethane on its surface (Stofan et al. 2007). It's the only astrophysical body in the Solar System where a liquid can exist stably on the surface, apart from Earth. And "we" actually landed there as well, when the *Cassini* mission released its *Huygens* probe in 2005. The origin of methane in Titan's N_2 atmosphere is unknown and puzzling, because photodissociation of CH_4 should not allow it to be present in the observed abundance, which is much larger than what can be supplied by the liquid surface reservoir (see, e.g., Mitchell & Lora 2016, and the references therein).

This last example especially shows us that the exploration history of the Solar System is fascinating and surprising, especially when in-situ measurements were made. In that sense planetary science made full use of the technical feasibility to actually "go" to, and physically visit the planets. This is, obviously, not possible for the exoplanets or their atmospheres for which only telescopic measurements are possible. Yet, as we will see in Section 1.4.1, the methods for sensing exoplanets and their atmospheres in use today can lead to astounding results, trying to maximize the scientific knowledge that we can glean from these far-away experiments which Nature has set up for us to evaluate. Even if we may never see exoplanets in the same level of detail as we see the Solar System planets, knowing that these worlds must be equally complex and beautiful should inspire us to push as hard as we can to unlock their secrets.

1.2 Exoplanet detection methods

Between 1992 and 1994 the first extrasolar planets were detected in orbit around a pulsar (Wolszczan & Frail 1992; Wolszczan 1994). One year later Michel Mayor and Didier Queloz detected the first planet around a main sequence star (Mayor & Queloz 1995), 51 Peg b, and a new period in exoplanet science research began. Exoplanets were elevated from the stage of theoretical speculation to reality. While the mass of the planet, 0.5 $\mathrm{M}_{♃}$[5], i.e. between Jupiter and Saturn, did not seem surprising, the orbital distance of 51 Peg b was completely unexpected, because it is only 0.05 AU. Considering the parameters of its host star (Fuhrmann et al. 1997; Baines et al. 2009), the mean atmospheric temperature of 51 Peg b is 1378 K, which is far hotter than any planet in the Solar System. This temperature was obtained by calculating the planet's equilibrium temperature, which is defined as the effective temperature of the planet, obtained from distributing the stellar energy received on its dayside over the whole planetary surface. It works out to be

$$T_{\mathrm{equ}} = T_* \sqrt{\frac{R_*}{2d}} \,, \tag{1.1}$$

[5] $\mathrm{M}_{♃}$ stands for the mass for Jupiter.

where T_* is the stellar effective temperature, R_* the stellar radius and d the planet's distance to the star. In that sense, already the very first exoplanet detection showed us that the exoplanetary population contains specimen very different from what we are used to from the Solar System.

1.2.1 Radial-velocity measurements

Since then 3572 planets have been found.[6] 51 Peg b was discovered with the so-called radial velocity (RV) method, for which it is used that planet and host star orbit their common center of gravity (see the schematic depiction in Panel (a) of Figure 1.2). The host star will therefore periodically move towards and away from Earth, with a velocity amplitude of the motion towards the observer being (see, e.g., Haswell 2010)

$$A_{\rm RV} = \frac{2\pi a M_{\rm Pl} \sin(i)}{(M_{\rm Pl} + M_*) P \sqrt{1-e^2}} \,, \tag{1.2}$$

where a is the planet's semi-major axis, $M_{\rm Pl}$ its mass, i its orbital inclination, M_* the mass of the host star, P the planet's orbital period and e the eccentricity of the planetary orbit. This so-called 'reflex motion' of the star can be detected by taking high-resolution spectra at different phases of the planet–star orbit, and recording the frequency shift of the absorption lines of the stellar spectrum as a function of time. This shift occurs due to the doppler shifting of the stellar light as the star moves back and forth, with the amplitude of the shift $\Delta\nu$ being

$$\frac{\Delta\nu}{\nu} = \frac{A_{\rm RV}}{c} \,, \tag{1.3}$$

where c is the speed of light. From the expression for $A_{\rm RV}$ we see that the RV method allows for a mass estimate of the planet, because $A_{\rm RV} \propto M_{\rm Pl}\sin(i)$. Until now, 698 planets have been detected using the RV method.[6]

Because it holds that $P \propto (a^3/(M_{\rm Pl} + M_*))^{1/2}$ it is easy to understand that the more massive the planet, and the closer-in its orbit, the faster the stellar orbital motion will become and the easier a planet can be detected. While for Jupiter-mass planets on year-long orbits the stellar reflex motion is of the order of 10 m/s, it will be of the order of 100 m/s for hot Jupiters. The detection thresholds of current instruments are approaching velocity amplitudes < 1 m/s, at which point the host star activity becomes dominant source of measurement uncertainties (Saar & Donahue 1997; Makarov et al. 2009).

1.2.2 Transit detection

The transit detection method makes use of the fact that a planet, if its orbital inclination with respect to the line of sight is large enough, will *transit* in front of its star when viewed from Earth (see Panel (b) of Figure 1.2). The condition for at least a partial superposition of the planet on the stellar disk is

$$a\cos(i) < R_* + R_{\rm Pl} \tag{1.4}$$

[6] as listed on `exoplanet.eu` on January 31, 2017.

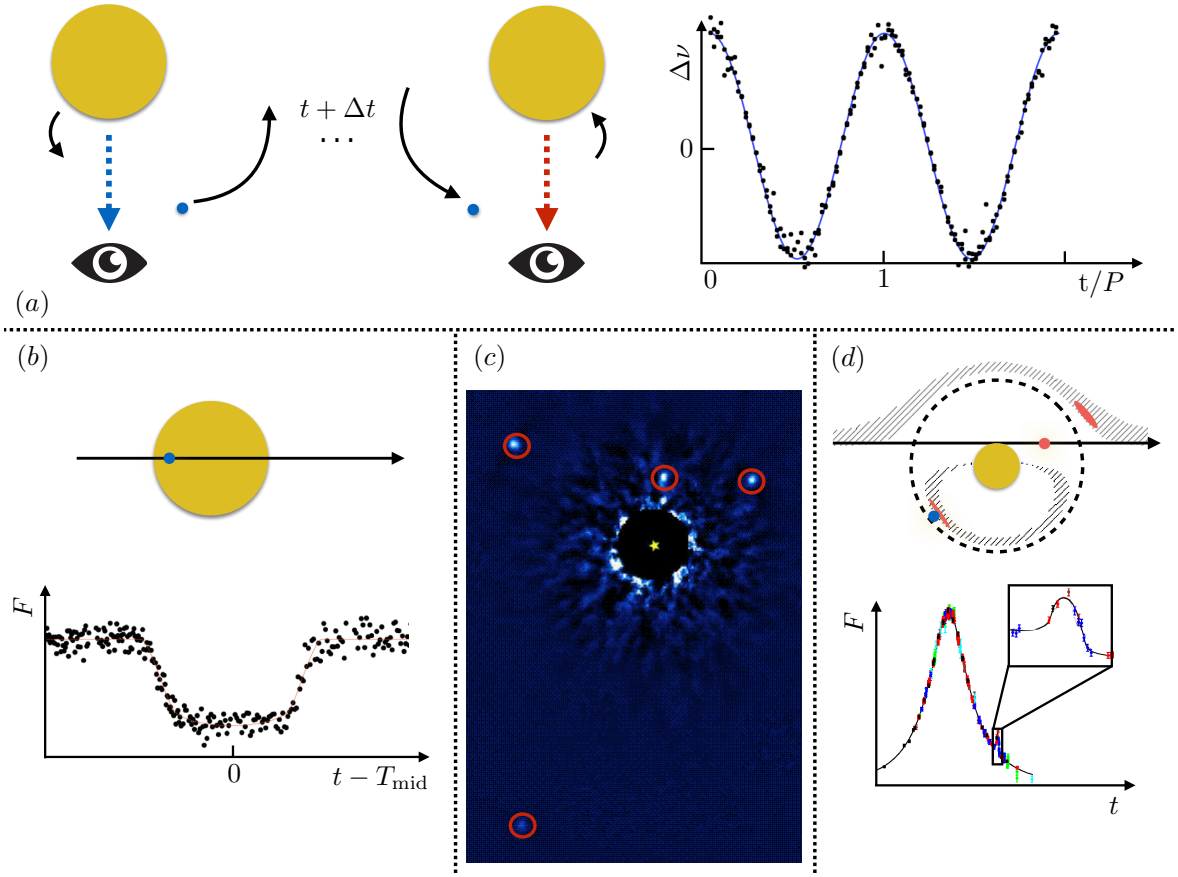

FIGURE 1.2: Methods of exoplanet detection. *Panel (a)*, radial velocity measurements: planet and star in orbit around each other, the stellar light is blueshifted as the star moves toward the observer and redshifted as it moves away from the observer. The graph on the right shows the corresponding frequency shift arising from the Doppler effect. *Panel (b)*, transit detection: The planet is shown on its path across the stellar disk, with the lower graph showing the corresponding decrease in stellar flux as the planet blocks the light of the star. *Panel (c)*: the directly imaged planetary system HR 8799. *Panel (d)*, microlensing: the (orange) background star passes behind the yellow foreground star and its flux is amplified due to the gravitational lensing effect of the foreground star. During the passage of the background star behind the foreground star the two distorted images of the background star will move along the hashed regions, always connected by the projected line passing through the fore- and background star. The lower graph shows the light curve resulting from the lens amplification, with a perturbation due to the presence of a planet around the foreground star, which acts itself as a gravitational lens.
Image credit: transit light curve of WASP-19b: TRAPPIST/M. Gillon/ESO, direct imaging picture of HR 8799 system: Jason Wang/Christian Marois/Quinn Konopacky/Bruce Macintosh/Travis Barman/Ben Zuckerman, gravitational microlensing light curve: Beaulieu et al. (2006), hashed regions of the microlensing image: Scott Gaudi

for circular orbits. If the planet is fully superimposed on the stellar disk during mid-transit, then the measured stellar flux F will have decreased by a fraction

$$\frac{\Delta F}{F} = \frac{R_{\rm Pl}^2}{R_*^2} \,, \tag{1.5}$$

which is of the order of 1 % for a gas giants around a Sun-like star and of the order of 0.01 % for Earth-like planets. The decreased signal strength explains why small planets are more easily found around smaller (e.g. M-type) stars, for which a detection becomes possible even with small, ground-based telescopes (see, e.g. Charbonneau et al. 2009), by monitoring the fluxes of stars and searching for periodically recurring decreases of brightness (the transits). Note that the above equation for the relative transit depth neglected the effect of stellar limb darkening. Limb darkening denotes that the star's limbs appear to be cooler, and thus less luminous, because the emerging flux of the stellar limbs travels horizontally through the

cooler parts of stellar photosphere on its way to the observer. Limb darkening can hence lead to an over or underestimation of the planetary radius, depending on the transit impact parameter. Similar to the radial velocity detection method, closer-in planets are more likely to be found because their transit probability, $(R_* + R_{\rm Pl})/a$ increases, and the fraction of the time where the planet is transiting its star, $\sim 2(2R_{\rm Pl} + R_*)/(v_{\rm K}P) \propto 1/a$, goes up, as well as the frequency of the transits. As seen above, there is also a bias on the planetary size, as the flux decrease is proportional to $R_{\rm Pl}^2$. This is important for atmospheric sensing, because as we will see in sections 1.4.1 and 1.4.2, studying the wavelength-dependent transit depth helps to infer the composition in the characterization of an exoplanet's atmosphere. If the potential signal of a transiting planet has been detected, a confirmation via the RV method is necessary, because the transit signal could also be caused by a transiting brown dwarf or low-mass star, by grazing stellar binaries or a stellar binary blended together with a third, bright star. The transit detection method has been the most successful method of detecting planets, with the largest number of confirmed planetary detections, 2300, made by NASA's space-borne *Kepler* mission, which continuously surveyed the same 115 deg^2 field in the sky for more than 3 years.[6]

In planetary systems with at least one transiting planet, additional, even non-transiting planets may be detected via their gravitational interaction with the transiting planet. This interaction causes a periodic shift in the transit-to-transit time interval, which is detectable if multiple transits of a planet are recorded. This method is called Transit Timing Variation (TTV) and has led to the detection of seven planets.[6]

1.2.3 Direct imaging

The first two detection measurements described above only indirectly detect the presence of the planet. Is it actually possible to really take a picture of a planet as it circles its star? As the picture shown in Panel (c) of Figure 1.2 indicates: it is! 76 planets have been detected using this so-called direct imaging technique.[6] This number is lower than the number of planets having been detected with transits or RV, indicative of the challenge to take a picture of a planet outside the Solar System. There are two main enemies which have to be beaten for such an imaging attempt to be successful, which are the small angular separation between the planet and its host star and the fact that the host star completely outshines its planets, being much hotter and bigger. As an example: the innermost planet of the HR 8799 planetary system shown in Figure 1.2 has an angular separation of $\sim$0.4" from its star (Marois et al. 2010). This is comparable to the magnitude of the atmospheric distortion (seeing) induced by turbulence at the best astronomical sites of Earth. Fortunately, adaptive optics systems, such as *SPHERE* at the *VLT* can correct for the atmospheric turbulence and allow for resolutions down to 0.03" in the optical.[7] However, simply resolving the planet–star distance is not enough. The resolution only states the width of the first maximum of the Airy diffraction pattern. Thus light from the star is still able to dominate the flux at the location of the planet. For example, in the visible wavelengths, a sun-like star is more than a

[7] https://www.eso.org/sci/facilities/paranal/instruments/sphere/inst.html

billion times brighter than a hot young gas planet with an effective temperature of 900 K, because the star is so much hotter and bigger. Even in the 10th Airy maximum, which is 0.01 % as bright as the first maximum, the star would still be 10^5 times brighter than the planet, and the detection of the planet still very challenging, because this is equal to the precision which modern-day detectors achieve (Guyon et al. 2012).[8] Two approaches can help here: (i) going to longer wavelengths: at 2 μm, e.g., the planet–star contrast in our example case is only 10^5, instead of 10^9, and decreases further with longer wavelengths. This can only be done to a certain extent, however, because the planet's flux will start to decrease for wavelengths longer than 3.2 μmm, if a blackbody is assumed. Additionally the telescope's resolution is linearly proportional to the wavelength and will thus get worse at the same time. (ii) Using a coronagraph, which is a mask within the telescope that blocks light entering the telescope exactly on-axis. With the telescope centered on the star under scrutiny, the glare of the star will be removed from the observation and any off-axis planets around the star, which are brighter than the detection threshold, will become visible. Needless to say, coronagraphs are not perfectly able to block all of the host star's light, due to mask leakage, imperfect telescope pointing and time-dependent deformations within the optical systems of the telescope, and will give rise to complex, albeit lower intensity, diffraction patterns also at the location of the planet (Shaklan et al. 2004). Nonetheless, the use of coronagraphs can improve the contrast between planet and star by multiple orders of magnitude (see, e.g., Snellen et al. 2015). Unfortunately the combined use of adaptive optics and coronagraph is sometimes still not sufficient, because the remaining diffractive patterns of the blocked star will cause so-called 'speckles' in the focal plane, each mimicking a planet. Two methods can be used to tackle this problem: Angular Differential Imaging (ADI, see Marois et al. 2006a) and Spectral Differential Imaging (SDI, see, e.g., Marois et al. 2006b). ADI uses that the stellar field, and thus the planet, will rotate on the detector of an alt-azimuth telescope over the course of the observation, because the telescope has to track the star as it moves across the sky. In this scenario the speckles remain stationary, because they are caused by an on-axis point source, while the planet rotates. Hence the planet can be identified. For a sufficiently large spectral coverage, one flavor of SDI uses that the telescope's resolution decreases linearly with wavelength, which is also reflected in the fact that the stellar speckles will appear to move outward if the wavelength of observation is increased. The planet remains stationary in this case, again making a distinction of planet and speckles possible. In conclusion we see that the direct imaging of exoplanets is possible, but very challenging, and that enormous technological and intellectual efforts were necessary to achieve observations such as shown in Panel (c) of Figure 1.2. Because this method works best for intrinsically high planet-to-star flux contrasts it is evident that the hotter and larger a planet is, the easier it is to detect. Because of this direct imaging has so far only detected young, and therefore hot, gas giant planets.

[8] It is doubtful if the Airy pattern in a real-world telescope is stable out to the 10th order. I merely use it here to estimate for the amount of stellar flux sufficiently far away from the first maximum.

1.2.4 Gravitational microlensing

From general relativity it is known that mass is a source of space-time curvature. Consequently, a ray of light originating from a background star which passes behind a foreground star will have its path altered due to the mass of the foreground star. It can be shown that the foreground star's effect is analogous to that of a lens, such that, due to the magnification, the flux of the background star is amplified as it passes behind the foreground star. If the background star passes directly behind the foreground star its image will appear to be that of an *Einstein ring* with an angular diameter of

$$\vartheta_{\mathrm{E}} = \sqrt{\frac{4GM_*}{c^2}\frac{d_{**}}{(d_{*\oplus}+d_{**})d_{*\oplus}}}\,, \tag{1.6}$$

with G being the gravitational constant, M_* the foreground star's mass, d_{**} the distance between the background and the foreground star and $d_{*\oplus}$ the distance between the foreground star and the observer on Earth. Background star passages with non-zero impact parameter will not lead to the occurrence of an Einstein ring, but to two distorted images of the background star appearing close to, and on opposite sides of the Einstein ring, connected by the projected line going through the background and the foreground star. An example of this setup can be seen in Panel (d) of Figure 1.2, with the hashed areas showing the regions that the two images of the background star will move through during the passage. If an additional mass, such as a planet, exists in the lens plane (i.e. at the location of the foreground star, and perpendicular to the line of sight) of this setup, then one image of the background star will be subjected to additional deformation and amplification. An example for the resulting light curve of such a double-lens system is likewise shown in Panel (d) of Figure 1.2. Because the planet acts as a second gravitational lens, described by its own Einstein radius, one can see that this phenomenon again favors more massive planets, as the lens radius is proportional to $\sqrt{M_{\mathrm{Pl}}}$. By checking the sky for chance alignments between stars, and recording the light curve of these events over the course of days, 51 planets have been found.[6] An inherent disadvantage of this method is that chance alignments are rare, such that microlensing observations cannot be repeated. This is, however, the only method available to detect planets around stars with distance to Earth of multiple kpc, and is effective for finding planets at multiple AU, because the angular separation between the planet and its host star must be close to the Einstein radius.

1.3 The exoplanet population and formation models

If one uses the planetary properties which result from the detection process itself, such as orbital period, mass, or radius, then the distribution of these quantities alone reveals a lot about the exoplanet population and its formation, as we will see in this section. Thus, while the study of individual planetary systems is exciting, the population of known exoplanets in its entirety can be regarded as one of the most important outcomes of the exoplanet detection efforts: a convincing model for planet formation has to be able to explain the key features

of this population (after appropriate correction for detection biases, that is). In this section I will summarize the two most popular paradigms for planet formation, as well as the key features of the exoplanet population. For the latter part I will point out which paradigm may be able to explain given features.

1.3.1 Models of planet formation

Core accretion paradigm

The text in this subsection is largely identical to the text I contributed to the DFG Antrag BO 2992/3-1.

The most commonly assumed formation pathway for planets is by the so-called core accretion paradigm. This paradigm draws on the foundations laid out by many contributors (Safronov 1972; Lynden-Bell & Pringle 1974; Perri & Cameron 1974; Mizuno et al. 1978; Lin & Papaloizou 1986; Bodenheimer & Pollack 1986; Lissauer 1993) and will be summarized in the following. The initial state of the planet formation process is thought to be a circumstellar disk consisting of mainly gas and some dust, with at least some of the dust locked into km-sized planetesimals. The planetesimals within the disk grow by collisions and the more massive ones will grow increasingly faster until the largest bodies compete for the smaller bodies, stirring up the disk of smaller bodies in the process, and enter the slower phase of so-called oligarchic growth. The planetesimal's gravitational reach within the disk, when compared to the host star, is limited. Therefore, if orbital migration is neglected, planetesimals with a few (tens of) Earth masses reach the so-called isolation mass, after which planetesimal accretion ceases. During this planetary build-up the gas disk evolves viscously and accretes onto the star such that planets which have masses below the isolation mass when the disk vanishes will remain mostly rocky/icy (they can still bind gaseous envelopes in the low single digit weight-percentage (wt-%) range). Planetary cores which reach the isolation mass during the disk lifetime will start to bind an ever-growing, slowly contracting gaseous envelope around them which extends out to the planet's Hill sphere.[9] Once the envelope mass becomes more massive than the core itself it cannot maintain hydrostatic equilibrium anymore and undergoes a quasi-hydrostatic collapse (collapse speed is much lower than sound speed) at a rate faster than the disk can transport gas to the edge of the planet's Hill sphere. The planet thus detaches from the disk nebula and accretes gas as rapidly as the disk is able to supply it. This phase is called the phase of runaway gas accretion. The planet stops accreting gas once the disk disperses, consequently the planet's final mass is set by the disk lifetime.

Many additional processes may complicate the formation theory outlined above, among the most important processes are orbital migration of the forming planet, as well as the drift and accretion of so-called pebbles, which are cm to meter-sized dust particles that are loosely coupled to the disk gas.

[9] The Hill radius marks the distance from the planet beyond which the host star's gravitational field starts to dominate the gravitational field of the planet.

Migration of planets may occur due to interactions with a far away perturber such as stars (so-called Kozai-Lidov oscillations, see Kozai 1962; Lidov 1962; Wu & Murray 2003; Fabrycky & Tremaine 2007) or due to planet-planet interactions once the disk has dispersed (Rasio & Ford 1996; Weidenschilling & Marzari 1996; Lin & Ida 1997). Another important process may be disk migration, where the planet migrates due to angular momentum exchange with the gaseous circumstellar disk. Depending on the mass of the planet different migrations regimes may exist. Planets with masses below Neptune to Saturn masses are expected to migrate via so-called type I migration, exchanging angular momentum with self-induced spiral arms in the disk (wake torques, see Tanaka et al. 2002; Paardekooper et al. 2010; Masset 2011) and gas co-rotating with the planet (corotation torques, see Paardekooper et al. 2010; Masset & Casoli 2010; Paardekooper et al. 2011; Lega et al. 2014; Masset & Benítez-Llambay 2016). Type I migration timescales can be very short (on the order of 0.5 Myr) and usually favor inward migration, although so-called planet traps may exist as well if outward migration regions lie inside of inward migration regions (see, e.g., Bitsch et al. 2013). For more massive planets the spiral arms induced by the planet will produce shocks which push the gas in and outside of the planet away from its orbital position. If the disk viscosity is low enough the planet will form a gap in which the co-rotation torque is significantly weakened and the planets migration speed is determined by wake torques. This migration regime is called type II migration. Due to the width of the gap the migration is slower than in type I. Migration rate and gap opening simulations have been carried out by, e.g., Lin & Papaloizou (1986); Papaloizou et al. (2004); Crida et al. (2006); Zhu et al. (2013); Duffell (2015); Dürmann & Kley (2015) but it must be noted that results depend on the assumption made for the sources of the disk's viscosity and the evolutionary state of the disk. Evidently, the process of planet migration may be crucial for the planet formation process: the planet may accrete gas from different locations within the disk and the reservoir of planetesimals to be accreted can be replenished by either migration of the planet or migration of planetesimals. Together these processes conspire to complicate the correlation between a planets final semi-major axis, composition and formation location.

The process of pebble accretion has been described in, e.g., Ormel & Klahr (2010); Johansen & Lacerda (2010); Perets & Murray-Clay (2011); Morbidelli & Nesvorny (2012); Lambrechts & Johansen (2014). In summary pebble accretion describes the accretion of particles which are coupled to the disk gas neither too strongly nor too weakly. Small particles, which are coupled to the disk gas too strongly, hydrodynamically flow around the planetary core instead of being accreted. Bodies which are big enough to be only weakly coupled to the gas (larger than $\sim$m size) will only be accreted if they hit the planetary core's surface directly on their ballistic trajectory. Only particles of intermediate size can decouple from the gas flow around the planetary core, spiral in on its surface and are accreted. The notion that pebble accretion may indeed be important for planet formation is underpinned by the detection of mm to cm sized particles in protoplanetary disks (Testi et al. 2003; Wilner et al. 2005; Rodmann et al. 2006; Natta et al. 2007; Ricci et al. 2010) which is in the size regime required for pebble accretion to work. The cross-section for this process is of the order of the planetary core's Hill radius (Baruteau et al. 2016), therefore pebble accretion may be more

important than planetesimal accretion once the planetary core is massive enough and if the circumstellar disk can supply a sufficiently large amount of pebbles for a long enough time.

As we will see in Section 1.3.2, formation by core accretion may be a natural explanation for some of the most important features of the exoplanet population.

Formation from gravitational instabilities in the disk

The motion of the gas within the protoplanetary disk is usually dominated by the gravitational field of the star. However, if the disk is sufficiently cool and massive (Toomre 1981), and can cool quickly enough (Gammie 2001), then local overdensities in the disk can collapse to gravitationally bound clumps of gas. The requirements stated above may be fulfilled in the early stages of the disk's formation and evolution, when it is still sufficiently massive, but only in the outer parts of the disk, typically beyond 50-100 AU (Boley et al. 2010; D'Angelo et al. 2010). In the inner part of the disk the requirements for collapse cannot be met simultaneously (Rafikov 2005). After the formation of the unstable clump of gas its evolution and orbital migration is strongly affected by the surrounding disk's cooling timescale, structure, and evolution (see, e.g., Helled et al. 2014; Kratter & Lodato 2016). Possible outcomes of the clump evolution may be planets, but also brown dwarfs or low-mass stars if the clumps go on to accrete mass during their post-collapse evolution (Stamatellos & Whitworth 2009). An additional possibility is the tidal disruption or downsizing of the clumps, which may destroy them if they migrate inwards on timescales faster than their contraction timescale, or simply cause them to lose a significant amount of mass (Nayakshin 2010a; Forgan & Rice 2013). Nayakshin (2010a,b) advertises the tidal disruption as a potential formation paradigm for terrestrial planets, where the solids in a collapsed clump settle to its center to form a core, and the gaseous envelope of the clump is stripped away by tidal forces.

As I will point out in Section 1.3.2, gravitational instabilities (GI) may be the origins of planets with large orbital separations of multiple tens of AUs, which are difficult to form via core accretion. At the same time the formation by gravitational collapse has difficulties in explaining key features of the exoplanetary population, such that core accretion may be the dominant mode for planet formation in the inner parts of stellar systems.

1.3.2 Notable features of the planetary population

First, I want to look into the most obvious properties of the distribution of exoplanets. To this end I show the mass–orbital period and radius–orbital period relations for all currently known exoplanets in Figure 1.3.[6] Note that these plots show the real detections of exoplanets, such that distribution visible here is affected by detection biases, as I will also discuss below. The most prominent features when studying these plots are

1. There is an overdensity of planets with $M_{\rm Pl} \sim \mathrm{M}_{\oplus}$ and $R_{\rm Pl} \gtrsim \mathrm{R}_{\oplus}$ and orbital periods of $\sim$3 days.

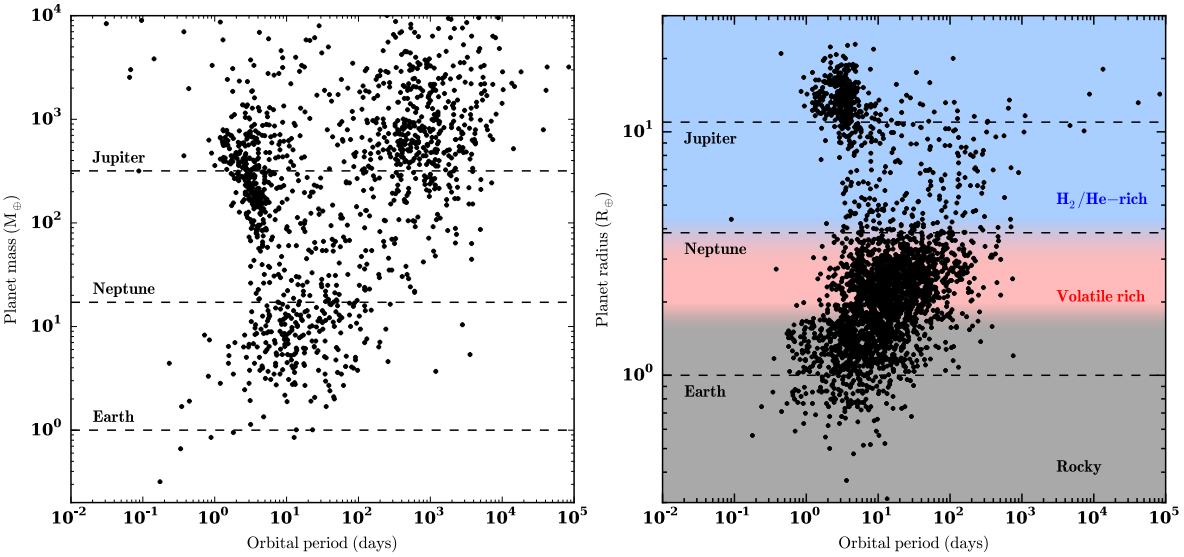

FIGURE 1.3: *Left panel:* masses of known exoplanets as a function of their orbital period. If the inclination is unknown, then $M_{\rm Pl}\sin(i)$ is plotted instead of $M_{\rm Pl}$. The three horizontal dashed lines denote the masses of Earth, Neptune and Jupiter, respectively. *Right panel:* radii of known exoplanets as a function of their orbital period. The region shaded in gray denotes planned which are considered to be predominantly rocky. The red region denotes planets that have a rocky or icy core and which may have a considerable envelope that can be strongly enriched in volatiles. For the region shaded in blue H_2 and He envelopes are expected to dominate the planetary radius. The exoplanet data used in these plots has been taken from `exoplanets.eu`.[6]

2. There is an overdensity of planets with $M_{\rm Pl} \gtrsim {\rm M}_{\rm 4}$ with periods between ∼200 and 2000 days, but not a corresponding overdensity in radius–period space.

3. There is an overdensity of planets with masses between ∼1 and 20 $\rm M_\oplus$, radii between ∼1 and 3 $\rm R_\oplus$ and orbital periods < 100 days.

Feature 1 is quite obvious, and was one of the first to be detected when the number of known exoplanets was still low: this is the-pile up of the so-called hot jupiters, which are the gas giants found in close-in orbits around their stars, with periods of mere days. The overdensity shown in Figure 1.3 overestimates these planet's fractional importance, however, because both the transit probability as well as the amplitude of the RV signal of such planets favor their discovery (see Section 1.2). It is now known that this pile-up is real, however, and that roughly 1.2 % of all F, G, and K stars host hot jupiters, and that there are more gas giant planets found at larger orbital separations (Cumming et al. 2008; Marcy et al. 2008; Mayor et al. 2011; Howard et al. 2012; Wright et al. 2012). One interesting aspect of hot jupiters is that their radii are often larger than 1 $\rm R_{4}$ (see radius–period plot in Figure 1.3) which is noteworthy because although insolation slows down the planetary contraction, most of the hot jupiters should to have radii lying in the range of 1-1.2 $\rm R_{4}$ if theoretical models are consulted (Guillot & Showman 2002). Some hot jupiters have radii approaching 2 $\rm R_{4}$ (for example WASP-17b, with $R_{\rm Pl} = 1.93$ $\rm R_{4}$, see Anderson et al. 2010)! Multiple theories exist to explain this so-called 'inflation' of hot jupiters (see, e.g., Baruteau et al. 2016), but there is no conclusive evidence to support any of them yet; apart from a minimum insolation necessary for the inflation to occur (Laughlin et al. 2011; Demory & Seager 2011), the solution of this problem still evades us.

Feature 2 shows the by now well established fact that the giant planet occurrence increases for increasing orbital periods P in a $\log(P)$ dependence, which allows to infer that about 15 % of all F, G, and K stars host gas giant planets with periods less than 2000 days (Mayor et al. 2011), and potentially up to 20 % if the period-dependence is extrapolated to longer times (with maximum semi-major axes of 20 AU, see Cumming et al. 2008). The overdensity is not visible in the radius–period plot because these planets are increasingly unlikely to transit, such that no radius measurement exists for them. This increase of the giant planet occurrence rate with increasing distance to the star can be explained and reproduced with the core accretion paradigm (Mordasini et al. 2012): although the gas surface density of an accretion disk decreases as one goes to larger semi-major axes, both the region of the planet's gravitational influence and the planetesimal surface density increase, the latter because volatiles[10] such as water, CO_2 and CO freeze out in the outer, cooler regions of the disk. Moving further out, core accretion formation predicts the occurrence of gas giant planets to decrease for semi-major axes larger than $\sim$5 AU, because of the dominating decrease of the disk surface density. It is important to test this prediction, but we are only now entering the time were observational baselines are long enough. If the planet occurrence rate is found to keep increasing, this may be a hint for formation by GI.

In addition to the period dependence, the gas planet occurrence exhibits a strong positive correlation with the metallicity of their host stars (Fischer & Valenti 2005; Udry & Santos 2007) which is reproduced by core accretion simply because more metal-rich star–disk systems have more material available for the formation of planetary cores which then trigger the onset of gas planet formation (Mordasini et al. 2009). GI cannot explain this correlation.

Feature 3 shows the simple fact that in the inner regions of the stellar systems planets with masses below 20 $M_\oplus$ and radii smaller than 4 $R_\oplus$ seem to be the most common type of planets (Howard et al. 2012; Batalha 2014), which are commonly called 'super-Earths'. Note that the detection bias disfavors super-Earths in comparison to larger, more massive planets. The super-Earths detections stem mostly from *Kepler* transit observations. They are thus less well represented in the mass–period plot, because their low masses increase the time investment necessary for a reliable mass estimate from RV measurements. Super-Earths thus appear to be the most common type of planet, but no planet of this type can be found in the Solar System! Again, the prevalence of super-Earths is a result well reproduced by core accretion population syntheses (Mordasini et al. 2012), indicating that planetary cores can be formed much more efficiently than they can be brought to undergo runaway gas accretion. Again, this is an observation which cannot be explained by GI.

For a subset of the Kepler super-Earth detections a reliable RV mass estimate has been obtained, allowing to assess the planets' densities and thus compositions. The scatter of radii found at a fixed mass is much larger than expected from measurement errors, indicating a considerable variation of composition (Weiss & Marcy 2014). Indeed, also theoretical models show that the radii of super-Earths are more strongly determined by their composition than by their mass (Lopez & Fortney 2014): adding a few wt-% of H_2–He gas on top

[10] 'Volatiles' generally denotes molecular species with a low condensation temperature, such as water, CH_4, NH_3, CO_2, or CO. Materials with a high condensation temperature, such as minerals, are referred to as 'refractories'.

of a rocky core can double a planet's radius, and the radius is then largely independent of the core mass. Furthermore a planet at a given mass and radius may have a rocky core with a gas envelope of a few wt-%, or it may be an ice core with no envelope at all. That being said, masses of planets with radii below 1.5 $R_\oplus$ are consistent with being fully rocky, while larger planets indicate the existence H_2–He, potentially volatile-enriched envelopes, covering cores which may consist of rocky and/or frozen volatile material (Weiss & Marcy 2014). For radii larger than 2.5-3 $R_\oplus$ a significant fraction of planets are less dense than water, indicating that the H_2–He contribution starts to dominate the planetary radii, smoothly transitioning into gas planets (Hadden & Lithwick 2014). The radius–period plot in Figure 1.3 has been shaded in different colors to distinguish the region of compositional degeneracy from the rock- and H_2–He-dominated regions.

From the description of a few of the most obvious features of the planetary population, which all already leave many open questions, the usefulness of the population analysis to improve our understanding of planet formation and planetary physics is obvious. And there are still many more interesting topics, such as the origin of planets of a few Earth masses but with radii comparable to Saturn or Jupiter (so-called 'super-puffs', see Lee & Chiang 2016), or the apparent dichotomy between planetary systems that contain either multiple planets with low mutual inclination or a single detectable planet (with more planets at larger mutual inclination? See Ballard & Johnson 2016), or simply the question why many exoplanets have large orbital eccentricities (with values going up to 0.93, see Udry & Santos 2007; Moorhead et al. 2011).

For all the exciting questions which are yet to be answered I want to end this section with some simple numbers: Based on *Kepler* detections it seems that 40 % of all main sequence F, G, and K stars (Fressin et al. 2013) and 50 % of all M stars (Dressing & Charbonneau 2013) harbor planets with orbital periods shorter than 50 days. From microlensing studies a planet occurrence rate of even one planet per star (out to 10 AU) has been inferred (Cassan et al. 2012). The quantity most hunted by exoplanets statisticians is $\eta_\oplus$, "Eta Earth", which denotes the occurrence rate of terrestrial (i.e. rocky) planets in the habitable zone[11] around their stars. *Kepler* detections currently constrain this quantity to be up to 50 % for M dwarfs and, with some extrapolation, 22 % for G and K stars (Batalha 2014).

1.4 From exoplanet detection to atmospheric characterization

Exoplanet detections have transformed many of the preconceived ideas we had about the formation of planets when only the Solar System specimens were known. This has been achieved by analyzing planets using their most fundamental properties, such as mass, radius or orbital distance. However, if one is interested in knowing more about an individual planet, such as its (atmospheric) composition or temperature, the combined constraining power of mass, radius and distance measurements is too crude. In such cases a detailed

[11]The habitable zone is the orbital distance range around a star where the existence of liquid water on a terrestrial planet's surface is possible.

observation of the planet is required, for which a theoretical understanding of planetary atmospheres is necessary, because such observations always probe the planets' atmospheres. The atmospheres, in turn, will determine a planet's cooling rate and surface conditions, which critically depends on the atmospheric composition. Hence learning more about the properties of exoplanets is inextricably connected to studying their atmospheres and atmospheric compositions. Finally, the atmospheric composition may hold clues on a planet's formation history, such that the systematic study of planetary atmospheres may link back to our understanding of planet formation.

In this section I will summarize how different observation methods allow to study atmospheres, which powers and limitations they have and what is to be expected in the future, with an upcoming era of new ground- and space-based telescopes.

1.4.1 Observational techniques

Transit spectroscopy

In section 1.2.2 I introduced the detection of planets using the transit method, where it was used that a planet blocks a certain amount of light as it transits across the host star disk. Transmission spectroscopy uses the same kind of observations, while observing the transit in multiple wavelengths. This can be done using either photometric or spectroscopic measurements.

The basic idea is that as a photon of a given wavelength passes through the planetary atmosphere in a grazing geometry, such as shown in the left panel of Figure 1.4, it will more likely be absorbed if a molecule in the planet's atmosphere can be a exited by the absorption of this photon. This works best at wavelengths with energies close to the excitable molecular transition, such that the planet will appear bigger in this wavelength, because more of the stellar light is absorbed. Because this measurement technique probes the limb of the planet, as it transits the star, it gives insight into the terminator region of the planet, i.e. the region between the day- and the nightside.

The first suggestion to make use of this detection method was made by Seager & Sasselov (2000) and one of the first successful detections of atmospheric constituents was the detection of sodium atoms in the atmosphere of the transiting hot jupiter HD 2095458b (Charbonneau et al. 2002). Not only absorption affects the transmission spectrum of exoplanets, also scattering is important, and the optical Rayleigh scattering of molecules or, potentially, small cloud particles has been observed for hot jupiters (see, e.g., Sing et al. 2016, and the plot adapted from their work in the right panel of Figure 1.4). While molecular features of water are now often detected in the near-IR (Deming et al. 2013; Sing et al. 2016), there also exist observations showing no, or muted molecular features (Kreidberg et al. 2014; Knutson et al. 2014; Ehrenreich et al. 2014; Sing et al. 2016), which speaks for the presence of clouds in the atmospheres of these planets, decreased molecular abundances, or, for less massive planets, atmospheres strongly enriched in volatiles, with resulting high mean molecular weights (Madhusudhan et al. 2014b; Benneke 2015; Sing et al. 2016; Barstow et al. 2017; MacDonald & Madhusudhan 2017).

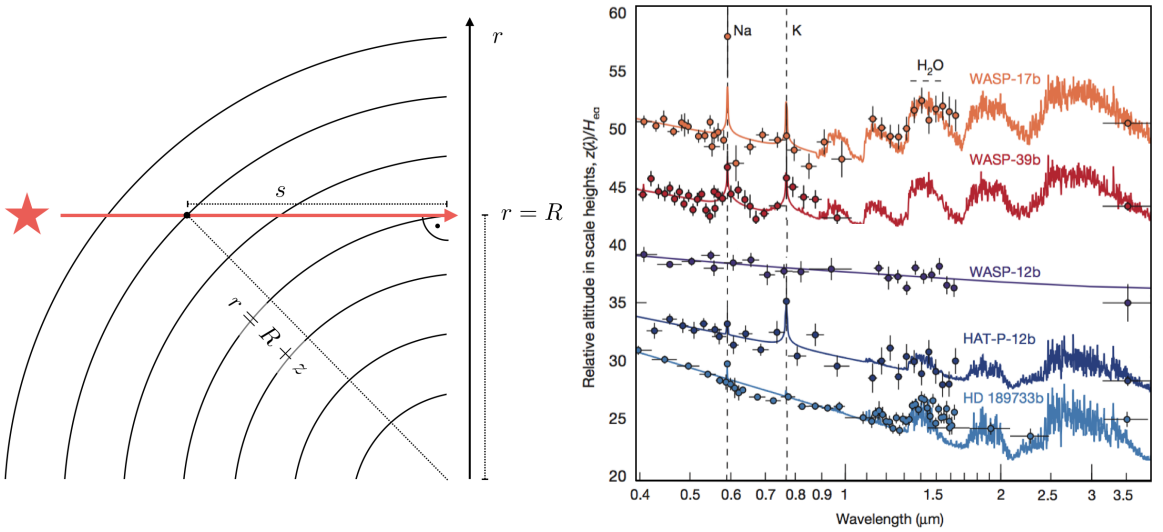

FIGURE 1.4: *Left panel:* Schematic drawing of a ray of light grazing through the planetary atmosphere in transit geometry. The host star is on the left, the observer is on the right. *Right panel:* Transmission spectra of hot jupiters (observational data and models, figure adapted from Sing et al. 2016). The two topmost spectra appear to be little affected by clouds, while the spectrum of WASP-12b in the middle is heavily affected by cloud blanketing. The two lowermost planets are hot jupiters with discernible molecular and atomic features, but seem to be affected by scattering caused by small particles towards the optical wavelengths.

Although the transit of the planet will produce a relative flux decrease of $(R_{\rm Pl}/R_*)^2$, the amplitude of the variation of the wavelength-dependent radius is far smaller, and causes relative flux decreases of $\gamma H_P R_{\rm Pl}/R_*^2$, where γ is a factor of a few, and $H_P = k_{\rm B}T/(\mu m_{\rm P} g)$ is the atmospheric pressure scale height, with $k_{\rm B}$ the Boltzmann constant, T the temperature, μ the mean molecular weight, $m_{\rm P}$ the proton mass, and g the planetary gravitational acceleration. H_P is much smaller than the planetary radius, leading to a relative flux decrease of $\sim 10^{-3}$ to 10^{-4} for giant planets (Crossfield 2015).

To derive this dependence of the amplitude strength we will define the 'optical depth', τ, which is the mean free path of the photon[12] divided by the distance travelled by the photon, which can be expressed as

$$\tau = \int n\sigma ds \,, \tag{1.7}$$

where s is the path length travelled by the photon, n is the number density of gas particles, and σ is the cross-section of the gas to either absorb or scatter the photon. From the geometry shown in the left panel of Figure 1.4 one can see that if the photon grazes the atmosphere with an impact parameter of R, its radial distance r to the planet's center can be expressed as $r^2 = (R+z)^2 = s^2 + R^2$, where we defined the atmospheric height z. If we assume that during the passages of photons through the limb of the planet it holds that $z \ll R$ we get that $z = s^2/(2R)$. Furthermore, in an isothermal, hydrostatic atmosphere (see Section 2.1) it holds that the planet's number density depends on the height as

$$\frac{dn}{n} = -\frac{dz}{H_P} \,, \tag{1.8}$$

[12] i.e. the distance it travels on average until being absorbed or scattered by the atmospheric gas.

which leads to

$$n(z) = n_0 \exp\left(-\frac{z}{H_P}\right) , \tag{1.9}$$

where n_0 is the atmospheric number density at $r = R$. Neglecting variations in σ with s we get for the total optical depth of the photon traveling through the atmosphere

$$\tau = n_0 \sigma \int_{-\infty}^{\infty} \exp\left(-\frac{s^2}{2RH_P}\right) ds , \tag{1.10}$$

and thus

$$\tau = n_0 \sigma \sqrt{2\pi R H_P} . \tag{1.11}$$

The planet will start to appear intransparent under transit geometry if $\tau \geq 1$, so the limiting case will be $\tau = 1$. However, because both R and n_0 are wavelength-dependent, we cannot simply solve this expression for R: the R and n_0 values are "selected" by the atmospheric extinction process as the impact parameter and planetary density (at $z = 0$), respectively, for which $\tau = 1$. In order to get rid of the wavelength dependence, at least in n_0, we define some deep, constant reference radius $R_{\rm ref}$ at which the number density is equal to $n_{\rm Ref}$, and express n_0 as $n_0(\lambda) = n_{\rm ref} \exp[-z'(\lambda)/H_P]$. It is then possible to solve for the new height $z'(\lambda)$ above $R_{\rm ref}$ where the planet becomes optically thick by setting $\tau = 1$, and one finds that

$$z'(\lambda) = H_P \log\left[n_{\rm ref} \sigma(\lambda) \sqrt{2\pi R H_P}\right] . \tag{1.12}$$

Strictly speaking also R depends on λ, but it only occurs inside the logarithm, so we neglect this dependence here. We thus see that the amplitude of the transit radius of the planet is linearly proportional to the atmospheric scale height, and has a log-dependence on the cross-section of the atmosphere. As the atmospheric scale height is proportional to the temperature and inversely proportional to the atmospheric mean molecular weight and gravity, this directly shows why these three quantities have a strong influence on whether a planet has a large or small expected transit amplitude. The relative transit signal strength $A/(\pi R_*^2)$ can finally be derived from calculating the planet's area A as seen under transit geometry, which is

$$A = \pi \left[R_{\rm ref} + z(\lambda)\right]^2 \approx \pi R_{\rm ref}^2 + 2\pi R_{\rm ref} z'(\lambda) , \tag{1.13}$$

and yields the desired dependence of $\propto H_P R_{\rm Pl}/R_*^2$ for the spectral amplitude. More details on the derivation summarized here can be found in (Fortney 2005; Lecavelier des Etangs et al. 2008; Heng et al. 2015). Assumptions made here, such as the atmosphere's temperature to be constant, or that σ does not depend on s, are motivated by the fact that temperature variations during a grazing transit of the photon are expected to be small, and that the atmosphere becomes optically thick (i.e. fully blocks all grazing light) in regions where the atmospheric cross-sections are not yet strongly dependent on pressure (see, e.g., Heng & Kitzmann 2017).

One effect not discussed so far is diffraction: as the stellar light travels through the planet's atmosphere, it encounters regions of varying density, and hence regions of varying refractive index. The light will thus be bent away from its original path, and towards the

regions of higher density. Light which travels through the planet's terminator at small impact parameters will be most strongly diffracted. Without diffraction, the rays which travel through the planet's terminator, and towards the observer, originate on the spot on the stellar surface which can be found by projecting the planet's terminator onto the star. However, the smaller the impact parameter becomes the larger the angular distance between the true origin and the projected origin of the rays becomes, because of diffraction. Hence, for small enough host stars, and/or large enough orbital separations, there exists a minimum impact parameter below which no grazing ray originating from the stellar surface can ever reach the observer, because they are bent too strongly (see, e.g., Bétrémieux & Kaltenegger 2014). For hot jupiters this effect is negligible, because the planets are so close to their stars that the atmospheres become optically thick at impact parameters larger than this critical impact parameter (Hubbard et al. 2001).

Emission spectroscopy

Planets which are in circular orbits will also be eclipsed by their stars. This means that as the planet vanishes behind its star the flux in a given wavelength bin exhibits a relative decrease of

$$\frac{\Delta F}{F} = \frac{F_{\rm day} R_{\rm Pl}^2}{F_{\rm day} R_{\rm Pl}^2 + F_* R_*^2} \approx \frac{F_{\rm day} R_{\rm Pl}^2}{F_* R_*^2} \,. \tag{1.14}$$

I write $F_{\rm day}$ for the planetary flux here because eclipse measurements probe the dayside flux of the planet's atmosphere, the planet's dayside being visible just shortly before and after the eclipse. If one assumes blackbody emission, and the planet's dayside temperature to be similar to the equilibrium temperature as defined in Equation 1.1, then one obtains contrast values of $\Delta F/F \sim 10^{-3}$ for hot jupiters in the near-IR (NIR) and mid-IR (MIR) wavelengths. This means that the measuring principle of transit and emission spectroscopy is very similar: One compares the wavelength-dependent star+planet flux shortly before the eclipse with the star-planet flux during the eclipse.

In conclusion, this means that eclipse measurements directly probe the temperature of the emitting layers of planetary atmospheres, especially from the NIR towards the MIR. This also lead to the name 'Emission Spectroscopy' for these kinds of measurements. In the optical and also the NIR the planetary flux may be affected by reflection of stellar light due to scattering, e.g. because of clouds on the planets' daysides.

If a planet is cooler than expected on its dayside this can mean that a significant amount of insolation energy is transported around to the nightside by winds, or that the planet has a high albedo, i.e. it scatters a large amount of the stellar light back to space instead of absorbing it. Thus, eclipse observations in the optical wavelengths, as well as observations of the emission of the planetary nightside (also see the next section on phase curves) help to determine the cause of cool daysides (also see Cowan & Agol 2011).

Emission spectra can also shed light on the molecular composition on the dayside of planetary atmospheres: as the emitted light travels out of the atmospheres molecules in overlying cooler (or hotter) regions of the planet may imprint absorption (or emission)

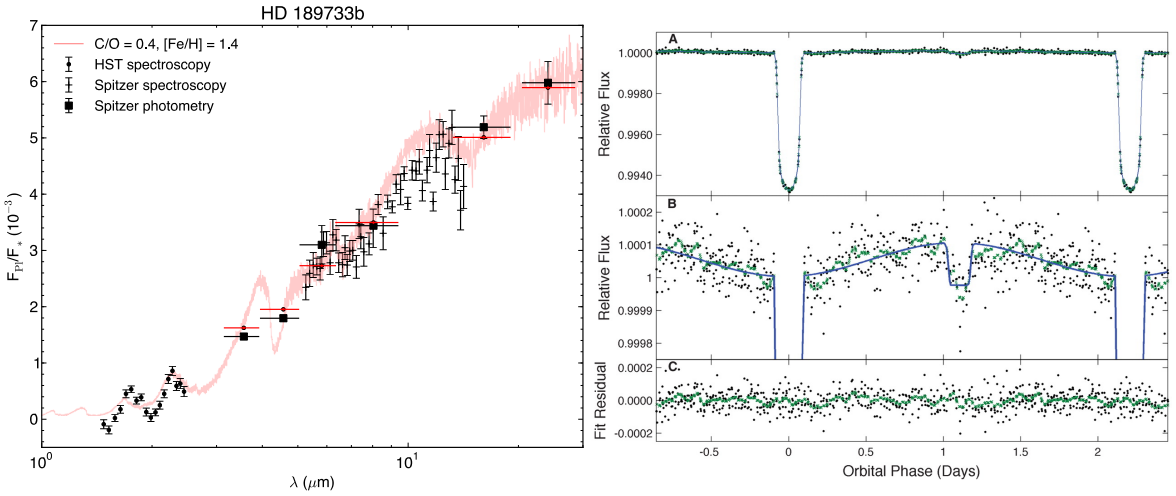

FIGURE 1.5: *Left panel:* Model emission spectrum of HD 189733b (from Mollière et al. 2015) with data taken from Knutson et al. (2012a); Charbonneau et al. (2008); Agol et al. (2010); Swain et al. (2010); Grillmair et al. (2008). The photometric and spectroscopic data obtained by *Spitzer* are shown as black squares and crosses, respectively. The *HST* spectrum is denoted by black dots. *Right panel:* Optical *Kepler* phase curve of the planet HAT-P-7b, showing the flux of the planet–star system as a function of orbital phase (figure taken from Borucki et al. 2009).

features onto the spectrum, which may be conclusively linked to the presence of a given molecule when observed.

Given that the emission signal of hot jupiter is of the same magnitude as the transmission signal amplitude, and that the amplitudes of molecular features imprinted in emission spectra are weaker still, it explains why emission spectral observations are challenging. One of the planets with the highest quality data is HD 189733b, an emission spectrum of which is shown in the left panel of Figure 1.5. In the data obtained for this planet (Knutson et al. 2012a; Charbonneau et al. 2008; Agol et al. 2010; Swain et al. 2010; Grillmair et al. 2008) the absorption features of water from 1.4 to 2.4 μm and in the MIR from $\sim$ 6 to 8 μm are clearly visible.

One additional question is to ask whether the data obtained from such measurements currently allow to estimate the composition of planetary atmospheres reliably, which seems to be difficult given the sparse data, often based on the *Spitzer* space telescope, (see, e.g., Line & Yung 2013; Madhusudhan et al. 2011b; Kammer et al. 2015). Here it seems that we may have to wait for the upcoming *James Webb Space Telescope* (JWST) to make the next leap forward in terms of data quality (see, e.g., Greene et al. 2016; Mollière et al. 2017). One question we may then also answer is why some of the hottest hot jupiters appear to have vertically isothermal dayside atmospheres, or even inversions (Haynes et al. 2015; Shporer et al. 2014; Nymeyer et al. 2011), which I also investigated in Mollière et al. (2017), see Chapter 5.

Phase curves

If the orbit of a planet has a large inclination, as it is the case for a transiting planet, then it is possible to observe the planet–star system for the whole duration of one or multiple orbits, and to detect the variation of the total flux as the planet's hot day- and cold nightside

periodically faces towards the Earth. Because such measurements will reveal the phase-dependent flux of the planet they are called 'phase curves'.

For large temperature gradients between the planetary day- and nightside, the phase curve will show a clear sinusoidal variation with a maximum flux measured around the time just before and after the eclipse, if the planet is transiting, because we are then seeing its full dayside. Similarly, the minimal flux value (neglecting the planet's transit) will reveal the planet's nightside emission, but only if the planet is indeed a transiting planet: the eclipse depth, which reveals the stellar flux without the contribution of the planet, is needed to set the planetary zero-flux baseline, see the example following immediately below.

In the right panel of Figure 1.5 I show an optical phase curve for the transiting hot jupiter HAT-P-7b, obtained with the *Kepler* telescope (figure taken from Borucki et al. 2009). The phase-dependent flux has been normalized to the total stellar flux, and the planetary transit, as well as the eclipse, are clearly visible. One sees that the eclipse depth is deeper than the minimum flux value, just before and after the transit, the latter of which consists of the stellar and the planet's nightside flux. Because the flux value measured during eclipse contains only the flux of the star, and is less than the planet's nightside + stellar flux, this indicates that Borucki et al. (2009) have indeed measured the nightside emission. The planet's dayside flux is most likely a combination of thermal emission and of reflected stellar light (Borucki et al. 2009).

From the shape of the periodic variation of the planetary flux it is thus possible to assess the longitude-dependent temperature of the planet. This also gives insight into the atmospheric dynamics of a planet: if the amplitude of the variation is weak this can mean that there is a small temperature gradient between the day- and the nightside, which indicates (for tidally locked planets) that the atmosphere is very efficient in transporting the insolation received on the dayside around to the planet's nightside. For hot jupiters we expect this energy transport to be dominated by strong, eastward blowing jets in the planet's atmospheres, which leads to another interesting effect: If this energy transport is efficient, i.e. if the timescale for the motion of the winds around the planet is shorter than the radiative cooling timescale of the planet, then we expect the hottest point of the planet to be not the substellar point, but to be offset in the eastward direction (see, e.g. Showman & Polvani 2011). This is because the cool gas brought around by winds from the nightside of the planet needs some time to heat up, and because it will retain the energy received from the star on the dayside for some time before re-radiating it back to space. Consequently, one expects the flux maximum to occur prior to the eclipse, which has indeed been observed for a number of planets (e.g. Knutson et al. 2007, 2012b; Zellem et al. 2014; Stevenson et al. 2014b).

Furthermore, carrying out phase curve observations at multiple wavelengths has made it possible to infer the phase-dependent vertical temperatures of hot jupiters (Stevenson et al. 2014b), because different wavelengths probe different depths in a planetary atmosphere. What is more, the same measurements enabled the authors to place constraints on the altitude-dependence of the horizontal jet's velocity, by analyzing the angular eastward shift of the hot spot as a function of wavelength.

An interesting exception to gas planet phase curves is the planet 55 Cancri e, which is a

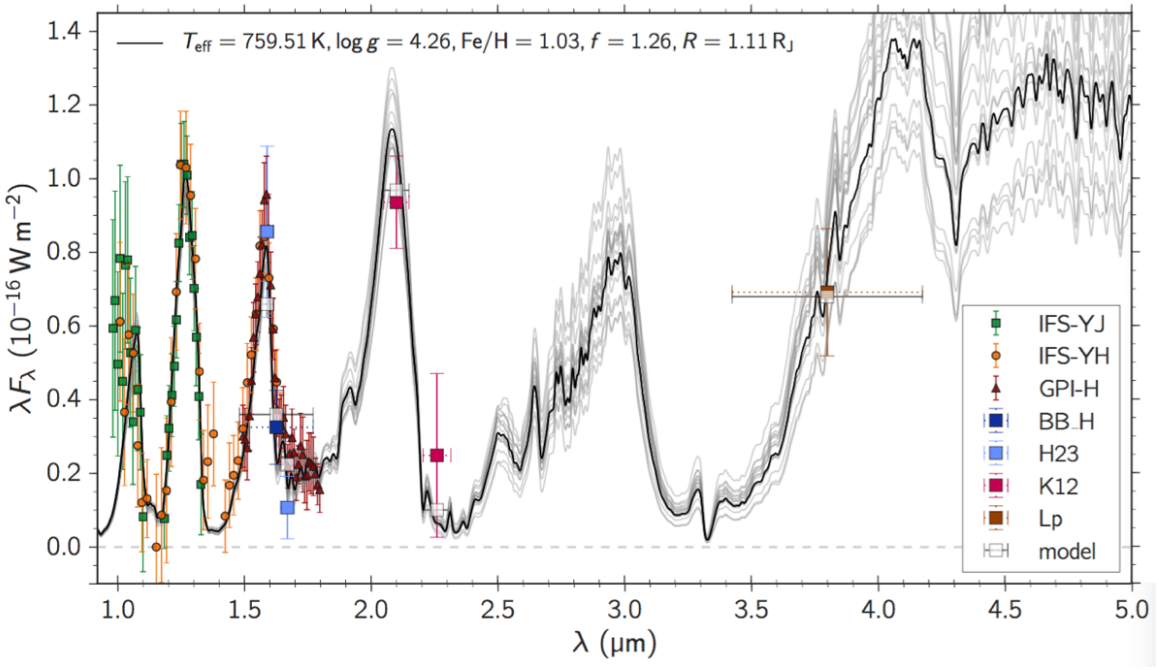

FIGURE 1.6: Spectrum of the directly imaged planet 51 Eri b, taken from (Samland et al. 2017). The data shown in this plot stems from the *SPHERE* instrument and *GPI* observations by Macintosh et al. (2015). The model fit to this data has been obtained by interpolating a grid of cloudy models calculated with my *petitCODE* using the version described in Mollière et al. (2017).

8.1 $M_\oplus$, 1.9 $R_\oplus$ super Earth in a 0.74 day orbit around a K0 host star (Fischer et al. 2008; Winn et al. 2011). The phase curve of this planet shows a strong offset, but no brightness variation on the nightside, indicating either a strong atmospheric temperature redistribution, exclusively on its dayside, or possibly the absence of an atmosphere, with magma flows being responsible for the high dayside temperatures (∼2700 K) and offset (Demory et al. 2016).

To summarize, wavelength-dependent phase curve observations, especially of transiting planets, are highly useful to assess the vertical and longitudinal temperature and velocity structure of hot jupiter atmospheres. At the same time they are very time-demanding, requiring continuous observation for a full orbital phase (∼days), which makes the use of space-based telescopes such as *HST*, *Spitzer*, and, in the future, *JWST* necessary. With the *JWST* especially the measurement of the planetary bolometric luminosity will be possible, if phase-curves are taken in the NIR and MIR wavelengths.

Direct imaging spectroscopy

Obtaining spectra of directly imageable planets makes use of the same techniques outlined above for the detection of planets by direct imaging (Section 1.2.3). For these spectra a given planet is imaged in different wavelengths. Hence such spectral observations can target young (i.e. luminous) planets in distances of tens to multiple tens of AUs around their host stars.

Notable examples of spectra and photometry taken of directly imageable planets are β Pictoris b (Bonnefoy et al. 2013; Currie et al. 2013), 51 Eri b (Macintosh et al. 2015; Samland

et al. 2017), the four HR 8799 planets (Konopacky et al. 2013; Bonnefoy et al. 2016; Zurlo et al. 2016) and GJ 504b (Skemer et al. 2016).

All of the above planets have photometric colors comparable, or redder than expected when compared with cloudy brown dwarfs of similar effective temperatures, or exhibit spectra which are inconsistent with spectral model predictions of cloudless atmospheres. The, potentially, increased cloudiness of directly imaged planets may in part be explained by their lower surface gravity in comparison to brown dwarfs: planets are, per definition, less massive. A lower surface gravity may allow for the mixing of cloud particles to higher altitudes in the atmosphere, which settle less strongly, but also to a higher-altitude location of the cloud deck in the atmosphere. Both processes may place cloud particles in or above the planets photosphere when compared to objects with higher surface gravity.[13]

That being said it is worth noting that a cloud-free explanation for the reddish brown dwarf and exoplanets spectra has been suggested: In the cooler, upper parts of these objects' atmospheres CH_4 and H_2O are expected to be the most abundant carbon and oxygen carrying molecular species at the expense of CO, which dominates the deeper, hotter atmospheric regions. Because the net chemical reaction in this case is $CH_4 + H_2O \rightleftharpoons CO + 3\,H_2$, one sees that the upper part of the atmosphere has a smaller number of molecules, and therefore a higher mean molecular weight. The atmosphere may thus be prone to the Rayleigh-Taylor instability. In this case, part of the planetary flux is carried by atmospheric motion, leading to smaller temperature gradients and spectral model predictions more in line with observations (Tremblin et al. 2015, 2016).

An example of the data quality attainable using today's direct imaging spectrographs is given in Figure 1.6, which shows *SPHERE* spectro-photometric and *GPI* spectroscopic data as published in (Macintosh et al. 2015; Samland et al. 2017). The molecular features of both H_2O and CH_4 between 1 and $\sim$1.8 μm are clearly visible in this plot, as well as the elevated flux in the K-band around 2 μm, which points to an increased metal content for this planet (Samland et al. 2017). Inferences on quantities such as the metallicity, but also the cloudiness, make the statistical comparison of the data and synthetic spectra necessary. In this case the synthetic predictions were obtained from my *petitCODE* which is described in Chapter 3.

High dispersion spectroscopy

The last observational technique I want to mention here is the so-called 'High dispersion spectroscopy'. This method uses that the planet and star are in orbit around each other. As we can see from Equation 1.2, the planet's orbital velocity will be faster by a factor $M_*/M_{\rm Pl}$ than that of the star, which puts it in the range of $\sim$100 km/s for hot jupiters, resulting in relative frequency shifts of the planetary spectra of 0.03 %. Thus high resolution spectrographs (i.e. those with a high *dispersion*) with a spectral resolution of multiple (tens of) thousands,

[13] The photosphere denotes the region where the atmosphere becomes optically thin, i.e. where radiation is able to leave the planet without subsequent absorption or scattering. The photosphere sits at smaller pressures in planets of lower $\log(g)$. At such smaller pressures the condensates form at lower temperatures than before, i.e. higher up in the atmospheres, if they are free of inversions.

but better even hundreds of thousands if individual lines are to be resolved, are able to detect such frequency shifts of molecular lines and features.

Furthermore, due to the temperature difference between planet and star, the planet's spectrum may contain spectral features of molecules such as CO, H_2O or CH_4, which are absent from stellar spectra, and have unique spectral line positions ("fingerprints"). This latter fact may be used to boost the SNR of the planet's spectrum, superimposed on that of the star, by a factor $\sqrt{N_{\rm lines}}$, where $N_{\rm lines}$ is the number of known lines in the spectral region of interest (see, e.g., Snellen et al. 2015). The means for recognizing such a molecular line pattern in the planet+star spectrum is to "slide" a molecular template spectrum (the 'mask') across the total spectrum, looking for the frequency offset where mask and spectrum agree best. Mathematically this is done by computing the cross-correlation between spectrum and mask, which is an operation essentially similar to a convolution. For frequency shifts corresponding to the planet's line-of-sight orbital velocity the cross-correlation signal will be maximal, and if high enough represent the successful detection of a molecular species in the planet's atmosphere.

One of the advantages of this atmospheric sensing technique is that the planet under consideration does not need to be transiting, which has been used for τ Boötis b (Brogi et al. 2012; Rodler et al. 2012) to detect CO, 51 Peg b (Birkby et al. 2017) to detect H_2O, and HD 179949 to detect both water and CO (Brogi et al. 2014), and allows to measure the planetary orbital inclination and hence its mass, in combination with RV. Further, the analysis of the dayside emission of transiting exoplanets has led to the detection of H_2O (Birkby et al. 2013) and CO (Rodler et al. 2013; de Kok et al. 2013) in HD 189733b.

However, not only the orbital dynamics of a planet–star system can be constrained by high dispersion measurements: When observing the transit of the hot jupiter HD 209458b Snellen et al. (2010) were able to detect CO molecules in this planet's atmosphere, as well as a blueshift of 2 km/s of the line center positions. Because during mid-transit the orbital line-of-sight velocity of the planet is zero, Snellen et al. (2010) concluded that this shift arises from the eastward blowing jets in this planet's atmosphere. This is a value consistent with theoretical predictions (see, e.g., Agúndez et al. 2014). Apart from the wind velocity on hot jupiters, also the rotation of a planet has been measured, by fitting for the line shape itself, using cross-correlation: Snellen et al. (2014) report on an equatorial rotational velocity of $\sim$25 km/s for β Pic b, based on the rotational broadening inferred for the CO lines in this planet.

High resolution spectroscopy has thus proven useful to characterize planets which are close to their stars, but not necessarily transiting, as well as directly imageable planets. At the same time it can give insight into the orbital dynamics, planetary wind speeds and spin rates. This is a remarkable yield. It also comes at a cost, however: The line contrast above the stellar component needs to be strong enough, and the availability of stable, high-resolution spectrographs on large telescopes is necessary (Snellen et al. 2015). Nonetheless, and most excitingly, it has been shown that high-dispersion measurements may allow to characterize the atmosphere of the newly discovered, habitable-zone (super?-)Earth Proxima Centauri b (Anglada-Escudé et al. 2016), once the 39 m telescope, *E-ELT* and its *METIS* spectrograph

become available (Snellen et al. 2015; Turbet et al. 2016).

1.4.2 Atmospheric characterization techniques

Once observations have been obtained, the analysis and interpretation of the data are the next steps. The result of an analysis can be evident, such as the clear (by-eye) detection of a known molecular feature in a spectrum. Yet, in most cases one wants to answer more complicated questions like *"what is the abundance of molecule X (with errorbars)"*, *"what is the upper abundance limit for an undetected molecule?"* or *"what is the vertical temperature profile of an atmosphere which gives rise to the observation?"*. The answers to such questions lie in *some* sort of comparison of the observational data with *some* sort of model, the choice of which can influence the results and the implications of which need to be kept in mind during the analysis. In this section I want to summarize the tools which are available for drawing such inferences, also known as 'retrievals', and concentrate mostly on methods using the Markov Chain Monte Carlo (MCMC) or Nested Sampling approach.

Self-consistent models and their data – model comparison

Self-consistent models typically calculate atmospheric observables such as emission or transmission spectra by solving for the atmospheric structure in a physically consistent fashion. This means that input parameters are physically meaningful quantities such as atmospheric elemental abundances, planetary mass, radius and luminosity, host star radius and temperature, and the orbital distance between the planet and star. The models then solve for the atmospheric temperature and abundance structure, as well as the planet's radiation field, by enforcing physical concepts such as radiative-convective equilibrium and chemical equilibrium (see sections 3.6 and 2.3.1, respectively). The result are the "correct" planetary observables, "correct" in the sense that they fulfill all the physical constraints that make up the model. Such models are highly useful to explore the influence of parameters as, say, the host star spectral type on planetary atmospheric structures and spectra. They allow to explore the atmosphere's physical behavior *if* the physical assumptions entering into the model are justified. The *petitCODE* which I constructed as part of my PhD project is such a self-consistent code (see Chapter 3), and the example of varying the host star spectral type is described in Chapter 4, Section 4.5.

For quantitative data evaluation self-consistent models are of limited use, however: they are usually computationally expensive, as they often try to satisfy the underlying physical constraints in an iterative fashion. Thus, it can be cumbersome to carry out a χ^2 minimization, for example, because many model realizations may have to be calculated. This problem can be circumvented by calculating, and interpolating in model grids, but only if the grid range and dimensionality is not too large. Results of my code were used for such an approach, in combination with an MCMC framework, see Samland et al. (2017). Alternatively, only a small set of models is calculated, and a first order, more qualitative characterization can be carried out by exploring which model realization is in closest agreement with the data. This has been done in, e.g., Fortney et al. (2005); Burrows et al. (2005, 2007); Fischer

et al. (2016), and also I contributed to such studies (Mancini et al. 2016a,b; Southworth et al. 2017; Mancini et al. 2017). The second disadvantage is more fundamental: If there is an important physical phenomenon which is not covered by the self-consistent model, then it will not be able to find a meaningful best-fit to the data.

Parametrized models and bayesian retrievals

A solution around the numerically costly self-consistent models is the construction of parameterized models. These models have the molecular abundances and temperature values of the atmospheric layers as free parameters. For computational convenience most retrieval codes use a few-parameter function to describe the atmospheric temperature profile, and use this function's parameters as free parameters instead. In this case, the need for fulfilling certain physical constraints is neglected, and the spectra of many model realizations can be calculated quickly.

There exist multiple forms of retrieval approaches. One is, for example, the so-called Optimal Estimation method, which is essentially a χ^2 minimization between the model and the data, but this method assumes a Gaussian distribution of the retrieved parameters, and thus their uncertainty estimate may be inaccurate (see, e.g., Line et al. 2013b, and the references therein).

MCMC and Nested Sampling make use of Bayes' Theorem, $P(B|A)P(A) = P(A|B)P(B)$, where $P(A)$ is the probability that event A is observed and $P(A|B)$ is the conditional probability that A is observed, given that the event B has been observed. Thus, the probability that a set of given free parameters $\mathbf{x}$ describes the observed spectral data $\mathbf{d}$ is

$$P(\mathbf{x}|\mathbf{d}) = \frac{P(\mathbf{d}|\mathbf{x})P(\mathbf{x})}{P(\mathbf{d})} \,, \tag{1.15}$$

where $P(\mathbf{d}|\mathbf{x})$ may simply be calculated from the χ^2 between the model and the data, such that $P(\mathbf{d}|\mathbf{x}) = e^{-\chi^2/2}$, and $P(\mathbf{x})$ encapsulates any prior knowledge about the parameter distribution, such as the fact that temperatures cannot become negative. It is thus also called 'prior'. Finally, $P(\mathbf{d})$, also called 'model evidence', is simply the integral of $P(\mathbf{d}|\mathbf{x})P(\mathbf{x})$ over all $\mathbf{x}$ values. Hence, all the quantities on the right hand side (RHS) of Equation 1.15 are straightforward to calculate. However, if the model describing the atmosphere is highly dimensional (such as 5 parameters describing the molecular abundances and 5 parameters describing the temperature structure, which yields 10 dimensions) getting a good estimate of $P(\mathbf{x}|\mathbf{d})$ can become quickly unwieldy, especially because we require the model evidence $P(\mathbf{d})$, which is a 10-dimensional integral! This is where MCMC comes into play, as it allows to efficiently sample $P(\mathbf{x}|\mathbf{d})$ using a Monte Carlo approach (also see Section 6.2), efficiently meaning that still of the order of 10^6 model evaluations need to be carried out. Nonetheless, one is rewarded with samples of the actual multidimensional parameter distribution functions, which allows to assess the parameter uncertainties, but also correlations between the retrieval parameters.

Even though I just said that the calculation of the model evidence is too numerically costly, there exists the method of so-called nested sampling Skilling (2004), which can do this

in a numerically efficient way, by estimating which volume $dX = P(\mathbf{x})d\mathbf{x}$ maps to a certain $P(\mathbf{d}|\mathbf{x})$ value interval. The algorithm goes to increasingly narrower $P(\mathbf{d}|\mathbf{x})$ iso-contours of larger $P(\mathbf{d}|\mathbf{x})$ values, which is why it is called 'nested sampling'. As a by-product, nested sampling generates samples of $P(\mathbf{x}|\mathbf{d})$. Because it is so efficient, nested sampling allows to carry out model comparisons, i.e. answering the question if a parametrized model M_a is better than another parametrized model M_b. Here "another model" really means a different model, not just a different value choice of the free parameters of model M_a. M_b may have completely different free parameters. Model comparisons are interesting because they allow to answer the question: *"Given the data, which of the two models is the most likely one?"*. This helps to prevent preferring model M_a, which may fit the data better than model M_b, but purely because model M_a has so many free parameters that it is essentially able to fit any data well (which is called 'overfitting'). For answering which of the two models is more likely, given the data, we can write, using Bayes' theorem,

$$P(M|\mathbf{d}) = \frac{P(\mathbf{d}|M)P(M)}{P(\mathbf{d})} \tag{1.16}$$

which yields

$$\frac{P(M_a|\mathbf{d})}{P(M_b|\mathbf{d})} = \frac{P(\mathbf{d}|M_a)P(M_a)}{P(\mathbf{d}|M_b)P(M_b)} = \frac{P(\mathbf{d}|M_a)}{P(\mathbf{d}|M_b)} = B_{ab}\,, \tag{1.17}$$

where it was assumed that we don't have any prior knowledge regarding which of the two models is more likely, in general. B_{ab} is also called 'Bayes factor'. Now, $P(\mathbf{d}|M_a)$ is nothing more than the model evidence, i.e. the norm for which I neglected to write "|M" in Equation 1.15. Hence, if a model M_a is favored over model M_b it will hold that $B_{ab} > 1$. During the calculation of the model evidences the nested sampling algorithm automatically draws samples of $P(\mathbf{x}|\mathbf{d}, M)$, such that the posterior parameter distributions are found at the same time as the preferred model. If more than two models are considered, the best of these models may be found by a pair-wise comparison of all model evidences.

There exist applications of optimal estimation (Line et al. 2012; Barstow et al. 2013), MCMC (Madhusudhan et al. 2011b; Benneke & Seager 2012; Line et al. 2013b), and nested sampling retrieval (Benneke 2015; Waldmann et al. 2015b; Line & Parmentier 2016; Lavie et al. 2016; MacDonald & Madhusudhan 2017) in the literature, with the latter becoming the state-of-the-art because in spite of nested sampling being the most numerically expensive method, it allows the direct comparison of different models. The most recent study by (MacDonald & Madhusudhan 2017) is a particularly good example to show the usefulness of nested sampling retrievals: the authors analyzed the transmission spectrum of HD 209458b, for which it was previously unclear if its weak water signals are due to its atmosphere being cloudy, or depleted in water. By carrying out a nested sampling retrieval they found that a third model is the most likely of the three, which mixes a clear and a cloudy transmission spectrum, corresponding to a partially cloudy terminator. Consequently the water abundance was slightly decreased, but not as much as in the case of the clear atmosphere.

1.5 Open questions

In the preceding sections I have tried to give an overview over the status quo of exoplanet detection and atmospheric sensing and characterization techniques, as well as some key results which the community has been able obtain so far. Before finishing this introduction, I want to revisit some of the most pressing open questions of atmospheric research. As we will see, these questions can have a direct connection to the physics of planetary formation.

1. *Inversions in hot jupiters:* in the eclipse spectroscopy part of Section 1.4.1 I already talked about the possibility of thermal inversions in hot jupiter atmospheres, i.e. high altitude regions which are heated by the absorption of UV and optical light from the star. Here the atmospheric temperature increases above the value of the deep, underlying atmosphere, causing the formation of emission (instead of absorption) features in the emission spectrum (see Section 1.4.1). As it turns out, the first claim for an atmospheric inversion in HD 209458b has been spurious (Diamond-Lowe et al. 2014; Line et al. 2016b), but there still are planets where an inversion may be a viable explanation for the data (Nymeyer et al. 2011; Shporer et al. 2014; Haynes et al. 2015). These planets should be revisited with, e.g., *JWST* to improve upon their current, sparse data, which often only consists of *Spitzer* photometry (except for the *HST WFC3* data of Haynes et al. 2015). Another question concerns the nature of the absorbers responsible for such inversions to form. The most likely candidates may be TiO and VO absorption, but their presence in the atmospheres seems challenging theoretically (Spiegel et al. 2009; Showman et al. 2009; Parmentier et al. 2013; Knutson et al. 2010; Madhusudhan 2012) and only tentative detections exist so far (Mancini et al. 2013; Haynes et al. 2015; Evans et al. 2016). Here, dedicated observations in the optical and NIR may help, although transmission spectroscopy may probe the too cool terminators, where TiO and VO condense, such that the more challenging eclipse observations are necessary (Madhusudhan et al. 2014c). Another likely absorber would be Na and K atoms in an atmosphere with C/O number ratios close to unity (Mollière et al. 2015, alse see Chapter 4, Section 4.4).

2. *Composition and non-equilibrium chemistry in exoplanet atmospheres:* eclipse, transit, direct imaging, and high dispersion spectroscopy have all been used to infer the abundances of molecules and atoms in planetary atmospheres, often using the so-called retrieval method (also see Section 1.4.2).

   While the detection of a molecule can often be unambiguous, one needs to keep in mind that the retrieved abundances can be affected by model assumptions and degeneracies: if the transmission spectra of partially cloudy atmospheres are fit with homogeneous cloud or cloud-free models, this can either lead to an over- or underestimation of molecular abundances, respectively (MacDonald & Madhusudhan 2017). On the other hand, if the mean molecular weight is adapted as a function of the abundance parameters (it is fixed at 2.3 $m_{\rm P}$ in MacDonald & Madhusudhan 2017), the spectra of

partially cloudy atmospheres may mimic clear atmospheres with a high mean molecular weight (Line & Parmentier 2016). Lastly, transmission spectra may only allow to infer atmospheric abundances to a limited degree altogether, because the transmission spectra of today's observations are not overly sensitive to the pressure being probed, and pressure and abundance can be degenerate,(Lecavelier des Etangs et al. 2008; Benneke & Seager 2012; Griffith 2014; Heng & Kitzmann 2017), but also see Rocchetto et al. (2016).

Additionally, the re-analysis of observational data has led to the refutal of claims of molecular detection or abundance values (see Swain et al. 2010; Mandell et al. 2011, and Madhusudhan et al. 2011b; Crossfield et al. 2012; Swain et al. 2013; Stevenson et al. 2014a; Line et al. 2014; Kreidberg et al. 2015; Benneke 2015).

Keeping in mind that reliable abundance measurements are difficult, it is still important to ask to what extent planetary atmospheres may be governed by non-equilibrium chemistry (also see sections 2.3.2 and 3.1.3), which occurs if the advection or photodissociation timescales in an atmosphere are shorter than chemical timescales.[14] Evidence for such non-equilibrium abundances has been found in GJ 436b and the nightside of HD 189733b, where strong atmospheric vertical mixing may dredge up CO, at the expense of CH_4, from the deeper atmospheric layers (Stevenson et al. 2010; Madhusudhan & Seager 2011; Knutson et al. 2012b). Further MacDonald & Madhusudhan (2017) report on the evidence of NH_3 or HCN in the terminator region of the hot jupiter HD 209458b, which may have been dragged around by winds from the cooler nightside. It has to be kept in mind that none of these measurements, indicating that non-equilibrium chemistry may be at play, have made conclusive detections: The measurements for GJ 436b depend on *Spitzer* broadband photometry, i.e. a CO feature could not possibly have been resolved, the HD 189733b claim stems from a mismatch of *Spitzer* broadband phase curves when compared with equilibrium chemistry model predictions, and the HD 209458b claim is based on the need for *some* additional opacity in the 1.45 to 1.65 μm wavelength range. Hence there seems to be evidence for non-equilibrium chemistry playing a role in exoatmospheres, but it is clear that especially the claims for GJ 436b and HD 189733b would strongly benefit from higher resolution data in the NIR and MIR, as could be provided with *JWST*.

Finally, another interesting question is why some hot jupiters seem to show both sodium and potassium absorption in their transmission spectra, why some only show one of the two, or none (see Sing et al. 2016, and their adapted Figure in the right panel of Figure 1.4 in this thesis). The planets in Sing et al. (2016), which show either one of the two alkali species are in the atmospheric temperature regime which is close to the condensation temperatures of alkali feldspars ($\sim$ 1400 K for orthoclase and albite, see Robie et al. 1978). Therefore one could, e.g., suspect a temperature- and condensation microphysics-dependent sequestration of alkalis as a possible cause. The condensation of these feldspars is debated, however, as the silicon atoms necessary to form

[14] 'Advection' is the transport of atmospheric gas due to winds.

them could be sequestered in minerals such as enstatite and forsterite in deeper layers of the atmosphere (e.g. Lodders 2010). Furthermore it has recently been shown that brown dwarfs do not seem to be affected by the sequestration of alkali atoms in feldspars (Line et al. 2016a). Likewise variations of factors 2-3 in the Na/K abundance ratio observed in stars (Gehren et al. 2004; Zhang et al. 2006; Takeda et al. 2012) are to small to explain the cases where only of of the two atoms is observed in transmission, as this would require relative variations by multiple orders of magnitude.

3. *Clouds and hazes in planetary atmospheres:* from what I have summarized so far it appears that the transmission of many hot jupiters and the emission of self-luminous planets is affected by atmospheric clouds. Further evidence for hot jupiter clouds are the equilibrium temperature-dependent offsets of the optical phase curves maxima of hot planets (Demory et al. 2013a; Esteves et al. 2015; Shporer & Hu 2015), thought to arise from a transition of largely reflecting (because of clouds) to largely absorbing planets. Also, the flat transmission spectrum of the super-Earth GJ 1214b indicates a highly cloudy atmosphere (Kreidberg et al. 2014). This ubiquitousness of clouds is in line with the cloudy Solar System planets. That being said, to date there exists not even a single conclusive identification of the responsible condensate species, although indirect evidence exists. The reason for this is two-fold: the often-observed transmission signal of clouds in the optical and NIR wavelengths is mostly dependent on the condensate abundance and particle size, but not the condensate species (Pont et al. 2013; Lee et al. 2014; Wakeford & Sing 2015; Sing et al. 2015; Barstow et al. 2017; Mollière et al. 2017). Secondly, *if* the particles are small enough, $\lesssim 1\ \mu\mathrm{m}$, and consist of equilibrium chemistry condensates, they would exhibit cloud resonance features in the MIR, starting from $\sim$9 μm towards longer wavelengths (Wakeford & Sing 2015; Mollière et al. 2017), the detection of which will become possible with the successful launch of *JWST*. Cloud and haze particles[15] may also form from non-equilibrium processes, such as the photodissociation of hydrocarbon or sulfur molecules which go on to form long-chained molecules or condense into S_8 droplets. Due to chemical stability constraints of these condensates, both of these pathways only work for cool exoplanets below 700 K, however (Zahnle et al. 2016; Liang et al. 2004).

   The aforementioned phase curve offsets and their temperature dependence have been compellingly explained in Parmentier et al. (2016) connecting dynamical simulations, equilibrium condensation and an ad-hoc 'cold trap' model, which traps condensates below the planetary photospheres if their cloud decks reside sufficiently deep within the photosphere. Here it seems that as the planets decrease in equilibrium temperature, the dominating cloud species are Al_2O_3 ($\sim$2200 K), $MgSiO_3$ ($\sim$1800 K) and MnS ($\sim$1500 K). While this explanation is consistent with the current data, it is only an indirect identification of the condensate species. A direct detection of a cloud resonance feature in transmission would strongly help to clarify the situation.

[15] The community sometimes denotes any particles giving rise to Rayleigh-like scattering signatures as 'hazes'. Larger particles which have flat absorption and scattering spectra are sometimes called 'clouds', but may also encompass the particles belonging to the 'haze' class at the same time.

4. *Super-Earth atmospheres:* As mentioned in Section 1.3.2, some super-Earths may have a substantial gaseous envelope, highly enriched in volatiles. If their radii imply that they are predominantly rocky, they may still have a thin atmosphere, as is the case with Earth, if the atmosphere is not eroded away by the star due to EUV and X-ray heating (Jin et al. 2014). However, the detection of a super-Earth atmosphere has been a challenging endeavor so far: transmission spectroscopy results for GJ 1214b have not revealed any molecular features and are consistent with a flat line (see Kreidberg et al. 2014, and the references therein). The planet's mass and radius are indicating that this planet must have an atmosphere, but the transmission signal indicates that it may be highly enriched (with large mean molecular weight), as well as harbor large-particle clouds (Morley et al. 2013, 2015; Mollière et al. 2017), while allowing no inference on the atmospheric, nor the cloud composition. For two more planets the existence of an atmosphere has been suggested. The first is 55 Cancri e (Tsiaras et al. 2016), which exhibits evidence for a hydrogen- and carbon-rich atmosphere, and a potential HCN absorption signal. As this planet is extremely hot, close to its star and has a low mass, it is unlikely that such an atmosphere could survive for long and would have to be constantly resupplied, e.g. from outgassing of molten rock (Kasting 1993). This may be consistent with the low inferred surface pressure of 0.1 bar (Tsiaras et al. 2016) and the evidence for a magma flows on this planet (Demory et al. 2016). The second planet is the super-Earth GJ 1132b, for which the transmission observations contain evidence of a water- and/or methane-rich atmosphere (Southworth et al. 2017), which also used results from my *petitCODE* for the atmospheric modeling. This measurement is interesting, but fully depends on one out of seven photometry points being elevated with respect to the others. As it is often the case with today's scarce and large-errorbar data, for this planet (and also the other two) an observation with *JWST* would improve our understanding of super-Earth atmospheres (also see Section 5.5.1).

5. *The planet formation – composition relation:* the observational techniques introduced in this chapter can be used to constrain the atmospheric abundances (also see Section 1.4.2). I have shown that these are based on challenging measurements, and the results are depending on the models used to evaluate the observations. Nonetheless, if a successful abundance measurements are obtained, and if we can correctly connect these abundances to the atmospheric elemental composition, using our knowledge on atmospheric chemistry, then we may be able to constrain the planets formation history by trying to back-engineer where in the circumstellar disk the planet accreted its material, and how much of it. The amount of prior knowledge and assumptions that would go into such assessments would be extensive, but the results which we could hope to glean from them could transform our understanding of planet formation fundamentally.

   Given the temptation of such interesting results, work on this subject has already started some years ago (Öberg et al. 2011; Ali-Dib et al. 2014; Thiabaud et al. 2014; Helling et al. 2014a; Marboeuf et al. 2014b,a; Madhusudhan et al. 2014a; Mordasini

et al. 2016; Cridland et al. 2016; Öberg & Bergin 2016; Madhusudhan et al. 2016; Espinoza et al. 2017). The depth of the studies mentioned here varies considerably, and so do the assumptions and sophistication of the planetary formation implementations.

The current consensus is that planets which form outside the water iceline in protoplanetary disks[16] should have superstellar C/O number ratios and substellar C/H ratios, *if* the atmospheric enrichment is dominated by gas accretion, and not by the pollution of planetesimals. More specifically, if such a planet forms between the CO_2 and CO icelines (CO_2 condenses inside of CO) then C/O number ratios can approach, but not exceed, unity, because then CO gas is the predominant enrichment source of the atmosphere. If gas accretion dominates the enrichment, and the planet forms within the iceline, then slightly superstellar C/O ratios are expected. However, if the planetary atmosphere is dominantly enriched by planetesimal accretion (which seems to dominate the bulk abundances of gas giants, but not necessarily their atmospheres, see Miller & Fortney 2011; Thorngren et al. 2016), then one would expect substellar C/O ratios as well as superstellar O/H number ratios. In the case where planetesimal enrichment dominates over gas enrichment of planetary atmospheres the substellar C/O ratio may still be used to assess whether a planet has formed within or outside the water iceline, but for this a better understanding of disk chemistry is necessary. While there is consensus on how different enrichment pathways are affecting the atmospheric abundances, the relative likelihoods of these are still largely unexplored, but necessary to connect atmospheric abundances and planetary formation. However, if it would become possible to tell at which distances planets formed, this would also constrain the possible migration mechanisms: A hot jupiter which formed outside the water, or even the CO_2 iceline, cannot have migrated to short orbital separations by disk migration, because then it would have accreted substantially from within the respective icelines. In this case migration pathways such as Kozai or planet–planet scattering would become more likely (see Section 1.3.1).

1.6 Thesis overview

The following chapters of this thesis are organized as follows:

- In Chapter 2 I will review the theory necessary for the construction of my atmospheric code, *petitCODE*. I will later make explicit reference to, and use of some of the equations contained in this chapter, such that in parts I reproduce rigorous derivations.
- In Chapter 3 I describe the setup and methods of *petitCODE*, which I wrote from scratch. I also list the laboratory data necessary for such a code, such as the molecular line lists.

[16] The ice line (or snow line) is the orbital distance in a protoplanetary disk beyond which water condenses, due to the radial temperature decrease.

- Chapters 4 and 5 describe my published applications of *petitCODE*, in which I investigate the global properties of hot jupiter atmospheres, and make detailed predictions for the diverse planet population which we expect to observe with *JWST*.
- Chapter 6 presents my ongoing work on atmospheric retrieval studies, and adapting the tools of *petitCODE* for that purpose.
- Chapter 7 contains the summary and outlook of this thesis.

2 Physical properties of planetary atmospheres

In this chapter I will outline the most important theoretical concepts used for constructing my numerical atmospheric model called *petitCODE*, which is described in Chapter 3. The description here is done in some detail, because I will later simply reference this chapter. Therefore Chapter 3, and the present chapter, can be understood as the full model description of *petitCODE*, treated such that there is a separation between methods and theory.

2.1 Dynamics and structure

Due to the large densities in planetary atmospheres, and thus short mean free paths of the atmospheric molecules, the behavior of the atmospheric gas can be well described by hydrodynamics. The differential heating of planets (equator vs. pole, day- vs. nightside), as well as their rotation and the resulting Coriolis force, give rise to atmospheric waves which in turn drive atmospheric circulation patterns. Numerical models which study the atmospheric circulation are commonly called 'General Circulation Models', or GCMs. In the discussion on phase curves I have already talked about the role of eastward moving jets, which transport the hot dayside gas to the nightside, and weaken the day-night temperature contrast (see Section 1.4.1). In principle the equations to be solved in such systems are the classical equations of hydrodynamics, which are

$$\frac{\partial \rho}{\partial t} = -\nabla \cdot (\rho \mathbf{u}) \tag{2.1}$$

for the conservation of mass, with ρ being the density and $\mathbf{u}$ the three-dimensional velocity vector, and

$$\rho \left(\frac{\partial \mathbf{u}}{\partial t} + \mathbf{u} \cdot \nabla \mathbf{u} \right) = -\nabla P - \rho g \mathbf{e}_r \, , \tag{2.2}$$

for the conservation of momentum, where P is the gas pressure, g the gravitational acceleration in the atmosphere, due to the planet's mass, and $\mathbf{e}_r$ is the planet's radial unit vector. Viscosity terms have been neglected for clarity. Note that the Coriolis and centrifugal force are not explicitly given in the above momentum equation, but can be obtained by transforming into a coordinate system rotating with angular velocity $\mathbf{\Omega}$. Here we have five unknowns,

ρ, $\mathbf{u}$ and P, but only four equations, such that a fourth equation is necessary to close the system. One possibility is to have a barotropic equation of state.[1] For planets, however, which can be heated by their star, and cool radiatively, the consideration of the energy conservation equation is necessary. For planetary atmospheres it is usually found that the vertical velocities are much lower than the sound speed (see, e.g., Heng & Showman 2015), such that the LHS of the vertical momentum conservation equation may be neglected (which does not mean that vertical velocities are zero!), and leaves us with the so-called equation of hydrostatic equilibrium:

$$\frac{dP}{dr} = -\rho g \,, \tag{2.3}$$

where spherical symmetry of the planet was assumed. This means that atmospheric pressure gradients balance the force of gravity with pressure increasing as the radius decreases. This is a central equation for the description of my atmospheric model to follow in Chapter 3.

2.1.1 Large-scale circulation and winds

Circulation on hot jupiters

The circulation on hot jupiters is driven by the large dayside–nightside as well as the equator–pole temperature contrasts, and the atmosphere's tendency of striving towards a global equilibrium. The global circulation pattern can be understood as the interaction between two kinds of waves, namely Rossby waves and Kelvin waves. The large temperature gradients in the latitudinal direction (equator vs. pole) create standing Rossby waves, propagating longitudinally westwards. Because Rossby waves are transverse waves, they will give rise latitudinal oscillations of the gas, i.e. in the north–south direction. Due to angular momentum conservation the latitudinally oscillating gas has to rotate, which leads to the formation of eddies.[2] At the same time, the dayside–nightside temperature contrast drives Kelvin waves, which propagate into the eastward direction, and the superposition of which onto the Rossby wave pattern leads to a tilting of the Rossby eddies from north-west to the south-east on the northern hemisphere, and from south-west to north-east one the southern hemisphere. These wave patterns are depicted in Figure 2.1, taken from (Showman & Polvani 2011). The tilted eddies transport angular momentum from the planet's poles to the equator, giving rise to eastward flowing jets. Because the jet transports gas eastwards, this kind of circulation is also called 'superrotation'.

As the jet transports heated gas from the day- to the nightside, it causes a dampening of the temperature contrasts between the two hemispheres. Here it is important to appreciate that this occurs in the photosphere of the planets, meaning that the jet can have a direct effect on the planetary emission, by changing its horizontal temperature structure. The analytical criterion of assessing whether or not the winds will have a large impact on the planetary

[1] 'Barotropic' means that the gas density depends on the pressure only, such as for adiabatic processes.
[2] An eddy can be thought of as a region of vortex-like rotation.

spectrum is by comparing the horizontal advection timescale of the jet, $\tau_{\rm adv}$, with the radiative cooling timescale of the atmosphere, $\tau_{\rm rad}$. If

$$\tau_{\rm rad} > \tau_{\rm adv} \ , \tag{2.4}$$

then the planet transports energy to the nightside more quickly than the atmosphere can cool radiatively, and one expects to see weakened day-night temperature contrasts, and a hot spot offset from the substellar points in phase curves. However, as has been pointed out by Heng & Showman (2015), this analytical relation is non-predictive: without solving for the planetary dynamics the atmospheric advection speed is unknown! Also, the above inequation does not always hold, especially when the dayside heating becomes weaker. In general, and not only in the case of weaker dayside heating, it has been suggested that the vertical advection timescale may provide a better timescale to compare the radiative timescale to (Perez-Becker & Showman 2013).

Finally, not all is lost when trying to predict the atmospheric susceptibility to a smearing out of the temperature gradients by superrotation: observations, as well as simplified analytical models, indicate that the stronger the dayside insolation becomes, the less efficient the jets become at equilibrating the dayside–nightside temperature gradients, in part because the cooling timescale strongly decreases as the planets become hotter (Perez-Becker & Showman 2013; Komacek & Showman 2016; Komacek et al. 2017). Observations show that as the planetary equilibrium temperature increases from 1000 to 2500 K, the day-night relative temperature contrast $(T_{\rm day} - T_{\rm night})/T_{\rm day}$ increases from 0.2 to 0.7, while outliers with contrasts around 1 exist at all temperature ranges (Komacek et al. 2017).

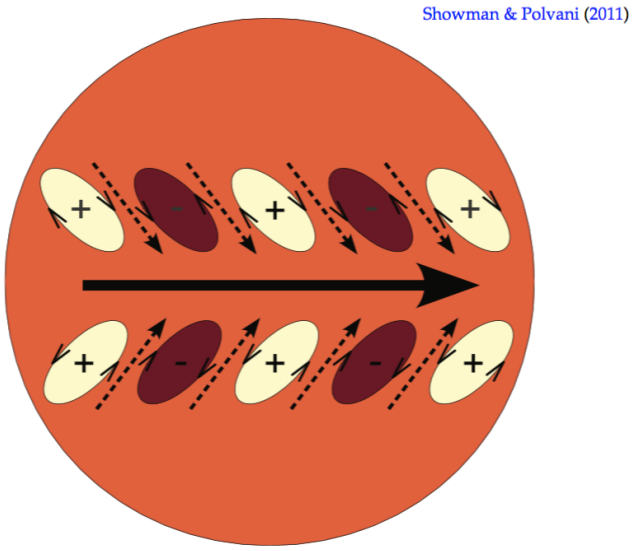

FIGURE 2.1: Dominating circulation pattern on hot jupiters: the equator–pole temperature contrast creates longitudinally propagating, standing Rossby waves traveling in the westward direction. The latitudinal oscillation of these waved forms eddies, due to angular momentum conservation. The dayside–nightside temperature forcing creates eastward propagating Kelvin waves, which tilt the eddies into the eastward direction, which then transport angular momentum from the high latitudes to the equator, and give rise to the eastward blowing jet on the equator (figure taken from Showman & Polvani 2011).

Circulation on other planets

Hot jupiters are strongly irradiated, and because they are tidally locked, they rotate comparatively slowly (multiple days) when compared to the Solar System planets.[3] A key difference is that on the cooler Earth, but also on the Solar System gas giants, the atmospheric radiative timescale is longer than the rotational timescale, which results in the day–night temperature contrasts to be of decreased importance and the equator–pole temperature contrasts to be dominant (Heng & Showman 2015). On Earth, and on the Solar System gas giants, there exist multiple jet bands, whereas hot jupiters only exhibit a single, broad jet centered on the equator. This can be understood by considering the Rossby deformation radius (Showman & Polvani 2011),

$$R_{\rm Ross} \propto \Omega^{-1/2} \,, \tag{2.5}$$

which gives the typical jet width, and decreases as the planetary spin rate Ω increases. It has to be compared to the planetary radius in order to estimate the number and width of the jets which can form, and be qualitatively understood as the length scale over which the Coriolis forces start to overrule the north/southward-motions which would otherwise work towards the broadening of the jet.

I conclusion, the above discussion on atmospheric dynamics merely tried to point out some of the most important features, and is far from being complete. A planet's circulation pattern is influenced by many factors and its size, insolation, rotation period, and the possible presence of magnetic fields may all play a role for the resulting circulation pattern (Batygin et al. 2013; Carone et al. 2015). Also clouds have been conjectured to be able to impact the flow pattern of planetary atmospheres (Heng & Showman 2015), either by changing the temperature structure due to their absorption and scattering properties, or even because of their dynamical interaction with the flow itself, if they have a high abundance and are coupled to the gas motions sufficiently well.[4]

2.1.2 Convection

In planetary atmospheres the vertical transport of energy is, for the most part, established by radiation. In the optically thick regions, radiative energy transport can only occur if it holds for the atmospheric temperature gradient that $dT/dr < 0$, where r is the planet's radial coordinate. Such a gradient allows for a net diffusion of energy to larger radii, until the photons reach the photosphere from which they escape to space. As one enters deeper regions of the atmosphere, however, the 'opacity' of the gas (i.e. the photon extinction cross-section per unit mass) becomes so large that the temperature gradient needs to increase more and more strongly in order to transport the planet's luminosity. In such cases the atmosphere may become convectively unstable, such that the energy is transported by the rise of hot gas blobs from deeper atmospheric layers and the fall of cold gas blobs from

[3] With the exception of Mercury and Venus, which have slow spin rates due to tidal interactions and orbit-spin resonances.

[4] Where coupling here is meant in the same way as for the pebbles in Section 1.3.1.

higher atmospheric layers. The atmosphere will consequently settle into a state with a less steep atmospheric gradient. The condition for convection to occur can be derived from considering a blob of gas which starts in a given layer and is moved by a radial distance Δr. The density difference between a rising blob of gas and the surrounding atmosphere then is

$$\Delta\rho = \left(\frac{d\rho_{\rm blob}}{dr} - \frac{d\rho_{\rm atmo}}{dr} \right) \Delta r \ . \tag{2.6}$$

This means that if $\Delta\rho < 0$ the blob will be buoyant and continue to rise, because it has a lower density than its surrounding, i.e. if

$$\frac{d\rho_{\rm blob}}{dr} - \frac{d\rho_{\rm atmo}}{dr} < 0 \ . \tag{2.7}$$

By the same token blobs displaced to smaller radii will start to sink. From assuming that the sounds speed is much faster than the motion of the blob[5], and hence a zero pressure difference between the blob and its surroundings, one can rewrite the above condition to

$$\nabla_{\rm atmo} > \nabla_{\rm blob}, \tag{2.8}$$

where $\nabla = d\log(T)/d\log(P)$, and radial gradients in the mean molecular weight where neglected. ∇ is often simply called 'temperature gradient', because in a hydrostatically stratified atmosphere the pressure can be regarded as the spatial coordinate in the vertical direction. If a blob rises sufficiently quickly, its temperature change can be regarded as adiabatic, such that $\nabla_{\rm blob} = \nabla_{\rm ad}$. Hence, an atmosphere where energy transport is dominated by radiation, with a corresponding temperature gradient $\nabla_{\rm rad}$, is stable against adiabatically rising blobs if

$$\nabla_{\rm rad} < \nabla_{\rm ad}. \tag{2.9}$$

This is the so-called 'Schwarzschild criterion' for stability against convection. Using the definition of the specific heat at constant pressure $c_P = (dq/dT)_P$, where q is the specific heat, as well as the first law of thermodynamics $dq = de + Pd\rho^{-1}$, where e is the specific internal energy, and furthermore the ideal equation of state $P = (\gamma - 1)\rho e$, and the equation of hydrostatic equilibrium, then one finds the more commonly used version of the Schwarzschild criterion, which is

$$\frac{dT}{dr} > -\frac{g}{c_P} \ . \tag{2.10}$$

More specifically Equation 2.9 means that the entropy cannot increase toward smaller radii, because then the atmosphere would become convectively unstable, and quickly rising and falling blobs of gas would bring the the atmospheric state back to a constant specific entropy s. Thus the Schwarzschild criterion can also be written as

$$\frac{ds}{dr} > 0 \ , \tag{2.11}$$

which is sometimes also dubbed as *"entropy likes to float"*.

[5] This also implies that the atmosphere is in hydrostatic equilibrium, see derivation for Equation 2.3.

Because the atmospheric opacity, in general, increases towards the planetary interior, so does the radiative temperature gradient, implying that all atmospheres and deep planetary envelopes are expected to be fully convective in their interior.[6]

Mixing length theory

The mixing length theory (MLT) provides a quantitative theory of convection by solving for the velocity of the rising and falling blobs, and thus the energy flux transported by convection. It has just one free parameter, which is the so-called mixing length $l_{\rm mix}$, signifying the mean distance traveled by a convective blob before it gets disrupted and mixes with its surroundings. A good introduction can be found in Kippenhahn & Weigert (1990), and I will reproduce the most important steps here.

An atmosphere with non-zero temperature gradient will always have some contribution to the flux from radiative energy transport. If the local mean free path of the photons is much smaller than the typical thickness of the atmosphere, then the radiative energy transport converts into a diffusion problem and one can write the diffusive flux as (see Kippenhahn & Weigert 1990):

$$F_{\rm rad} = \frac{16\sigma g}{3}\frac{T^4}{\kappa_{\rm R} P}\nabla_{\rm atmo}\ , \tag{2.12}$$

where σ is the Stefan-Boltzmann constant, and $\kappa_{\rm R}$ the atmospheric Rosseland mean opacity

$$\kappa_{\rm R}^{-1} = \frac{\int_0^\infty \kappa_\nu^{-1}[\partial B_\nu(T)/\partial T]d\nu}{\int_0^\infty [\partial B_\nu(T)/\partial T]d\nu}\ , \tag{2.13}$$

where $B_\nu(T)$ is the Planck function. Thus $\kappa_{\rm R}$ is sensitive to the lowest values of the frequency-dependent opacity κ_ν. Next, if the radiative flux as well as the convective flux where to be fully transported by radiation, the radiative temperature gradient would be

$$F_{\rm conv} + F_{\rm rad} = F_{\rm tot} = \frac{16\sigma g}{3}\frac{T^4}{\kappa_{\rm R} P}\nabla_{\rm rad}\ . \tag{2.14}$$

Next, a convective blob which has travelled by $l_{\rm mix}$ and has a corresponding temperature difference ΔT to its surroundings will release a specific energy of $c_P \Delta T$ as it dissolves. If the blobs travel with a mean velocity of $v_{\rm mix}$ before they dissolve, this leads to a mass flux of $\rho v_{\rm mix}$. Hence the convective flux can be written as

$$F_{\rm conv} = \rho v_{\rm mix} c_P \Delta T\ . \tag{2.15}$$

In order to find $v_{\rm mix}$ we use the definition of the pressure scale height (which I already used for the transmission signal derivation in Section 1.4.1)

$$H_P = -P\frac{dr}{dP}, \tag{2.16}$$

[6] Although detached radiative zones can exist, if the temperature-dependent opacities have a local minimum somewhere on the way towards the planetary center (see, e.g., Burrows et al. 1997; Fortney et al. 2011).

which allows us to express a blobs temperature difference to its surroundings as

$$\frac{\Delta T}{T} = \frac{\nabla_{\rm atmo} - \nabla_{\rm blob}}{H_P} \frac{l_{\rm mix}}{2} \ , \tag{2.17}$$

which assumed that the average blob has on average travelled $l_{\rm mix}/2$ as it passes through an atmospheric shell. Note that Equation 2.3 yields that

$$H_P = \frac{P}{g\rho} = \frac{k_{\rm B}T}{\mu m_{\rm P} g} \ , \tag{2.18}$$

where the last equality sign assumes an equation of state for an ideal gas. Using that a blob has a zero pressure difference with respect to its surroundings one can write the density difference as $\Delta\rho/\rho = -\delta\Delta T/T$ with $\delta = -\partial\log(\rho)/\partial\log(T)$. With a specific buoyancy force of $f_{\rm b} = -g\Delta\rho/\rho$ the work done over a radial length of $l_{\rm mix}/2$, with an average force of $f_{\rm b}/2$ leads to the average kinetic energy of

$$v_{\rm mix}^2 = g\delta \frac{\nabla_{\rm atmo} - \nabla_{\rm blob}}{H_P} \frac{l_{\rm mix}^2}{8} \ . \tag{2.19}$$

Finally, by assuming that the blob radiatively heats its surroundings as it rises, one has to modify its adiabatic temperature change. In the end one finds the following expression (Kippenhahn & Weigert 1990):

$$\frac{\nabla_{\rm blob} - \nabla_{\rm ad}}{\nabla_{\rm atmo} - \nabla_{\rm blob}} = \frac{24\sigma T^3}{\kappa_{\rm R}\rho^2 c_P l_{\rm mix} v_{\rm mix}} \ . \tag{2.20}$$

Using the five equations 2.12, 2.14, 2.15, 2.19, and 2.20 it is now possible to solve for the five unknown quantities $F_{\rm rad}$, $F_{\rm conv}$, $\nabla_{\rm blob}$, $\nabla_{\rm atmo}$, and $v_{\rm mix}$. This is done in Appendix A.2.3.

MLT further allows to define a quantity Γ, which is defined as the ratio of the convective energy flux and the flux which arises from the blobs' radiative losses (Kippenhahn & Weigert 1990). By rearranging the equations correctly one finds that

$$\lim_{\Gamma\to\infty} \nabla_{\rm blob} = \nabla_{\rm ad} \ , \tag{2.21}$$

$$\lim_{\Gamma\to\infty} \nabla_{\rm atmo} = \nabla_{\rm ad} \ , \text{ and} \tag{2.22}$$

$$\lim_{\Gamma\to 0} \nabla_{\rm atmo} = \nabla_{\rm rad} \ . \tag{2.23}$$

Because the transition from $\nabla_{\rm atmo} = \nabla_{\rm rad}$ in higher atmospheric altitudes to $\nabla_{\rm atmo} = \nabla_{\rm ad}$ in lower altitudes usually occurs over very short distances as the atmospheric convection sets in, convection is usually "implemented" by setting the atmospheric temperature gradient to

$$\nabla_{\rm atmo} = \min\left(\nabla_{\rm rad}, \nabla_{\rm ad}\right) \ , \tag{2.24}$$

where I made use of the Schwarzschild criterion (Equation 2.9). If MLT is implemented, then the mixing length is usually chosen to be

$$l_{\rm mix} = \alpha H_P \ , \tag{2.25}$$

where α is a factor of order unity (Papaloizou & Nelson 2005).

2.2 Radiation field and opacity sources

In the upper part of planetary atmospheres the energy arising from the planet's intrinsic luminosity is transported by radiation. Additionally, the insolation of the host star impinges on the atmosphere from above, such that the atmosphere is sandwiched by two heating sources. To qualitatively understand the atmospheric response to this heating in its radiative part, the so-called 'double-gray approximation', an analytical formula for the atmospheric temperature profile, is of great help (see, e.g., Thomas & Stamnes 2002; Hansen 2008; Guillot 2010). Making certain simplifying assumptions, it solves for the atmosphere's temperature structure in the so-called 'radiative equilibrium', i.e. in a state where every layer of gas in the atmosphere emits exactly as much radiative energy as it absorbs (see Section 3.6.1). This approximative formula can be derived as a byproduct of the temperature iteration scheme of *petitCODE* in Section 3.6, and the derivation is given in Appendix A.3, so here I merely state it for now:

$$T^4 = \frac{3T_{\rm int}^4}{4}\left(\frac{2}{3}+\tau\right) + \frac{3T_{\rm equ}^4}{4}\left[\frac{2}{3}+\frac{1}{\gamma\sqrt{3}}+\left(\frac{\gamma}{\sqrt{3}}-\frac{1}{\gamma\sqrt{3}}\right)e^{-\gamma\tau\sqrt{3}}\right] \ , \tag{2.26}$$

with $\tau = P\kappa_{\rm IR}/g$. Here, τ is again the optical depth, $\kappa_{\rm IR}$ is the atmospheric opacity in the IR wavelengths (i.e. the cross-section per unit mass), $T_{\rm equ}$ the atmospheric equilibrium temperature as defined in Equation 1.1, and $T_{\rm int}$ is the planetary internal temperature such that its intrinsic luminosity (arising from contraction, see Section 2.2.2) can be expressed as

$$L_{\rm int} = 4\pi R_{\rm Pl}^2 \sigma T_{\rm int}^4 \ . \tag{2.27}$$

The γ factor contains the solution to why this kind of atmospheric temperature structure is called 'double-gray': in the derivation of Equation 2.26 it is assumed that the wavelength-dependent opacity in the IR range can be approximated by a single constant value, $\kappa_{\rm IR}$. As the planet is much cooler than its host star, most of the radiation arising within its atmosphere will be within the IR wavelengths. So $\kappa_{\rm IR}$ is the mean opacity for the planetary radiation field. The γ factor defines the mean opacity in the optical (i.e. visible to humans) wavelengths as $\kappa_{\rm vis} = \gamma\kappa_{\rm IR}$. Likewise, here it is assumed that $\kappa_{\rm vis}$ is constant both vertically and within the optical wavelength range. As we will see later, this assumption is not entirely correct, but it helps to understand the situation in irradiated planetary atmospheres qualitatively. The majority of the insolation will be in the optical wavelength regime, such that $\kappa_{\rm vis}$ is the mean opacity for the stellar irradiation. I have discussed that the dynamics in the planetary atmosphere can redistribute the insolation energy on the planetary surface.

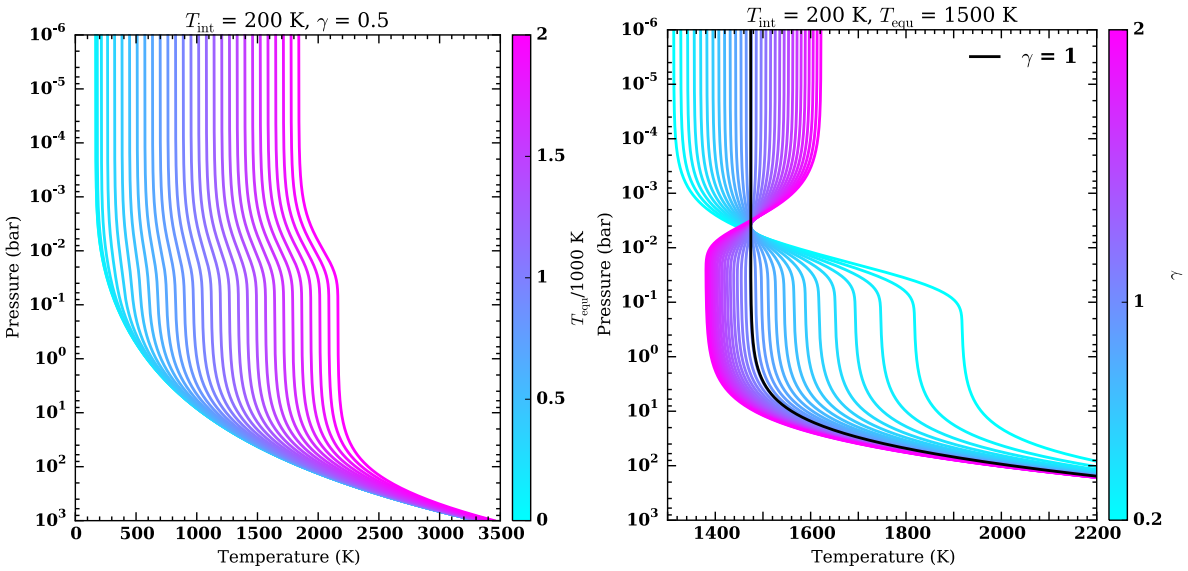

FIGURE 2.2: Vertical temperature structures calculated with the double-gray approximation of Guillot (2010). The vertical coordinate is the pressure, where low pressures correspond to high altitudes in the planet's atmosphere. *Left panel:* temperature structures for $T_{\rm int}$ = 200 K, and γ = 0.5 atmospheres with varying equilibrium temperatures, as indicated in the color coding. *Right panel:* temperature structures for $T_{\rm int}$ = 200 K, and $T_{\rm equ}$ = 1500 K atmospheres with varying γ, as indicated in the color coding. The solid black line denotes the $\gamma = 1$ case.

This is taken into account to some degree in the above double-gray approximation, namely by taking the equilibrium temperature as the incident radiation temperature of the host star, and thus assuming a planet-wide average of the insolation flux. This is, admittedly, a strong simplification, but it is not always a bad one (see Section 3.1.1), and we are only interested in qualitative effects here. Finally, an opacity constant across the wavelength space is called 'gray', and we have two such opacities here, hence the name 'double-gray approximation'.

2.2.1 Nature and effect of the insolation

The stellar light impinges on the upper part of the atmosphere, is absorbed or scattered[7], and heats the atmosphere in the process. In the MLT part of Section 2.1.2 I discussed that an atmosphere needs to have a negative (with altitude) radial temperature gradient in order to transport flux to its outer boundary. However, because the atmosphere of an irradiated planet is heated from above, its temperature gradient will become less negative. I show this phenomenon in the left panel of Figure 2.2, where I plot the vertical atmospheric temperature structure of a planet with $T_{\rm int}$ = 200 K, and γ = 0.5 for different values of $T_{\rm equ}$, i.e. for different irradiation strengths. Note that all these cases have the same total net luminosity, $L_{\rm int}$, because we look at equilibrium solutions of the atmospheric structure here, where the planet re-emits all the light received by its star. Otherwise the planet would experience a net gain of energy, heat up, and emit a larger flux: this cannot be a steady-state, equilibrium solution (we are considering the atmospheric structure after this has happened). It is evident from the plot that as the irradiation strength increases from $T_{\rm equ}$ = 0 K to $T_{\rm equ}$ = 2000 K, the

[7]Equation 2.26 does not contain any scattering, and we neglect it for now. Its effect will be discussed in Section 4.2.1.

atmospheric structure become increasingly isothermal, due to the increased heating from the top.

In the left panel of Figure 2.2 I assumed a γ value of 0.5, i.e. the atmosphere's IR opacity was twice as large as its optical opacity. What occurs in the case where we increase γ, and thereby increase the opacity responsible for absorbing the stellar flux? This is shown in the right panel of Figure 2.2, which shows planetary atmospheres with $T_{\rm int}$ = 200 K, $T_{\rm equ}$ = 1500 K when γ is varied from 0.2 to 2. Here one can see the so-called 'greenhouse effect' as well as the formation of so-called 'temperature inversions' (or 'anti-greenhouse effect').

The greenhouse effect

In cases where $\gamma < 1$ the optical opacity of the planet is lower than its IR opacity. Consequently the stellar radiation is absorbed less strongly than light in the IR would be. When the stellar energy flux has reached the location where has been fully absorbed, it has penetrated deeply into the planetary atmosphere, where it heats the gas, and prompts re-emission of energy in the IR wavelengths. At this location in the planetary atmosphere one is already well below the photosphere, in the atmosphere's optically thick part, where radiation can only escape via slow, diffusive transport. In order to ensure that all of the stellar irradiation energy gets re-emitted to space (otherwise the atmosphere would not be in equilibrium) this deep part of the atmosphere needs to attain a very high temperature, in order to have a sufficient number of photons at sufficiently high energy diffuse upward in the planetary atmosphere. This is the greenhouse effect, and one can see in Figure 2.2 that the smaller γ becomes, the hotter the deep atmosphere becomes.

The anti-greenhouse effect

The opposite effect can be seen in the 'inversion' case, where $\gamma > 1$. Because the optical opacity is larger than the IR opacity, the stellar light is absorbed in locations much higher in the atmosphere, and above the planet's nominal IR photosphere. This means that a this location the atmosphere is still optically thin in the IR, and can therefore cool poorely, such that the gas needs to heat up considerably in order to ensure that the absorbed stellar light is re-emitted to space. The local radial temperature gradient can even become positive, which explains the name 'inversion'. This seems to contradict the above statement that the temperature gradient needs to be negative with increasing altitude, but remember that we are not in the atmospheres diffusive part. Checking the atmosphere's behavior in Figure 2.2, one sees that the larger the γ value, the larger the temperatures in the upper atmosphere. Because then less irradiation remains to heat the atmospheres deeper regions, their temperatures will be lower when compared to the low γ cases.

In conclusion, one can thus say that low optical opacities lead to a greenhouse heating of the atmosphere's deeper layers, whereas large optical opacities lead to an inversion heating of the high atmospheric layers, and a cooling of the deep layers. The special case of $\gamma = 1$ is marked in the right panel of Figure 2.2: here $\kappa_{\rm IR} = \kappa_{\rm vis}$, and neither strong inversions, nor

greenhouse heating occur, and hence the atmosphere is largely isothermal. This effect will become important in Section 4.5.

The irradiation from the star has not only an effect on the atmosphere in terms of the radiative heating. It can also affect the chemical abundances of the planet by driving photochemistry, see Section 2.3.2.

2.2.2 Nature and effect of the intrinsic luminosity

The intrinsic luminosity of a gasous planet stems from its contraction and cooling. This intrinsic luminosity is constrained by the planet's mass and internal entropy, where the value of the latter is set by the heat retained from the planet's formation (see, e.g., Marleau & Cumming 2014). It is important to appreciate that the planetary interior really cools down over time (see, e.g., Burrows et al. 1997), which is in contrast to the usual statement that contracting, self-gravitating spheres of gas have a negative heat capacity. The reason for this is the partial degeneracy of the electrons in the planet's envelope, and can be derived in an approach similar to the one in, e.g., Mollière & Mordasini (2012): we start from the hydrostatic form of Equation 2.2:

$$\nabla P + \rho \nabla \phi = 0 \tag{2.28}$$

where we replaced the gravitational acceleration $-g\mathbf{e}_r$ with the gradient of the gravitational potential $\nabla\phi$. We now make a typical virial analysis and for this integrate $\mathbf{r}\cdot$(Equation 2.28) over the planetary volume

$$\int_{V_{\rm Pl}} \mathbf{r} \cdot \nabla P d\mathbf{r} + \int_{V_{\rm Pl}} \rho \mathbf{r} \cdot \nabla \phi d\mathbf{r} = 0 \, . \tag{2.29}$$

Using Gauss' theorem repeatedly one can show that

$$\int_{V_{\rm Pl}} \rho \mathbf{r} \cdot \nabla \phi d\mathbf{r} = -E_{\rm pot} \, , \tag{2.30}$$

where

$$E_{\rm pot} = \int_{V_{\rm Pl}} \rho \phi d\mathbf{r} \tag{2.31}$$

is the gravitational potential energy of the planet. The first term on the LHS of Equation 2.29 transforms to

$$\int_{V_{\rm Pl}} \mathbf{r} \cdot \nabla P d\mathbf{r} = -3(\gamma - 1) \int_{V_{\rm Pl}} \rho e d\mathbf{r} = -3(\gamma - 1) E_{\rm int} \, , \tag{2.32}$$

where Gauss' theorem, $P(R_{\rm Pl}) = 0$ and $P = (\gamma - 1)\rho e$ were used. $E_{\rm int}$ is the planet's internal thermal energy. We thus finally obtain

$$E_{\rm int} = -\frac{1}{3(\gamma - 1)} E_{\rm pot} \, . \tag{2.33}$$

As the planet leaks energy into space by the emission of photons from its atmosphere the total energy $E_{\rm tot} = E_{\rm int} + E_{\rm pot}$ will decrease. Because for this $E_{\rm pot}$ has to decrease this corresponds to a contraction of the planet.

To show that the planet actually cools one can take a limiting case where the planetary interior is fully ionized, and the electrons are fully degenerate. The internal energy can then be split into $E_{\rm int,\ ion} + E_{\rm int,\ e-}$. In the fully degenerate case the distribution of the absolute value of the electron momenta is $f_p \propto p^2$, indicating that most of the electrons are at the largest possible momentum, the Fermi momentum $p_{\rm F}$. One can then approximate that $E_{\rm int,\ e-} = N_{\rm e-} E_{\rm F}$, where $N_{\rm e-}$ is the number of electrons and $E_{\rm F}$ is the Fermi energy $\propto p_{\rm F}^2$. The Fermi momentum itself is $\propto n_{\rm e-}^{1/3}$, where $n_{\rm e-} \propto R_{\rm Pl}^{-3}$ is the electron number density, thus it holds that

$$\frac{d\log E_{\rm int,\ e-}}{d\log R_{\rm Pl}} = -2\ , \tag{2.34}$$

as well as the fact that $E_{\rm int,\ e-}$ depends ∼only on the planetary radius. Furthermore, for the gravitational potential energy it usually holds that

$$\frac{d\log E_{\rm pot}}{d\log R_{\rm Pl}} = -1\ , \tag{2.35}$$

such that

$$\frac{dE_{\rm pot}}{dE_{\rm int,\ e-}} = \frac{E_{\rm pot}}{2E_{\rm int,\ e-}} \tag{2.36}$$

For the ion internal energy it thus holds that (using Equation 2.33)

$$\frac{dE_{\rm int,\ ion}}{dR_{\rm Pl}} = -\left[1 + \frac{1}{3(\gamma-1)}\frac{dE_{\rm pot}}{dE_{\rm int,\ e-}}\right]\frac{dE_{\rm int,\ e-}}{dR_{\rm Pl}} \tag{2.37}$$

And using that $E_{\rm int} \approx E_{\rm int,\ e-}$, because the electrons dominate the internal energy, one finds from equations 2.33 and 2.36 that

$$\frac{dE_{\rm pot}}{dE_{\rm int,\ e-}} = -\frac{3(\gamma-1)}{2}\ , \tag{2.38}$$

and thus

$$\frac{dE_{\rm int,\ ion}}{dR_{\rm Pl}} = -\frac{1}{2}\frac{dE_{\rm int,\ e-}}{dR_{\rm Pl}} > 0\ . \tag{2.39}$$

This shows that as the planet evolves, and the planetary radius decreases, the non-degenerate ionic matter cools, because the degenerate electrons account for the necessary increase in internal energy.

For terrestrial planets the mass of the gas envelope is negligible. In this case the intrinsic luminosity arises from heating by radioactive decay in their interiors, as well as from the cooling of the interiors which are still hot from the planetary formation (Urey 1955; Hofmeister & Criss 2005). For Earth the flux arising from the intrinsic luminosity is only 0.03 % of the received insolation, such that the surface conditions are determined by the Sun's irradiation (Kamland Collaboration et al. 2011).

Now that we have some insight as to the origin of the planetary intrinsic luminosity I want to discuss how the intrinsic luminosity affects the atmospheric temperature structure. In Figure 2.3 I show atmospheric temperature structures for $T_{\rm equ}$ = 1500 K, and γ = 0.5 atmospheres with internal temperatures varying from 0 to 800 K. In the case with $T_{\rm int} = 0$ K one

sees that the upper atmosphere exhibits a negative radial temperature gradient (with altitude), but the deep atmosphere is perfectly isothermal. The upper atmosphere temperature gradient arises from the re-radiation of the incident stellar flux. However, as one goes to deeper atmospheric layers, no intrinsic luminosity needs to be transported. Hence the temperature gradient becomes zero. Small, but non-zero internal temperature cases similarly exhibit deep isothermal regions, but these shrink in size as the planets' internal temperature increases: At some point the atmosphere needs to develop a negative temperature gradient (with increasing altitude) in order to transport the intrinsic luminosity, and the larger $T_{\rm int}$, the higher up in the atmosphere this has to occur in order to output the required amount of photons with high enough energies.

One more effect is worth mentioning here: I have derived above that the planetary intrinsic temperature decreases as the planet evolves. In this sense the temperature structures shown in Figure 2.3 can be regarded as a time sequence for the temperature profile of an irradiated planet. I have also discussed that in the deep interior the planet becomes convective, starting from the point where the temperature gradient is too strong. Furthermore, the transport of energy by convective motions is very effective, and it obviously dominates over the radiative energy transport in the atmosphere's deep, convective region. Therefore, the cooling timescale of a planet is effectively determined by its radiative atmosphere, which acts like an insulating blanket, covering the planet. Consequently, as the planet evolves and cools over time, the cooling and the irradiation by its host star will cause a growing isothermal region in the planetary atmosphere, which stabilizes the atmosphere against convection, due to the ∼zero temperature gradient. The thickness of the radiative part thus increases, and so does its insulating effect on the planet. This slows down planetary cooling and contraction, such that we expect hot jupiters to have a hotter interior than isolated planets of the same age (see, e.g., Guillot et al. 1996; Burrows et al. 2000; Arras & Bildsten 2006). Especially Arras & Bildsten (2006) make a case for this deep isothermal zone to exist planet-wide, i.e. also on the nightside, because the radiative timescale becomes very long in the deep atmospheric regions, such that even slow horizontal transport processes may drive the nightside to the isothermal temperature profile.

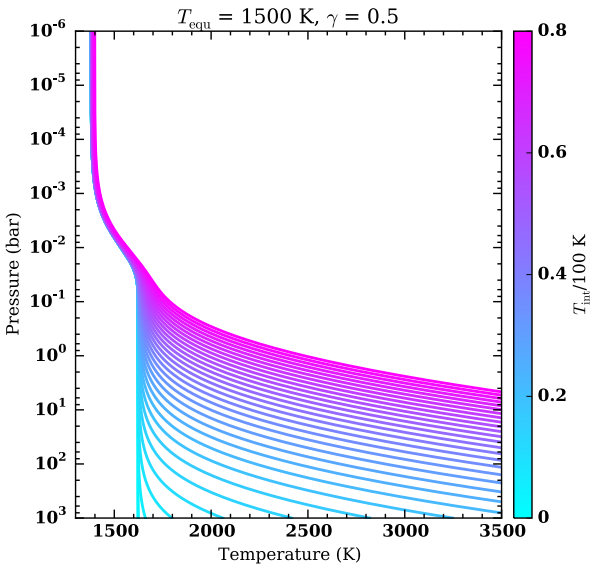

FIGURE 2.3: Temperature structures for $T_{\rm equ}$ = 1500 K, and γ = 0.5 atmospheres with varying internal temperatures, as indicated in the color coding, calculated with the Guillot (2010) temperature model.

2.2.3 Molecular and atomic lines

One major carrier of atmospheric absorption arises from molecular or atomic transitions, i.e. the change of energy associated with an atom entering a different electronic quantum state, or a molecule entering a different rotational, vibrational, or electronic state. These transitions can be excited by the absorption of photons in a narrow frequency range, corresponding to the transition energy. This is why this source of opacity is called 'line opacity', as it gives rise to narrow absorption lines in the spectra. Due to the mean temperatures associated with planetary atmospheres, which are comparatively lower than in stars, the electronic transitions of atoms (and molecules) are of reduced importance, with the very important exception of the alkali atoms, also see Section 3.3.1. The majority of the line opacity in the NIR and MIR stems from so-called roto-vibrational transitions, which arise from molecules changing their vibrational and rotational state at the same time, the larger part of the energy being used for the vibrational state transition. At the same time, by de-excitation of a higher energy state a molecule can also emit radiation.

Derivation of line absorption

The opacity arising from such multilevel energy systems can be derived from considering the co-called 'Einstein coefficients', which start from considering a two-level system, but turn out to be applicable to multilevel systems as well. A very good introduction can be found in (Rybicki & Lightman 1986), and I will reproduce a modified version of the most important steps below.

There are three events which can occur in a two-level system, where state "2" is the higher energy state and state "1" the lower energy state:

1. 'Spontaneous emission', expressed by the probability A_{21} for the system to spontaneously decay from state 2 to 1 per unit time, which has the units $[A_{21}] = \mathrm{s}^{-1}$.

2. 'Stimulated emission', expressed by the probability for the system to decay from state 2 to 1 per unit time, $B_{21}\bar{J}$, triggered by the presence of a radiation field with mean intensity J_ν.[8] $\bar{J}$ is the mean intensity average in the energy regime of the transition,

$$\bar{J} = \int_0^\infty J_\nu \phi_{12}(\nu) \mathrm{d}\nu \tag{2.40}$$

with $\phi_{12}(\nu)$ being the line profile function for the transition under consideration, with

$$\int_0^\infty \phi_{12}(\nu) \mathrm{d}\nu = 1 \,, \tag{2.41}$$

where ν is the radiation frequency. The profile function is centered on the frequency ν_0, corresponding to the state transition energy $h\nu_0$, where h is the Planck constant. The profile function encapsulates the fact that although the quantum energy transitions

[8] The intensity I_ν is the energy of the radiation field per area, per unit frequency, and per solid angle (i.e. direction). The mean intensity J_ν is the solid angle average (i.e. direction average) of the intensity. See Section 3.2.1 for a proper definition of these quantities.

occur at discrete energy values, multiple effects can allow for a (small) range of photon frequencies to stimulate emission, see below. Likewise, the units of the probability are $[B_{21}\bar{J}] = \mathrm{s}^{-1}$.

3. 'Absorption', expressed by the probability for the system to be excited to state 2 from 1 per unit time, $B_{12}\bar{J}$, in the presence of radiation corresponding to the frequency regime of the transition. Again we have that $[B_{12}\bar{J}] = \mathrm{s}^{-1}$.

The three Einstein coefficients A_{21}, B_{21}, and B_{12} can be related by the so-called 'Einstein relations'. For deriving the Einstein relations one can assume a gas of molecules which is in equilibrium,

$$n_1 B_{12}\bar{J} = n_2 B_{21}\bar{J} + n_2 A_{21}, \tag{2.42}$$

meaning that transitions from state 1 to state 2 are as likely as transitions from state 2 to 1, and the number densities of molecules in state 1 and 2, denoted by n_1 and n_2, are constant. Solving this for $\bar{J}$ yields

$$\bar{J} = \frac{n_2 A_{21}}{n_1 B_{12} - n_2 B_{21}} = \frac{A_{21}/B_{21}}{(n_1/n_2)(B_{12}/B_{21}) - 1}. \tag{2.43}$$

Additionally, if the system is in thermal equilibrium with a temperature T_{gas}, then from statistical mechanics we know that

$$\frac{n_1}{n_2} = \frac{g_1}{g_2}\exp\left(-\frac{E_1 - E_2}{k_B T_{\mathrm{gas}}}\right) = \frac{g_1}{g_2} e^{h\nu_0/k_{\mathrm{B}}T_{\mathrm{gas}}}, \tag{2.44}$$

where E_1 and E_2 are the energies of state 1 and 2, respectively, and it holds that $E_2 - E_1 = h\nu_0$. The factors g_1 and g_2 express the degrees of degeneracy of state 1 and 2. This yields

$$\bar{J} = \frac{A_{21}/B_{21}}{(g_1/g_2)(B_{12}/B_{21})e^{h\nu_0/k_{\mathrm{B}}T_{\mathrm{gas}}} - 1}. \tag{2.45}$$

At this point one can make the assumption that the radiation field is in thermal equilibrium with an associated temperature T_{rad}, and that the radiation field is in thermal equilibrium with the gas, such that $T \equiv T_{\mathrm{rad}} = T_{\mathrm{gas}}$. Then we get that

$$B_\nu(T) = \frac{A_{21}/B_{21}}{(g_1/g_2)(B_{12}/B_{21})e^{h\nu_0/k_{\mathrm{B}}T} - 1}, \tag{2.46}$$

where we used that the mean intensity of a radiation field in thermal equilibrium is the Planck function,

$$B_\nu(T) = \frac{2h\nu^3}{c^2}\frac{1}{e^{h\nu_0/k_{\mathrm{B}}T} - 1}. \tag{2.47}$$

This yields

$$g_1 B_{12} = g_2 B_{21} \tag{2.48}$$

and

$$A_{21} = \frac{2h\nu^3}{c^2} B_{21}, \tag{2.49}$$

which are the well-known Einstein relations.

Note that the Einstein relations hold for all two level systems, independent of whether the gas or the radiation field are in thermal equilibrium, or in thermal equilibrium with each other. These assumptions were merely used as a trick to obtain the relations between the Einstein coefficients. The Einstein relations even hold when one considers a system of more than two states. In equilibrium one normally has simple balancing: due to all transitions occurring together, the number of molecules in a certain state is constant. From statistical mechanics one finds, however, that any pair of states coupled via a transition must be balanced individually, which is called 'detailed balance'. This follows from the fact that all transitions must be symmetric upon time reversal. If there were more molecules changing from state 1 to 2 than vice versa, with the total number of atoms per level balanced by other transitions with other states, this behavior would not be symmetric with respect to time. The non-zero flux of molecules from state 1 to 2 would show in which direction time is flowing, breaking time-reversal symmetry. Thus all pairs of transitions must balance individually.

Using the Einstein coefficients one can now set out to derive the opacity of the gas. Consider an incident ray of light I_ν traveling into the solid angle $\Delta\Omega$. The corresponding mean intensity is

$$J = \frac{1}{4\pi}\int I_\nu d\Omega \approx \frac{\Delta\Omega}{4\pi} I_\nu \,. \tag{2.50}$$

The absorption processes per unit volume, frequency, and solid angle are then

$$N_{\mathrm{abs},\nu} = n_1 B_{12}\frac{I_\nu}{4\pi}\phi_{12}(\nu) - \underbrace{n_2 B_{21}\frac{I_\nu}{4\pi}\phi_{12}(\nu)}_{\text{Stimulated emission}} \,, \tag{2.51}$$

where stimulated emission acts like negative absorption, because stimulated emission is radiated into the same solid angle as the stimulating emission. The absorbed energy of the ray traveling into solid angle $\Delta\Omega$ per unit time, frequency, solid angle and volume then is

$$E_{\mathrm{abs},\nu} = \frac{I_\nu}{4\pi}\phi_{12}(\nu)(n_1 B_{12} - n_2 B_{21})h\nu_0, \tag{2.52}$$

Thus, the energy per area[9] absorbed over a length Δs parallel to the direction $\Delta\Omega$ is

$$\Delta I_\nu = -\frac{I_\nu}{4\pi}\phi_{12}(\nu)(n_1 B_{12} - n_2 B_{21})h\nu_0 \Delta s \tag{2.53}$$

Comparing this to the formal radiative transfer equation for absorption only (see Equation 3.11),

$$\mathbf{n}\cdot\nabla I_\nu = -\alpha_\nu I_\nu \,, \tag{2.54}$$

where $\mathbf{n}$ is the unit vector pointing into the direction of $\Delta\Omega$, and α is the inverse mean free path of the photons, yields

$$\alpha_\nu = \frac{h\nu_0}{4\pi}(n_1 B_{12} - n_2 B_{21})\phi_{12}(\nu) \,, \tag{2.55}$$

[9] "Energy" again meaning energy per unit solid angle, time, and frequency.

or, using the Einstein relations:

$$\alpha_\nu = \frac{h\nu_0}{4\pi} n_1 B_{12} \left(1 - \frac{n_2 g_1}{n_1 g_2}\right) \phi_{12}(\nu) \,. \tag{2.56}$$

Assuming local thermal equilibrium (LTE) for the gas one finds that

$$\alpha_\nu = \frac{h\nu_0}{4\pi} n_1 B_{12} \left(1 - e^{-h\nu_0/k_\mathrm{B}T_\mathrm{gas}}\right) \phi_{12}(\nu) \,. \tag{2.57}$$

Thus we have derived the inverse mean free path of the photons in the gas, which is related to the opacity κ_ν via

$$\alpha_\nu = \kappa_\nu \rho \,, \tag{2.58}$$

with ρ being the local gas density. Publicly available line lists sometimes give the Einstein A_{21} coefficient, but these can be converted to B_{12} using the Einstein relations. Also other formats are used, but clearly stated in the associated publications, such that a conversion to the format shown above is possible. Fractional level populations n_i can be obtained from

$$\frac{n_i}{n_\mathrm{tot}} = \frac{g_i e^{-E_i/k_\mathrm{B}T}}{Q(T)} \,, \tag{2.59}$$

where n_tot is the total particle number density of the gas, and $Q(T)$ is the partition function

$$Q(T) = \sum_i g_i e^{-E_i/k_\mathrm{B}T} \,. \tag{2.60}$$

In principle $Q(T)$ can be calculated from the line lists, which also give the degeneracy degrees and energies of each state, but the use of precalculated, tabulated partition functions is more common.

For a gas consisting of N_species different molecular and atomic species, the total opacity can thus be expressed as

$$\kappa_\mathrm{tot} = \sum_{i=1}^{N_\mathrm{species}} X_i \kappa_i \,, \tag{2.61}$$

where $X_i = \rho_i/\rho_\mathrm{tot}$ is the mass fraction of species i.

Line profiles

The last ingredient needed to calculate line opacities is the line profile function, which expresses in which wavelengths absorption and emission of light by the molecule is possible. There are three contributions to the line profile functions, two of which result in similar line profile shapes, and I will start with these.

The Einstein coefficient for spontaneous emission is A_{12}. One method to describe this process in a classical (i.e. non-quantum mechanical) approach is to approximate an excited state as an oscillatory motion. I will follow Demtröder (2010) here and use the example of an excited electron, but we could also picture a vibrating or rotating molecule instead. The

excited electron's motion can be described by the differential equation

$$\ddot{x} + 2\gamma\dot{x} + \omega_0^2 x = 0 \,, \tag{2.62}$$

where $\omega_0 = 2\pi\nu_0$, and γ describes the dampening of the electrons motion, brought about by the limited lifetime of the excited state $\sim 1/A_{12}$. With $\dot{x}(0) = 0$, $x(0) = x_0$, one finds (considering that usually $\gamma \ll \omega_0$):

$$x(t) = x_0 \cdot \mathrm{e}^{-\gamma t}\cos(\omega_0 t) \tag{2.63}$$

To get the frequency spectrum of the resulting damped oscillation one takes the Fourier transform

$$\begin{aligned} f(\omega) &= \frac{1}{\sqrt{2\pi}} \int_0^\infty x_0 \cdot \mathrm{e}^{-\gamma t}\cos(\omega_0 t)\mathrm{e}^{-i\omega t}\mathrm{d}t \\ &\approx \frac{x_0}{\sqrt{8\pi}} \frac{1}{i(\omega_0 - \omega) + \gamma} \,. \end{aligned} \tag{2.64}$$

Now, the electrical field arising from an electron oscillation has a spectral power of $P(\omega) \propto f(\omega) \cdot f(\omega)^*$ (Demtröder 2010), such that one finds

$$P_\nu(\nu) \propto \frac{1}{\gamma^2 + (\nu_0 - \nu)^2} \,, \tag{2.65}$$

where $\gamma/2\pi$ was renamed to γ. Normalization then yields for the line profile of the transition connecting states i and j:

$$\phi_{ij}(\nu) = \frac{1}{\pi} \frac{\gamma}{\gamma^2 + (\nu_{ij} - \nu)^2} \,, \tag{2.66}$$

where for clarity I wrote ν_{ij} instead of ν_0 for the frequency of the ij-transition. This profile is also called 'Lorentz profile', with a 'half width at half maximum' (HWHM) of γ, because $\phi_{ij}(\pm\gamma) = \phi_{ij}(0)/2$. Finally, one can show that $\gamma = A_{ij}/(4\pi)$. Because this line broadening mechanism depends only on the internal properties of the molecule, namely the spontaneous emission rate A_{ij}, this broadening source is called 'natural line broadening', with the natural HWHM $\gamma_{\mathrm{nat}} = A_{ij}/(4\pi)$.

The second important process is the so-called 'pressure broadening'. This corresponds to the case where close encoutners between molecules lead to a collisional de-excitation of the higher energy state j. The rate for this to occur can be approximated as

$$R_j = n\sigma_j v_{\mathrm{therm}} \,, \tag{2.67}$$

where n is the number density of molecules, σ_j the cross-section for the collisional de-excitation to occur, and v_{therm} the thermal velocity of the molecules. Because v_{therm} of a gas in LTE is $\sqrt{8k_{\mathrm{B}}T/(\pi\mu m_{\mathrm{P}})}$ one finds that for an ideal gas

$$R_j \propto \frac{P}{\sqrt{T}} \,. \tag{2.68}$$

With the rate of collisional de-excitation added to the spontaneous de-excitation rate one finds that the total width of the Lorentz line profile is

$$\gamma_{\mathcal{L}} = \frac{A_{ij}}{4\pi} + \frac{R_j}{4\pi} = \gamma_{\rm nat} + \gamma_{\rm press} \,. \tag{2.69}$$

A very important property of $\gamma_{\rm press}$ is that $\gamma_{\rm press} \propto P$ (Equation 2.68), which shows that pressure broadening will be the dominating source of line broadening at large pressures.

At distances far away from the line center frequency ν_{ij} the assumptions made for the derivation of the spectral power start to break down, such that the wings attain a different shape and become smaller than the Lorentz profile, also dubbed 'sub-Lorentzian' (see, e.g., Sharp & Burrows 2007). Here one often takes the approach to truncate the line profile at distances far away from the line center, or considers dedicated calculations of the line wing shapes, see Section 3.3.1.

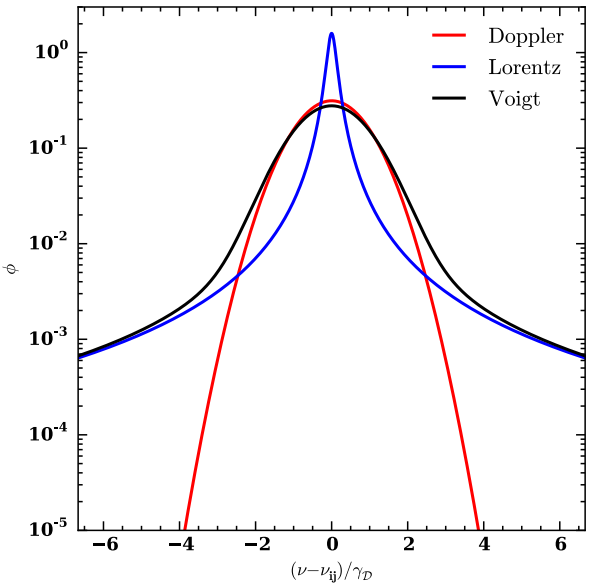

FIGURE 2.4: A Doppler line profile (red line), a Lorentz line profile (blue line) and their convolution, a Voigt profile (black line).

The third broadening process, after natural and pressure broadening, arises from the thermal motion of the molecules. In LTE, it is known that the velocity of gas particles will follow a Maxwell-Boltzmann distribution. A photon which approaches a moving molecule will therefore appear to be frequency shifted, due to the Doppler effect. This results in a shift $\Delta\nu_{ij}$ of the molecular transition frequency ν_{ij}

$$\frac{\Delta\nu_{ij}}{\nu_{ij}} = -\frac{v}{c}, \tag{2.70}$$

where v is the gas velocity component parallel to the direction of the radiation. The simple linear relation between $\Delta\nu_{ij}$ and v shows that the distribution of the frequency shift must be of the same shape as the velocity distribution, and is thus Gauss-shaped. Performing a coordinate transformation from v to ν for the 1-dimensional Maxwell-Boltzmann distribution, one obtains

$$\phi_{ij}(\nu) = \frac{1}{\sqrt{\pi}\gamma_{\mathcal{D}}} \mathrm{e}^{-(\nu-\nu_{ij})^2/\gamma_{\mathcal{D}}^2} \,, \tag{2.71}$$

with

$$\gamma_{\mathcal{D}} = \frac{\nu_{ij}}{c}\sqrt{\frac{2k_{\rm B}T}{m}} \,, \tag{2.72}$$

and m being the molecular mass. This profile is commonly called 'Doppler profile'.

In conclusion this means that the total line profile function will arise from both Lorentz and Doppler broadening, with respective profiles $\phi_{\mathcal{L}}(\nu, \gamma_{\mathcal{L}})$ and $\phi_{\mathcal{D}}(\nu, \gamma_{\mathcal{D}})$. The combined

line profile can thus be obtained by means of convolving both profiles

$$\phi_{\mathcal{V}}(\nu, \gamma_{\mathcal{L}}, \gamma_{\mathcal{D}}) = \int_{-\infty}^{\infty} \phi_{\mathcal{L}}(\nu', \gamma_{\mathcal{L}}) \phi_{\mathcal{D}}(\nu - \nu', \gamma_{\mathcal{D}}) d\nu' \tag{2.73}$$

with the convolution called 'Voigt profile'. An example is shown in Fig 2.4.

One notices that a Doppler profile in general always has a much faster drop-off than a Lorentz profile. Thus the Lorentz wings will always dominate the Voigt profile sufficiently far from the line center. The core shape of the line depends on the ratio of the Lorentz and Doppler width, $y = \gamma_{\mathcal{L}}/\gamma_{\mathcal{D}}$. For $y \gg 1$ one has essentially a Lorentz profile, while for $y \ll 1$ one sees effectively a Doppler shaped core that has Lorentzian wings sufficiently far from the center. There exists no analytical expression for the Voigt profile, and one has to carry out a numerical integration for every line. However, there are fast techniques to approximate Voigt profiles, such as by Humlícek (1982), which computes the Voigt profile using an efficient approximation of the so-called 'Faddeeva function' H. The input parameters of the function $H(x, y)$ are $x = (\nu - \nu_{ij})/\gamma_{\mathcal{D}}$ and $y = \gamma_{\mathcal{L}}/\gamma_{\mathcal{D}}$, and the final profile is

$$\phi_{\mathcal{V}}(\nu) = \frac{\mathrm{Re}[H(x, y)]}{\sqrt{\pi}\gamma_{\mathcal{D}}} \,. \tag{2.74}$$

2.2.4 Molecular continuum opacities

Apart from line opacities, molecules can give rise to so-called continuum opacities as well, which are called like that because the corresponding opacities are only slowly varying with wavelength. I will introduce the two most important contributions, 'Rayleigh scattering' and 'collision induced absorption' (CIA) below.

Rayleigh scattering

For deriving the Rayleigh scattering cross-section one can return to the classical treatment of a bound electron, as outlined in (Rybicki & Lightman 1986), where I follow their most important steps here. We return to the motion of the electron as a damped oscillator

$$\ddot{x} + 2\gamma\dot{x} + \omega_0^2 x = 0 \,. \tag{2.75}$$

If this electron is subjected to an incoming electro-magnetic wave, then the corresponding equation of motion will become

$$\ddot{x} - \alpha\dddot{x} + \omega_0^2 x = \frac{e}{m_e} E_0 e^{i\omega t} \,, \tag{2.76}$$

where the RHS of the equation is the driving force of the incoming light. I replaced $2\gamma\dot{x}$ with $-\alpha\dddot{x}$, because the change of acceleration of an electron causes it to emit radiation, and imposes a dampening force $\propto -\dddot{x}$ in the process (Rybicki & Lightman 1986). For small α and an unforced electronic oscillator one recovers the homogeneous form in Equation 2.75,

because then $\dddot{x} \propto -\dot{x}$. Using the ansatz $x(t) = Ae^{i\tilde{\omega}t}$ one obtains

$$Ae^{i\tilde{\omega}t} = \frac{eE_0}{m_e} \frac{1}{(\omega_0^2 - \tilde{\omega}^2 + \alpha i\tilde{\omega}^3)} e^{i\omega t} \,. \tag{2.77}$$

This shows that the incoming light will prompt the electron to oscillate at the same frequency, hence the electron will emit light at the same frequency. Thus, when viewing the bound electron – incoming photon system from outside, the photon is not absorbed, but scattered. Now, the power emitted by an accelerated electron is

$$P = \frac{2e^2 \left\langle |\ddot{x}|^2 \right\rangle}{3c^3} \,, \tag{2.78}$$

which is also known as 'Lamor's formula', where $\left\langle |\ddot{x}|^2 \right\rangle$ describes the time-average of $|\ddot{x}|^2$. For the scattering electron this results in

$$P = \frac{e^4 E_0^2}{3c^3 m_e^2} \frac{\omega^4}{(\omega_0^2 - \omega^2)^2 + \alpha^2 \omega^6} \,. \tag{2.79}$$

The Poynting flux of the incoming photon is $F = cE_0^2/(8\pi)$ (see, e.g., Rybicki & Lightman 1986), such that the cross-section of the scattering bound electron is

$$\sigma = \frac{P}{F} = \frac{8\pi e^4}{3c^4 m_e^2} \frac{\omega^4}{(\omega_0^2 - \omega^2)^2 + \alpha^2 \omega^6} \,. \tag{2.80}$$

Finally for $\omega \ll \omega_0$ and not too strong dampening one obtains

$$\sigma_{\text{Rayleigh}} = \frac{8\pi e^4}{3c^4 m_e^2} \left(\frac{\omega}{\omega_0} \right)^4 \,, \tag{2.81}$$

which is the Rayleigh scattering cross-section, with the well known wavelength-dependence $\sigma \propto \lambda^{-4}$. Because we assumed $\omega \ll \omega_0$ this means that the incident photons must have a wavelength larger than the radius of the electron's orbit, $r \sim c/\omega_0$, i.e. larger than the atomic or molecular radius, because otherwise they could excite internal electronic transitions. Thus Rayleigh scattering can occur if the scattering particle's size r satisfies

$$r < \frac{\lambda}{2\pi}, \tag{2.82}$$

where λ is the wavelength of the incoming photon. Because the electron reacts to the slowly varying incoming light wave by moving at the same frequency as the incident light, this corresponds to the atom/molecule being polarized by the radiation.

For H_2/He dominated atmospheres with no clouds, it is indeed the Rayleigh scattering which dominates the opacity in the optical wavelengths. The cross-sections for these molecules can be obtained from the literature, in the parametrized form $\sigma_0(\lambda_0/\lambda)^4$, see Section 3.3.2.

Collision Induced Absorption

In a gas at large pressures the molecular constituents often approach each other closely, such that effects arising from van der Waals forces become important, because the close encounters perturb the charge distributions in molecules and atoms. This creates non-permanent dipole moments in the collision partners and makes the photon excitation of previously inaccessible energy transitions possible. What is more, the close approach and interaction of molecules can lead to structures called 'supramolecules', with opacity arising from the energy transitions of these short-lived conglomerates. The resulting opacity is called 'collision induced absorption' (CIA). Because of the short collision times, and the energy–time uncertainty principle, the energy values of the transitions have a large dispersion, making CIA opacities varying only slowly with wavelength. As CIA it depends on the collision rate it has a cross-section proportional to the squared particle density n^2.

The inverse of the temperature-dependent photon mean free path $l_{\rm m}$ can be written in the form (see, e.g., Birnbaum et al. 1984; Borysow et al. 1989)

$$\frac{1}{l_{\rm m}(\lambda)} = \alpha_{X-Y}(\lambda, T)\frac{n_X n_Y}{L_0^2} \,, \tag{2.83}$$

where X and Y denote the collision species, and $\alpha_{X-Y}(\lambda, T)$ is available in tabulated form, based on theoretical modeling of the collision processes. L_0 is the so-called Loschmidt number, defined as

$$L_0 = \frac{1}{k_{\rm B}}\frac{1\ {\rm atm}}{273.15\ {\rm K}} = 2.68676 \times 10^{19}\ {\rm cm}^{-3}. \tag{2.84}$$

Using the standard definition of the mean free path $1/l_{\rm m}(\lambda) = \sigma(\lambda) n_{\rm tot}$ one finds that the absorption cross-section is

$$\begin{aligned}\sigma_{X-Y}(\lambda) &= \frac{1}{n_{\rm tot}}\left[\alpha_{X-Y}(\lambda, T)\frac{n_X n_Y}{L_0^2}\right] \\ &= n_{\rm tot}\left[\alpha_{X-Y}(\lambda, T)\frac{f_X f_Y}{L_0^2}\right],\end{aligned} \tag{2.85}$$

where $n_i = f_i n_{\rm tot}$. Thus it is convenient to write

$$\sigma_{X-Y}(\lambda) = \frac{f_X f_Y}{L_0^2}\frac{P}{k_{\rm B}T}\alpha_{X-Y}(\lambda, T) \,. \tag{2.86}$$

In giant planets the most abundant molecular and atomic species are dominating the CIA opacities. Therefore the atmospheric opacity of these planets is dominated by the collisions of H_2–H_2 and H_2–He (Sharp & Burrows 2007).

2.2.5 Clouds

In Section 1.5 I summarized how clouds appear to be very common in exoplanets, and models show that they can have a strong influence on an atmosphere's absorption and scattering, and hence thermal properties. Nonetheless, on no exoplanet have the actual cloud species

yet been conclusively identified. The problem is actually even more severe: while qualitatively the picture of cloud formation often seems straightforward, the theory and data needed for a quantitative description of clouds is still incomplete, which is symptomatically shown in the wide-spread use of parametrized, or strongly idealized cloud models (see, e.g., Tsuji et al. 1996; Ackerman & Marley 2001; Allard et al. 2001, 2003a; Zsom et al. 2012 and also my models, Mollière et al. 2017).

In what follows, I try to summarize the cloud formation processes which are thought to be most important and how they interact. This summary is based on Rossow (1978), in which a much more detailed description can be found. An example for two different simple models of cloud parametrization can be found in the description of *petitCODE* in Section 3.5.

The basic processes and how they are related is shown in Figure 2.5, which has been taken from Rossow (1978). This schematic drawing shows how the cloud interacts with the sources which provide it with material. This sources themselves can also act as sinks.

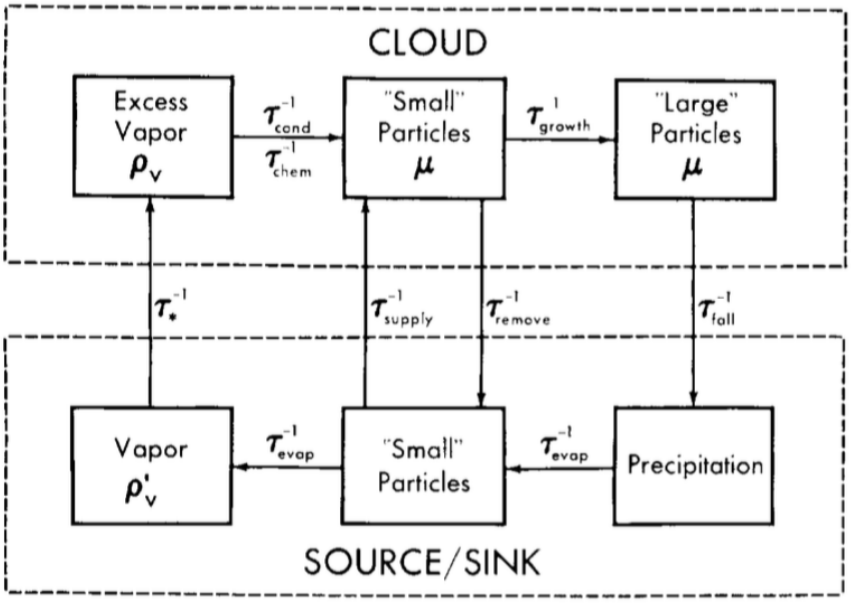

FIGURE 2.5: Schematic drawing showing the relations between various cloud microsphysics processes. Figure taken from Rossow (1978).

A cloud always forms from the vapor phase which contains the cloud species, or the required chemical building blocks, in its not yet condensed form. If a packet of gas is cooled on a timescale τ_*, until its vapor density exceeds the saturation vapor density, it becomes possible to form cloud particles.

The condensation of cloud particles out of the gas phase proceeds on a timescale $\tau_{\rm cond}$. It gives rise to a so-called population of "small" particles. These "small" particles can also be brought to the location of the cloud on a timescale $\tau_{\rm supply}$ by winds. The winds could, e.g., be streaming over a particle covered surface. But winds can also deplete the cloud in small particles on a timescale $\tau_{\rm remove}$ when streaming over a surface which is not covered by particles.

If the removal of "small" particles is faster than the process of collisional growth (occurring on a timescale $\tau_{\rm growth}$) of the "small" particles, then the cloud will not contain any "large" particles and it will not be precipitating. If the collisional growth occurs on a shorter timescale than the removal of "small" particles, then the cloud will form "large" particles, which are defined by requiring that they fall through the atmosphere on a shorter timescale than they can be supplied or removed by winds.

As soon as the "large" particles have formed, they will start to fall and settle out of the cloud in a process called precipitation or rain. As they are defined by the fact that they cannot be supplied more quickly than they fall, "large" particles will always rain out. They will start to evaporate when they reach hotter regions, this happens on a timescale $\tau_{\rm evap}$. They can make their way back up to the cloud if they are advected by winds on a timescale $\tau_{\rm supply}$, but if $\tau_{\rm supply} > \tau_{\rm evap}$ they will evaporate further and go back to the vapor phase.

Note that there also exist so-called "chemical clouds", in which the "small" particles are produced by chemical reactions on a timescale $\tau_{\rm chem}$, rather then by cooling and condensation.

All of the complex physics was hidden in simple timescales here, but they correspond to a plethora of physical processes and I will start with a short summary of the bottleneck for cloud formation to even start, which are the nucleation processes.

Nucleation processes

If equilibrium chemistry is considered (see Section 2.3.1), a species with a vapor (i.e. gas) pressure larger than its saturation vapor pressure will undergo condensation by forming condensation nuclei. It is useful to define the 'saturation' as

$$S = \frac{\rho_{\rm v}}{\rho_{\rm s}} \tag{2.87}$$

and the 'supersaturation' as

$$\mathcal{S}_\infty = S - 1 \ , \tag{2.88}$$

where $\rho_{\rm v}$ and $\rho_{\rm s}$ are the species' vapor and saturation vapor densities, respectively. $\rho_{\rm s}$ corresponds to the maximum density which the species can have in equilibrium, after which condensation must set in. Consequently, species with $\mathcal{S}_\infty > 0$ will undergo condensation, if only equilibrium condensation is considered. In reality, however, multiple effects can come into play which either hamper or promote the formation of the first nuclei. In general, the condition for forming nuclei and starting condensation can be expressed as

$$\mathcal{S} > 0 \ , \tag{2.89}$$

where

$$\mathcal{S} = \mathcal{S}_\infty - \mathcal{S}_{\rm curv} + \mathcal{S}_{\rm gas} + \mathcal{S}_{\rm ion} + \mathcal{S}_{\rm chem} + \mathcal{S}_{\rm CCN} \ , \tag{2.90}$$

is the 'effective supersaturation'. The individual terms in the above equation each describe a process affecting the nucleation efficiency. Some of the above term strongly depend on

the conditions in which the nuclei form and some also depend on the nuclei's size. The condition $\mathcal{S} = 0$ therefore also defines a minimum nucleii radius. If $\mathcal{S} < 0$ the particles will start to evaporate, which then represents the thermodynamically favored state. The individual processes controlling the nucleation of cloud particles are

- *Homogeneous homomolecular nucleation of liquid droplets:* here nucleii form from "spontaneous condensation" of a *single* species (hence homomolecular) from the gas phase. A nucleus has to have a minimum size in order to overcome its own surface tension, thus the vapor density needs to be high enough. This lowers the effective supersaturation by an amount $\mathcal{S}_{\mathrm{curv}}$.
- *Heterogeneous homomolecular nucleation of liquid droplets:* spontaneous incorporation of chemically inert gas molecules ($\mathcal{S}_{\mathrm{gas}}$) or ions ($\mathcal{S}_{\mathrm{ion}}$) of another species energetically favor the nucleation process.
- *Chemical nucleation:* here the nuclei form directly out of the gas phase by means of chemical reactions, which is different from "simple" condensation, and captured by introducing $\mathcal{S}_{\mathrm{chem}}$.
- *Heterogeneous nucleation:* if there is a pre-existing population of small particles, the resulting intermolecular forces arising at the various interfaces (gas–surface, liquid–surface, gas–liquid) will lower the surface tension of the nucleus considerably, which favors nucleation. This is included through the term $\mathcal{S}_{\mathrm{CCN}}$, where CCN stands for 'cloud condensation nuclei'. Water droplets in Earth's atmosphere more or less exclusively form through this pathway, as they have a large $\mathcal{S}_{\mathrm{curv}}$ of 5 to 8. (Rossow 1978).

Thus, in an complete nucleation theory, all of the above processes need to be included, and their modeling is necessary to determine the nucleation rates. If the nucleation occurs in presence of a CCN population, which is by far the most efficient nucleation catalyst, it can be shown that the nucleation rate τ_{nuc}^{-1} is very large compared to the cooling rate τ_{*}^{-1} and can therefore be neglected in the timescale comparison. In any case, *if* nucleation occurs then it is usually faster than the subsequent growth of large particles (Rossow 1978).

After the particles have nucleated, they will grow by either collisions or condensation, both processes are summarized below.

Condensational growth

For a nucleus to grow further one needs to provide it with an influx of vapor molecules. This flux competes with the release of latent heat from the nucleus' surface. In order to model the nucleus–gas interaction one requires treatments for both the hydrodynamical or ballistical interaction regime, with the former including a treatment of whether or not the flow is laminar or turbulent. An a-priori unknown free parameter is the sticking efficiency α, which determines the efficiency with which the vapor molecules are captured. For solid nuclei, the sticking efficiency furthermore depends on the shape of the nucleus (Rossow 1978).

Collisional growth

Collisions between the cloud particles can lead to further growth. The collisions can occur either because of Brownian motions of because of gravitational coalescence, where more massive particles will settle through the atmosphere and sweep up the smaller ones. Again, different hydrodynamical regimes need to be modeled, and the cross-sections are velocity dependent, as collisions can lead to different outcomes, such as bouncing, sticking, or fragmentation. The growth processes are typically locally described by the 'Smoluchowski equation'

$$\frac{\partial n(a)}{\partial t} = \frac{1}{2}\int_0^a \mathcal{K}(a-b,b)n(a-b)n(b)db - \int_0^\infty \mathcal{K}(a,b)n(a)n(b)db\,, \tag{2.91}$$

where $n(a)$ is the differential number density of particles of mass a, and $\mathcal{K}(a,b)$ is the 'coagulation kernel', which contains all the physics, and for which $\mathcal{K}(a-b,b)n(a-b)n(b)$ is the number of particles of differential mass a produced by coagulation of the particles of mass $a-b$ and b.

Cloud opacities

If the size and shape of a cloud particle are known, the particle's corresponding opacity can be calculated. For this one needs to know its optical properties, i.e. its real and imaginary refractive indices, $n(\lambda)$ and $k(\lambda)$. Most often one assumes a spherical, homogeneous particle. Then the solution is obtained by expanding the incoming and scattered radiation field in vector spherical harmonics, an by imposing the surface boundary conditions known from the Maxwell equations on the particle's surface. The absorption and scattering cross-sections can then be found as expansions in sums of terms which contain the refractive indices and Bessel functions, and for which the effective variable is $x = 2\pi r/\lambda$, where r is the particle radius (see, e.g., Bohren & Huffman 1998). The corresponding theory is also called 'Mie scattering', named after its inventor Gustav Mie. The larger x is, the more terms need to be considered for the cross-sections, such that their calculation becomes more and more cumbersome. For $x \ll 1$ one recovers that the particle scattering becomes Rayleigh-like, with $\sigma_{\rm scat} \propto \lambda^{-4}$. This means that one recovers the Rayleigh scattering criterion derived in Equation 2.82.

Due to the comparative ease with which they can be calculated, cloud opacities in atmospheric calculations are usually obtained from Mie theory (see, e.g., Helling et al. 2008; Madhusudhan et al. 2011a; Morley et al. 2012; Benneke 2015; Baudino et al. 2015). For solid particles however, it is uncertain if this is the correct approach: silicate grains have been observed in multiple contexts in astronomy: in disks around Herbig Ae/Be stars (Bouwman et al. 2001; Juhász et al. 2010), also in AGB stars, post-AGB stars, planetary nebulae, and massive stars (Molster et al. 2002). In these cases a good fit to the data could only be obtained when non-spherical, non-homogeneous shapes for the particles were assumed, such as in the case of 'Distribution of Hollow Spheres' (DHS) (Min et al. 2003), where the particles

are modeled as spheres with a spherical cavity in the middle, which is still comparatively easy to treat with a modified Mie theory.

2.3 Chemistry

In order to know the total opacity of a given atmospheric layer it is necessary to know its composition, i.e. its molecular and atomic abundances. In order to obtain the composition, the chemical reactions between the individual species, at the atmospheric pressure–temperature conditions, need to be modeled. In *petitCODE* I solve this problem by assuming that the atmosphere is in chemical equilibrium, which speeds up the computation of the composition significantly. Both equilibrium and non-equilibrium chemistry are summarized in the sections below.

2.3.1 Equilibrium chemistry

Consider a gas at pressure P, temperature T, and known atomic composition. Equilibrium chemistry corresponds to the answer to the question which ionic, atomic and molecular abundances the system would attain, due to chemical reactions, in the limit of $t \rightarrow \infty$, where t is the time. To answer this one can make use of the Gibbs free energy G, which is a thermodynamic state function, and its properties. The change in Gibbs free energy can be expressed as (see, e.g., Schwabl 2006)

$$dG = VdP - SdT + \sum_{j=1}^{N_{\text{species}}} \mu_j dN_j \, , \tag{2.92}$$

where V is the volume, P the pressure, S the entropy, T the temperature, $\mu_j(P,T)$ the chemical potential, and N_j the number of particles of species j.

From statistical mechanics it can be shown that for an isolated thermodynamical system evolving with time, it holds that the Gibbs free energy G decreases

$$\Delta G < 0, \tag{2.93}$$

which follows from the second law of thermodynamics, $\Delta S > 0$. Because systems that equilibrate evolve towards the state of maximum entropy, a system in equilibrium (i.e. all state functions are constant in time) has evolved towards minimum Gibbs free energy G.
From Equation 2.92 one sees that at constant pressure and temperature, the Gibbs free energy may be expressed as

$$G = \sum_{j=1}^{N_{\text{species}}} \mu_j N_j + \text{cst} \, , \text{ with } dG = \sum_{j=1}^{N_{\text{species}}} \mu_j dN_j \, . \tag{2.94}$$

Thus, in order to find the equilibrium chemical abundances of molecules and atoms of a given system one has to minimize Equation 2.94, while keeping the number of elemental

building blocks of all molecular species (i.e. atoms) constant. The latter condition corresponds to the $N_{\rm atom}$ constraints

$$\sum_{j=1}^{N_{\rm species}} a_{ij} N_j = b_i \tag{2.95}$$

$$b_i = \text{cst} \; \forall \; i \; \in \; \{1, \ldots, N_{\rm atom}\}, \tag{2.96}$$

where the a_{ij} are the so-called stoichiometric factors, giving the number of atoms of species i in a given molecule of species j. $N_{\rm atom}$ is the number of the atomic species that need to be included for the system under consideration. This problem formally corresponds to the task of minimizing a function $G(N_1, \ldots, N_{N_{\rm species}})$ while having to fulfill $N_{\rm atom}$ different constraints. This can be done using the method of 'Lagrange multipliers'. For this one defines and minimizes the function

$$\mathcal{L}(N_1, \ldots, N_{N_{\rm species}}, \lambda_1, \ldots, \lambda_{N_{\rm atom}}) = \sum_{j=1}^{N_{\rm species}} \mu_j N_j - \sum_{i=1}^{N_{\rm atom}} \lambda_i \left(\sum_{j=1}^{N_{\rm species}} a_{ij} N_j - b_i \right) \; , \tag{2.97}$$

where λ_i are the so-called Lagrange multipliers. This is approach leads to the desired result because the minimum value will satisfy

$$\nabla \mathcal{L} = 0 \; , \tag{2.98}$$

with

$$\nabla = \left(\frac{\partial}{\partial N_1}, \ldots, \frac{\partial}{\partial N_{N_{\rm species}}}, \frac{\partial}{\partial \lambda_1}, \ldots, \frac{\partial}{\partial \lambda_{N_{\rm atom}}} \right)^T \; , \tag{2.99}$$

which is the mathematical description of minimizing G while conserving the atom numbers.

Such equilibrium chemistry models are commonly known as 'Gibbs minimizers', and a good introduction can be found in Gordon & McBride (1994). Note that one does not require *any* knowledge about the chemical reactions involved in driving the system to equilibrium, considering the individual species' chemical potentials, and their stoichiometric factors, is sufficient.

2.3.2 Non-equilibrium effects

A crucial assumption for equilibrium chemistry is that it yields the chemical abundances of an isolated parcel of gas at constant P and T, *in the limit of* $t \to \infty$. If $\tau_{\rm chem}$ is the timescale of the slowest chemical reaction in a chemical network, this means that equilibrium chemistry will break down if

$$\tau_{\rm chem} > \tau_{\rm change} \; , \tag{2.100}$$

where $\tau_{\rm change}$ is the timescale of any process which changes the state of the parcel of gas under consideration. Such processes can be the transport of the gas to regions of different P or T, or the dissociation and ionization of molecules and atoms by incident radiation, and the resulting reactions of the ions and dissociation products, which drive the system

further away from equilibrium. If equilibrium breaks down, then the chemical abundances can be obtained by bookkeeping of the available number of atomic building blocks, and by modeling the individual chemical reactions in a so-called chemical network. The equations describing the change in number density n_i of a given species i then take the form (see, e.g., Venot et al. 2012)

$$\frac{\partial n_i}{\partial t} = P_i - n_i L_i - \nabla \cdot F_{\rm adv} \ , \tag{2.101}$$

where P_i is the production rate of species i, arising from reactions and photolytic dissociation and ionization processes, L_i is the corresponding loss term due to the same processes, and $F_{\rm adv}$ is the flux of particles, arising from atmospheric circulation, convection, or other vertical diffusion processes. If production and loss terms are negligible, the equation takes the form of the continuity equation Equation 2.1, as expected. Because the production and loss terms depend on the densities of other chemical species, the chemical reaction network, described by equations like Equation 2.101, corresponds to a set of coupled, non-linear differential equations. For the full solutions one requires knowledge of the spatial temperature and velocity distribution within the atmosphere, which is in itself challenging.

That being said, there exist numerous studies which tackle reduced versions of this problem, an we now know that diffusive processes in the radiative zones of planets may transport abundances from the hot, deep atmospheric layers to the photosphere (see, e.g. Zahnle & Marley 2014). This is called 'quenching', and may affect planets with $T_{\rm equ} \lesssim 1000-1500$ K, depending on the strength of diffusion (Miguel & Kaltenegger 2014; Zahnle & Marley 2014). For hot jupiters with strong horizontal circulation the eastward blowing jet may distribute the hot spot abundances around the whole planet (Agúndez et al. 2014). In both of the above scenarios cooler regions are overwhelmed by the equilibrium abundances of hotter regions, because the chemical timescale is temperature-dependent. The effect of photodissociation and ionization by stars and flares has been studied in, e.g., Venot et al. (2012, 2015, 2016). This so-called 'photochemistry' usually only affects the molecular abundances in the high, low-pressure regions of the atmospheres, such that the observational signatures may be challenging to see.

2.4 Summary of atmospheric processes

I have summarized the processes described in this chapter in the schematic drawing shown in Figure 2.6.

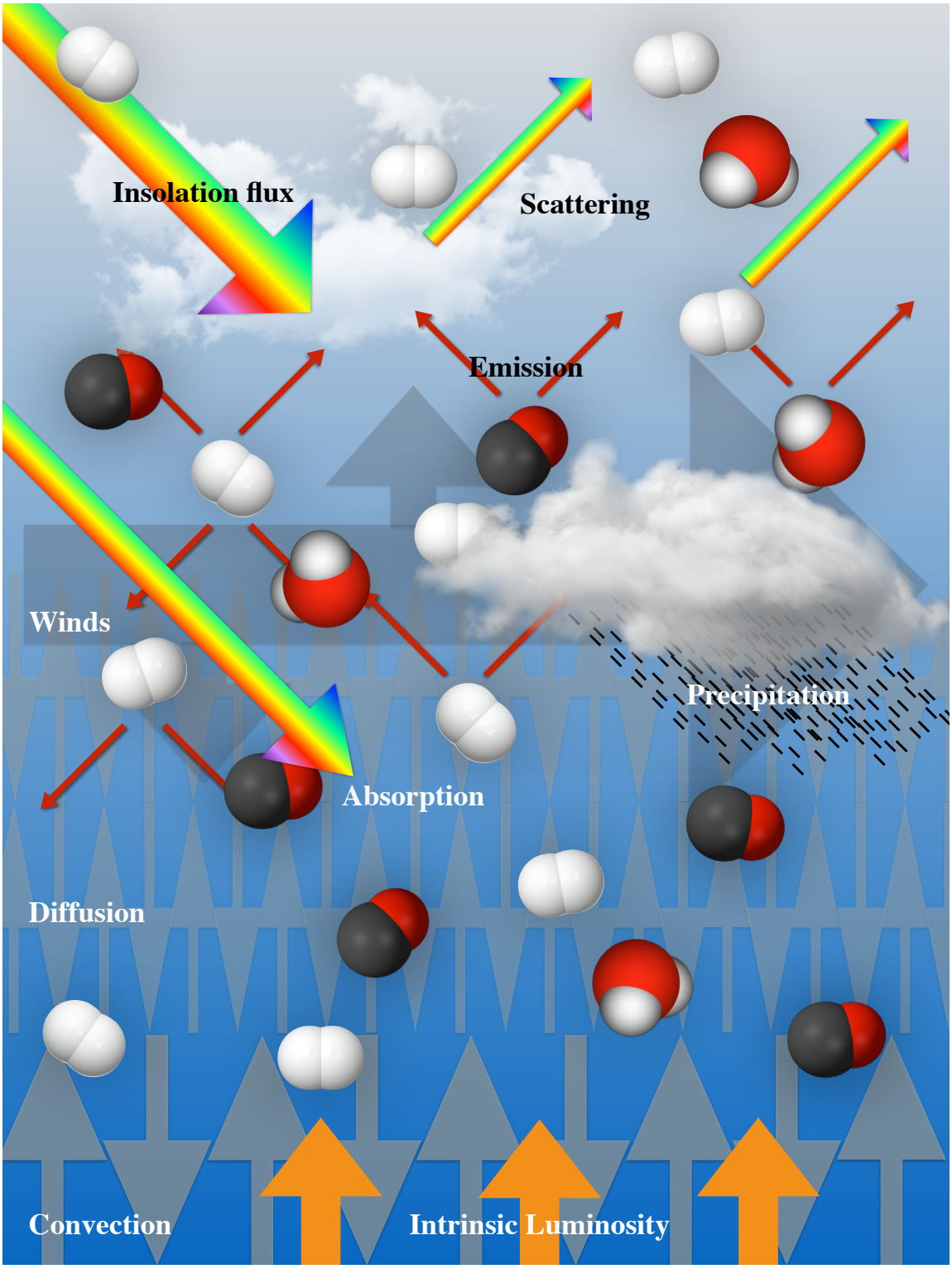

FIGURE 2.6: Schematic drawing summarizing the atmospheric processes mentioned in this chapter.

3 Building *petitCODE*, a code for self-consistent exo-atmospheres

In parts based on Mollière et al. (2015) and Mollière et al. (2017).

In this Chapter I will describe the methods and data from which my atmospheric code, *petitCODE*, is built. *petitCODE* stands for **P***re***s***sure*–**T***emperature* **It***erator and Spectral Emission and Transmission Calculator for Planetary Atmospheres*. *petitCODE* calculates self-consistent atmospheric structures for the input parameters which describe the planet–star system, such as the planetary mass, radius, internal temperature, elemental abundance, opacity species, host star radius, host star effective temperature, and the planet's semi-major axis.

Apart from *petitCODE*, there are a number of codes in the literature which are able to calculate the atmospheric structures and spectra of brown dwarfs and/or (exo)planets. However, when I started my thesis, there existed no publicly available codes, and the goal of being able to study atmospheres in depth, as well as to understand the physics behind the various processes in detail, represented the motivation for me to construct *petitCODE*. Other codes, which have been adopted from stellar or Solar System body codes, or have been specifically written for exoplanet atmospheres, are, e.g., *PHOENIX* (Hauschildt & Baron 1999; Barman et al. 2001), *UMA* (Gustafsson et al. 1975; Seager et al. 2000), *COOLTLUSTY* (Sudarsky et al. 2003; Hubeny et al. 2003), the "*McKay-Marley*" code (McKay et al. 1989), which is used by various groups (see, e.g., Marley et al. 1996; Burrows et al. 1997; Fortney et al. 2005; Morley et al. 2012), *ATMO* (Tremblin et al. 2015), *Exo-REM* (Baudino et al. 2015), and the codes by Goukenleuque et al. (2000) and Malik et al. (2017). A recent review and comparison of most of these codes, and their capabilities, can be found in Hubeny (2017)

The solutions of my *petitCODE* are obtained by iterating the atmospheric structure until the atmospheric abundances, and the resulting opacities and radiation fields, are in equilibrium with the temperature structure. The atmosphere is then in 'radiative-convective equilibrium' (convection is also included). The results returned by *petitCODE* are the planet's temperature and abundance structures. After the atmospheric structure has converged, both emission and transmission spectra can be calculated at high resolution ($\lambda/\Delta\lambda = 1000$). A summary of the how the code's individual modules work together is given in Section 3.9.

3.1 Basic assumptions

Here I will summarize some basic assumptions, which underpin the setup of *petitCODE*.

3.1.1 Atmospheric structure and treatment of stellar irradiation

One of the most important equations for the description of the atmospheres is the equation of hydrostatic equilibrium,

$$\frac{dP}{dr} = -\rho g \,, \tag{3.1}$$

which was derived in Section 2.1, and the validity of which was justified. I will also make use of the 'plane-parallel approximation', based upon the assumption that the vertical extent of the atmosphere is much smaller than the planetary radii, which means that the angle ϑ between a ray of light traveling in direction $\mathbf{n}$ and the atmospheric normal,

$$\mu = \cos\vartheta = \mathbf{e}_r \cdot \mathbf{n} \,, \tag{3.2}$$

is constant along the ray's path. This means that the atmospheric layers can be regarded as parallel, non-curved planes, with all physical quantities being constant on a given plane. The normal vector of the planes defines the vertical, i.e. radial direction. Because the atmosphere is assumed to be much thinner than the planetary radius it is also assumed that the planetary gravity is constant along a ray, and I set

$$g = \frac{GM_{\rm Pl}}{R_{\rm Pl}^2} \,. \tag{3.3}$$

Further, because it turns out to be more convenient, the spatial coordinate within the code is P, and can be related to the radius by means of Equation 3.1, if a reference pressure P_0 with $r(P_0) = R_{\rm Pl}$ is specified.

Finally, my code will concentrate on planets with an optically thick gas atmosphere, such as (hot) jupiters, neptunes and large-radius super-Earths. The atmosphere of such planets will be able to transport energy from the day to the nightside, thereby decreasing the flux of the planet measured during an eclipse measurement. As mentioned in Section 2.1.1, this process depends on the equilibrium temperature of the planet: The hotter the equilibrium temperature, the weaker the redistribution becomes, meaning that radiative cooling increasingly dominates over advection.

To account for the different possibilities of energy transport I consider three different scenarios for my calculations, which are also shown in Figure 3.1:

(a) globally averaged insolation, where the insolation flux is homogeneously spread over the full surface area of the planet, assuming the stellar radiation field impinges on the atmosphere isotropically. In this case the atmosphere is modeled by a single vertical structure. This is also the standard setting for the calculation of transmission spectra, because it was found that 3D GCM calculations lead to similar transmission spectra

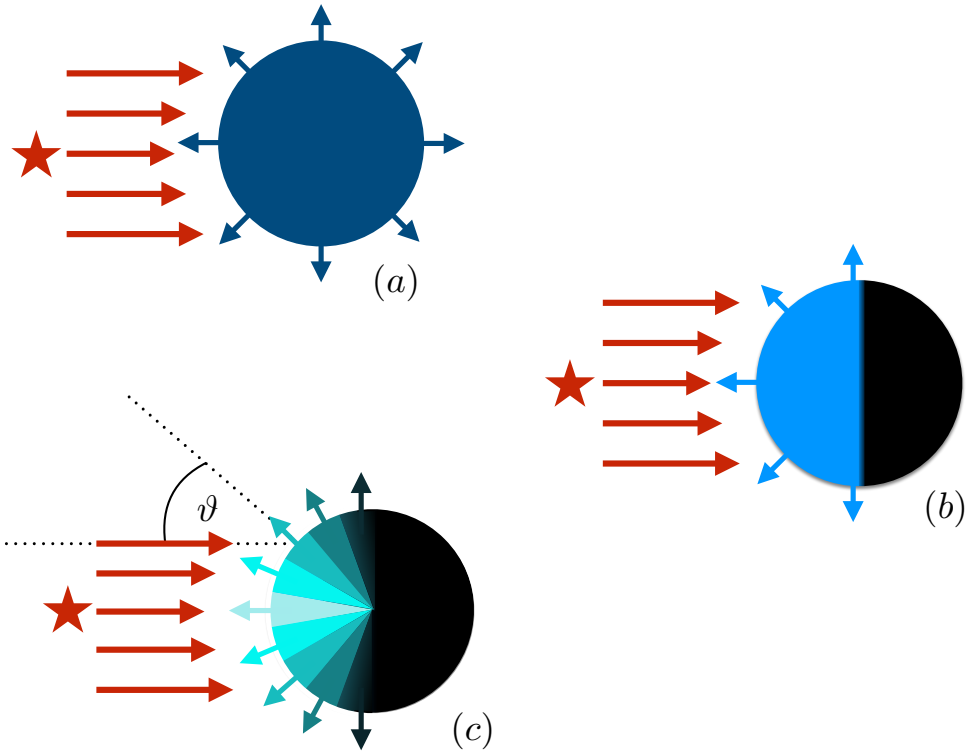

FIGURE 3.1: Schematic drawing of the three energy redistribution cases *(a)*, *(b)*, and *(c)* of *petitCODE*, as described in the text.

as the planet-wide averaged insolation 1D modes (but exceptions may exist, for more details see Fortney et al. 2010).

(b) day side averaged insolation, where the insolation flux is homogeneously spread over the dayside hemisphere of the planet, again assuming isotropic incidence, and modeling the atmosphere using a single vertical structure.

(c) case of no redistribution: for the very hot planets the brightness temperature of the dayside is higher than the temperature expected for both the dayside and the global average case (see, e.g., Nymeyer et al. 2011; Shporer et al. 2014). In such cases I calculate emission spectra by combining individual structures and spectra for planetary annuli at angular distances ϑ between 0 and $\pi/2$ from the substellar point. For every annulus I assume that it has to reemit all the flux it receives from the star, impinging at an angle ϑ. This corresponds to the case where the energy advection by winds is fully neglected. For computing the planetary emission spectra, only the intensities of the rays headed into the direction of the observer are taken into account.

3.1.2 Radiative processes

petitCODE treats the absorption and scattering of the radiation fields of both the star and the planet. The scattering is assumed to be isotropic, i.e. the direction of light scattered

off a particle is independent of the direction of the incident light. The case of non-isotropic scattering is included in an approximative fashion, see Section 3.2.1.

3.1.3 Chemistry

petitCODE use a self-written Gibbs minimizer to calculate the atomic, molecular, and condensate abundances, and thus makes the assumption of equilibrium chemistry, which I introduced in Section 2.3.1. The data used for my Gibbs minimizer are described in Section 3.4.1).

In order to assess the validity of the equilibrium chemistry assumption one must concentrate on the regions which shape the spectral appearance of the planet, i.e. from where light is emitted to space, or absorbed during transmission spectral measurements. These atmospheric regions of interest are also called the 'spectrally active' regions. The spectrally active region of a planetary atmosphere usually lies in the pressure range from 10^{-4} to 10 bars (see, e.g., the supplementary material in Madhusudhan et al. 2011b).

One can obtain a reasonable assessment of the importance of non-equilibrium chemistry by considering the work by Miguel & Kaltenegger (2014), who analyzed the chemical properties of planetary atmospheres around FGKM-stars. They used stellar model spectra compiled by Rugheimer et al. (2013) for the FGK stars and a spectral model for an inactive M dwarf by Allard et al. (2001) as an input for the photochemical model, in which the photodissociation of molecules was treated. Furthermore they consider vertical mixing. By comparing figures 6 and 7 in Miguel & Kaltenegger (2014), one can identify the temperature region where the spectrally active region is not affected by non-equilibrium effects (mainly vertical mixing) to start at $T_{\rm equ} \gtrsim 1500$ K. However, it is worth noting that the temperature below which non-equilibrium effects are noticeable also depends on the chemical scheme being used and on whether or not the planets are irradiated, as calculations by Zahnle & Marley (2014) indicate. Here the non-equilibrium effects of non-irradiated planets, due to vertical mixing, become important for $T_{\rm eff} \lesssim 1000$ K.

Hot jupiters can thus often be considered to be well described by equilibrium chemistry, but one needs to keep in mind that for $T_{\rm equ} < 1500$ K non-equilibrium effects may start to become important.

3.2 Radiative transfer

3.2.1 The formal radiative transfer equation and its solution

The propagation of light though planetary atmospheres can be described by geometric optics, i.e. the light itself is treated as the transport of energy along straight rays. This is a valid approach because the atmospheric extent is much larger than any wavelengths of interest (UV to MIR). However, if a ray encounters a cloud particle comparable to the wavelength of the light, this approximation breaks down, such that the propagation of light through the particle the has to be described by the Maxwell equations. However, I am not interested in

the solution of the radiation field within the particles itself, only in the outcome of this interaction. Thus, for cloud particles I use scattering and absorption cross-sections derived from a treatment essentially similar to Mie theory (see Section 3.3.2), which solves the Maxwell equations. For the light propagation in the atmosphere it is thus sufficient to use geometric optics.

The quantity of interest in geometric optics is the intensity of a ray, I_ν, which is defined as

$$I_\nu(\mathbf{x}, \mathbf{n}) = \frac{dE}{dt\, d\nu\, d\Omega\, dA} , \tag{3.4}$$

i.e. the transported energy E per unit time t, frequency of the light ν, direction (expressed by the solid angle Ω), and area A. I_ν is a scalar field, where $\mathbf{x}$ denotes the position where I_ν is evaluated, and $\mathbf{n}$ the direction of the ray, pointing into the solid angle $d\Omega$. From this the scalar energy flux, passing through an area ΔA, and into the direction parallel to its normal vector $\Delta\mathbf{A}$ is given by

$$F(\mathbf{x}) = \frac{1}{\Delta A} \int_{2\pi} (\mathbf{n} \cdot \Delta\mathbf{A}) I_\nu(\mathbf{x}, \mathbf{n}) d\Omega . \tag{3.5}$$

The solution of the intensity can be obtained from solving the radiative transfer equation,

$$\mathbf{n} \cdot \nabla I_\nu(\mathbf{x}, \mathbf{n}) = -\alpha_\nu(\mathbf{x}) I_\nu(\mathbf{x}, \mathbf{n}) + j_\nu(\mathbf{x}, \mathbf{n}) , \tag{3.6}$$

where $\mathbf{n} \cdot \nabla I_\nu$ is the spatial derivative of I_ν along the direction of the ray, α_ν is the inverse mean free path of a photon, and $j_\nu(\mathbf{x}, \mathbf{n})$ is the 'emissivity' of the material through which the ray passes, i.e. it encapsulates the intensity emitted into the direction of the ray per unit distance traveled by the ray.

One can now define the 'source function' as $S_\nu = j_\nu/\alpha_\nu$ which yields

$$\mathbf{n} \cdot \nabla I_\nu = \alpha_\nu (S_\nu - I_\nu) , \tag{3.7}$$

where the $\mathbf{x}$ and $\mathbf{n}$ dependencies were dropped for notational convenience. If scattering can be neglected, and if the emitting material is in LTE, then it holds that

$$S_\nu = B_\nu(T) , \tag{3.8}$$

which is 'Kirchhoff's law'.

In the case including scattering one can define $\alpha_\nu^{\mathrm{tot}} = \alpha_\nu^{\mathrm{abs}} + \alpha_\nu^{\mathrm{scat}}$, where $\alpha_\nu^{\mathrm{abs}}$ and $\alpha_\nu^{\mathrm{scat}}$ are the inverse mean free paths of absorption and scattering, respectively. One can further define the 'albedo' as

$$\eta_\nu = \frac{\alpha_\nu^{\mathrm{scat}}}{\alpha_\nu^{\mathrm{tot}}} , \tag{3.9}$$

and the 'photon destruction probability' as

$$\epsilon_\nu = \frac{\alpha_\nu^{\mathrm{abs}}}{\alpha_\nu^{\mathrm{tot}}} = 1 - \eta_\nu , \tag{3.10}$$

such that one finally obtains

$$\mathbf{n} \cdot \nabla I_\nu = \alpha_\nu^{\text{tot}} (S_\nu - I_\nu) \,, \tag{3.11}$$

with

$$S_\nu = \epsilon_\nu B_\nu(T) + \eta_\nu \int_{4\pi} I_\nu(\mathbf{n}') p_\nu(\mathbf{n}', \mathbf{n}) d\Omega' \,, \tag{3.12}$$

where LTE was assumed for the emission. The second term on the RHS is the 'scattering source function', with p_ν being the 'scattering phase function', i.e. the probability distribution that a ray $I_\nu(\mathbf{n}')$, traveling in direction $\mathbf{n}'$, is scattered into direction $\mathbf{n}$. The scattering phase function has the properties $p_\nu(\mathbf{n}', \mathbf{n}) = p_\nu(\mathbf{n}, \mathbf{n}')$, $p_\nu(\mathbf{n}', \mathbf{n}) \geq 0$, and

$$\int_{4\pi} p_\nu(\mathbf{n}', \mathbf{n}) d\Omega' = 1 \,. \tag{3.13}$$

As said before, I will make the assumption of isotropic scattering, i.e. neglecting the directional dependence arising from p_ν. However, there is a treatment which allows to approximate non-isotropic scattering if the radiation is in the diffusive regime (i.e. in regions where the free mean path is very short). To this end one can define the 'scattering anisotropy' g_ν as

$$g_\nu = \int_{4\pi} (\mathbf{n}' \cdot \mathbf{n}) p_\nu(\mathbf{n}', \mathbf{n}) d\Omega' \,, \tag{3.14}$$

which is zero in the case of isotropic scattering, where $p_\nu = 1/4\pi$. One then finds that (see, e.g. Wang & Wu 2007)

$$S_\nu = \epsilon_\nu B_\nu(T) + \eta_\nu (1 - g_\nu) J_\nu \,, \tag{3.15}$$

where

$$J_\nu = \frac{1}{4\pi} \int_{4\pi} I_\nu(\mathbf{n}) d\Omega \tag{3.16}$$

is the mean intensity. Because this treatment yields the correct behavior in the limit of diffusive radiation transport I will use it as the standard approach for scattering.

In conclusion, the equations which need to be solved are Equation 3.11 and 3.15, where the well-known problem arises that the source function depends on the solution of the problem, because S_ν contains J_ν. As I am simultaneously solving for the atmospheric temperature, $B_\nu(T)$ also depends on I_ν, because the atmospheric matter is treated in 'radiative equilibrium', which means that it thermally reemits all the energy it absorbs from the radiation field. To overcome this problem one usually starts with an initial guess for the intensity, calculates the source function, updates the intensity, an iterates until convergence is reached. If one is in the diffusive regime, however, this can take quite long, because the photons which are scattered carry out a random walk, and every iteration is one random walk step. In these cases methods for speeding up convergence need to be used, see below (after the explanation of Feautrier's method).

Feautrier's method

In this section I will show how to solve the radiative transfer equation for a known source function, using Feautrier's method. This is the method used in *petitCODE* to solve for the

planet's radiation field, and to calculate emission spectra.

In order to treat the diffusive regime correctly on needs to use a third order method for solving the radiative transfer equation, otherwise the properties of the solution in the limits of large optical depths will be incorrect (see, e.g., Dullemond 2012). Feautrier's method is such a third-order method, and my description of it in the following is partially based on Dullemond (2012).

I already defined the optical depth as

$$\tau_\nu = \int \alpha_\nu ds \; . \tag{3.17}$$

Using hydrostatic equilibrium, and $\alpha_\nu = \kappa_\nu \rho$, where κ_ν was defined as the cross-section per unit mass, one obtains

$$\tau_\nu^{\rm vert} = \int \frac{\kappa_\nu}{g} dP \tag{3.18}$$

for the vertical optical depth. For a ray of light traveling at an angle ϑ to the atmospheric normal the optical depth is

$$\tau_\nu(\vartheta) = \frac{\tau_\nu^{\rm vert}}{\mu} \; , \tag{3.19}$$

with

$$\mu = \cos\vartheta \; , \tag{3.20}$$

where μ is the only angular quantity of interest in plane-parallel atmospheres, because the atmospheric variation in the azimuthal direction around the atmospheric normal can be neglected (the special case of the stellar light, impinging from a given solid angle $\Delta\Omega_*$, is explained later).

I will now solve the radiative transfer equation along the direction the ray is traveling in, and I will express the distance traveled in units of τ. If the ray is traveling toward increasing pressure, I will denote it by I_+, where the ν-dependence has been omitted for notational convenience. One then gets

$$\frac{dI_+}{d\tau} = S - I_+ \; . \tag{3.21}$$

For a ray I_- traveling in the opposite direction one thus gets

$$\frac{dI_-}{d\tau} = -S + I_- \; . \tag{3.22}$$

Defining

$$I_J = \frac{1}{2}(I_+ + I_-) \; , \tag{3.23}$$

and

$$I_H = \frac{1}{2}(I_+ - I_-) \; , \tag{3.24}$$

one finds from the equations for I_+ and I_- that

$$\frac{dI_J}{d\tau} = -I_H \; , \tag{3.25}$$

and

$$\frac{dI_H}{d\tau} = S - I_J \,, \tag{3.26}$$

which yields

$$\frac{d^2 I_J}{d\tau^2} = I_J - S \,. \tag{3.27}$$

Equation 3.27 has the shape of a diffusion equation, and thus leads to the correct behavior in the diffusive regime. It is the equation solved in *petitCODE* to obtain the solution for the radiation field.

For the planetary radiation field the upper boundary condition is

$$I_+(P = 0, \vartheta) = 0 \; \forall \; \vartheta \,, \tag{3.28}$$

because no planetary light will enter the atmosphere at its top: it can only leave the planet. Furthermore, deep down in the planet the radiation field is assumed to be diffusive, such that the lower boundary condition is

$$I_+(P \to \infty, \vartheta) = I_-(P \to \infty, \vartheta) \; \forall \; \vartheta \,, \tag{3.29}$$

For I_J and I_H this translates into

$$\frac{d}{d\tau} I_J(0) = I_J(0) \,, \tag{3.30}$$

and

$$\frac{d}{d\tau} I_J(P \to \infty) = 0 \,. \tag{3.31}$$

The solution can then be obtained by discretizing Equation 3.27 into

$$\begin{pmatrix} b_1 & c_1 & 0 & \cdots & 0 \\ a_2 & b_2 & c_2 & \ddots & \vdots \\ 0 & \ddots & \ddots & \ddots & 0 \\ \vdots & \ddots & a_{N-1} & b_{N-1} & c_{N-1} \\ 0 & \cdots & 0 & a_N & b_N \end{pmatrix} \cdot \begin{pmatrix} I_{J,1} \\ I_{J,2} \\ \vdots \\ I_{J,N-1} \\ I_{J,N} \end{pmatrix} = \begin{pmatrix} S_1 \\ S_2 \\ \vdots \\ S_{N-1} \\ S_N \end{pmatrix} \,, \tag{3.32}$$

or

$$M \mathbf{I_J} = \mathbf{S} \,, \tag{3.33}$$

where N is the number of atmospheric layers.

The elements of the tridiagonal matrix can be obtained from discretizing Equation 3.27 in the following form for $i \neq 1, i \neq N$ (and writing I_J as I):

$$- \frac{\left(\frac{I_{i+1} - I_i}{\tau_{i+1} - \tau_i}\right) - \left(\frac{I_i - I_{i-1}}{\tau_i - \tau_{i-1}}\right)}{\left(\frac{\tau_{i+1} + \tau_i}{2}\right) - \left(\frac{\tau_i + \tau_{i-1}}{2}\right)} + I_i = S_i \,, \tag{3.34}$$

and an appropriate discretization of the boundary conditions for b_1, c_1 and a_N, b_N. A tridiagonal matrix may be inverted using standard numerical procedures, and I use the `tridag` routine of the Numerical Recipes collection (Press et al. 1992).

Once I_J has been obtained, then I_H can be calculated from Equation 3.25. The emergent flux at the top of the atmosphere can then be obtained from

$$F_\nu = \int_{2\pi} I_\nu \mathbf{n} \cdot \mathbf{e_z} d\Omega \,, \tag{3.35}$$

where the atmospheric normal in the plane-parallel case has been defined to point in the z-direction, if cartesian coordinates are used. Thus one gets

$$\begin{aligned} F_\nu &= \int_0^{2\pi} \int_0^{\pi/2} I_\nu(P=0) \cos(\vartheta) \sin(\vartheta) d\phi d\vartheta \,, \\ &= 2\pi \int_0^1 I_\nu(P=0) \mu d\mu = -4\pi \int_0^1 I_H(P=0) \mu d\mu \,, \end{aligned} \tag{3.36}$$

where $\partial I_\nu / \partial \phi = 0$ (plane-parallel), $\mu = \cos(\vartheta)$, and $I_+(P=0) = 0$ were used. Similarly, for the mean intensity one finds that

$$J_\nu(P) = \frac{1}{4\pi} \int_{4\pi} I_\nu(P) d\Omega = \int_0^1 I_J(P) d\mu \,. \tag{3.37}$$

Speeding up convergence: Accelerated Lambda Iteration and Ng acceleration

The solution of Feautrier's method yields the radiation field for a given, fixed source function. The new solution for I_ν is then used to obtain the new source function etc. In a purely scattering atmosphere with optical depth τ a photon will undergo $\sim \tau^2$ scattering events to diffuse through the atmosphere, but less if the photon destruction probability ϵ is non-zero. One thus finds that in order to converge the number of iterations needs to be higher than

$$N_{\mathrm{iter}} \gg \min\left(\tau^2, \frac{1}{\epsilon}\right) \,. \tag{3.38}$$

I expect planetary atmospheres to be dominated by molecular absorption, but in the case of thick, vertically extended clouds it is better to play save and implement schemes which converge faster than given by the equation above. To that end I implemented 'Accelerated Lambda Iteration' (ALI, see Olson et al. 1986) and Ng acceleration (Ng 1974), as described in Dullemond (2012). Below I show how I adapted ALI to Feautrier's method and give a half-page summary of the description of the Ng method as described in Dullemond (2012).

The quantity of interest for the scattering source function is the mean intensity J_ν. ALI starts from defining the Λ operator as

$$\mathbf{J}_\nu = \Lambda \mathbf{S}_\nu \,, \tag{3.39}$$

where one evaluation of the Λ operator is, for the *petitCODE* case, simply one call of the Feautrier method, and the solid angle integral over the resulting I_ν to obtain J_ν. Because the

radiative transfer equation as well as the J_ν integral are linear in S_ν and I_ν, it holds that Λ is a linear operator. The radiative transfer problem can then be expressed as (see Equation 3.15)

$$\mathbf{S}_\nu = \mathrm{diag}(\epsilon_\nu)\mathbf{B}_\nu + [E - \mathrm{diag}(\epsilon_\nu)]\Lambda\mathbf{S}_\nu \ , \tag{3.40}$$

where the anisotropy factor $(1-g_\nu)$ has been absorbed into the scattering cross-section. Here E is the unity matrix, and $\mathrm{diag}(\epsilon_\nu)$ is the diagonal matrix containing the values of the ϵ_ν on its diagonal. The formal solution is

$$\mathbf{S}_\nu = M_\nu^{-1}\mathrm{diag}(\epsilon_\nu)\mathbf{B}_\nu \ , \tag{3.41}$$

with

$$M_\nu = E - [E - \mathrm{diag}(\epsilon_\nu)]\Lambda \ . \tag{3.42}$$

Computing M and its inverse would immediately lead to the solution, without any iteration, but both the computation and inversion of the matrix are computationally infeasible. One thus usually tries to solve Equation 3.40 in an iterative fashion, by writing

$$\mathbf{S}_\nu^{\mathrm{n}+1} = \mathrm{diag}(\epsilon_\nu)\mathbf{B}_\nu + [E - \mathrm{diag}(\epsilon_\nu)]\Lambda\mathbf{S}_\nu^{\mathrm{n}} \tag{3.43}$$

for obtaining the source function of the $(n+1)$th iteration, hence the name 'Lambda iteration'. This process may suffer from the aforementioned slow convergence, however.

Rather, to at least partially speed up the convergence, one splits $\Lambda = (\Lambda - \Lambda^*) + \Lambda^*$, where $\Lambda^* = \mathrm{diag}(\Lambda)$ is the 'local accelerated lambda iterator', which contains only the diagonal elements of Λ, and thus how the mean intensity in the ith layer, J_i, depends on S_i. This split will then take care of the photons scattered in the cells where they originate from. One then gets

$$\{E - [E - \mathrm{diag}(\epsilon_\nu)]\Lambda^*\}\mathbf{S}_\nu = \mathrm{diag}(\epsilon_\nu)\mathbf{B}_\nu + [E - \mathrm{diag}(\epsilon_\nu)](\Lambda - \Lambda^*)\mathbf{S}_\nu \ , \tag{3.44}$$

such that one obtains for the source function of the $(n+1)$th iteration, $\mathbf{S}_\nu^{\mathrm{n}+1}$, that

$$\begin{aligned} \mathbf{S}_\nu^{\mathrm{n}+1} &= M^{-1}\left\{\mathrm{diag}(\epsilon_\nu)\mathbf{B}_\nu + [E - \mathrm{diag}(\epsilon_\nu)](\Lambda - \Lambda^*)\mathbf{S}_\nu^n\right\} \ , \\ &= M^{-1}\left\{\mathrm{diag}(\epsilon_\nu)\mathbf{B}_\nu + [E - \mathrm{diag}(\epsilon_\nu)](\mathbf{J}_\nu^n - \Lambda^*\mathbf{S}_\nu^n)\right\} \ , \end{aligned} \tag{3.45}$$

where

$$M = E - [E - \mathrm{diag}(\epsilon_\nu)]\Lambda^* \ . \tag{3.46}$$

This is easy to invert, as M is a purely diagonal matrix.

From Feautrier's method, and Equation 3.37 one can then derive that

$$\Lambda^*_{1,1} = \sum_{j=1}^{N_\mu} \left[1 + \frac{2}{(\tau_2 - \tau_1)^2} + \frac{2}{\tau_2 - \tau_1}\right]^{-1} \Delta\mu_j \tag{3.47}$$

$$\Lambda^*_{i,i} = \sum_{j=1}^{N_\mu} \frac{\Delta\mu_j}{b_i(\mu_j)} \text{ for } i \in [2, N-1] \text{ , and} \tag{3.48}$$

$$\Lambda^*_{N,N} = \sum_{j=1}^{N_\mu} \left[1 + \frac{2}{(\tau_N - \tau_{N-1})^2}\right]^{-1} \Delta\mu_j \text{ ,} \tag{3.49}$$

where N_μ is the number of angles μ_j, and

$$b_i(\mu) = \left[1 + \frac{2}{(\tau_{i+1} - \tau_{i-1})(\tau_{i+1} - \tau_i)} + \frac{2}{(\tau_{i+1} - \tau_{i-1})(\tau_i - \tau_{i-1})}\right] \text{ .} \tag{3.50}$$

Ng acceleration (Ng 1974) makes use of the fact that $\mathbf{S}^n_\nu$ converges linearly, because the iteration equation derived from Equation 3.40 takes the form

$$\mathbf{S}^n_\nu = \mathbf{A} + \Psi\mathbf{S}^{n-1}_\nu \text{ ,} \tag{3.51}$$

indicating that the solution, $\mathbf{S}_\nu = \lim_{n\to\infty} \mathbf{S}^n_\nu$, depends linearly on all previous iterations. It can be shown that such linearly converging systems can exhibit false convergence, because one can write

$$\mathbf{S}^n_\nu - S = \Psi^n \left(\mathbf{S}^0_\nu - S\right) \text{ ,} \tag{3.52}$$

where $\mathbf{S}^0_\nu$ is the initial guess for $\mathbf{S}_\nu$. If ψ has eigenvalues both $\ll 1$ and close to 1, then the convergence in the eigenvectors associated with the eigenvalues $\ll 1$ may make the system appear to have converged too early. Ng acceleration speeds up the convergence by finding the optimal linear combination of the last iterative solutions of $\mathbf{S}^{n-2}_\nu$, $\mathbf{S}^{n-3}_\nu$, $\mathbf{S}^{n-4}_\nu$,

$$\mathbf{S}' = (1 - a - b)\mathbf{S}^{n-2}_\nu + a\mathbf{S}^{n-3}_\nu + b\mathbf{S}^{n-4}_\nu \tag{3.53}$$

that will minimize the difference $|\mathbf{S}'' - \mathbf{S}'|$ between $\mathbf{S}'$ and $\mathbf{S}''$ (which woulf indicate good convergence), where

$$\mathbf{S}'' = \mathbf{A} + \Psi\mathbf{S}' = (1 - a - b)\mathbf{S}^{n-1}_\nu + a\mathbf{S}^{n-2}_\nu + b\mathbf{S}^{n-3}_\nu \text{ .} \tag{3.54}$$

One can find the associated values of a and b which minimize $|\mathbf{S}'' - \mathbf{S}'|$ (I use the solution presented in Dullemond 2012), and the convergence is then sped up by setting

$$\mathbf{S}^n_\nu = \mathbf{S}'' \text{ .} \tag{3.55}$$

In this way, Ng acceleration predicts the next step by analyzing the convergence behavior of the previous four steps. Thus, after every Ng acceleration step, three additional ALI steps have to be carried out in order to use Ng again.

Separating stellar and planetary radiation fields

petitCODE treats the radiation field of planet and star separately, which makes the problem easier to tackle conceptually. Splitting up a radiation field in different components is allowed because the radiative transfer equation depends only linearly on I_ν.

The planetary radiation field arising from emission in the planet's atmosphere is treated exactly as described in the above sections, using Feautrier's method, as well as ALI and Ng acceleration. How the temperature is found for the emission part of the source function will be explained in Section 3.6.

The stellar intensity I_* is split in in two components:

$$I_* = I_*^{\rm ini} + I_*^{\rm scat} \,, \tag{3.56}$$

where $I_*^{\rm ini}$ is the stellar ray initially impinging on the the top of the planetary atmosphere, which is affected by extinction (due to absorption and scattering) only, whereas $I_*^{\rm scat}$ is the processed stellar light arising from the scattering of $I_*^{\rm ini}$. I omit writing the frequency dependence of the intensity I_ν, here and below. Note that I do *not* neglect emission in the wavelengths of the stellar light, because this is part of the planetary emission, and coupled to the absorption of the stellar light via the temperature obtained from radiative equilibrium.

One can then write the equation of radiative transfer as

$$\begin{aligned} \frac{dI_*^{\rm ini}}{d\tau} + \frac{dI_*^{\rm scat}}{d\tau} &= -(I_*^{\rm ini} + I_*^{\rm scat} - S) \,, \\ &= -[I_*^{\rm ini} + I_*^{\rm scat} - (1-\epsilon)(J_*^{\rm ini} + J_*^{\rm scat})] \,. \end{aligned} \tag{3.57}$$

I separate this equation into two equations for $I_*^{\rm ini}$ and $I_*^{\rm scat}$, leading to

$$\frac{dI_*^{\rm ini}}{d\tau} = -I_*^{\rm ini} \,, \text{ and} \tag{3.58}$$

$$\frac{dI_*^{\rm scat}}{d\tau} = -[I_*^{\rm scat} - (1-\epsilon)(J_*^{\rm ini} + J_*^{\rm scat})] \,. \tag{3.59}$$

Equation 3.59 is solved using Feautrier's method as well as ALI and Ng acceleration, but for this $J_*^{\rm ini}$ needs to be known. $J_*^{\rm ini}$ depends solely on $I_*^{\rm ini}$, which can be calculated from simple attenuation

$$I_*^{\rm ini}(\tau) = I_*^{\rm ini}(0) e^{-\tau} \,, \tag{3.60}$$

where for the isotropic stellar irradiation case one gets

$$I_*^{\rm ini}(0,\mu) = \begin{cases} F_*^{\rm ini}(0)/\pi & \text{for } \mu < 0 \,, \\ 0 & \text{else} \,, \end{cases} \tag{3.61}$$

where $F_*^{\rm ini}(0)$ is the stellar flux impinging onto the planet's surface. This follows from the requirement that

$$F_*^{\rm ini}(0) = 2\pi \int_{-1}^{0} \mu I_*^{\rm ini}(0) d\mu \tag{3.62}$$

$$= 2\pi I_*^{\rm ini}(0) \int_{-1}^{0} \mu d\mu \ , \tag{3.63}$$

where I used the same reasoning as used in Equation 3.36, and that $I_*^{\rm ini}(0)$ is isotropic.

For non-isotropic radiation, incident under an angle μ_*, one finds for the flux component parallel to the atmospheric normal that

$$F_*^{\rm ini}(0) = \int_{\Delta\Omega_*} I_*^{\rm ini} \mu d\Omega \tag{3.64}$$

$$\approx I_*^{\rm ini}(0) \mu_* \Delta\Omega_* \ , \tag{3.65}$$

where $\Delta\Omega_*$ is the solid angle subtended by the stellar disk, from the atmospheric location. Similarly it holds that $J_*^{\rm ini} = I_*^{\rm ini}\Delta\Omega_*/4\pi$, because the angle of the initial ray does not change within the atmosphere. Thus one gets that

$$J_*^{\rm ini} = \frac{I_*^{\rm ini}(0)}{4\pi} e^{-\tau^{\rm vert}/\mu_*} \Delta\Omega_* \ ,$$

$$= \frac{F_*^{\rm ini}(0)}{4\pi\mu_*} e^{-\tau^{\rm vert}/\mu_*} \ . \tag{3.66}$$

Hence, for the non-isotropic irradiation case, Equation 3.66 may be used in Equation 3.59.

3.2.2 The correlated-k assumption for molecular and atomic opacities

Molecular and atomic line opacities are the major source of opacity in cloud-free atmospheres. Molecules can have line lists containing millions to billions of lines, and if the pressure is low enough, the cores of the lines will be very narrow. If pressure broadening is negligible the line cores will be Doppler-shaped. For a water molecule at $T = 400$ K one finds that (see Equation 2.72)

$$\frac{\nu_{ij}}{\gamma_{\mathcal{D}}} \sim 5 \times 10^5 \ , \tag{3.67}$$

which means that the frequency spacing between two adjacent wavelengths bins would have to be $R/\Delta R \sim 10^6$ to properly resolve a given line. Most of the spectrum of a planet is formed at larger pressures, but my own experiments showed that a wavelength binning of 2×10^4 is not enough to correctly calculate fluxes, see Section 6.3.4, the reason for this being that also at larger pressures, with stronger pressure broadening, there is still a non-negligible contrast between line cores and the line wing continuum.

It is thus crucial to do calculations at a high enough resolution. At a fixed frequency grid of low resolution one may, by chance, not sample an important line, and hence underestimate the atmospheric absorption. Or, by chance, one samples a line core spot-on and

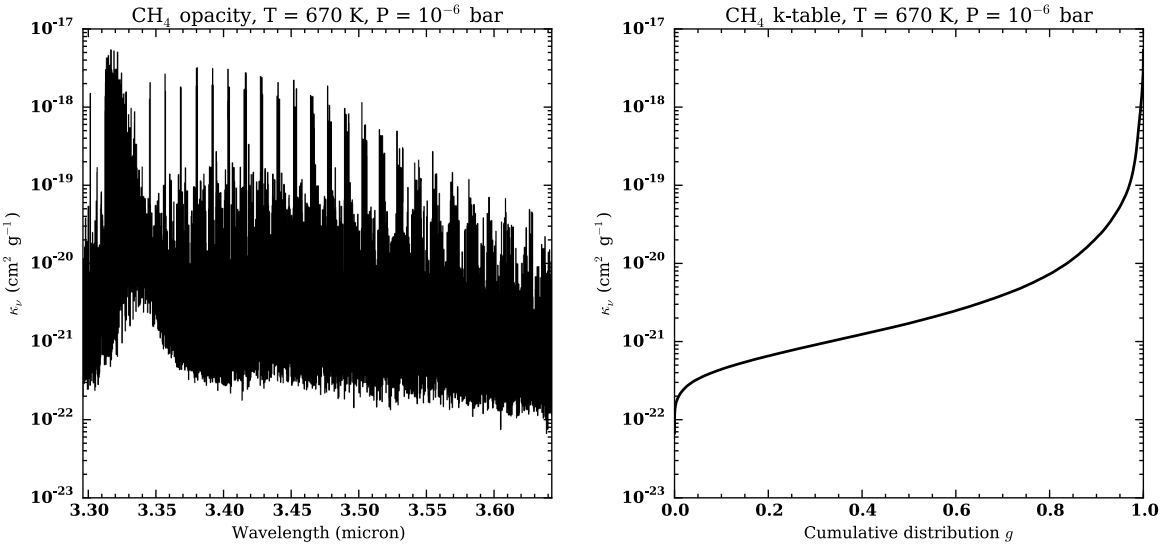

FIGURE 3.2: *Left panel:* CH_4 opacity at $T = 670$ K, $P = 10^{-6}$ bar in the 3.3-3.65 μm region, showing 100,000 frequency points at a resolution of $\lambda/\Delta\lambda = 10^6$. *Right panel:* cumulative opacity distribution function g for the opacity shown in the *left panel*.

strongly overestimates atmospheric absorption, because there can be many orders of magnitude difference between the line core and the line wing continuum. To demonstrate this I plot the opacity for CH_4 at 670 K and 10^{-6} bar in the left panel of Figure 3.2. The opacity varies by four order of magnitude within the range shown here! Note that I plot κ_ν as a function of $\lambda = c/\nu$ here.[1] Random line sampling within a frequency bin can alleviate the situation somewhat, but leads to noise, and usually still systematically overestimates the opacities if a line core is hit. Taking the frequency average of the opacity within a frequency bin is also prohibitive, because then the absorption of the bin will be strongly overestimated, with the line cores dominating the line wings completely.

If one takes these observations at face value, then for the wavelength range used in *petitCODE* (110 nm to 250 μm, see Section 3.3.1), $\sim N_\nu = 10^6$ frequency points need to be considered, if $\lambda/\Delta\lambda = 10^5$ is used. This means that for every spectral calculation $N_{\rm layers} \times N_\nu \times N_\mu$ intensity integration steps would need to be carried out. For 100 atmospheric layers, and 10 angles μ, this would require 10^9 integration steps for a single spectrum. Because the radiation field needs to be calculated once every temperature iteration step (see Section 3.9), this is totally unfeasible.

A solution to this problem can be seen in the right panel of Figure 3.2: it shows the cumulative distribution function g for the opacities shown in the left panel, where $dg = f(\kappa)d\kappa$, and $f(\kappa)$ being the opacity distribution function. This means that $f(\kappa)\Delta\kappa$ is the fraction of all opacities between κ and $\kappa + \Delta\kappa$. As one can see $\kappa(g)$ is a smooth function, which can be sampled sufficiently using a lot fewer points than in the case when $\kappa(\nu)$ was plotted.

Now, if the atmosphere was isothermal at 670 K, and at constant pressure of 10^{-6} bar,

[1] Flux plots in atmospheric modeling are often plotted as F_ν as a function of λ, and I follow this convention for the opacity here as well.

one could exchange the spectral coordinate ν with g, and carry out all radiative calculations, not as a function of ν, but as a function of g. This could be done using a fraction of the resolution necessary in the frequency case. Once one reaches the top of the atmosphere, the mean emergent planetary flux across the frequency bin ν can be obtained from

$$\begin{aligned}\langle F_\nu \rangle &= \frac{1}{\Delta\nu}\int_\nu^{\nu+\Delta\nu} F_\nu d\nu \\ &= \int_{-\infty}^{\infty} f(\kappa) F_\kappa d\kappa \\ &= \int_0^1 F_g dg \ , \end{aligned} \tag{3.68}$$

where Equation 3.68 holds for all frequency-dependent quantities, not just the flux.

The final step to arrive at the so-called 'correlated-k' assumption is to use g as a spectral coordinate not only in the case of homogeneous atmospheres, i.e. atmospheres at constant T, P, and composition, but to use it for atmospheres where all these quantities vary. However, the *true* spectral coordinate is ν. Thus one has to assume that κ_ν values at constant ν, but in different atmospheric layers, map to the same g values. The κs ('k's) must thus be correlated, hence the naming 'correlated-k'. Correlated-k was first used by (Goody et al. 1989; Lacis & Oinas 1991; Fu & Liou 1992). It speeds up the calculations significantly, and the relative errors one obtains for the flux are usually in the low, single-digit percentage regime, and scatter about zero (see Fu & Liou 1992; Lacis & Oinas 1991, and Section 3.2.3).

A new fast method for k-table sampling

Instead of obtaining κ_ν opacities, the goal is now to get κ_g opacities for every atmospheric layer, at given P, T and composition. To this end, one first obtains the κ_g opacities (so-called 'k-tables') for every species by interpolating to the P and T values (see Section 3.3.1 for the opacity grid definition). One cannot simply add the κ_g values for different species, like it is done in frequency space, however (cf. Equation 2.61). Instead one has to sample the opacity distribution functions of the various species, and obtain the total opacity from the sum of samples.

A method commonly described to combine the k-tables of multiple species is numerically quite expensive, as it is of order $\mathcal{O}(N_g^{N_{\rm species}})$, where N_g is the number of grid points used in g-space and $N_{\rm species}$ is the number of species. The computation of the total opacity $\kappa_{\rm tot}$ works as follows: In a spectral region of the frequency interval $[\nu, \nu+\Delta\nu]$ the transmission of light $\mathcal{T}$ through a layer of thickness ΔP which contains 2 spectrally active species is

$$\mathcal{T} = \int_\nu^{\nu+\Delta\nu} \exp\left[-\frac{X_1\kappa_1(\nu) + X_2\kappa_2(\nu)}{a}\Delta P\right]\frac{d\nu'}{\Delta\nu} \ , \tag{3.69}$$

where X_i and κ_i are the mass fractions and opacities of the two species, a is the gravitational acceleration in the atmosphere and ΔP is the atmospheric layer thickness in units of pressure. For simplicity it is assumed that X_i and κ_i are constant within the atmospheric layer.

If one assumes the opacities of species 1 and 2 to be uncorrelated, i.e.

$$f_{\rm tot}(\kappa_1, \kappa_2) = f_1(\kappa_1) \cdot f_2(\kappa_2) \,, \tag{3.70}$$

where f are the opacity distribution functions, one can rewrite the transmission T as

$$\mathcal{T} = \left[\int_{\nu}^{\nu+\Delta\nu} e^{-X_1\kappa_1(\nu)\Delta P/a} \frac{d\nu'}{\Delta\nu}\right] \cdot \left[\int_{\nu}^{\nu+\Delta\nu} e^{-X_2\kappa_2(\nu)\Delta P/a} \frac{d\nu'}{\Delta\nu}\right] \,. \tag{3.71}$$

Going from frequency space to g space, and approximating the integrals with sums yields

$$\mathcal{T} \approx \sum_{i=1}^{N_g}\sum_{j=1}^{N_g} \exp\left[-\frac{X_1\kappa_{1,i} + X_2\kappa_{2,j}}{a}\Delta P\right] \Delta g_i \Delta g_j \,. \tag{3.72}$$

The combined total k-table of species 1 and 2 therefore has the opacity values

$$\kappa_{12,ij} = X_1\kappa_{1,i} + X_2\kappa_{2,j} \tag{3.73}$$

which have to be weighted with

$$\Delta g_{ij} = \Delta g_i \Delta g_j. \tag{3.74}$$

Ordering the opacity values $\kappa_{{\rm tot},ij}$ by size, and taking the cumulative sum of their weights Δg_{ij} as the new g coordinate, yields the new $\kappa_{\rm tot}(g)$ distribution. For multiple species one would have to order the values

$$\kappa_{1,\ldots,N_{\rm species},i_1,\ldots,i_{N_{\rm species}}} = \sum_{j=1}^{N_{\rm species}} X_j \kappa_{j,i_j} \,, \tag{3.75}$$

with the weights

$$\Delta g_{i_1,\ldots,i_{N_{\rm species}}} = \prod_{j=1}^{N_{\rm species}} \Delta g_{i_j} \,. \tag{3.76}$$

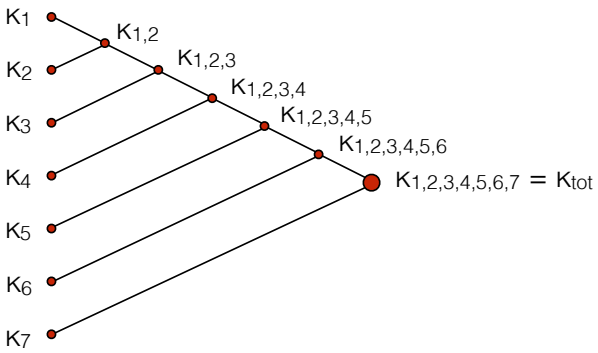

FIGURE 3.3: Schematic drawing of the principle of fast opacity combination.

Thus, as is commonly pointed out the number of operations that need to be carried out in order to combine the k-tables of multiple species is thus $\mathcal{O}(N_g^{N_{\rm sp}})$, which can make the consideration of multiple species computationally expensive (see, e.g., Lacis & Oinas 1991; Marley & Robinson 2015).

In order to overcome this problem I have constructed a set of methods which iteratively combine two species. One starts out by combining the first two species, to obtain κ_{12}, and interpolates the resulting combined opacity back to the original g grid. κ_{12} is then combined with κ_3 to yield κ_{123} etc. The working principle of this method is sketched in Figure 3.3. I have developed such a method for both low and high resolution correlated-k cases, to be

used in the temperature iteration and the spectral calculation modes of *petitCODE*, see Section 3.2.3. These methods have a computational cost of order $\mathcal{O}(N_g^2 N_{\rm sp})$, or even $\mathcal{O}(N_g N_{\rm sp})$ for the low resolution case , see the detailed description in Appendix A.1. The appendix also contains a comparison to the true total k-table, which is obtained from mixing the opacities first in frequency space, and calculating their κ_g after that. The errors are found to be in the low single digit percentage range.

3.2.3 Wavelength binning and the treatment of continuum opacities

The radiative transport calculations are carried out at a wavelength binning of $\lambda/\Delta\lambda = 10$ for the atmospheric temperature and abundance structure iteration, and at $\lambda/\Delta\lambda = 1000$ for the spectral calculations of a converged atmospheric structure. Additionally, a $\lambda/\Delta\lambda = 50$ case has been implemented to verify the $\lambda/\Delta\lambda = 10$ structure iteration results. The wavelength interval of the radiative transfer calculations, and hence the opacities, goes from 110 nm to 250 μm, which encompasses at least 99.9 % of the blackbody flux of objects with temperatures between 200 and 9600 K. For the $\lambda/\Delta\lambda = 1000$ case this results in 7729 spectral bins, and 78 bins for the $\lambda/\Delta\lambda = 10$ case.

For the $\lambda/\Delta\lambda = 1000$ case I approximate g on a grid of 20 Gaussian quadrature points, consisting of a 10-point Gaussian quadrature grid going from $g = 0$ to $g = 0.9$ and a 10-point Gaussian quadrature grid going from $g = 0.9$ to $g = 1$.

For the $\lambda/\Delta\lambda$ = 10 and 50 cases I take a finer grid in g. The g-grid has 36 points, consisting of a 6-point Gaussian quadrature grid ranging from $g = 0$ to $g = 0.95$, an 8-point Gaussian grid ranging from $g = 0.95$ to $g = 0.99$, a 20-point Gaussian grid ranging from $g = 0.99$ to $g = 0.99999$ and a two-point trapezoidal quadrature grid ranging from $g = 0.99999$ to 1.

See Appendix A.1 for the methods for obtaining the combined c-k opacity of all species at the resolutions of $\lambda/\Delta\lambda = 1000$, $\lambda/\Delta\lambda$ = 10 and $\lambda/\Delta\lambda$ = 50.

The wavelength dependence of the CIA, cloud and Rayleigh scattering opacities is much weaker than for the line opacities. In the worst case, for crystalline features of cloud particles, I found that a wavelength binning of $\lambda/\Delta\lambda = 50$ is required to resolve the resonance peaks. I thus take the frequency average of the continuum opacities within the spectral bins, and add them as a global offset to the k-table of the total opacity.

With this setup I present a test of the correlated-k opacity treatment: I calculated the emission spectrum of a hot jupiter at the three different resolutions 10, 50, and 1000, using correlated-k. I compared these to the results of a frequency-space calculation at a resolution $\lambda/\Delta\lambda = 10^6$.[2] As an example P–T structure I took a self-consistent *petitCODE* result for a 1 $\mathrm{M}_{\mathrm{Jupiter}}$, 1 $\mathrm{R}_{\mathrm{Jupiter}}$ planet around a Sun-like star with an effective temperature T_* = 5730 K with radius $R_* = \mathrm{R}_\odot$. The planet was assumed to be in a circular orbit at a distance of d = 0.04 AU, have an internal temperature $T_{\rm int}$ = 200 K and a C/O number ratio of 1.17. The irradiation was treated using the dayside-averaged approximation.

The resulting emission spectra of the planet can be seen in the upper panel of Figure 3.4. In the lower panel I plot the relative errors of the correlated-k calculations when compared

[2] Such calculations are also called 'line-by-line', because they are of high enough resolution to resolve molecular lines.

to the frequency averaged line-by-line calculation. If the c-k assumption was perfectly valid the error would be zero, because the flux values of a c-k calculation should be identical to the frequency-averaged flux of a higher resolution line-by-line calculation. One sees that in regions of appreciable flux the relative deviation between the rebinned $\lambda/\Delta\lambda = 10^6$ line-by-line calculation and the correlated-k calculations is always smaller than 5 % and usually much less. Thus our results are within the accuracy limits commonly found for correlated-k (see, e.g., Fu & Liou 1992; Lacis & Oinas 1991).

3.3 Opacity database

3.3.1 Molecular and atomic line lists

I calculated all line opacities on a wavelength grid ranging from 110 nm to 250 μm, 80-3000 K in temperature, and 10^{-6}-10^{3} bar in pressure. The pressure and temperature points are spaced equidistantly in log-space on a 10×13 point grid. Because the line lists can contain up to 10^{10} lines (see the CH_4 list by Yurchenko & Tennyson 2014), an online calculation during the atmospheric structure calculation is totally unfeasible and a pre-calculation and storage in κ_g tables is necessary.

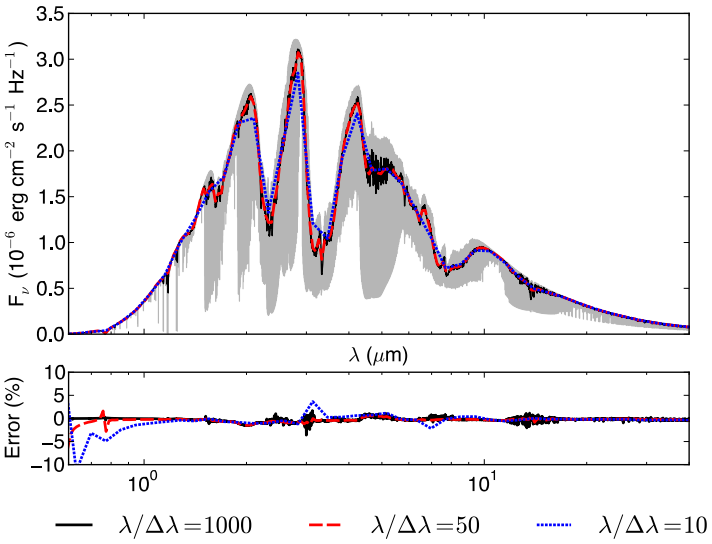

FIGURE 3.4: *Upper panel:* Emission flux of a hot jupiter calculated with *petitCODE*. The gray solid line shows the full line-by-line radiative transfer calculation at a resolution of $\lambda/\Delta\lambda = 10^6$. Overplotted one can see the correlated-k calculations at $\lambda/\Delta\lambda = 1000$ (black dashed line), $\lambda/\Delta\lambda = 50$ (red long dashed line) and at $\lambda/\Delta\lambda = 10$ (blue short dashed line). *Lower panel:* Relative error of the $\lambda/\Delta\lambda = 1000,\ 50,\ 10$ calculations when comparing to the rebinned $\lambda/\Delta\lambda = 10^6$ calculation. Figure taken from Mollière et al. (2015)

The *HITEMP* and *HITRAN* line lists (see Rothman et al. 2010, 2013, respectively) give the pressure broadening coefficients for (Earth-)air broadening in the parametrized form

$$\gamma_{\rm press}(P,T) = \left(\frac{T_{\rm ref}}{T}\right)^n \left(\frac{P}{1\ {\rm atm}}\right) \gamma_{\rm air}, \tag{3.77}$$

where $\gamma_{\rm air}$ is the pressure broadening of air at P = 1 atm = 1.01325 bar and $T_{\rm ref}$ = 296 K. $\gamma_{\rm press}$ thus has the general shape outlined in Equation 2.68, where n usually is of magnitude $n \sim -1/2$. Both n and $\gamma_{\rm air}$ are listed in the *HITRAN*/*HITEMP* line lists.

It is obviously not optimal to use pressure broadening coefficient derived for air, but often no better information is available. In cases where pressure broadening information is missing altogether I use the approximate formula given by Equation 15 in Sharp & Burrows (2007).

Opacity source	Spectral range [μm]	Line list	Partition function	Pressure broadening
CH_4	$0.83 < \lambda$	YT14	F03	Eq. (15), SB07
C_2H_2	$1 < \lambda < 16.5$	*HITRAN*	F03	$\gamma_{\rm air}$
CO	$1.18 < \lambda$	*HITEMP*	F03	$\gamma_{\rm air}$
CO	$0.112 < \lambda < 0.43$	K93	F03	Eq. (15), SB07
CO_2	$1 < \lambda < 38.76$	*HITEMP*	F03	$\gamma_{\rm air}$
H_2S	$0.88 < \lambda$	*HITRAN*	F03	$\gamma_{\rm air}$
H_2	$0.28 < \lambda$	*HITRAN*	F03	$\gamma_{\rm air}$
H_2	$0.08 < \lambda < 0.18$	K93	F03	Eq. (15), SB07
HCN	$2.92 < \lambda$	HT06, BS14	F03	Eq. (15), SB07
H_2O	$0.33 < \lambda$	*HITEMP*	F03	$\gamma_{\rm air}$
K	$0.05 < \lambda$	PK95	ST84	N. Allard[(a)], SH96
Na	$0.1 < \lambda$	PK95	ST84	N. Allard, SH96
NH_3	$1.43 < \lambda$	*HITRAN*	F03	$\gamma_{\rm air}$
O_3	$1.43 < \lambda$	*HITRAN*	F03	$\gamma_{\rm air}$
OH	$0.52 < \lambda$	*HITEMP*	F03	$\gamma_{\rm air}$
PH_3	$2.78 < \lambda$	*HITRAN*	F03	$\gamma_{\rm air}$
TiO	$0.32 < \lambda$	B. Plez[(b)]	U. Jørgensen[(c)]	Eq. (15), SB07
VO	$0.36 < \lambda < 2.6$	B. Plez	B. Plez	Eq. (15), SB07

TABLE 3.1: References for the atomic and molecular opacities available for use in *petitCODE*. Reference codes: *HITEMP* Rothman et al. (2010), *HITRAN*: Rothman et al. (2013), SB07: Sharp & Burrows (2007), F03: Fischer et al. (2003), ST84: Sauval & Tatum (1984), K93: Kurucz (1993), YT14: Yurchenko & Tennyson (2014), SH96: Schweitzer et al. (1996), HT06: Harris et al. (2006), BS14: Barber et al. (2014), PK95: Piskunov et al. (1995), (a): line profile available at `http://mygepi.obspm.fr/~allard/alkalitables.html`, (b): line list available at `http://www.pages-perso-bertrand-plez.univ-montp2.fr/`, (c): partition function retrievable from `http://www.astro.ku.dk/~uffegj/scan/scan_tio.pdf`. If names are given without a footnote, then the data have been obtained from private communication.

The available line opacity sources within *petitCODE*, together with a reference to the corresponding line lists, pressure broadening parameters and partition functions can be found in Table 3.1.

For all lines I apply a sub-Lorentzian line treatment far away from the line center. I use measurements by Hartmann et al. (2002) for all molecules but CO_2, for which I use of a fit to the CO_2 measurements by Burch et al. (1969). This fit was obtained from Bruno Bezard (private communication). The cutoff is modeled by means of an exponential line wing decrease. In Hartmann et al. (2002), CH_4 lines broadened by H_2 have been measured. Because measurements for other species different from CH_4 and CO_2 do not exist, I use the CH_4 cutoff for all remaining species as well.

A special line shape treatment is needed when considering the Na (589.16 & 589.76 nm) and K (766.7 & 770.11 nm) doublet lines, because the broadening profile of these lines is very important for the atmospheric absorption in the optical: the lines of these two species are one of the main absorbers in this spectral range, and their wings act as a pseudo-continuum contribution to the total opacity (see, e.g., Sharp & Burrows 2007; Freedman et al. 2008). Various groups have tried to estimate the line shapes for Na and K, taking into account collisions with H_2 and He (Burrows & Volobuyev 2003; Allard et al. 2003b; Zhu et al. 2006), and the efforts are ongoing (Allard et al. 2012). In particular Allard et al. (2003b) showed that for brown dwarfs the use of correct Na and K wing profiles improves the agreement between synthetic spectra and observations. The line profiles I use for Na and K were obtained from Nicole Allard (in parts from private communication, see Table 3.1). As H_2 should be the main perturber for alkali atoms in the atmosphere of giant planets, only H_2-broadening is currently considered.

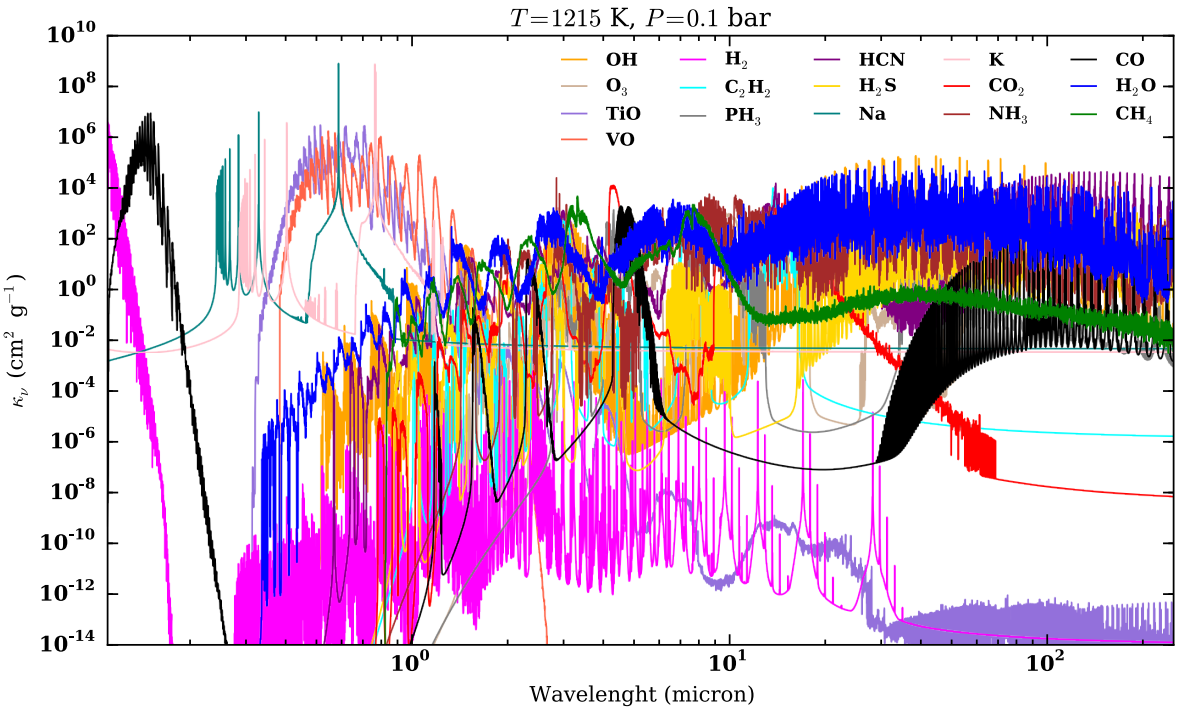

FIGURE 3.5: Molecular and atomic line opacities available in *petitCODE*, shown at a temperature of 1215 K and a pressure of 0.1 bar.

In Figure 3.5 I show all molecular and atomic line opacities of my database at a temperature of 1215 K and a pressure of 0.1 bar. This figure shows the mean value $\langle \kappa_\nu \rangle = \sum_i \kappa_i \Delta g_i$ of every wavelength sub grid, at a binning of $\lambda/\Delta\lambda = 1000$.

3.3.2 Continuum opacities

The continuum opacities described below are summarized in Table 3.2.

CIA opacities

For the work published in Mollière et al. (2015) I used the H_2–H_2 and H_2–He opacities from Borysow et al. (1988, 1989); Borysow & Frommhold (1989); Borysow et al. (2001); Borysow (2002), while for Mollière et al. (2017) I changed to the CIA literature compilation of Richard et al. (2012), see the references therein.

Cloud opacities

I calculate cloud opacities for both homogeneous spheres and irregularly shaped cloud particles. Applying two different cloud particle treatments may allow for the distinction between spherical and irregular cloud particles in the case of small enough grain sizes, for which the cloud material's resonance features are most clearly visible (Min et al. 2005). I approximate the opacity of the irregularly shaped cloud particles by taking the opacities obtained for a distribution of hollow spheres (DHS). The cross-sections for the spherical and DHS cloud particles were calculated using the dust opacity code of Min et al. (2005), which

CIA	Reference	Clouds	Reference	Rayleigh	Reference
H_2–H_2	BR, RG12	Fe	Henning & Stognienko (1996)	H_2	Dalgarno & Williams (1962)
H_2–H_e	BR, RG12	KCl	Palik (2012)	He	Chan & Dalgarno (1965)
		$MgAl_2O_4$	Palik (2012)	CO	Sneep & Ubachs (2005)
		$MgSiO_3$	Scott & Duley (1996), Jaeger et al. (1998)	CO_2	Sneep & Ubachs (2005)
		Mg_2SiO_4	Servoin & Piriou (1973)	CH_4	Sneep & Ubachs (2005)
		Na_2S	Morley et al. (2012)	H_2O	Harvey et al. (1998)

TABLE 3.2: Continuum opacities available im *petitCODE*. References BR stand for: Borysow et al. (1988, 1989); Borysow & Frommhold (1989); Borysow et al. (2001); Borysow (2002), while RG12 stands for Richard et al. (2012), and the references therein.

makes use of software reported in Toon & Ackerman (1981). The code uses Mie theory for the homogeneous spheres and an extended Mie formulation to take into account the hollowness of grains for DHS. I currently can include $MgAl_2O_4$, $MgSiO_3$, Mg_2SiO_4, Fe, KCl and Na_2S clouds with the real and complex parts of the refractive indices taken from Palik (2012) for $MgAl_2O_4$, Scott & Duley (1996); Jaeger et al. (1998) for $MgSiO_3$, Servoin & Piriou (1973) for Mg_2SiO_4, Henning & Stognienko (1996) for Fe, Palik (2012) for KCl and Morley et al. (2012) for Na_2S. For the particles that have their optical properties described by DHS, I use a porosity of $P = 0.25$ (as in Woitke et al. 2016) and an irregularity parameter $f_{\max} = 0.8$ as defined in Min et al. (2005).

Rayleigh scattering cross-sections

I include the Rayleigh scattering of H_2, He, CO_2, CO, CH_4, and H_2O. For the cross-sections we use the values reported in Dalgarno & Williams (1962) (H_2), Chan & Dalgarno (1965) (He), Sneep & Ubachs (2005) (CO_2, CO, CH_4) and Harvey et al. (1998) (H_2O).

3.4 Chemistry

3.4.1 Obtaining equilibrium abundances using Gibbs-minimization

The chemical equilibrium abundances in *petitCODE* are calculated with a Gibbs minimizer that I wrote myself. The chemistry code is implemented closely following the methods and equations outlined in the *CEA* manual (Gordon & McBride 1994). The Gibbs free energy must be minimized while conserving the total elemental composition, the minimization is carried out by making use of Lagrange multipliers and a multi-dimensional Newton-Raphson method (also see Section 2.3.1). The code converges reliably between 60 and 20000 K. Moreover, it was checked for consistency with the *CEA* code (Gordon & McBride 1994; McBride & Gordon 1996), leading to excellent agreement in the temperature range for which the *CEA* thermodynamic data are valid (also see Appendix B.8).

For condensed material with no available thermodynamic data at cold temperatures the heat capacity c_P was extrapolated to low temperatures by fitting a Debye curve to the higher

temperature (usually > 300 K) c_P data, assuming $c_V = c_P$ for the solid material:

$$c_P \propto \left(\frac{T}{T_D}\right)^3 \int_0^{T_D/T} \frac{x^4 e^x}{(e^x - 1)^2} dx \,, \tag{3.78}$$

where T_D is the 'Debye temperature'. The fitted function could then be used to obtain c_P at low temperatures. The entropy S and enthalpy H were obtained using $dS = c_P T^{-1} dT$ and $dH = c_P dT$. The thermodynamic data used for the solids were either the ones used in the *CEA* code[3], the data given in the *JANAF* database[4] or data described in Robie et al. (1978).

In addition to the gaseous species, the condensible species which the code can currently treat are Al_2O_3, Fe, Fe(l), FeO, Fe_2O_3, Fe_2SiO_4, H_2O, H_2O(l), H_3PO_4, H_3PO_4(l), KCl, $MgSiO_3$, $MgSiO_3$(l), Mg_2SiO_4, Mg_2SiO_4(l), $MgAl_2O_4$, Na_2S, SiC, SiC(l), TiO, TiO(l), TiO_2, TiO_2(l), VO, and VO(l), where the phase of all species is solid unless its name is followed by an '(l)', which stands for the liquid phase.

3.5 Cloud modeling

The inherent difficulties when trying to correctly model clouds were described in Section 2.2.5. Moreover, the cloud opacities are only one of many ingredients contributing to *petitCODE*, such that a deeper investigation of the microphysics of cloud formation was, unfortunately, beyond the scope of this thesis. I implemented two simple, parametrized cloud models in *petitCODE*, the first of which, by Ackerman & Marley (2001), solves for the cloud mass density, and has some very interesting properties, as I show in a new derivation of this method.

3.5.1 The Ackerman & Marley (2001) scheme

New derivation of the Ackerman & Marley (2001) scheme

In this section I derive the cloud density equation used in Ackerman & Marley (2001). The goal is to vertically solve for the cloud density of a given species. As I will show, it turns out that this equation is completely independent of any cloud particle nucleation, condensation, coagulation, coalescence or shattering processes, except for the mass-averaged settling speed in a given layer.

I define the mass fraction of cloud particles with radius $r \in [a, a + da]$ as $X'_c(a)da$. The evolution of the cloud particle mass fraction per unit radius can then be described by

$$\rho \frac{\partial X'_c}{\partial t} = \frac{\partial}{\partial z}\left(K\rho \frac{\partial X'_c}{\partial z}\right) - \frac{\partial}{\partial z}\left(v_f \rho X'_c\right) + S'_{\text{cond+nuc}} + S'_{\text{coag+dest}} \,, \tag{3.79}$$

where z is the atmospheric altitude, ρ the total atmospheric density, K the eddy diffusion coefficient, $v_f(r)$ is the particle settling speed, $S'_{\text{cond+nuc}}$ the amount of mass added to particles in the radius bin due to condensation and nucleation and $S'_{\text{coag+dest}}$ the gain and loss of

[3] http://www.grc.nasa.gov/WWW/CEAWeb/ceaThermoBuild.htm
[4] http://kinetics.nist.gov/janaf/

particles in the radius bin due to coagulation and collisional shattering. See Agúndez et al. (2014) (and the references therein) for the motivation of the functional form of the cloud particle diffusion term (first term on the RHS of Equation 3.79).

In order to obtain the time derivative of the cloud particle mass density $\rho_c = X_c \rho$, I set

$$\frac{\partial \rho_c}{\partial t} = \rho \frac{\partial X_c}{\partial t} = \rho \int \frac{\partial X_c'}{\partial t} da \, , \tag{3.80}$$

where it was used that ρ is constant in time (hydrostatic equilibrium). The unprimed X (instead of X') is the mass fraction integrated over particle radius. This yields

$$\frac{\partial \rho_c}{\partial t} = \frac{\partial}{\partial z} \left(K \rho \frac{\partial X_c}{\partial z} \right) - \frac{\partial}{\partial z} \left(\langle v_f \rangle \, \rho X_c \right) + S_{\mathrm{cond+nuc}} \, , \tag{3.81}$$

where the coagulation/destruction term vanishes because it does not add or remove any mass in the condensed phase of the cloud species. $\langle v_f \rangle$ is the cloud particle mass averaged settling velocity.

For the gas phase of the cloud species, the change in density works out to be

$$\frac{\partial \rho_g}{\partial t} = \frac{\partial}{\partial z} \left(K \rho \frac{\partial X_g}{\partial z} \right) - S_{\mathrm{cond+nuc}} \, , \tag{3.82}$$

where settling of the gas molecule has been neglected: to first order gravity is balanced by the pressure gradient in the atmosphere. To obtain the total density evolution of the cloud species within the atmosphere, one adds equations 3.81 and 3.82 to obtain

$$\frac{\partial \rho_{g+c}}{\partial t} = \frac{\partial}{\partial z} \left(K \rho \frac{\partial X_{g+c}}{\partial z} - \langle v_f \rangle \, \rho X_c \right) . \tag{3.83}$$

For a steady state solution and a net zero mass flux one thus finds that

$$K \frac{\partial X_{g+c}}{\partial z} - \langle v_f \rangle \, X_c = 0, \tag{3.84}$$

which is equal to the equation solved in Ackerman & Marley (2001) except for the fact that they express the settling speed in units of the atmospheric mixing speed v_{mix}.

If one wants to solve for the condensate mass fraction, assuming that the gas mass fraction is known, then one finds from the previous equation that

$$K \frac{\partial X_c}{\partial z} - \langle v_f \rangle \, X_c = -K \frac{\partial X_g}{\partial z} \, . \tag{3.85}$$

In the case of effective heterogeneous nucleation, that is, if the nucleation timescale is shorter than the atmospheric mixing or settling timescale, it can be assumed that X_g is a known quantity:

$$X_g = X_s \, , \tag{3.86}$$

where X_s is the saturation gas mass fraction. This corresponds to a supersaturation of $\mathcal{S} = \mathcal{S}_\infty = 0$, as defined in equations 2.88 and 2.89. One then finds

$$K\frac{\partial X_\mathrm{c}}{\partial z} - \langle v_\mathrm{f}\rangle X_\mathrm{c} = -K\frac{\partial X_\mathrm{s}}{\partial z} \,. \tag{3.87}$$

In this case X_s can be obtained from an equilibrium chemistry module. For species such as $MgSiO_3$, no gaseous phase exists because the molecule forms through chemical nucleation, therefore $\partial X_\mathrm{s}/\partial z$ cannot be calculated using equilibrium chemistry. However, $-\partial X_\mathrm{c}^\mathrm{equ}/\partial z$, that is, the negative gradient of the equilibrium chemistry condensate mass fraction, is a measure for the gas mass gradient between two layers. It arises due to the chemical nucleation of various gaseous species in order to form the condensate (for MgSiO3 it's Mg(g), SiO(g) and O_2(g), where (g) stands for the gas phase). This yields

$$K\frac{\partial X_\mathrm{c}}{\partial z} - \langle v_\mathrm{f}\rangle X_\mathrm{c} = -K\frac{\partial X_\mathrm{c}^\mathrm{equ}}{\partial z} \,. \tag{3.88}$$

For species that can exist in the gas phase, and for which the condensation occurs on a small enough spatial range such that the total chemical abundances (gas+solid) are approximately constant, one can assume that $\partial X_\mathrm{t}^\mathrm{equ}/\partial z = 0$, with $X_\mathrm{t}^\mathrm{equ} = X_\mathrm{c}^\mathrm{equ} + X_\mathrm{s}$. This leads to $\partial X_\mathrm{s}/\partial z = -\partial X_\mathrm{c}^\mathrm{equ}/\partial z$, therefore I use Equation 3.88 in all cases.

A test carried out for a self-luminous planet with $T_\mathrm{eff} = 500K$, set up identically as in Ackerman & Marley (2001), but using my form of the cloud equation as written in Equation 3.88, yielded very good agreement (see Appendix B.7). Equation 3.88 is solved in *petitCODE* using a Runge-Kutta 4th order method.

For every species, only a single cloud region within the atmosphere is allowed, implicitly assuming that the lowest possible cloud region for a given species traps the cloud forming material.

The particle sizes for the clouds are calculated as described in Ackerman & Marley (2001). This is done by giving the parameter $f_\mathrm{sed} = \langle v_\mathrm{f}\rangle / v_\mathrm{mix}$ as a free parameter, as well as assuming a log-normal particle size distribution, and then solving for the mean particle size. For this the mixing velocity v_mix of the atmosphere (arising from convection, convective overshoot, and diffusion) have to be known, which is why the the mixing length theory was introduced in Section 2.1.2. The solution of the particle size, as well as the calculation of the mixing properties is summarized in Appendix A.2.

Note that with $\langle v_f\rangle = -f_\mathrm{sed} v_\mathrm{mix}$, $v_\mathrm{mix} = K/H_P$, and the assumption of hydrostatic equilibrium, Equation 3.88 can be cast into the following form:

$$\frac{\partial X_\mathrm{c}}{\partial P} - \frac{f_\mathrm{sed} X_\mathrm{c}}{P} = \frac{\partial X_\mathrm{c}^\mathrm{equ}}{\partial P} \,, \tag{3.89}$$

therefore, above the condensation region of the cloud, where $\partial X_\mathrm{c}^\mathrm{equ}/\partial P = 0$, one finds that

$$X_\mathrm{c}(P) \propto P^{f_\mathrm{sed}} \,, \tag{3.90}$$

which shows that the cloud density will decrease ever faster for larger $f_{\rm sed}$, as one goes to smaller pressures P.

3.5.2 A simple three-parameter cloud model

In addition to the Ackerman & Marley (2001) cloud model, I introduce a parametrized model which corresponds to vertically homogeneous clouds, with the cloud mass fractions per species equal to the values derived from equilibrium chemistry, but not larger than a predefined $X_{\rm max}$. In that sense, $X_{\rm max}$ can be thought of as a proxy for the settling strength, where smaller $X_{\rm max}$ values correspond to stronger settling. Further, the mean cloud particle radius for the grains can be chosen freely, as well as the width of the log-normal particle size distribution. A value $\sigma_g \rightarrow 1$ for the width of the size distribution corresponds to mono-disperse particle sizes. As for the Ackerman & Marley (2001) cloud model described above, only a single cloud layer per species is allowed.

3.6 Iterative temperature solution

3.6.1 Radiative equilibrium

The temperature in a given atmospheric layer can be found by requiring that the radiation emitted by a parcel of gas is equal to the radiation it absorbs. If it were to emit more or less, it would have to cool down or heat up, respectively.

The amount of radiation emitted by a spherical parcel of gas with optical thickness $\Delta\tau$, temperature T, and radius r can be written as

$$\Delta I_\nu^{\rm parcel} = B_\nu(T)\Delta\tau_\nu^{\rm abs} = B_\nu(T) r \kappa_\nu^{\rm abs} \rho \,, \tag{3.91}$$

which follows from equations 3.11 and 3.15. Because the gas parcel is spherical, $\Delta I_\nu^{\rm parcel}$ is isotropic, such that the mean intensity at the location of the gas parcel, due to its emission, is

$$J_\nu^{\rm parcel} = \Delta I_\nu^{\rm parcel} = B_\nu(T) r \kappa_\nu^{\rm abs} \rho \,, \tag{3.92}$$

the wavelength integration of which is

$$J^{\rm parcel} = \int_0^\infty J_\nu d\nu = \rho r \kappa_{\rm P} \frac{\sigma}{\pi} T^4 \tag{3.93}$$

where $\kappa_{\rm P}$ is the 'Planck opacity',

$$\kappa_{\rm P} = \frac{\int_0^\infty \kappa_\nu^{\rm abs} B_\nu(T) d\nu}{\int_0^\infty B_\nu(T) d\nu} \,, \tag{3.94}$$

and it holds that $\int_0^\infty B_\nu(T)d\nu = \sigma T^4/\pi$, where σ is the Stephan-Boltzmann constant. By the same token, the solid angle-average of the intensity absorbed by the gas parcel is

$$J^{\rm tot} = \rho r \kappa_J J + \rho r \int_0^\infty \kappa_\nu^{\rm abs} J_\nu^* d\nu \ , \tag{3.95}$$

which can likewise be derived from the absorption part of Equation 3.11. Here, J is the frequency-integrated mean intensity of the planetary radiation field I_ν, and J_ν^* is the mean intensity of the stellar irradiation I_ν^*. κ_J is defined as

$$\kappa_J = \frac{\int_0^\infty \kappa_\nu^{\rm abs} J_\nu d\nu}{\int_0^\infty J_\nu d\nu} \ . \tag{3.96}$$

To find the atmospheric temperature one sets $J^{\rm parcel} = J^{\rm tot}$, because of radiative equilibrium, which leads to

$$\kappa_{\rm P} \frac{\sigma}{\pi} T^4 - \kappa_J J - \int_0^\infty \kappa_\nu^{\rm abs} J_\nu^* d\nu = 0 \ . \tag{3.97}$$

Because $\kappa_{\rm P}$ depends on T itself, this is usually solved using numerical root finding algorithms, or simply by the iterative evaluation of

$$T_{\rm new} = \left[\frac{\pi}{\sigma \kappa_{\rm P}(T_{\rm old})} \left(\kappa_J J + \int_0^\infty \kappa_\nu^{\rm abs} J_\nu^* d\nu \right) \right]^{1/4} \ . \tag{3.98}$$

Equation 3.97 thus represents the method used in *petitCODE* to find the atmospheric temperature. It is solved using the `zbrent` routine of the Numerical Recipes collection (Press et al. 1992).

There is one more constraint which has not been imposed on the atmospheric radiation field yet: in plane-parallel geometry, in every atmospheric layer, the vertical flux must satisfy

$$F_{\rm tot} = F + F_* = \int_0^\infty \int_{4\pi} I_\nu \mu d\Omega d\nu + \int_0^\infty \int_{4\pi} I_\nu^* \mu d\Omega d\nu = \sigma T_{\rm int}^4 \ , \tag{3.99}$$

where $\mu = \mathbf{n} \cdot \mathbf{e}_z = \cos(\vartheta)$. This means that the net energy leaving the planet is equal to the intrinsic luminosity of the planet. All stellar flux absorbed in the atmosphere of the planet must be radiated back to space, otherwise the planet would heat up, which cannot be an equilibrium solution. I will explain how to incorporate this constraint in the next Section 3.6.2.

3.6.2 The Variable Eddington Factor (VEF) method

Here I explain how flux conservation (see Equation 3.99) was implemented in the temperature finding algorithm. This method has been adapted from Dullemond et al. (2002), in which it was used to solve for the vertical temperature profiles of non-scattering protoplanetary disks. I included scattering here, as well as changed the vertical coordinate to the atmospheric pressure.

We start from the equation of radiative energy transport:

$$\mathbf{n} \cdot \nabla I_\nu = -\alpha^{\rm tot} \left(I_\nu - S_\nu \right) \ . \tag{3.100}$$

I make the plane-parallel assumption and chose the atmospheric altitude z to increase towards the upper layers of the atmosphere. The equation of radiative transport then transforms to

$$\mu \frac{d}{dz} I_\nu = -\alpha^{\rm tot}_\nu \left(I_\nu - S_\nu \right) \ , \tag{3.101}$$

where $\mu = \cos(\vartheta)$ and ϑ being the angle between the vertical and the direction of the ray.

The zeroth, first and second radiative moments are defined as

$$[J_\nu, \mathbf{H}_\nu, K_\nu] = \frac{1}{4\pi} \int I_\nu \left[1, \mathbf{n}, \mathbf{nn}\right] d\Omega \ , \tag{3.102}$$

where $\mathbf{n}$ is the vector pointing along the direction of the ray. For the planetary radiation field in the plane-parallel approximation, it holds that there is a rotational symmetry around the z-axis, and only the z- and zz-components of $\mathbf{H}$ and K are non-zero. One can then define

$$H(z) = H_z(z), \tag{3.103}$$

$$K(z) = K_{zz}(z), \tag{3.104}$$

where the ν subscript has been omitted. The definition of the three plane-parallel moments then is

$$[J_\nu, H_\nu, K_\nu] = \frac{1}{2} \int_{-1}^{1} I_\nu(z, \mu) \left[1, \mu, \mu^2\right] d\mu. \tag{3.105}$$

Integration of Equation 3.101 over the whole solid angle yields for the planetary radiation field that

$$\frac{d}{dz} H_\nu = -\alpha^{\rm tot}_\nu \left(J_\nu - S_\nu \right), \tag{3.106}$$

where I used that the source function arises from Planck emission and isotropic scattering, which are both isotropic. Multiplying Equation 3.101 by μ and integrating over the whole solid angle again yields

$$\frac{d}{dz} K_\nu = -\alpha^{\rm tot}_\nu H_\nu, \tag{3.107}$$

where again the isotropy of the source function was used.

In what follows below, I will switch from z to P as the vertical coordinate of the atmosphere, my making use of hydrostatic equilibrium:

$$dP = -\rho g dz \ , \tag{3.108}$$

This allows to express the optical depth $\tau^{\rm tot}_\nu$

$$d\tau^{\rm tot}_\nu = -\alpha^{\rm tot}_\nu dz = -\rho \kappa^{\rm tot}_\nu dz \tag{3.109}$$

as

$$d\tau_\nu^{\rm tot} = \frac{\kappa_\nu^{\rm tot}}{g} dP \,. \tag{3.110}$$

Imposing flux conservation on the planetary radiation field

Due to flux conservation, the total net flux leaving the planet is $\sigma T_{\rm int}^4$. From Equation 3.102 we see that the flux F and the first moment H are related by $F = 4\pi H$, where

$$H = \int_0^\infty H_\nu d\nu. \tag{3.111}$$

The stellar flux in a given layer arises from absorption and scattering processes, and is solved as lined out in the 'Separating stellar and planetary radiation' part of Section 3.2.1.

The total, net flux in the atmosphere is

$$H_{\rm tot} = H + H_* = \frac{\sigma T_{\rm int}^4}{4\pi} \,, \tag{3.112}$$

where H is the flux arising from emission within the planet. Flux conservation then implies

$$\frac{dH_{\rm tot}}{dP} = 0. \tag{3.113}$$

In a given atmospheric layer it must then hold that

$$H(P) = \frac{\sigma T_{\rm int}^4}{4\pi} - H_* \tag{3.114}$$

Therefore, once H_* is obtained from the solution of Feautrier's method as outlined in Section 3.2.1, one can immediately solve for the planetary flux, using flux conservation. However, for the temperature solution one needs to know the planet's mean intensity J, and not H, see Equation 3.97.

For obtaining J one solves the for the planetary radiation field at the current temperature guess of the atmosphere, using Feautrier's method as outlined in Section 3.2.1. From this solution one calculates $J_\nu^{\rm Feautrier}$ and $K_\nu^{\rm Feautrier}$, and obtains their ratio $f_\nu = K_\nu^{\rm Feautrier}/J_\nu^{\rm Feautrier}$, which is called the 'Eddington factor'.[5] One can then calculate

$$f = \frac{\int_0^\infty f_\nu J_\nu^{\rm Feautrier} d\nu}{\int_0^\infty J_\nu^{\rm Feautrier} d\nu} \tag{3.115}$$

Equation 3.107 then yields, together with f and equations (3.109) and (3.110):

$$\frac{d}{dP}(fJ) = \frac{1}{g}\int_0^\infty \kappa_\nu^{\rm tot} H_\nu d\nu \tag{3.116}$$

and finally

$$\frac{d}{dP}(fJ) = \frac{1}{g}\kappa_H H, \tag{3.117}$$

[5] As the method uses an iteration to find the correct Eddington factor (see below), it is called 'Variable Eddington Factor' (VEF) method.

where κ_H is the $H_\nu^{\rm Feautrier}$-averaged $\kappa_\nu^{\rm tot}$ opacity. For the solution of J one takes

$$J(P=0) = \frac{1}{\psi} H(P=0) \, , \tag{3.118}$$

for which one uses $\psi = H^{\rm Feautrier}(P=0)/J^{\rm Feautrier}(P=0)$ from the Feautrier solution of the planetary radiation field. One then makes use of $f(P)$ and $\kappa_H(P)$ from the Feautrier solution, and the results of Equation 3.114 to integrate Equation 3.117 from $P = 0$ to the pressure of interest.

Using the Feautrier-method based estimates of ψ, f, κ_H and H, one thus obtains a solution for the planetary mean intensity J, *which fulfills the constraint of flux convergence*. J can then be used to find the atmospheric temperature, using Equation 3.97 and the stellar radiation field from the Feautrier solution.

Hence, the temperature is found from integrating the radiation field both in the frequency- and angle-dependent space, as well as in the frequency- and angle-integrated (J, H, K)-moment space. If the temperature and scattering source function used in the Feautrier step were not yet leading to a flux-conserving atmospheric structure, then ψ, f, κ_H and H will be slightly off, and lead to not yet correct new temperatures. However, because the Feautrier and the temperature step are applied iteratively, the atmosphere will converge to the correct state.

3.6.3 Treatment of convection

After the radiative structure of the atmosphere has converged I switch on convection and restart the temperature iteration. During the ensuing VEF moment solution of the temperature, the radiative temperature profile is solved from top to bottom (starting at low P_0, typically $P_0 = 10^{-10}$ bar). I check in each layer i whether it should be convective or not by comparing the effective radiative temperature gradient between two layers,

$$\nabla_{\rm rad} = \left(\frac{T_i - T_{i-1}}{P_i - P_{i-1}} \right) \cdot \left(\frac{P_i + P_{i-1}}{T_i + T_{i-1}} \right) \, , \tag{3.119}$$

with the radiative temperature gradient $\nabla_{\rm ad}$, where

$$\nabla_{\rm ad} = \frac{P}{c_P \rho T} \frac{\chi_T}{\chi_\rho} \, , \tag{3.120}$$

with $\chi_T = (\partial {\rm log}P / \partial {\rm log}T)_\rho$ and $\chi_\rho = (\partial {\rm log}P / \partial {\rm log}\rho)_T$ (see, e.g., Hansen et al. 2004). All required quantities can be obtained from my equilibrium chemistry code. One can then define Γ_2 via $\nabla_{\rm ad} = (\Gamma_2 - 1)/\Gamma_2$. I evaluate Γ_2 as $\Gamma_2 = (\Gamma_{2,i} + \Gamma_{2,i-1})/2$ on the atmospheric grid.

I then employ the Schwarzschild criterion (see Section 2.1.2), such that if $\nabla_{\rm rad} > \nabla_{\rm ad}$, I adjust the temperature in layer i to be

$$T_i = T_{i-1} \cdot \frac{P_{i-1} + P_i(2\Gamma_2 - 1)}{P_i + P_{i-1}(2\Gamma_2 - 1)} \, , \tag{3.121}$$

such that the local atmospheric temperature gradient is equal to $\nabla_{\rm ad}$. Once a given layer is convective, the energy in the layer is not transported by radiation anymore. Thus the integration of J via Eq. (3.117) is not possible in this layer. However, in order to be able to discriminate between radiative and convective energy transport in layers lying below a currently convective layer, I need to solve the radiative temperature in deeper layers. For this I need to continue to computation of J down to deeper layers.

I thus chose the approach to set $J_i^n = \alpha_i^{n-1} B(T_i^n)$ in a convective layer i during the n-th iteration , with $\alpha_i^{n-1} = J_i^{\rm Feautrier,n-1}/B(T_i^{n-1})$, and $J_i^{\rm Feautrier,n-1}$ being the mean intensity taken from the Feautrier solution of the previous iteration. The superscripts indicate the iteration number from which the respective quantity is used. I chose this approach as in the case of very efficient convection ($\nabla_{\rm atmo} \rightarrow \nabla_{\rm ad}$, see Equation 2.22) the atmospheric layer should be optically thick, i.e. $J_i \rightarrow B(T_i)$. Because in the higher atmospheric layers this will not yet be perfectly valid, the α corresponds to a correction factor for this approximation, based on the previous Feautrier iteration. When going from a convective layer i to the next layer $i+1$, I use this approximative J_i^n to radiatively integrate J to this next layer, using Eq. (3.117), and compare the resulting $\nabla_{\rm rad}$ with $\nabla_{\rm ad}$ again.

As in Marley et al. (1996); Burrows et al. (1997) I only allow a limited number atmospheric layers to be changed to convective energy transport in every atmospheric temperature iteration step. This is done to allow the atmospheric structure to adapt to the introduction of convective layers. In Marley et al. (1996); Burrows et al. (1997) only 1 layer per iteration is allowed to change. I allowed for the change of 2 layers per iteration, because sometimes a layer on the brink to being convectively unstable will switch back and forth between between being radiative or convective, preventing the overall convergence of the atmospheric structure.

3.7 Insolation flux

For the spectrum of the stellar insolation I use theoretical spectral templates from the *PHOENIX* models, as compiled for use in van Boekel et al. (2012). In the run setup of *petitCODE* the effective temperature of a main-sequence host star is specified, and the appropriate spectrum is interpolated from the *PHOENIX* models, assuming a stellar age of 1/3 of the main sequence lifetime. The stellar evolution is obtained from the Yonsei-Yale tracks (Yi et al. 2001; Kim et al. 2002; Yi et al. 2003; Demarque et al. 2004) and the evolutionary calculations of Baraffe et al. (1998). Fore more details see van Boekel et al. (2012).

3.8 Calculation of transmission spectra

Transmission spectra are not needed for the planetary structure iteration, so are carried out only once convergence has been obtained. Moreover, for the transmission spectrum the planetary radius needs to be defined, which is essentially a free parameter. This is done by fixing the planetary radius at $r(P_0) = R_{\rm Pl}$, and by then using the Equation of hydrostatic equilibrium (Equation 2.3) to solve for $r(P)$. This maps the pressure grid values P_i to the

radius values r_i. While P_0 is a free parameter, I usually follow the example of Fortney et al. (2010), who set $P_0 = 10$ bar.

For the transmission of light through a given latitude of the planet I neglect any longitudinal changes of the terminator atmospheric structure. I usually assume a planet-wide averaged insolation, as comparisons to 3d transmission spectra obtained from GCMs indicate that such a treatment provides a good agreement to the GCM case (Fortney et al. 2010). Once the radius values r_i have been calculated, one next has to calculate the optical depths for the stellar light rays. If a ray grazes the atmosphere at an impact parameter r_i above the planetary center, the total optical depth can be written as

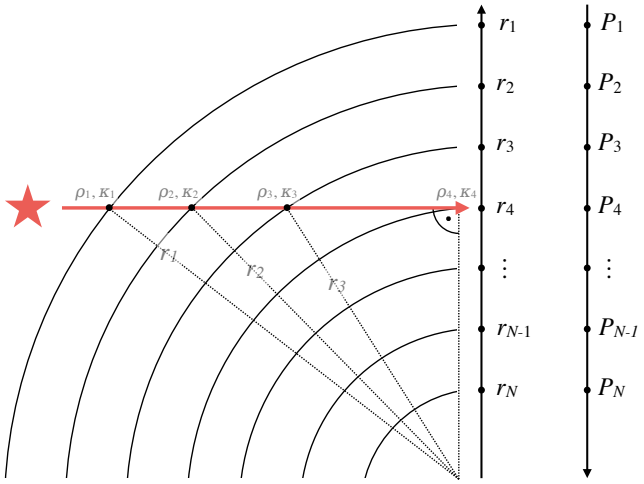

FIGURE 3.6: Geometry of the transmission problem and coordinate systems of the transmission problem. The red line shows a stellar grazing light ray as it passes through the planetary atmosphere.

$$\tau_i = \sum_{j=1}^{i-1} \left(\kappa_j \rho_j + \kappa_{j+1} \rho_{j+1}\right) \left(\sqrt{r_j^2 - r_i^2} - \sqrt{r_{j+1}^2 - r_i^2}\right) , \tag{3.122}$$

where ρ_j is the mass density of the atmospheric layer at radius r_j. The geometry of the transmission problem is sketched in Figure 3.6. The effective area of the planet is then calculated as

$$A = 2\pi \int_0^{R_{\rm pl}} r \left(1 - \mathcal{T}\right) dr , \tag{3.123}$$

where $\mathcal{T} = e^{-\tau}$ denotes the transmission of light through the atmosphere in grazing geometry.

3.9 Full model synopsis

In Figure 3.7 I summarize how the the different modules described in this chapter are connected to each other.

The code is started once the user has prepared the necessary input files. In these files the planet–star system parameters are specified, and the corresponding quantities are

- The planetary internal temperature (such that $F_{\rm int} = \sigma T_{\rm int}^4$), and its mass and radius (or its surface gravity). For transmission spectra the radius has to be specified.
- The host star's radius and effective temperature.

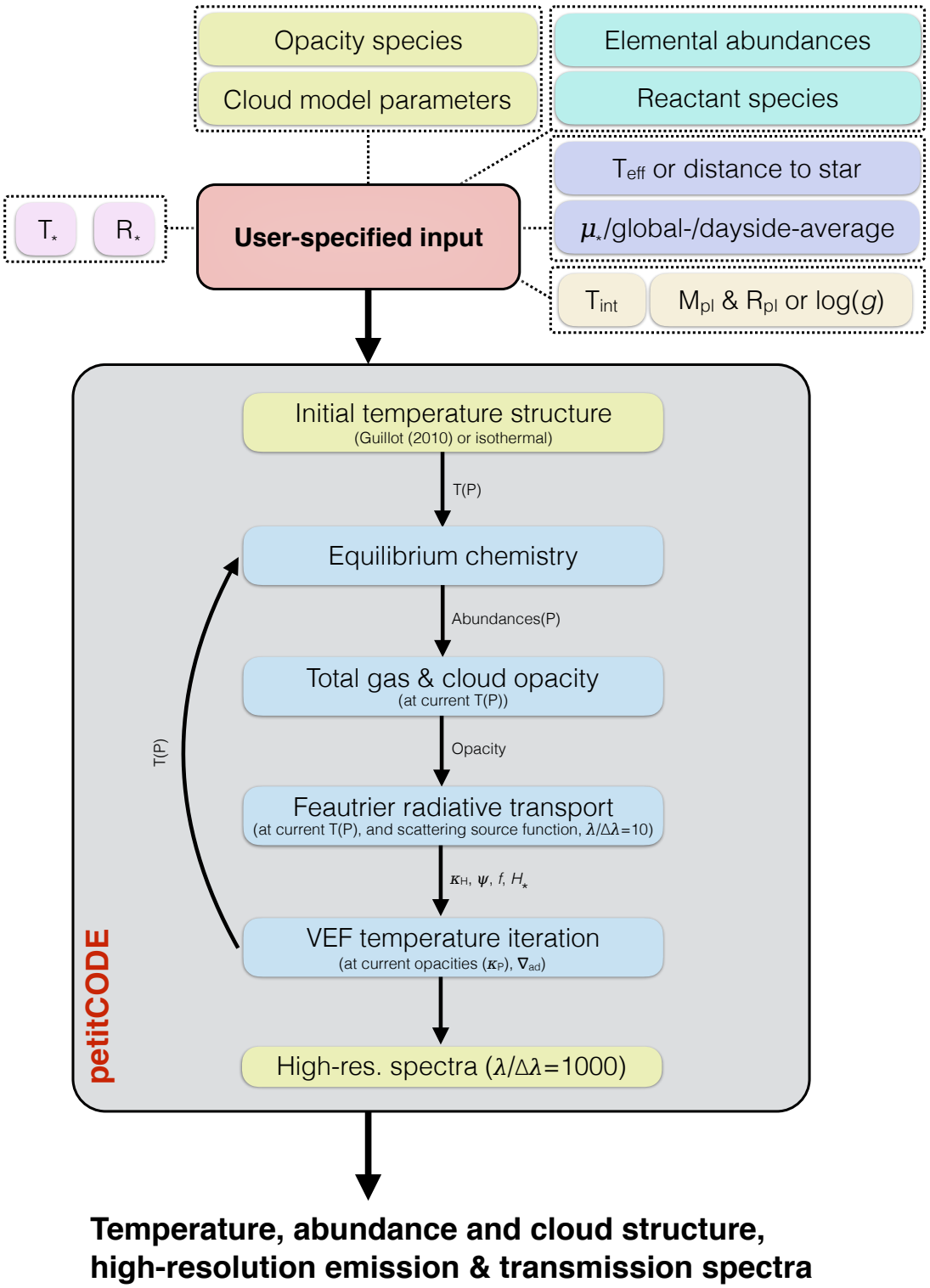

FIGURE 3.7: Schematic drawing summarizing the modules and setup of *petitCODE*.

- The planet–star distance, as well as whether a dayside or planet-wide average of the insolation is assumed, or an incidence angle ϑ_*, which must be provided in the form

$\mu_* = \cos(\vartheta_*)$. Alternatively the desired planetary effective temperature can be specified. This will lead to the code choosing the appropriate distance, depending on the redistribution treatment of the stellar irradiation.

- The atmospheric elemental (i.e. atomic) abundances in units of number fractions and the chemical reactant species to be considered.
- The opacity species to be considered (line, CIA, Rayleigh, clouds) and, if clouds are to be included, the free parameters of the cloud models.

To start the code an initial temperature structure is chosen, taken to be isothermal, or using the analytical models by Guillot (2010). Then, until convergence is attained, the code iterates the atmospheric structure in the following fashion

1. Using the elemental composition and current temperature structure, the code calculates the atmospheric equilibrium abundances.
2. The abundances, temperature structure, and cloud parameters are used to calculate the total absorption and scattering opacities.
3. The Feautrier method solves the angle- and frequency-dependent radiative transfer equation for both the planetary and the stellar radiation field. The source function is calculated in using ALI. In addition, the source function is boosted with Ng acceleration if a sufficient number of iterations since the last boost has been carried out.
4. The Feautrier step yields the vertically varying values for $\kappa_{\rm H}$, f, and H_*, as well as the ψ value. These are then used in the VEF method to update the atmospheric temperature, assuming radiative-convective equilibrium. Then code then returns to step 1.

Convergence is defined as the moment when the maximum change in temperature between the current iteration and the temperature found 60 iterations ago is smaller than 0.01 K, and if the planetary emerging flux F is equal to the imposed total flux with a relative maximum deviation of 0.001, such that $F + F_* = \sigma T_{\rm int}^4$ (where $F_* < 0$).

3.10 Testing the code

The code has been extensively tested and compared to other codes. I summarize these tests in Appendix B.

4 The theoretical properties of hot jupiters

Based on Mollière et al. (2015).

4.1 Systematically studying hot jupiters

The planetary class of hot jupiters has already been mentioned in chapters 1 and 2, and I systematically investigated their properties in Mollière et al. (2015), which has been adopted for this chapter.

As such, the term 'hot jupiter' is not strictly defined. It usually describes predominantly gaseous planets, with radii $\gtrsim$ R_{J}, and in orbits very close to their star, with orbital periods of a few days and temperatures in the range of $T_{\mathrm{equ}} \gtrsim 1000$ K. Studies which systematically study hot jupiter properties are, e.g. Sudarsky et al. (2003); Hubeny et al. (2003); Burrows et al. (2006); Fortney et al. (2008); Madhusudhan (2012), which vary in their extent and model sophistication. Sudarsky et al. (2003) investigated the effect of the planets' effective temperature (i.e. orbital distance), surface gravity, and clouds, while Burrows et al. (2006) studied how the strength of energy redistribution affects planetary phase curves. Further, Fortney et al. (2008); Madhusudhan (2012) attempted to divide hot jupiters into different classes, where Fortney et al. (2008) predicted planets with $T_{\mathrm{equ}} > 1250$ K to have inversions caused by TiO/VO absorption, whereas Madhusudhan (2012) expanded this classification by adding the planets' C/O number ratio as an additional classification coordinate. The C/O ratio can have a profound impact on the atmospheric structure of planets and their emergent spectra, as we will see in this chapter.

The first application (and test) of *petitCODE* was to calculate a large grid of hot jupiter atmospheres, in which I varied the planetary effective temperature, metallicity, C/O number ratio, surface gravity, and host star spectral type. I did not yet include TiO/VO opacities when this study was carried out. The evidence for TiO/VO in planetary atmospheres, as well as for inversions, has so far been inconclusive, and there exist theoretical arguments which may negate the presence of TiO/VO in said atmospheres (see discussion in 'Open Question' 1, Section 1.5). Including C/O as a parameter in my study improved upon the investigation of Madhusudhan (2012): because I calculated self-consistent atmospheric models, I found that C/O ratios around 1 can give rise to atmospheric inversions (the solar C/O ratio is 0.55, when using the solar composition published by Asplund et al. 2009).

Madhusudhan (2012) did not model the atmospheric temperature structure self-consistently, consequently they did not observe this phenomenon.

Calculating a grid of hot jupiters on this high-dimensional parameter space (see Section 4.2) provided an ideal testbed for the capabilities and the stability of *petitCODE*. Moreover, in addition to obtaining interesting and new results on the properties of hot jupiters, I could compare my findings to already known properties of this class of planets. The version of the code which was used for this study did not yet include scattering or the calculation of transmission spectra, also clouds and TiO/VO opacities were not yet incorporated. The chemical abundances were still calculated with the *NASA CEA* code (Gordon & McBride 1994; McBride & Gordon 1996). The validity of the results without these processes and opacity sources will be discussed in Section 4.2. The qualitative behavior found for the planets studied in Mollière et al. (2015) was also reproduced in Mollière et al. (2017), however.[1] Finally, the treatment of the sub-Lorentzian line wings (see the 'Line profile' part of Section 2.2.3, and Section 3.3.1) was not yet included, except for the detailed wing profiles of the Na and K lines. Grimm & Heng (2015) show that the differences when applying no line cut-off, when compared to an arbitrary cut-off, can be of the order of 10 % (but also larger) when considering layer transmissions. They studied an arbitrary cutoff, because there exist only a limited number of measurements for a limited number of molecules, see Section 3.3.1. For the Mollière et al. (2017) study I included a line cutoff, which is described in Section 3.3.1 as well.

4.2 The hot jupiter parameter space

The novelty of the work presented in Mollière et al. (2015) was to explore the systematic behavior of self-consistent atmospheres when additionally varying the C/O number ratio and the host star spectral type. As summarized in the 'Open Question' 5 in Section 1.5, large planetary C/O ratios, close to unity, are possible even when considering disks of solar composition (the solar value is $\mathrm{C/O}_\odot \sim 0.55$, see Asplund et al. 2009), if the planet's enrichment is dominated by gas accretion. For disks with super-solar C/O ratios the planetary C/O ratios should be even higher, although stars with C/O ratios close to and bigger than 1 may be quite rare (Fortney 2012). Additionally, planets with an enrichment dominated by planetesimals enriched in organic carbon may have C/O ratios > 1, but it is unclear if such cases are feasible (Mordasini et al. 2016).

The C/O ratio is particularly interesting because of the net chemical reaction already mentioned in the direct imaging description in Section 1.4.1:

$$\mathrm{CH_4 + H_2O} \underset{T \lesssim 1000\ \mathrm{K}}{\overset{T \gtrsim 1000\ \mathrm{K}}{\rightleftharpoons}} \mathrm{CO + 3H_2}\ . \tag{4.1}$$

In chemical equilibrium, at $T \gtrsim 1000$ K, CO is the most abundant C and O bearing molecule in planetary atmospheres. In an oxygen-rich atmosphere (C/O < 1) the remaining oxygen is

[1] I did not carry out a calculation of the atmospheric grid introduced in this chapter with the current version of the code yet.

then partly found in the form of H_2O, and almost no CH_4 is present, as most C is locked up in CO. In a carbon-rich atmosphere (C/O $>$ 1) the excess C is put partly into CH_4, with no O left to form water. This C/O-dependent transition from H_2O to CH_4 dominated atmospheres happens quite sharply (see, e.g., Kopparapu et al. 2012; Madhusudhan 2012). For $T \lesssim 1000$ K the low temperature direction in Eq. (4.1) is dominant, leading to appreciable amounts of both CH_4 and H_2O, and negligible amounts of CO.

Furthermore, condensation processes can potentially lead to local C/O ratios of $\sim$ 1-2 in the gas phase, even if the global atmospheric C/O ratio is smaller than 1 (see, e.g., Helling et al. 2014b). The reason for this is the locking-up of oxygen in silicates, as has already been suggested by Fortney et al. (2006).

Interestingly, both H_2O and CH_4 have strong absorption features, and their main absorption bands between $\sim$ 1.3 and 5 μm are alternately located in wavelength space. Thus hot gaseous planets with C/O $<$ 1 and C/O $\gtrsim$ 1 in the spectrally active regions should be quite easily distinguishable, and might give hints on the planet's formation history such as the location of formation in the protoplanetary disk and its migration through it (see 'Open Question' 5, Section 1.5).

For even higher temperatures ($T \gtrsim 1750$ K), and C/O $\gtrsim$ 1, HCN, and possibly C_2H_2, take over as the most important carbon-carrying infrared absorber. This is due to equilibrium chemistry predicting that they become more abundant than CH_4 in the spectrally active parts of the atmospheres (see, e.g., Moses et al. 2013). The respective atmospheres are then not dominated by CH_4 anymore, but by HCN. Distinguishing H_2O and HCN absorption features should be possible, due to the different spectral signatures of HCN and H_2O in the NIR and IR. Therefore, a distinction between O- and C-dominated atmospheres is possible also at high temperatures.

As mentioned above, hot jupiters of high enough temperatures may harbor inversions due to TiO and VO absorption. However, as pointed out in Madhusudhan (2012), atmospheres with C/O ratios $\gtrsim$ 1 are depleted in TiO/VO, due to the decreased abundance of O. Hence, TiO/VO based inversions are not expected in carbon-rich (C/O $>$ 1) atmospheres. As I will show in Section 4.4, atmospheres with C/O $\sim$ 1 may still develop inversions.

Observationally, the evidence for planets with C/O $\gtrsim$ 1 is scarce. The most prominent case, WASP-12b (Madhusudhan et al. 2011b), has probably been based on challenging and erroneously reduced observational data. For the corrected data it was discussed whether or not it contained evidence for C/O$\gtrsim$ 1, (Crossfield et al. 2012; Swain et al. 2013; Stevenson et al. 2014a; Line et al. 2014; Benneke 2015), but the clear detection of water in the planet's transmission spectrum seems to have settled the matter (Kreidberg et al. 2015), clearly indicating that C/O$<$1.

A C/O ratio close to unity has been reported for the self-luminous planet HR 8799b, however, for which C/O = 0.96 ± 0.01 or $0.97^{+0.00}_{-0.01}$ has been estimated (Lee et al. 2013), depending on whether clouds are included in the model or not. This result was recovered in the retrieval study by Lavie et al. (2016), who report a C/O value of $0.93^{+0.01}_{-0.02}$.

In conclusion, the C/O ratio, together with the effective temperature, may be a key parameter constraining a hot jupiter's spectral appearance, and thus I studied how the interplay between the C/O ratio and other parameters affect the atmospheric properties of planets.

In the following Section 4.2.1 I discuss the assumptions made in *petitCODE* for calculating the grid, and how these relate to the physical processes occurring in the atmospheres. In Section 4.2.2 I explain how the grid was set up, and how the calculations were carried out. The grid results are described and interpreted in sections 4.3, 4.4, 4.5, 4.6, and 4.7, followed by a summary in Section 4.8.

4.2.1 Model assumptions

In this Section I discuss important physical processes which govern the atmospheres of hot jupiters, and assess how well the version of *petitCODE*, used in Mollière et al. (2015), was suited to describe them.

Chemistry

As summarized in Section 3.4.1, *petitCODE* uses a chemical equilibrium model for obtaining molecular and atomic abundances, where in Mollière et al. (2015) we still used the *CEA* code, and switched to my self-written Gibbs minimizer in Mollière et al. (2017, this study is described in Chapter 5).

The knowledge of the abundances is fundamental for constructing the atmospheric opacities. As summarized in Section 2.3.2, there are different regions in hot jupiter atmospheres, in which different chemical assumptions are fulfilled: usually the equilibrium abundances of the planet's hot regions (dayside vs. nightside, deep atmosphere vs. upper atmosphere) dominate the cool regions, if the mixing processes in the horizontal or vertical direction are fast enough.

As explained in Section 2.3.2, planets with equilibrium temperatures above $1000-1500$ K should not be affected by non-equilibrium effects too much. This may change if photochemical reactions produce hazes, but the temperatures of hot jupiters are too high for the usually assumed photochemical haze species to be stable (see 'Open Question' 3, Section 1.5). Because the grid of model atmospheres I describe here goes down to atmospheric effective temperatures of 1000 K, the lowest temperature atmospheres in the grid may have needed non-equilibrium chemistry for a correct abundance computation. This should be kept in mind for deductions made with the cool grid models.

The following elemental species were assumed for the model calculations: H, He, C, N, O, Na, Mg, Al, Si, P, S, Cl, K, Ca, Ti, V, Fe and Ni. Based on Seager et al. (2000) I considered the following reaction products: e^-, H, He, C, N, O, Na, Mg, Al, Si, P, S, K, Ca, Ti, Fe, Ni, H_2, CO, OH, SH, N_2, O_2, SiO, TiO, SiS, H_2O, C_2, CH, CN, CS, SiC, NH, SiH, NO, SN, SiN, SO, S_2, C_2H, HCN, C_2H_2, CH_4, AlH, AlOH, Al_2O, CaOH, MgH, MgOH, VO, VO_2, PH_3, CO_2, TiO_2, Si_2C, SiO_2, FeO, NH_2, NH_3, CH_2, CH_3, H_2S, KOH, NaOH, NaCl, KCl, H^+, H^-, Na^+, K^+, Fe (condensed), Al_2O_3 (condensed), $MgSiO_3$ (condensed), SiC (condensed).

The choice of condensed species is motivated by Seager et al. (2000); Sudarsky et al. (2003). Additionally, I also added SiC as a condensable species, to account for condensation of C in atmospheres with a high C/O ratio, as has also been suggested by Seager et al. (2005).

Clouds

Clouds appear to be widespread in all planetary atmospheres (see 'Open Question' 3, Section 1.5). The most commonly stated evidence for clouds or hazes in hot jupiter atmospheres is the fact that the transmission spectra of many of these objects show no or only weak features at optical wavelengths (see the 'Transit spectroscopy' part of Section 1.4.1). A prominent example for such a planet, which appears to be cloudy in transmission, is HD 189733b, featuring a nearly flat transmission spectrum at optical wavelengths, except for the alkali line cores (e.g. Sing et al. 2011).

Assessing the influence of clouds on the P–T structure and emission spectra of hot jupiters is not an easy task.[2] In the case of HD 189733b, which shows a nearly featureless optical transmission spectrum, Barstow et al. (2014) find that the temperature structure they retrieve, using the planet's emission spectrum, is insensitive to whether or not a cloud model is included (they use various $MgSiO_3$ models). At the same time many of their cloud model setups are able to reproduce HD 189733b's transmission spectrum. This indicates that for hot jupiters, at least for HD 189733b, the treatment of clouds is important for the appearance of the planet's transmission spectrum, but not so much for the actual absorption of the bulk of the stellar light in the deeper layers of the dayside atmosphere. In this case the influence of clouds on the P–T structure and the emission spectrum would be minor. The reason why such situations can arise is straightforward to see: in Equation 1.11 it was derived that the slant optical depth for a stellar ray of light is set by a length scale $\sim \sqrt{R_{\rm Pl} H_P}$, whereas for the emission, which leaves the planet ∼vertically, it is of the order of $\sim H_P$. Due to this, the slant optical depths of possible cloud species can be ∼35-90 times larger than the vertical optical depth (Fortney 2005). This is in agreement with the work by Fortney et al. (2008), who find that clouds have a minor effect on their self-consistently calculated PT-profiles and emission spectra of hot jupiters, and therefore neglect clouds.

The Mollière et al. (2015) grid did not yet consider the formation of clouds. However, from the previous discussion I concluded that it may be permissible to neglect clouds, as long as only emission spectra are calculated. However, as pointed out by Fortney (2005), in cases of high metallicity planets the effects of clouds may become important, especially if appreciable amounts of silicate, iron or corundum condensates can form. This has to be stressed in light of the fact that hot jupiters seem to be most prevalent in stellar systems of high metallicity (Fischer & Valenti 2005).

Because I neglected clouds, I further concluded that the omission of scattering in the Mollière et al. (2015) grid was not introducing too large an error, thus no strong scattering contribution to the opacity in the NIR and MIR is to be expected. In addition, the reported optical albedos of hot jupiters are very low, in the low single digit percentage range, as

[2] Note that in Mollière et al. (2015) transmission spectra were not yet included.

$T_{\rm eff}$ (K)	$\Delta T_{\rm eff}$	[Fe/H] (dex)	Δ[Fe/H]	C/O	ΔC/O	SpT	Δ SpT	$\log(g)$	$\Delta\log(g)$
1000–2500	250	-0.5–2.0	0.5	0.35–1.4	0.1[(a)]	M5–F5	"1"[(b)]	2.3–5	1.0[(a)]

TABLE 4.1: Grid range and step size of the Mollière et al. (2015) grid. Footnotes: (a): more finely or coarser spaced regions may exist, see Section 4.2.2. (b): spectral types are stepped by "one" spectral type, with the associated temperature being 3000, 4345, 5570, and 6560 K for M5, K5, G5, and F5, respectively.

summarized by Madhusudhan et al. (2014c). Absorption appears much more important than scattering in these objects. Exceptionally cloudy hot jupiters may exist, however, such as Kepler 7b, having a geometric albedo of 0.32 ± 0.03 (Demory et al. 2011). In general, if scattering was important, then it would cause the incoming stellar radiation to traverse, on average, a somewhat longer distance through the atmosphere before reaching a certain pressure level (because it will carry out a random walk). Hence, the photons will on average be absorbed at lower pressures (higher altitudes), if they are not scattered back to space before. This will result in the deeper atmospheric regions to be cooler, also see Section 2.2.1.

Horizontal winds

Based on GCM simulations and theoretical considerations, winds are expected to be present on hot jupiters, driven by the temperature contrasts between the day and nightside, and the polar and equatorial regions (see summary in Section 2.1.1). In Section 2.1.1 I already mentioned that the higher the effective temperature of a hot jupiter, the less efficient the transport of energy by wind becomes (Perez-Becker & Showman 2013; Komacek & Showman 2016; Komacek et al. 2017). For "cool" planets with effective temperatures of ~ 1000 K redistribution of energy may be quite efficient unless the planet has a mass of a few Jupiter masses or more (Kammer et al. 2015).

As summarized in Section 3.1.1 (and Figure 3.1 therein) *petitCODE* has three possible ways to treat the distribution of the incident stellar light across the atmosphere, to at least partially accommodate the effect of heat redistribution by winds: (a) global averaging, and (b) dayside averaging (or (c), no wind transport of energy). For the grid presented in Mollière et al. (2015), which goes from atmospheres at temperatures of 1000 to 2500 K (see Section 4.2.2), I decided to consider a dayside-averaged case for the stellar irradiation as a compromise between of the two limiting cases (a) and (c).

A fourth way would be to use a redistribution parameter for the incident stellar irradiation which adds a fraction of the absorbed stellar energy to the night side internal temperature and decreases the amount of light to be absorbed on the dayside (Burrows et al. 2006). Other possibilities include the mimicking of planetary winds by assuming that the atmosphere carries out a rigid body rotation, and to follow a vertical atmospheric structure as it rotates around the planet, while modeling its time-dependent cooling (Iro et al. 2005).

4.2.2 Parameter setup

For the Mollière et al. (2015) paper I set up a grid of 10,640 models, which are defined by the following parameters (also see Table 4.1 for a summary):

1. $T_{\rm eff}$ = **1000, 1250, 1500, 1750, 2000, 2250, 2500 K**
   I chose to start at temperatures at the lower edge of where they may not be affected by non-equilibrium chemistry effects (1000-1500 K, see Section 4.2.1). Furthermore, high metallicity models with low $\log(g)$ and high $T_{\rm eff}$ will have temperatures larger than 3000 K in the higher pressure regions of the atmosphere. However, the line opacities are only calculated up to temperatures of 3000 K (see Section 3.3.1).[3] Thus, if $T >$ 3000 K in regions of the atmosphere which are not yet convective, I use the opacities at 3000 K.

2. **[Fe/H] = -0.5, 0.0, 0.5, 1.0, 2.0**
   The metallicity is chosen to range from sub-solar to strongly enriched. I assumed scaled solar compositions, according to Asplund et al. (2009). It is not generally expected that enriched exoplanets have a scaled solar composition. Nonetheless, I use this approximation as a proxy for various degrees of enrichment. A further degree of freedom regarding the composition is introduced to the grid by varying the C/O ratio. For my grid, I focus on metallicities higher than the solar value. The reason for this is that giant exoplanets are expected to be enriched in metals, with objects of several hundred Earth masses having metallicities of up to several tens of the solar metallicity (Fortney et al. 2013).

3. **C/O = 0.35, 0.55, 0.7, 0.71, 0.72, 0.73, 0.74, 0.75, 0.85, 0.9, 0.91, 0.92, 0.93, 0.94, 0.95, 1.0, 1.05, 1.12, 1.4**
   I investigate C/O values which are sub-solar, or super-solar but < 1 (with C/O$_\odot \sim$ 0.55), as well as values around and above 1. A finer sampling is used around C/O $\sim$ 0.73 and C/O $\sim$ 0.92, because I wanted to resolve the transition from oxygen- to carbon-dominated spectra, which is quite sharp. For the hotter atmospheres this transition occurs at C/O = 0.92, while for cooler planets it shifts to 0.73, due to silicate condensation. The C/O ratio at a given metallicity was obtained from varying the O abundance. This means that for super-solar C/O ratios the O abundance was decreased, corresponding to the accretion of water-depleted gas or planetesimals during the planet's formation.

4. **Spectral type of host star: F5, G5, K5, M5**
   In order to assess the dependence of the atmospheres on the spectral shape of the stellar irradiation, I calculated the models at four different host star spectral types. For the earlier spectral types the energy received by the planet is absorbed predominantly by the alkalis in the optical wavelengths, whereas for the later spectral types the wavelength range of the absorption shifts more and more to the NIR. The effective temperatures associated with the stellar types are 3000, 4345, 5570, and 6560 K for M5, K5, G5, and F5, respectively.

5. $\log(g)$ **= 2.3, 3.0, 4.0, 5.0**
   The $\log(g)$ grid was chosen such that it encompasses hot jupiters of every conceivable

[3] The reason for this is that the partition functions are only tabulated up to 3000 K.

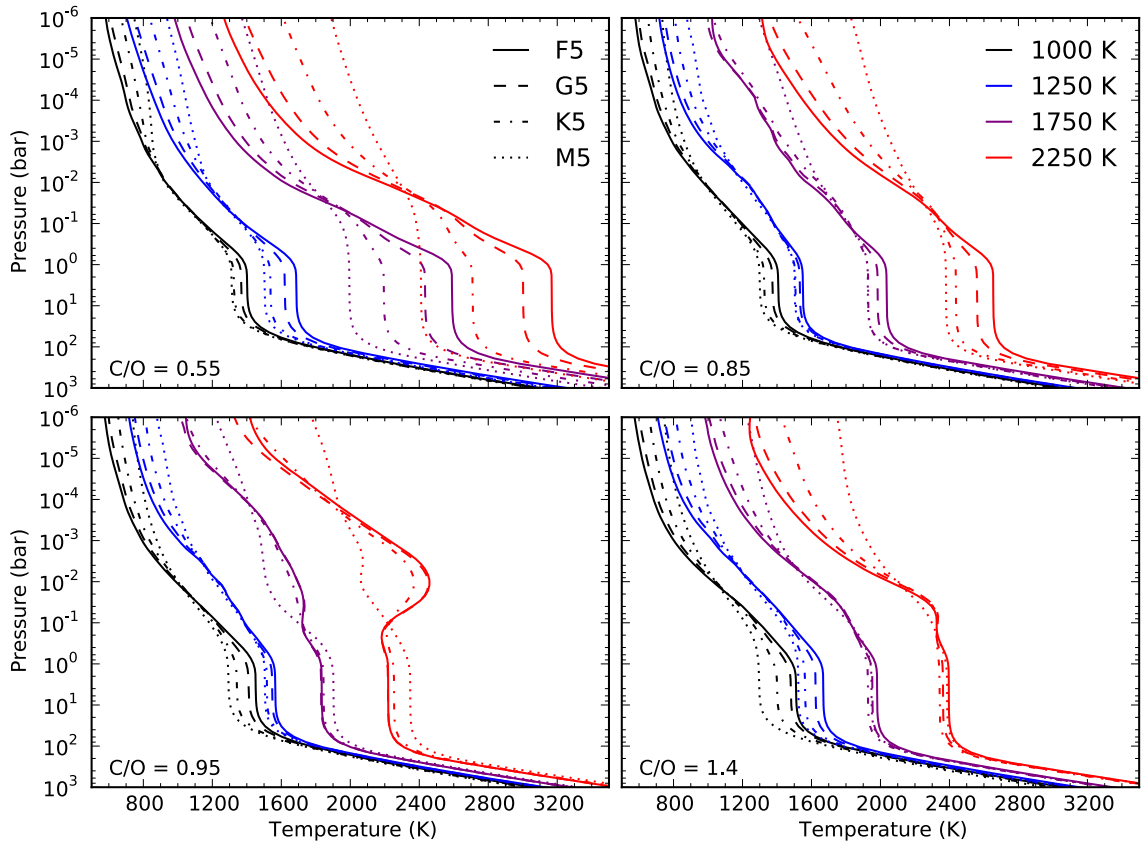

FIGURE 4.1: Atmospheric P–T structures for planets of varying host star spectral types, effective temperatures and C/O ratios with $\log(g) = 3$ and [Fe/H] = 1, as obtained with *petitCODE*. The line style varies with host star spectral type as follows: F5 (solid), G5 (dashed), K5 (dot-dashed), M5 (dotted). The line color indicates the following planetary effective temperatures: 1000 K (black), 1250 K (blue), 1750 K (purple), 2250 K (red). The four different panels correspond to 4 different C/O ratios: C/O = 0.55 (*upper left panel*), C/O = 0.85 (*upper right panel*), C/O = 0.95 (*lower left panel*), C/O = 1.4 (*lower right panel*). Figure taken from Mollière et al. (2015)

mass–radius combination, including bloated hot jupiters as well as compact ($R_{\rm Pl} \sim R_{♃}$) planets of varying masses.[4]

4.3 Global atmospheric properties

To give a first overview of the grid results I show atmospheric P–T structures of $\log(g) = 3$ and [Fe/H] = 1 planets for varying host star spectral types (F5, G5, K5, M5) and effective temperatures (1000 K, 1250 K, 1750 K, 2250 K) at four different C/O ratios (0.55, 0.85, 0.95, 1.4) in Figure 4.1. Some general, expected trends can quite easily be made out from looking at this plot:

- The later the host star spectral type, the more isothermal the atmospheric structure becomes. This is expected because for increasingly cooler stars the wavelength range of the received stellar irradiation becomes more and more similar to the wavelength range of the internal planetary radiation field, such that effective opacity for absorbing

[4] All planets listed on http://exoplanets.org with a mass and radius measurement fall within our adopted $\log(g)$ range.

the stellar radiation at the top of the atmosphere is similar to the opacity absorbing the planetary radiation field. This is the same atmospheric behavior discussed in Section 2.2.1: when the ratio γ of the visual and IR opacities approached unity, the atmospheric temperature structure became more and more isothermal (also see Figure 2.2). Here the phenomenon does not come about by changing the opacity itself, but by changing the spectral shape of the irradiation.

- The P–T structures with C/O = 0.55 are hotter than the P–T structures with C/O = 0.85. The main reason for this is that the atmosphere with the lower C/O ratio has, everything else being equal, more oxygen and thus a higher opacity due to a higher H_2O abundance. This results in a stronger green house effect, as the excess H_2O leads to a less efficient escape of radiation from the atmosphere (corresponding to the $\gamma < 1$ cases in Section 2.2.1, Figure 2.2). In order to radiate away the required amount of energy (set by $T_{\rm eff}$) the atmospheres need to be hotter.

Another striking result is that for C/O ratios close to 1 temperature inversions form in the atmospheres for effective temperatures above ∼2000 K. In general, they can even occur at effective temperatures as low as 1500 K, see Section 4.7. This is interesting because only Na and K are used as optical absorbers, with no additional optical absorbers such as TiO and VO. For host stars later than K5 there are no inversions in the planetary atmospheres. This phenomenon will be further studied in Section 4.4.

4.4 Inversions at C/O ratios close to unity

As outlined above, C/O ratios of ~ 1 can lead to inversions in atmospheres with high enough effective temperature, if the stellar host is of K spectral type or earlier. The reason for the inversions to occur for these spectral types is that an appreciable amount of stellar flux is received from the star in the optical wavelength regime. This means that the alkali lines, and the pseudo-continuum contribution of the alkali line wings, will become very effective in absorbing the stellar irradiation. At the same time, close to C/O = 1, most of the oxygen and carbon is locked up in CO, leading to low H_2O, CH_4 and HCN abundances and, hence, low opacities.

The combined effect of the effective absorption of the strong irradiation and a decreased ability of the atmospheric gas to cool, because of too little CH_4, H_2O, and HCN leads to the inversion in the atmospheres. In the simple analytic model introduced for the atmospheres in Section 2.2.1, this would mean that the IR opacity decreases, such that γ increases (cf. Figure 2.2).

The absorption of the stellar light as a function of depth can be seen in Figure 4.2, where I plotted the P–T structure of a $\log(g) = 3$, [Fe/H] = 1, $T_{\rm eff}$ = 2250 K, C/O = 0.95 atmosphere of a planet in orbit around a G5 star, as well as the local stellar flux at the pressure levels 3.47 $\times 10^{-5}$, 9.07 $\times 10^{-3}$ and 1.27 $\times 10^{-1}$ bar in the atmosphere. Also a plot of the logarithm of the (rescaled) opacity $\log(\kappa)$ is shown in the figure, for each pressure level. The respective pressure levels are indicated by red points in the P–T structure.

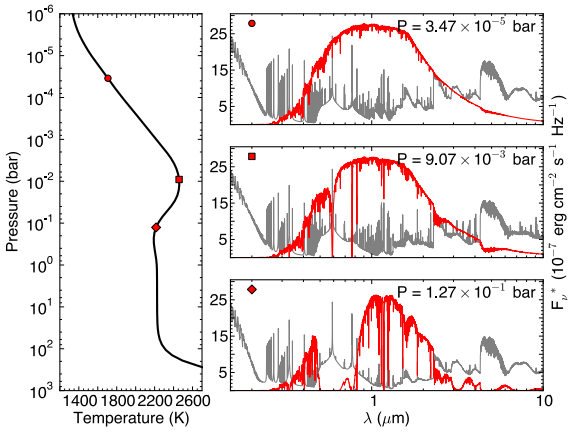

FIGURE 4.2: *Left panel:* P–T-structure of a $\log(g) = 3$, [Fe/H] = 1, $T_{\rm eff}$ = 2250 K, C/O = 0.95 atmosphere of a planet in orbit around a G5 star. *Right panels:* Local stellar flux (red solid line) at the three pressure levels at 3.47 $\times$ 10^{-5} *(top panel)*, 9.07 $\times$ 10^{-3} *(middle panel)* and 1.27 $\times$ 10^{-1} bar *(bottom panel)* in the atmosphere. The local opacity $\log(\kappa)$ for each layer is shown as a gray solid line (rescaled). The respective pressure levels are indicated by a red circle, square and diamond in the P–T structure. Figure adapted from Mollière et al. (2015).

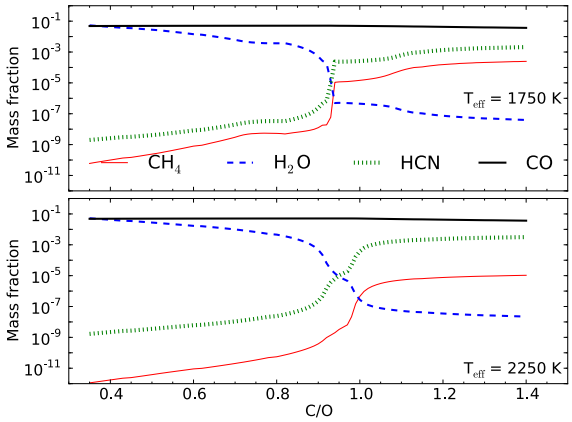

FIGURE 4.3: Mass fractions of CH_4 (thin solid red line), H_2O (dashed blue line), HCN (dotted green line) and CO (thick solid black line) as a function of the C/O ratio for a $\log(g) = 3$, [Fe/H] = 1 atmosphere of a planet in orbit around a G5 star at a pressure level of 9.07 $\times$ 10^{-3} bar. The *top panel* shows the mass fractions for a planet with $T_{\rm eff}$ = 1750 K while the *bottom panel* shows the mass fractions for a planet with $T_{\rm eff}$ = 2250 K. Figure adapted from Mollière et al. (2015).

Figure 4.2 nicely shows how the alkali pseudo-continuum absorbs the full stellar flux in its wavelength domain at the position of the inversion: At the highest pressure shown in the spectral plots (3.47 $\times$ 10^{-5} bar) the stellar flux is still completely unaffected by any absorption effects: the atmosphere is still optically thin at all wavelengths (except for right at the core of the alkali lines). At the hottest point in the temperature inversion (at 9.07 $\times$ 10^{-3} bar) one can see that the alkali wings have already started to absorb non-negligible amounts of energy, and just after the inversion (at 1.27 $\times$ 10^{-1} bar) the stellar flux in the alkali wings has been completely absorbed. Interestingly, the inversions obtained in this calculations, due to alkali heating, seem to abide by the rule that the tropopause[5] should commonly be found at $\sim$ 0.1 bar for a wide variety of possible atmospheres (Robinson & Catling 2014).

As can be seen in the stellar flux spectrum at the highest pressure, the absorption of the stellar light outside of the alkali wings is rather sluggish, showing the importance of the alkali wings in the formation of the inversion.

As mentioned above, in a small region of C/O ratios around 1, the atmosphere's ability to efficiently radiate away the absorbed stellar light decreases due to the involved chemistry. This can be seen well by looking at Figure 4.3, which shows the CH_4, H_2O, HCN, and CO mass fractions in a $\log(g) = 3$, [Fe/H] = 1 atmosphere of a planet in orbit around a G5 star as a function of C/O at a pressure level of 9.07 $\times$ 10^{-3} bar, i.e. close to the pressure where the inversion temperature, if an inversion occurs, is maximal. Two cases for planets with $T_{\rm eff}$ = 1750 K and $T_{\rm eff}$ = 2250 K are shown and I carried out 100 self-consistent atmospheric calculations for both cases with C/O going from 0.35 to 1.4 in equidistant steps.

One sees that for the $T_{\rm eff}$ = 2250 K case, at C/O = 0.95, the H_2O abundance has already decreased by 4 orders of magnitude when compared to the lowest C/O values, while the

[5]The tropopause denotes the atmospheric layer at minimum temperature just after the inversion.

CH_4 abundance is still more than 2 magnitudes smaller than its highest abundance at the highest C/O values. Further, also HCN has not yet risen to a high enough abundance to take over the cooling. The C/O = 0.95 point at $T_{\rm eff}$ = 2250 K is thus very close to the aforementioned point of minimum IR opacity, leading to the inversions seen in my results for all host spectral types except M5. For higher C/O ratios the IR opacity, and the atmosphere's ability to cool, increases, such that no inversions are observed anymore, mainly because HCN takes over the cooling.

For the particular case of $T_{\rm eff}$ = 1750 K in Figure 4.1 the situation must be different, as there is no inversion present in the atmosphere. The reason for this can be seen in the panel for $T_{\rm eff}$ = 1750 K in Figure 4.3: for this atmosphere the transition from water-rich to methane-rich atmospheres occurs much quicker as a function of C/O than it does for the $T_{\rm eff}$ = 2250 case. The methane mass fraction jumps from 10^{-8} to 10^{-5} at C/O = 0.93 and the HCN mass fraction jumps from 10^{-6} to 10^{-4} and no extended region of low water, methane and HCN abundance is seen. In conclusion, this atmosphere can cool more efficiently. Further, as this atmosphere is cooler, the overall CH_4 content is higher than in the hotter case. This is expected to occur and has been studied before both in equilibrium and disequilibrium chemical networks (see, e.g., Moses et al. 2013), showing that CH_4 becomes less abundant as the temperature increases in carbon-rich atmospheres.

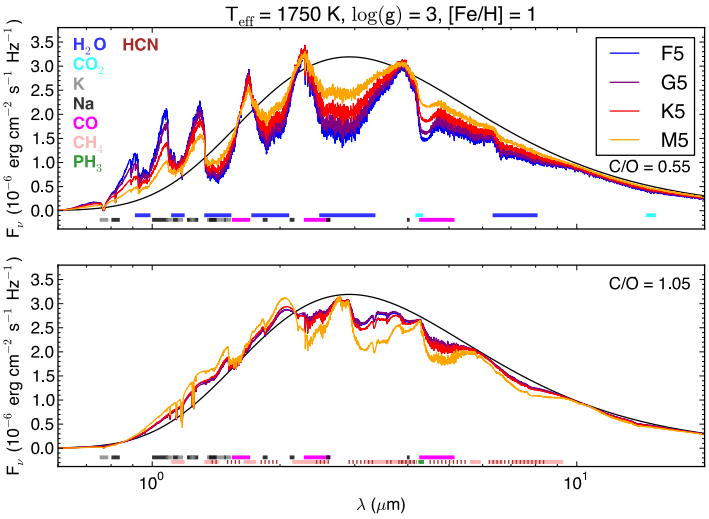

FIGURE 4.4: Emission spectra as a function of host star spectral type for a $T_{\rm eff}$ = 1750 K, log(g) = 3, [Fe/H] = 1 planet with C/O = 0.55 (*upper panel*) and C/O = 1.05 (*lower panel*). The spectra are shown for a F5 (blue lines), G5 (purple lines), K5 (red lines) and M5 (orange lines) host star. The colored bars indicate the position of the absorption maxima of various species. The black line shows the blackbody flux at the atmosphere's effective temperature. Figure taken from Mollière et al. (2015).

4.5 The influence of the host star

As described above, planets orbiting increasingly cooler host stars will approach an increasingly isothermal atmospheric structure, because the spectral energy distribution (SED) of the insolation becomes more and more comparable to the SED of the planetary radiation field, and hence the mean opacities at which the stellar and planetary light are absorbed.

I show the emission spectra of atmospheres with varying host star spectral type for a planet with $T_{\rm eff}$ = 1750 K, log(g) = 3, [Fe/H] = 1 for two different C/O ratios (0.55, 1.05) in Figure 4.4. The positions of absorption features of H_2O, CO_2, K, Na, CO, CH_4, PH_3 and HCN are indicated in the plots. For the atmospheres with C/O = 0.55 the emission spectra clearly become more blackbody-like as the host star gets cooler: the excess emission (with respect to the blackbody curve at 1750 K) of the atmospheres for $\lambda < 1.3$ μm decreases for

cooler host stars. Furthermore the molecular absorption bands in the emission spectra start to get shallower. As expected for a C/O ratio < 1, the spectra are clearly water-dominated (also see Section 4.6).

For the atmospheres with $\mathrm{C/O} = 1.05$ the situation is different. First, the atmospheres are clearly carbon-dominated, showing strong HCN and CH_4 features. Moreover, the latest type host star (M5) causes the least isothermal planetary spectrum, while all earlier type host stars result in a much more isothermal atmospheric structure and, therefore, spectra. This is the opposite of what was happening for the C/O = 0.55 atmosphere, now host stars of an earlier type are making the planetary spectra more isothermal. This is merely the spectral consequence of early type host stars creating inversions or isothermal atmospheres for planets with C/O ~ 1, which was explained in Section 4.4. As the M5 star is not able to heat the atmosphere enough, due to a lack of energy in the optical wavelengths, the corresponding P–T structure and spectra are less isothermal. The P–T structures producing the spectra shown here for C/O = 1.05, and early type hosts, do not have inversions, they are just more isothermal due to the heating. Nonetheless, as we will see in Section 4.7.3, atmospheres at T_{eff} = 1750 K can, in general, exhibit inversions.

4.6 The influence of the surface gravity and the metallicity

4.6.1 Surface gravity effects

Atmospheric structures

The behavior of the atmospheric P–T structures as a function of $\log(g)$ is studied in Figure 4.5. If one considers gray opacities which are constant as a function of P and T, and assumes hydrostatic equilibrium, one obtains the following simple relation between the optical depth τ and the pressure P (cf. Equation 3.18)

$$\tau = \frac{\kappa}{g} P \,, \tag{4.2}$$

where κ is the gray opacity and g is the gravitational acceleration (taken to be constant). τ is the effective spatial coordinate for the radiation field. Thus the $T(\tau)$ structure will not change upon variation of the gravity. The mapping from τ to P, however, will change, resulting in locations of a given optical depth and temperature to move to larger pressure values when g is increased. This is equivalent to saying that the location of the planetary atmospheric photosphere moves in terms of pressure if the surface gravity is changed.

Thus, when plotting the P–T structures as a function of planetary gravitational acceleration, as can be seen in Figure 4.5, one notices that at higher $\log(g)$ values the temperature structure appears to be shifted to larger pressures, when comparing to cases with lower $\log(g)$. For demonstration purposes I show the P–T structures up to 10^{-14} bar. Note, however, that I only calculate the opacities down to pressures of 10^{-6} bar and adopt the 10^{-6}

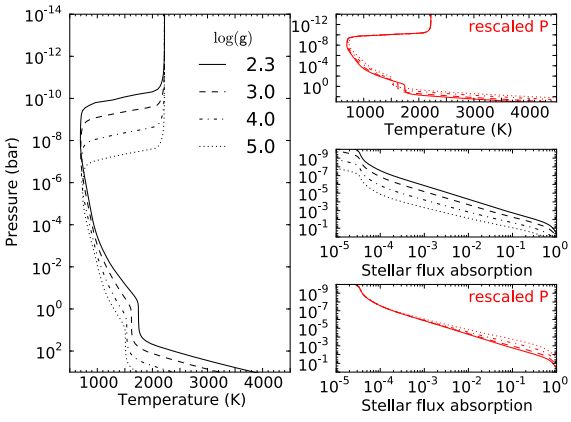

FIGURE 4.5: Atmospheric P–T structures and stellar light absorption as a function of $\log(g)$ for planets with $T_{\rm eff}$ = 1250 K, [Fe/H] = 1 and C/O = 0.55 in orbit around a G5 star. The linestyles correspond to $\log(g)$ = 2.3 (solid line), 3.0 (dashed line), 4.0 (dot-dashed line), 5.0 (dotted line). *Left panel*: P–T structures. *Top right panel*: P–T structures with pressure rescaled by $10^{2.3-\log(g)}$. *Middle right panel*: Fraction of absorbed stellar flux as a function of pressure. *Bottom right panel*: Fraction of absorbed stellar flux as a function of rescaled pressure. Figure taken from Mollière et al. (2015).

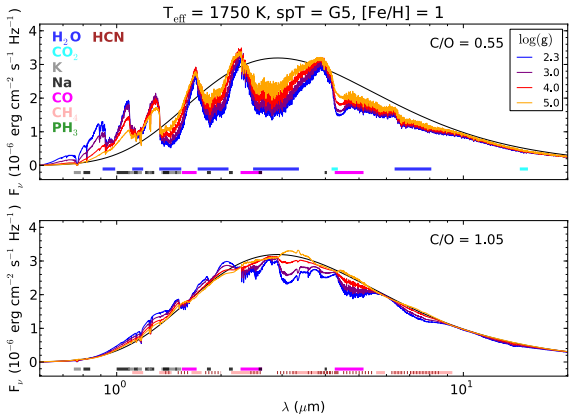

FIGURE 4.6: Emission spectra as a function of surface gravity for a $T_{\rm eff}$ = 1750 K, [Fe/H] = 1 planet with C/O = 0.55 (*upper panel*) and C/O = 1.05 (*lower panel*) in orbit around a G5 star. The spectra are shown for $\log(g)$ = 2.3 (blue lines), $\log(g)$ = 3 (purple lines), $\log(g)$ = 4 (red lines) and $\log(g)$ = 5 (orange lines). The colored bars indicate the position of the absorption maxima of various species. The black line shows the blackbody flux at the atmosphere's effective temperature. Figure taken from Mollière et al. (2015).

bar values at all smaller pressures, i.e. $\kappa(P < 10^{-6}\ \mathrm{bar}) = \kappa(P = 10^{-6}\ \mathrm{bar})$.[6] The "highest altitude inversion" visible in this plot for pressures much smaller than 10^{-6} bar is due to the heating by the alkali line cores.

In the top right panel of Figure 4.5 I show the P–T structures once more. In this case I have re-scaled the pressures of P–T structures with $\log(g)$ higher than 2.3 (which is the lowest $\log(g)$ value I consider, see Table 4.1) with $10^{2.3-\log(g)}$. To first order, his should counterbalance the pressure shift of the temperature structure induced by gravity when compared to the $\log(g)$ = 2.3 case. However, as the opacities are non-gray and varying vertically one expects differences. Nonetheless, the resulting P–T structures lie on top of each other quite well.

When comparing in greater detail one notices that the deep isothermal regions (at $\sim$ 1-100 bars) are at higher temperatures for lower $\log(g)$. Here the pressure dependence of the opacity comes into play: for lower $\log(g)$ values the stellar light is absorbed at lower pressures, where the atomic and molecular lines are less broadened, and the CIA opacities are less important. This results in the stellar light being able to penetrate deeper in terms of rescaled pressure when comparing to high $\log(g)$ atmospheres. This means that more stellar light reaches regions of the atmosphere which are optically thick in the near-infrared, which does, in turn, heat up the atmosphere deep in these IR optically thick regions.

In the middle and bottom panel on the right side of Figure 4.5 I show the fraction of the absorbed stellar flux with respect to the stellar flux at the top of the atmosphere. The middle panel shows this fraction as a function of pressure, the bottom panel shows this fraction as

[6] The P–T structures for pressures below 10^{-6} bar are not necessarily unphysical, however: at altitudes above the 10^{-6} bar level the contribution of the pressure-broadened line wings to the total opacity is negligible and the opacity is dominated by the line cores, whose shape is given by thermal broadening and is independent of pressure. As only little mass is above any given pressure lower than 10^{-6} bar, the line wings are not able to significantly alter the radiation field.

a function of rescaled pressure. One sees that the stellar light is able to penetrate deeper in terms of rescaled pressure in the case of low $\log(g)$.

In order to test that our above observations for the oxygen-rich atmosphere are not caused by pressure and temperature dependent chemistry effects, I calculated self-consistent structures with vertically constant abundances of molecules, varied the surface gravity, and found the same behavior.

Emission spectra

In Figure 4.6 I show the emission spectra of atmospheres with varying surface gravity for a planet with $T_{\rm eff} = 1750$ K, and $[{\rm Fe/H}] = 1$, in orbit around a G5 host star, again for two different C/O ratios (0.55, 1.05). As mentioned above, a variation in the surface gravity rescales the temperatures profiles in terms of pressure. Also the photosphere is located at higher pressures for a higher surface gravity. It is therefore less transparent, due to the line wing pressure broadening, decreasing the contrast between opacity minima (line wings) and opacity maxima (line cores). This leads to shallower absorption troughs in the C/O = 0.55 case. This behavior was verified by the atmospheric structures with vertically constant molecular abundances as well.

In the C/O = 1.05 case the same behavior can be seen, except for the atmospheres with the highest $\log(g)$, which shows emission features. For increasing $\log(g)$ stellar light is absorbed over ever narrower pressure ranges because the alkali line wings become increasingly stronger. The atmospheric cooling ability, however, is largely independent of pressure, because the emission of light depends on the Planck opacity $\kappa_{\rm P}$ (cf. Equation 3.93) and $\partial\kappa_{\rm P}/\partial P = 0$, if the pressure dependence of the chemistry is omitted. This causes the atmosphere at highest $\log(g)$ to develop an inversion.

4.6.2 Metallicity effects

Atmospheric structures

The influence of the metallicity on the P–T structures at low C/O ratios is as one would expect: the temperature structure is scaled to lower pressures as the metallicity, and thus the opacity κ, increases, as a higher optical depth is reached earlier in the atmosphere (see Equation 4.2).

The stellar light can penetrate deeper than suggested by a simple pressure scaling, however: the pressure dependent line wings are weaker (as the atmospheric structures shift to smaller pressures for higher metallicities). This increases the temperature of the atmospheres in the deep isothermal regions at 1-100 bars (see left panel of Figure 4.7), just like it did for low surface gravities studied in Section 4.6.1. Similar to the test carried out for varying surface gravities I calculated test atmospheres with vertically constant molecular abundances, scaling the abundances by different factors for different structures, mimicking variations in metallicity without having to deal with effects introduced by chemistry. These calculations showed the same behavior as the nominal calculations, when varying the metallicity.

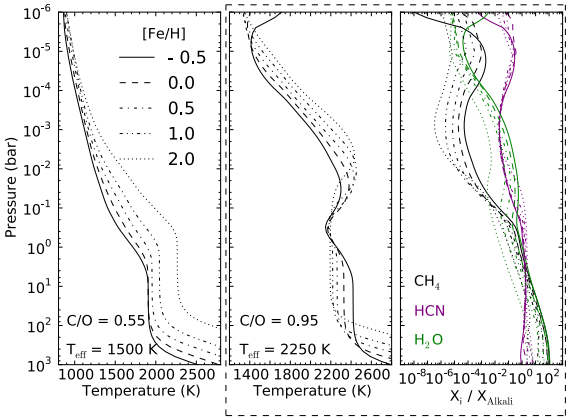

FIGURE 4.7: Atmospheric P–T structures and mass fractions as a function of metallicity for $\log(g) = 3$ planets around a G5 star. The *left panel* shows the P–T structures of the cases with C/O = 0.55, $T_{\rm eff}$ = 1500 K planets, the *middle panel* shows the cases with C/O = 0.95, $T_{\rm eff}$ = 2250 K. The *right panel* shows the mass fractions of CH_4 (black lines), HCN (purple lines) and H_2O (green lines) divided by the alkali mass fraction for the P–T structures shown in the middle panel. The different line styles in all panels stand for different metallicities: [Fe/H] = -0.5 (solid line), 0.0 (dashed line), 0.5 (dot-dashed line), 1.0 (double dotted dashed line), 2.0 (dotted line). Figure taken from Mollière et al. (2015).

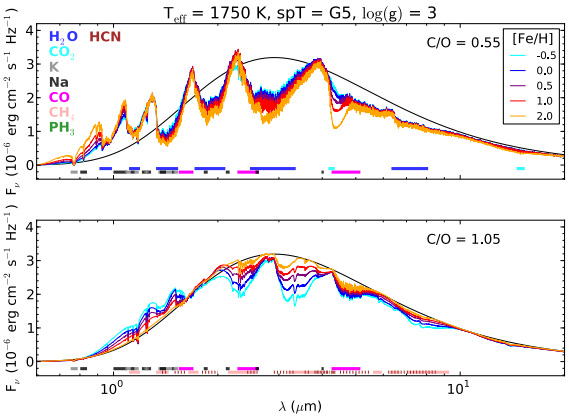

FIGURE 4.8: Emission spectra as a function of metallicity for a $T_{\rm eff}$ = 1750 K, [Fe/H] = 1 planet with C/O = 0.55 (*upper panel*) and C/O = 1.05 (*lower panel*) in orbit around a G5 star. The spectra are shown for [Fe/H] = -0.5 (cyan lines), [Fe/H] = 0.0 (blue lines), [Fe/H] = 0.5 (purple lines), [Fe/H] = 1 (red lines) and [Fe/H] = 2 (orange lines). The colored bars indicate the position of the absorption maxima of various species. The black line shows the blackbody flux at the atmosphere's effective temperature. Figure taken from Mollière et al. (2015).

In the case of P–T structures with C/O $\sim$ 1, that harbor inversions, an increase in metallicity causes the inversion temperature to increase, and the temperature in the region directly beneath the inversion (i.e. at higher pressure) to decrease (see middle panel of Figure 4.7). It is, at first, not evident why this should happen, because if all the metal atomic abundances scale with $10^{\rm [Fe/H]}$, one would expect the same for the resulting molecular abundances and opacities, and therefore the heating vs. cooling ability of the atmosphere should stay approximately the same. The behavior we see in the atmospheres suggests that

$$\frac{d\gamma}{d{\rm [Fe/H]}} > 0\,, \tag{4.3}$$

where $\gamma = \kappa_{\rm vis}/\kappa_{\rm IR}$, as defined in Section 2.2.1. This would cause the strength of the inversions to increase (cf. Figure 2.2). This should only be possible if $\kappa_{\rm vis}$ and $\kappa_{\rm IR}$ (and the molecular abundances giving rise to these opacities) do not just simply scale linearly with metallicity.

In order to test this I checked the abundances of the major absorbers and emitters as a function of metallicity throughout the atmospheres for the P–T structures shown in the middle panel of Figure 4.7. Indeed I found that the ratios of mass fractions $X_{\rm H_2O}/X_{\rm Alkali}$ and $X_{\rm CH_4}/X_{\rm Alkali}$ decreased when the metallicity was increased (see right panel of Figure 4.7). $X_{\rm HCN}/X_{\rm Alkali}$ increases, at the relevant temperatures already being the dominant carbon opacity carrier. However, the increase in $X_{\rm HCN}/X_{\rm Alkali}$ is apparently not enough to act as a counterweight, and cannot compensate the loss of infrared opacity due to the lower $X_{\rm H_2O}/X_{\rm Alkali}$. This leads to less efficient cooling as [Fe/H] increases. This abundance change is likely caused by the pressure dependence of the chemistry, as higher metallicities shift the

temperature structure to smaller pressures, where, for carbon-dominated atmospheres, CH_4 and H_2O are less abundant, while the HCN abundance increases.

Emission spectra

As summarized above, an increase in metallicity (and thus opacity) can be regarded as a pressure rescaling of the atmospheric temperature structure, analogous to the $\log(g)$ case. I argued that for a gray atmosphere with vertically constant opacity κ it holds that $\tau = \kappa/gP$. Because κ is in the numerator, atmospheric structures with increased metallicity should behave similarly to structures with *de*creased surface gravity. Analogous to the case where $\log(g)$ was varied one thus expects the contrast between emission minima and maxima to become less strong as the metallicity decreases. This can be seen in the upper panel of Figure 4.8, and was confirmed by the vertically constant molecular abundance calculations as well, when rescaling the abundances as described above. In summary, more pronounced absorption troughs can mean either a lower surface gravity or a higher metallicity (see figures 4.8 and 4.6).

In the C/O = 1.05 case one can again draw on the studies of the P–T structures: we saw that for atmospheres with inversions, due to the chemistry involved, the cooling ability of the atmospheres relative to the heating by the alkalis decreases if the metallicity is increased (see middle and right panel of Figure 4.7). The spectra shown in the lower panel of Figure 4.8, although they do not exhibit inversions (and thus no emission features), are consistent with these observations: the corresponding atmospheric structures become increasingly isothermal, and so do the spectra, as the metallicity is increased.

4.7 The influence of the atmospheric temperature

4.7.1 Low temperature atmospheres ($T_{\rm eff} \lesssim 1250$ K)

At low enough temperatures ($T_{\rm eff} \lesssim 1250$ K) HCN does not yet play a significant role for the atmospheric spectra. Additionally the left pointing arrow of the chemical reaction in equation (4.1) can still be of importance, meaning that both H_2O and CH_4 are significant carriers of C and O atoms, at the expense of CO. It is important to note, however, that while chemical equilibrium abundances are strongly depending on the temperature, they are also pressure dependent: for increasing pressures CH_4 will become more abundant, in an oxygen-rich atmosphere, while H_2O will become more abundant in carbon-rich atmospheres. At decreasing pressures CO will become increasingly abundant, such that the oxygen-rich atmospheres will contain less methane and the carbon rich ones will contain less water.

As seen in the above discussions, [Fe/H] and $\log(g)$ can strongly influence to which pressure levels the optical depth-dependent temperature structure will be be scaled, as for a gray atmosphere it would hold that $\tau = \kappa/gP$. Therefore, low metallicity atmospheres (causing a small κ) at high surface gravities cause the temperature structure to be scaled to very high pressures. To illustrate this further I show emission spectra of planets with $T_{\rm eff}$ = 1000 K in orbit around a G5 star in Figure 4.9. The spectra are shown for C/O = 0.55 and 1.12

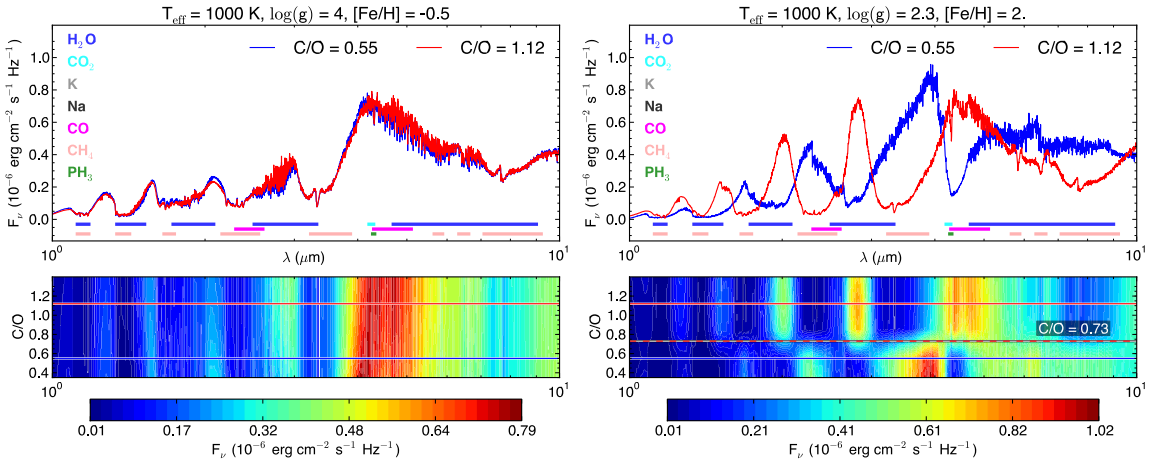

FIGURE 4.9: Atmospheric emission spectra of planets in orbit around a G5 star with $T_{\rm eff}$ = 1000 K. *Left panel:* Planets with $\log(g)$ = 4, [Fe/H] = -0.5. *Right panel:* Planets with $\log(g)$ = 2.3, [Fe/H] = 2. *Upper sub-panels:* Emission spectra as a function of wavelength for planets with C/O = 0.55 (blue solid line) and C/O = 1.12 (red solid line). The absorption bands of dominant absorbers are indicated by the colored bars below the spectra. *Lower sub-panels:* Emission spectra as a function of wavelength (x-axis) and C/O ratio (y-axis). The flux values are indicated as a color map. The red-white dashed horizontal line in the right panel indicates the C/O value where the atmosphere switches from being rich in water to being methane-rich. The corresponding C/O value of this transition is indicated in the plots. The red and blue horizontal lines indicate the C/O values of the wavelength dependent spectra shown in the upper sub-panels. Figure taken from Mollière et al. (2015).

in the upper sub-panels. Furthermore I indicate the positions of absorption features of H_2O, CO_2, K, Na, CO, CH_4 and PH_3 in the plots. The left panel shows the emission spectra for planets with $\log(g)$ = 4, [Fe/H] = -0.5. This means that here the surface gravity is high and the metallicity is low, causing the temperature structures to be scaled to vary high pressures. The right panel shows planets with $\log(g)$ = 2.3, [Fe/H] = 2, i.e. with low surface gravities and high metallicities, leading to temperature structures to be scaled to very low pressures. In the lower sub-panels I show color maps of emission spectra as a function of wavelength (x-axis) and C/O ratio (y-axis).

In the right upper sub-panel, one sees that the two spectra are very different, showing either water or methane features for the atmospheres with C/O =0.5 or 1.12, respectively. As described above, this is expected, corresponding to a low pressure scaling of the temperature structure and due to the pressure dependence of the CO–CH_4–H_2O chemistry. In the lower right sub-panel there is an overall shift from H_2O to CH_4 dominated spectra at C/O $\sim$ 0.73.

In the left panel there is only little difference between the oxygen-rich and carbon-rich case. Further, the lower left sub-panel does not show any transition between a water- and methane-dominated atmosphere, as both molecules are present in the atmospheres at all C/O ratios. This is expected, because in this case, i.e. for low metallicity and high $\log(g)$, the photosphere of the atmosphere is scaled to high pressures, where the chemistry dictates that CO is not the major carbon and oxygen carrier, but instead CH_4 and H_2O dominate, at least at the low atmospheric temperatures considered here. Therefore, although the CH_4/H_2O number ratio may change as a function of C/O, this change is not sufficient to affect the spectrum significantly.

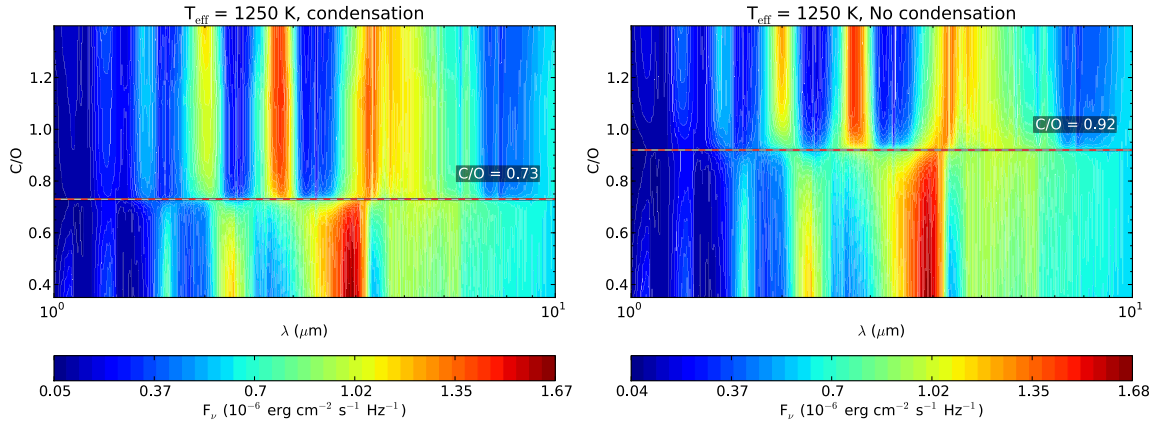

FIGURE 4.10: Emission spectra as a function of wavelength (x-axis) and C/O ratio (y-axis) of planets with $T_{\rm eff}$ = 1250 K, $\log(g)$ = 3, [Fe/H] = 1 in orbit around a G5 star. The flux values are indicated as a color map. The red-white dashed horizontal lines indicate the C/O values where the atmospheres switch from being rich in water to being methane-rich. The corresponding C/O value of this transition is indicated in the plots. *Left panel*: Nominal chemical model (including condensation), *right panel*: Chemical model without condensation. Figure taken from Mollière et al. (2015).

Therefore, the spectral appearance of a planet is not only given by the C/O ratio and the effective temperature but also by a factor

$$\beta = [\mathrm{Fe/H}] - \log(g)\ , \tag{4.4}$$

which is a measure for the optical depth – pressure mapping in the atmospheres and gives insight to which pressure levels a given atmospheric temperature profile $T(\tau)$ is scaled. I found that C/O-dependent transitions between water- and methane rich atmospheres occur at $\beta \gtrsim -4$ or -3.5 for $T_{\rm eff}$ = 1000 K. For $T_{\rm eff}$ = 1250 K I found that $\beta \gtrsim -5.0$, indicating that a transition between water and methane dominated spectra should always be expected at these temperatures. However, values of β close to this threshold should always exhibit some methane or water features, even if the atmosphere is water or methane dominated, respectively.

C/O dependence with and without condensation

For atmospheres with effective temperatures $\lesssim$ 1750 K, the spectrally active parts of the atmosphere have temperatures low enough for the condensation of $MgSiO_3$ to occur (also see, e.g., Ackerman & Marley 2001). This condensation of O in $MgSiO_3$ can shift the C/O ratio-dependent transition between the water or methane-dominated atmospheres, as I explain below.

If an atmosphere has a C/O value in the vicinity to, but less than 1, then the condensation of $MgSiO_3$ decreases the amount of oxygen available to form CO and H_2O considerably. In turn the H_2O features in the spectra will weaken and CH_4 can form in noticeably higher abundances as C atoms are more available due to the lower amount of CO being formed.

This results in shifting the transition from H_2O to CH_4/HCN dominated spectra from C/O = 0.92, which I obtain for atmospheres with $T_{\rm eff} \gtrsim$ 1750 K, to C/O = 0.73 which I obtain for $T_{\rm eff} \lesssim$ 1750 K, as I described in the previous section.

In order to test this condensation dependance further I carried out atmospheric calculations at $T_{\rm eff}$ = 1250 K, neglecting the effect of condensation.

A comparison of the resulting emission spectra as a function of C/O for both cases ($T_{\rm eff}$ = 1250 K, with and without considering condensation) can be seen in Figure 4.10. I calculated atmospheres with C/O ratios spaced equidistantly between 0.35 and 1.4 using 100 grid points for both cases. The difference in location for the shift from water to methane dominated spectra, moving from C/O = 0.73 (condensation) to C/O = 0.92 (no condensation), is very prominent in these plots.

To further verify this finding I plot the mass fractions of H_2O, CH_4, CO and $MgSiO_3$ in Figure 4.11 for an atmosphere with $T_{\rm eff}$ = 1250 K, C/O = 0.8, $\log(g)$ = 3, [Fe/H] = 1 in orbit around a G5 star. The C/O value is chosen such that the atmosphere is water dominated in the model neglecting condensation, but it is methane dominated in our nominal atmospheric model, which includes condensation.

One clearly sees that for high pressures, where the temperatures are too high for $MgSiO_3$ to condense, the abundances of H_2O, CH_4 and CO for both models are nearly identical. The small differences are due to differences in the PT-structures found for the 2 chemical models.

For pressures smaller than 10^2 bar, however, $MgSiO_3$ starts to condense, noticeably decreasing the CO and H_2O abundances. CH_4 becomes much more abundant than H_2O, which is in contrast to the behavior of the model without condensation, where H_2O stays more abundant than CH_4 throughout the atmosphere.

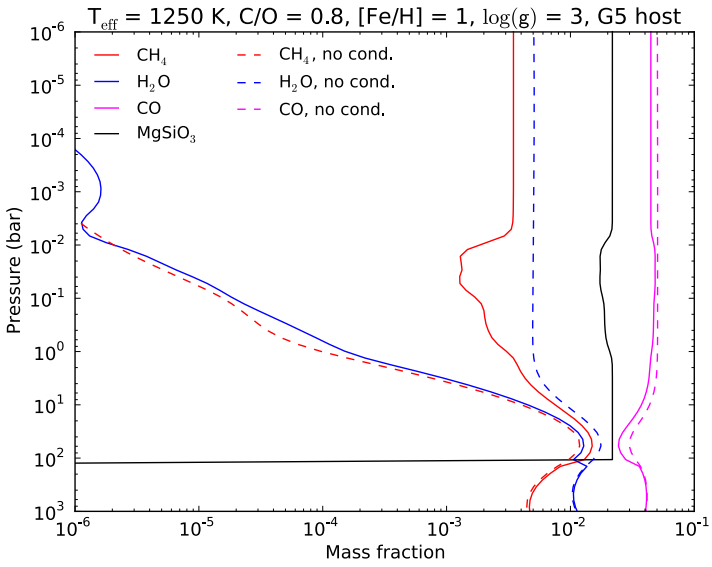

FIGURE 4.11: Mass fractions of components in the atmosphere of a planet with C/O = 0.8, $T_{\rm eff}$ = 1250 K, $\log(g)$ = 3, [Fe/H] = 1 in orbit around a G5 star. The solid lines show the mass fractions of H_2O (blue), CH_4 (red), CO (magenta) and $MgSiO_3$ (black) for our nominal model, including condensation, while the dashed lines show the results for an atmosphere without condensation. Figure taken from Mollière et al. (2015).

I therefore conclude that the transition from water- to methane-rich spectra may occur at C/O ratios considerably smaller than 1 if the planetary effective temperature is not too high. Especially for retrieval analyses of planetary spectra, which measure the local *gas* C/O ratio in the spectrally active regions of the atmosphere, the above findings are relevant. If condensation is expected to occur, a result such as "C/O <1", due to the absence of methane features, could actually indicate an even lower total (gas + condensates) C/O ratio $\lesssim 0.7$. If a given atmosphere were enriched in Mg and Si one would expect this effect to be even stronger, shifting the transition between carbon and oxygen rich spectra to even lower C/O ratios.

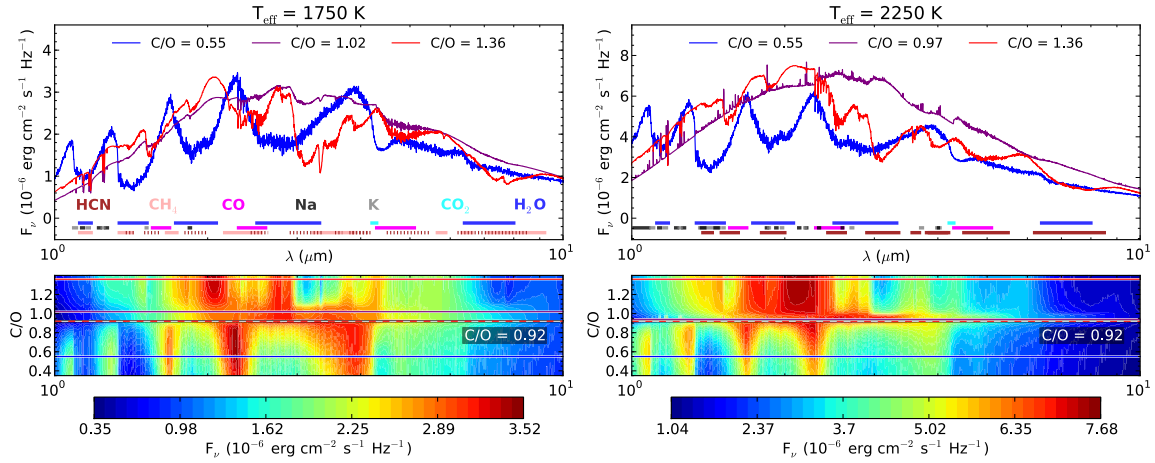

FIGURE 4.12: Plots as shown in Figure 4.9, but for planets with [Fe/H] = 1, $\log(g) = 3$ in orbit around a G5 star. *Left panel:* $T_{\rm eff}$ = 1750 K, *Right panel:* $T_{\rm eff}$ = 2250 K. Figure taken from Mollière et al. (2015).

Finally, one has to keep in mind the simplifications of the chemistry model used in *petitCODE*, which does neither include settling, nor properly accounts for the effects of homogeneous or heterogeneous nucleation (see Section 2.2.5). Furthermore the absence of quenching in our models may be problematic if the timescales for condensation and chemistry in general are longer than the vertical eddy-diffusion timescales. Nevertheless, similar results have been found with much more sophisticated condensation models: Helling et al. (2014b) were able to produce local C/O $\sim$ 1-2 values in the gas phase for an atmosphere with a global C/O = 0.99 due to the condensation of O in dust species. Their model for condensation and cloud formation is much more complete and includes homogeneous and heterogenous nucleation, settling, traces the growth and evaporation of grains, and considers more condensable species than my model.

4.7.2 Inversions at $T_{\rm eff}$ = 1500 K and C/O $\sim$ 1

At $T_{\rm eff}$= 1500 K and C/O $\sim$ 1, condensation can lead to weak inversions in the P–T structures. For C/O ratios $\sim$ 1 the atmospheres are carbon-dominated. At the same time, the atmospheres are still too cool to contain significant amounts of HCN, such that H_2O and CH_4 are the main absorbers and the H_2O–CH_4–CO chemistry is important. While the irradiation is not yet strong enough to cause strong inversions, the occurrence of weak inversions is facilitated by the condensation of SiC. An increased SiC abundance results in a lower abundance of SiO, as less Si is available. The O atoms which are not bound in SiO anymore form more CO and thus decrease the C budget available to form CH_4, therefore decreasing the atmosphere's ability to cool. This effect can be further enhanced by the evaporation of $MgSiO_3$ in the inversion regions, which frees additional O to be put into CO, subsequently locking up more C atoms. As for the atmospheres which have inversions at C/O $\sim$ 1 at higher effective temperatures, the inversions vanish for higher C/O ratios $>$ 1: less oxygen is present to form CO in the first place. Therefore more CH_4 can be formed.

4.7.3 High temperature atmospheres ($T_{\rm eff} \gtrsim 1750$ K)

At high temperatures condensation processes do not play an important role anymore. Therefore, the transition between water and carbon-dominated spectra shifts from C/O = 0.73 to 0.92. Furthermore, the carbon-rich atmospheres become more and more HCN dominated and CH_4 becomes less and less important as the temperature increases. As mentioned before, the chemistry is not only temperature but also pressure-dependent, favoring HCN over CH_4 at high temperatures and low pressures.

- $T_{\rm eff}$ = *1750 K:* at $T_{\rm eff} = 1750$ K, we find that the higher the β-factor (see Equation 4.4) of an atmosphere is, the more HCN dominates the spectrum. Methane features are visible for all βs, however. Due to the chemistry, a low β-factor allows for some presence of water in the carbon-rich atmospheres. Thus at low βs we find a weak water absorption signature imprinted on the rather opacity free region extending from 2.4-3 μm, which is bracketed by two CH_4 features. Because of the strong stellar irradiation the atmospheric structures at C/O $\sim$ 1 become either more isothermal or exhibit inversions. I show spectra of atmospheres with $T_{\rm eff}$ = 1750 K and varying C/O ratios in the left panel of Figure 4.12.

- $T_{\rm eff}$ = *2000 K:* at even higher temperatures HCN becomes more dominant. Inversions at C/O $\sim$ 1 predominantly form for low $\beta <$ -2.5 (or -2) in these atmospheres. For the larger β values the methane features fade away.

- $T_{\rm eff}$ = *2250 K:* for $T_{\rm eff}$ = 2250 K the atmospheres with C/O $>$ 1 are strongly HCN dominated. Only for low β values weak methane features are present. Furthermore, more or less all atmospheres with C/O $\sim$ 1 have inversions if the spectral type of the host star is K or earlier. I show spectra of atmospheres with $T_{\rm eff}$ = 2250 K and varying C/O ratios in the right panel of Figure 4.12.

- $T_{\rm eff}$ = *2500 K:* for $T_{\rm eff}$ = 2500 K the atmospheres with C/O $>$ 1 are completely HCN dominated, and the methane features have vanished. All atmospheres with C/O $\sim$ 1 have inversions if the spectral type of the host star is K or earlier.

4.8 Summary

In this chapter I presented the systematic parameter study of hot jupiter atmospheres which was published in Mollière et al. (2015). In addition to "classical" grid parameters such as metallicity, effective temperature and surface gravity I studied the effects of the atmospheric C/O ratio as well as the host star spectral type. I summarize the key findings of the study in Figure 4.13 and in the text below.

- *At low effective temperatures ($T_{\rm eff} < 1500$ K), depending on their C/O number ratios, the atmospheres can be either water or methane dominated, but not always:* if $\beta = [{\rm Fe/H}] - \log(g)$ is small, the spectra at $T_{\rm eff} \lesssim 1000$ K are quite similar, showing both strong water and methane features. The optical depth (and hence temperature) versus pressure profile

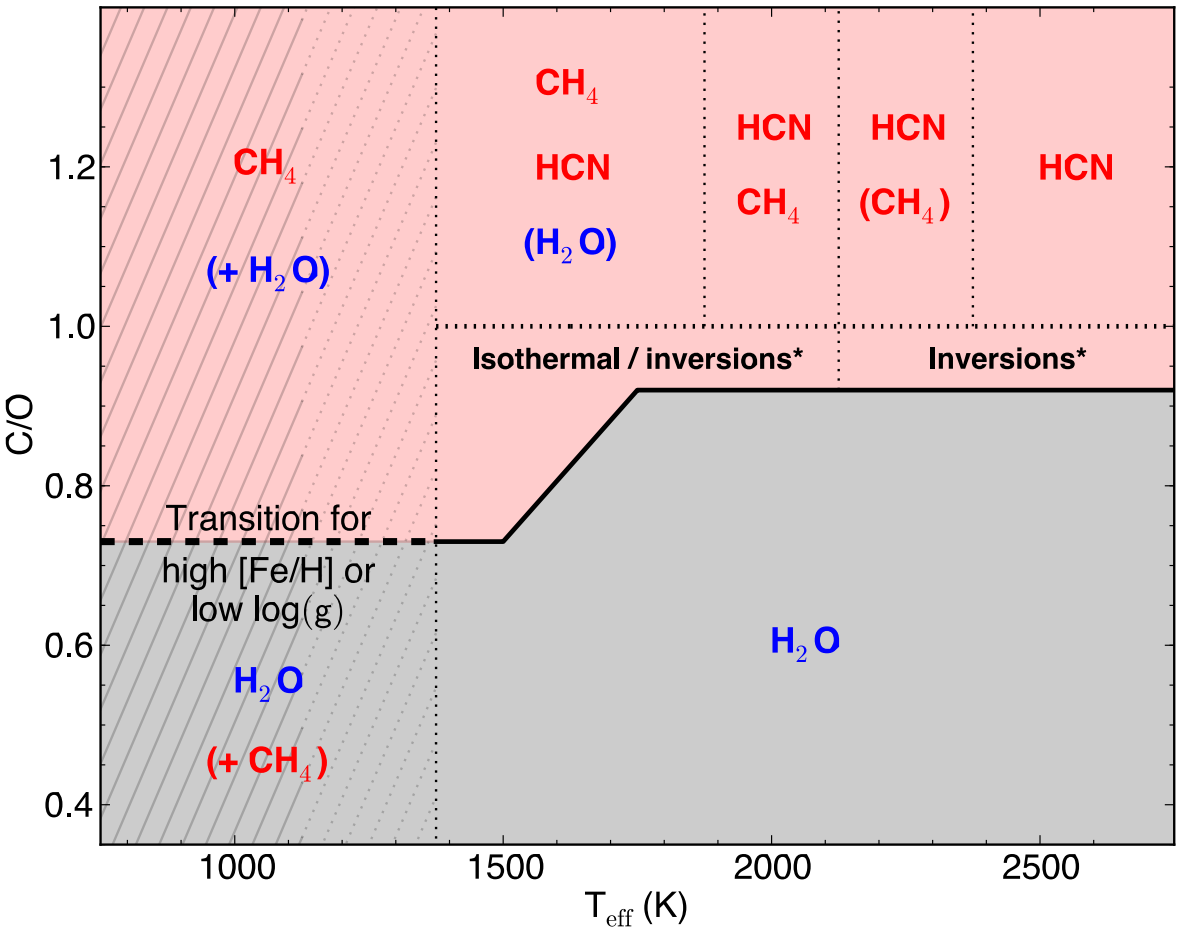

FIGURE 4.13: Dominating IR absorbing/cooling species as a function of $T_{\rm eff}$ and C/O. The red shaded region denotes carbon-dominated atmospheres, whereas the gray shaded region denotes oxygen-dominated atmospheres. The gray-hatched region denotes the temperature range where the atmospheric spectra can be dominated by CH_4 and H_2O at the same time, independent of the C/O value. This occurs if [Fe/H] is low or $\log(g)$ is high. Within each region, defined by the black dotted lines, the dominating IR absorbing/cooling species is indicated. The region in which inversions occur is shown as well. *Only host stars of type K and earlier can cause inversions. Figure taken from Mollière et al. (2015).

scales approximately with β. Hence, a given optical depth (temperature) is reached at high pressure when beta is low and vice versa. It is important to keep in mind, however, that I neglected non-equilibrium chemistry for this grid, which could potentially alter the methane and water mixing ratios. For high pressures and low temperatures CH_4 and H_2O co-exist as the dominant oxygen and carbon opacity carriers, and are both visible in the spectrum. At β values above -4 to -3.5, the atmospheres are either water- or methane-dominated at $T_{\rm eff}$ = 1000 K. For atmospheres with $T_{\rm eff}$ = 1250 K the spectra look similar only for the highest surface gravities ($\log(g) = 5$) and lowest metallicities ([Fe/H] $\lesssim 0$), such that these atmospheres should be either water or methane dominated for most planets.

- *At $T_{\rm eff} \lesssim$ 1500 K the condensation of $MgSiO_3$ is a relevant effect at the local atmospheric temperatures.* The condensation effectively lowers the amount of oxygen which can be put into CO and H_2O, such that more carbon atoms are available to form CH_4. *As a result the atmospheres start to be methane dominated at C/O = 0.73.* For higher temperatures $MgSiO_3$ can no longer condense, shifting the transition from oxygen to carbon

dominated spectral signatures to C/O = 0.92.

- *For planets with $T_{\rm eff} \gtrsim$ 1500 K, and C/O $\sim$ 1, host stars with spectral type earlier than M5 (I considered M5, K5, G5, F5) can lead to temperature inversions in the atmospheres.* The reason for this is that under these circumstances all the main coolants of the atmosphere, H2O, HCN, and CH_4, are depleted, whereas the absorption of optical radiation by the alkali metals remains effective. For $T_{\rm eff} = 1500$ K the condensation of SiC can sufficiently lower the cooling ability, facilitating the development of inversions. For $T_{\rm eff} = 2000$ K all atmospheres with $\beta <$ -2 to -2.5 will exhibit inversions. For $T_{\rm eff} \geq$ 2250 K all atmospheres with C/O $\sim$ 1 exhibit inversions.

- *The lower β = [Fe/H] - $\log(g)$, the more methane-dominated the spectra are at C/O ratios $\gtrsim$1.* At higher temperature and/or higher β values, such planets have HCN-dominated spectra. I show the dominant absorbers as a function of temperature and C/O ratio in Figure 4.13.

- *The host star spectral type is an important factor for the spectral appearance of the atmosphere.* For planets with C/O $\sim$ 1 host stars of spectral type K or earlier can give rise to inversions if the planets are at small enough orbital distances, whereas for M-type host stars inversions do not occur. Further, the later the host star spectral type, the more isothermal the planetary atmospheres become (if the C/O ratio is not $\sim$ 1). This is because the SED of the stellar irradiation becomes increasingly similar to the planetary radiation field, such that both the effective opacities for both radiation fields become similar. Hence neither strong greenhouse heating nor inversion formation occurs.

- *Planetary metallicity and surface gravity determine the location of the planetary photosphere.* High surface gravities or low metallicities will shift it to larger pressures, whereas low surface gravities or high metallicities shift it to low pressures. Because the molecular and atomic line wing strength, as well as the CIA opacities, scale approximately linearly with pressure, for photospheres at low pressures the contrast between opacity minima and maxima increases, such that the flux in the respective wavelength regions is stemming from atmospheric regions further apart, with a larger temperature difference. This leads to a larger contrast between the flux minima and maxima. The deep isothermal temperature increases in these cases of low pressure photospheres, as the insolation can probe, comparatively, deeper into the atmospheres. Similar results for the surface gravity dependence of the emission spectral contrasts have also been reported in Sudarsky et al. (2003).

It is interesting to see that at low temperatures the strength of methane or water features does not only depend on the C/O ratio, but also on the pressure level of the photosphere, which can be quantified using the the β factor. For higher temperatures the β factor plays a role as well, as it determines whether CH_4 or HCN dominates the spectra of carbon-rich atmospheres. Also, the occurrence of an inversion at C/O $\sim$ 1 can be tied to the β factor, at least for the atmospheres with $T_{\rm eff} \sim$ 2000 K. Therefore the β factor can be used as a

third dimension to characterize the spectral appearance of an exoplanet, in addition to the effective temperature and the C/O ratio.

Moreover, the fact that the transition from water to methane rich spectra shifts due to the condensation of silicates, which lock up oxygen, is important when carrying out retrieval analyses of planetary atmospheres. The C/O ratio is often measured by taking into account the abundances of only the gaseous carbon and oxygen carrying molecules. This can potentially overestimate the total (gas + condensates) C/O ratio. It is important to note that the condensation model in *petitCODE* is simplified, assuming instantaneous condensation once the saturation vapor pressure is exceeded.

The fact that inversions can potentially occur at C/O ~ 1 is interesting, because we did not require any additional absorbers such as TiO and VO: the absorption of stellar light by the alkali atoms is sufficient. To further study the inversions it is necessary to obtain molecular line lists as complete as possible as the occurrence of the inversions is strongly depending on the atmospheric cooling ability.

5 Forecasting of *JWST* observations

Based on Mollière et al. (2017).

5.1 The *James Webb Space Telescope*'s science objectives

The most exciting observational tool to become available in the coming years is the space-borne *James Webb Space Telescope*, or *JWST*. It consists of a 6.5 m segmented mirror, and instrumentation that allows it to to carry out imaging, but also spectroscopic measurements, ranging from the orange part of the visible (0.6 μm) to the MIR wavelengths at $\sim$ 28 μm (see, e.g., Beichman et al. 2014). Due to its large primary mirror, and large wavelength coverage, *JWST* will be an excellent instrument for exoplanet science, with hoped-for achievements including reliable abundance constraints from the detection of molecular features in the NIR and MIR (in emission and transmission), the measurement of near-continuous phase curves, the unambiguous detection of inversions, the conclusive identification of cloud resonance features, and the detection of Super-Earth atmospheres (see sections 1.4.1 and 1.5)

As mentioned above, one very exciting avenue of *JWST* lies in observing exoplanet transit spectra in the MIR, which may be key (Wakeford & Sing 2015) to identify cloud species which often weaken or even fully blanket the atomic and molecular features in the optical and NIR, see, e.g., GJ1214b (Kreidberg et al. 2014), HD 189733b (Sing et al. 2011), WASP-6b (Jordán et al. 2013) and WASP-12b (Sing et al. 2013). The instrument of *JWST* which will enable such observations is called *MIRI*, and allows to take spectra in the wavelength interval from 5 to 28 μm (Beichman et al. 2014). While it was theorized that muted water features could also be caused by depletion of water (Madhusudhan et al. 2014b), or a general depletion of metals in the atmospheres, evidence nowadays seems to point to the presence of clouds (Sing et al. 2016; Iyer et al. 2016) or a combination of clouds and metal depletion (Barstow et al. 2017; MacDonald & Madhusudhan 2017).

At the same time, the nature of these clouds is still unknown. Depending on the size of the cloud particles, their opacity in the optical and NIR transitions from a Rayleigh slope (for small particles, see the 'cloud opacities' part of Section 2.2.5) to a flat, gray opacity (large particles). The resonance features of possible chemical equilibrium cloud species all lie in the MIR (Wakeford & Sing 2015) such that a distinction between cloud species may only be possible within the MIR region. The formation of clouds and hazes by non-equilibrium processes is another possibility, although hot jupiters, especially, seem to be too hot for the

'classical' case of hydrocarbon hazes (Liang et al. 2004) as well as for newly suggested pathways such as photolytic sulfur clouds (Zahnle et al. 2016).

While the question of the origins of clouds is fundamental, and not yet answered, another important objective of *JWST* is the quantitative abundance estimation in planetary atmospheres, which may be possible in emission in spite of the presence of clouds (see the 'Clouds' part of Section 4.2.1), and may allow to place constraints on a planet's formation history (see 'Open Question' 5 in Section 1.5).

As the launch of *JWST* (currently projected for October 2018) draws nearer, the exoplanet community is in increased need of predictions by both instrument and exoplanet models in order to maximize the scientific yield of observations. The actual performance of *JWST* will only be known once the telescope has been launched and the first observations have been analyzed (Stevenson et al. 2016b). Nonetheless, the modeling efforts of the telescope performance in conjunction with models of exoplanet atmospheres have already been started and include Deming et al. (2009); Batalha et al. (2015); Mordasini et al. (2016). Studies which additionally look into the question of retrievability of the atmospheric properties as a function of the planet-star parameters can be found in Barstow et al. (2015); Greene et al. (2016); Barstow & Irwin (2016). Barstow et al. (2015) also included time-dependent astrophysical noise (starspots) for stitched observations.

This chapter is based on Mollière et al. (2017), in which I presented detailed self-consistent atmospheric model calculations for a set of exoplanets which my collaborators and I identified as prime scientific targets for observations with *JWST*. The target selection was carried out considering the planets' expected signal-to-noise ratio for both transit and emission measurements, putting emphasis on a good SNR for observations with *JWST*'s *MIRI* instrument, to allow measurements in the MIR. The planets uniformly cover the $\log(g)$–$T_{\rm equ}$ parameter space which may also allow prediction of the objects' cloudiness (Stevenson 2016). I calculated a suite of models for every candidate planet and varied the planetary abundances by adopting different values for [Fe/H] and C/O, including very high enrichments (and high mean molecular weights) for super-Earth and neptune-sized planets. For all planets, I additionally calculated models including clouds, setting the free parameters of the cloud models to produce either small or large cloud particles, which I assumed to be hollow spheres, in order to mimic irregularly shaped dust aggregates. Alternatively, I assumed a spherically-homogeneous shape. For the hottest target planets, TiO and VO opacities are optionally considered. The irradiation is treated as either assuming a dayside or global average of the received insolation flux. For some very hot planets I additionally calculated emission spectra neglecting any energy redistribution by winds.

For all target planets, I calculated synthetic emission and transmission spectral observations for the full *JWST* wavelength range and compared them to any existing observational data.

Following the study published in Mollière et al. (2017), I present an exemplary analysis for a subset of the targets. To this end, I selected three specimen belonging to the classes of extremely cloudy super-Earths, intermediately irradiated gas giants, and extremely hot,

strongly irradiated gas giants, respectively. I discuss how *JWST* may shed light on the nature of these planetary classes, by detecting molecular features in the NIR transmission spectra for cloudy super-Earths, or by identifying cloud resonance features in the MIR for hot jupiters. For the hottest planets I study how well *JWST* can distinguish between various models which individually fit well to the data currently available.

For all targets, I published the atmospheric structures, spectra, and simulated observations online. These results can help to facilitate the prediction of the expected signal quality of existing prime exoplanet targets for *JWST*.

The calculations were carried out with the full version of *petitCODE*, as described in Chapter 3. This means that scattering and clouds were included, as well as a sub-Lorentzian treatment for all line opacities (see Section 3.3.1). The chemical abundances were obtained using my self-written Gibbs minimizer.

The simulated *JWST* observations were carried out with the *EclipseSim* package (van Boekel et al. 2012). For this I considered observations in the *NIRISS* (Doyon et al. 2012), *NIRSpec* (Ferruit et al. 2012), and *MIRI* instruments (Wright et al. 2010). The length of each observation is taken to be the full eclipse duration, bracketed by 'baseline' observations before and after the eclipse, which each have a duration of the eclipse itself.

The synthetic observations where carried out at the instrumental resolution. For the *NIRISS* instrument I used the slit-less spectroscopy (*SOSS* mode) in first order. For *NIRSpec*, I used the *G395M* mode, and for *MIRI* the *LRS* mode. Using these modes, one obtains a close to complete spectral coverage between 0.8 and 13.5 microns. However, since *JWST* can only observe in one instrument at a time, one needs three separate observations to obtain the complete spectral coverage. More information on the instrument characteristics is given in Section 5.5.

This chapter is organized as follows: in Section 5.2, the candidate selection criteria and target list are described. In Section 5.3 I describe which parameter setups were considered for the planets. This is followed by a general characterization of the results in Section 5.4. Next, I analyze the synthetic observations of a selected subsample of targets in Section 5.5. Finally I summarize the results in Section 5.6.

5.2 Exoplanet target identification

5.2.1 Candidate selection criteria

In order to obtain a list of well observable candidates, we only considered planets for which the transit times are known accurately. As an additional criterion, we checked if a candidate is observable in transmission and/or emission with signal amplitude (at 7 μm) of SNR $>$ 5, where the noise is assumed to be photon noise + a 50 ppm noise floor. For this initial check we approximated the planetary emission using a blackbody spectrum, whereas for the transmission signal we assumed a transit signal amplitude of five pressure scale heights.

This initial analysis results in a large number of possible targets, given the wealth of transiting exoplanets known already today. In order to maximize the scientific yield of the

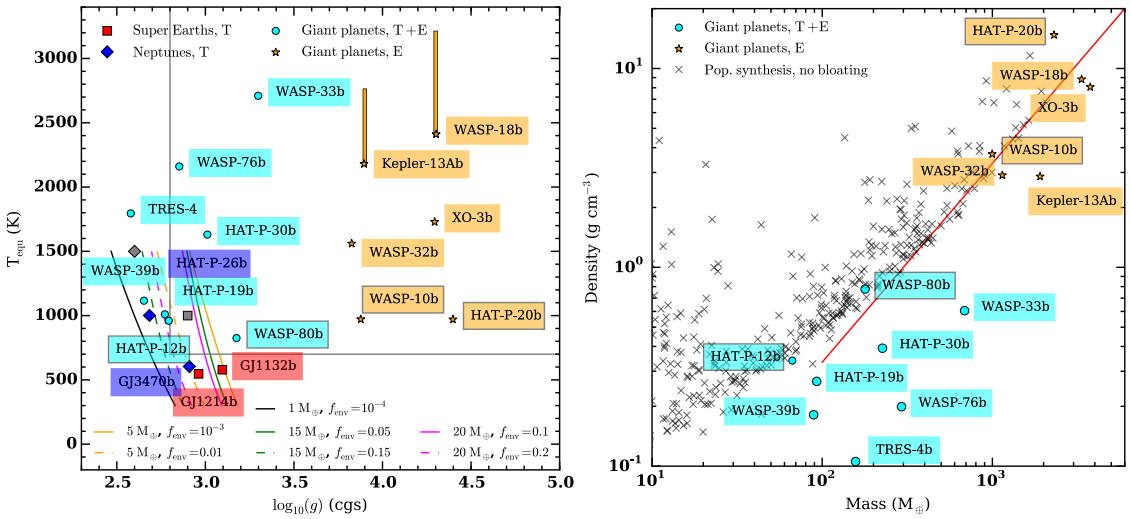

FIGURE 5.1: *Left panel:* Transit candidates in $\log(g)$–$T_{\rm equ}$ space. See the legend for the meaning of the symbols. Candidates with gray symbols are artificial and have been introduced to fill in the parameter space. 'T' and 'E' in the legend stand for planets which can be observed in transmission or emission, respectively. The vertical and horizontal lines separate the mostly cloud-free (upper right region) from the potentially cloudy atmospheres (left and bottom regions) as defined in Stevenson (2016). The black, orange, green, and magenta lines show $\log(g)$–$T_{\rm equ}$ curves of super-Earths and Neptune-like planets (Lopez & Fortney 2014) for the masses and envelope mass fractions as described in the legend. The giant planets which have a gray frame around their name box are not inflated. The upper ends of the vertical orange lines shown for Kepler-13Ab and WASP-18b denote the maximum brightness temperatures observed for these planets. *Right panel:* Planetary mean density as a function of mass. Only the giant planet candidates are plotted here, in the same style as in the left panel. A sample of synthetic, non-inflated planets calculated using the model of Mordasini et al. (2012); Alibert et al. (2013); Jin et al. (2014) is shown as gray crosses. The value of the straight red line shown in the model is a linear function of the planetary mass, as is expected for non-inflated giant planets (see, e.g., Baruteau et al. 2016). Figures adatpted from Mollière et al. (2017).

first *JWST* observations, it may be instructive to first observe a planetary sample as diverse as possible and to embark on more detailed studies within a given planetary class later on. Thus, the goal pursued here was to define such a diverse target list, and to map out the parameter space defining different planetary classes as well as possible.

The main physical parameter space for candidate selection presented here is the $\log(g)$–$T_{\rm equ}$ space. This space is quite fundamental in the sense that the equilibrium temperature and the planetary surface gravity are two key parameters impacting the pressure temperature structure and spectral appearance of a planet (see, e.g., Sudarsky et al. 2003; Mollière et al. 2015, and the adaptation of the latter in Chapter 4). The total atmospheric enrichment can be of importance too, but for scaled solar compositions variations of $\log(g)$ and [Fe/H] are degenerate to some degree (again, see Mollière et al. 2015, and its adaptation in Chapter 4). Additionally, for every target planet, I present calculations assuming a larger or smaller enrichment than used in the fiducial case. Further, a planet's location in the $\log(g)$–$T_{\rm equ}$ space may allow to assess if the planet is cloudy or not (see Stevenson 2016). I aimed for a broad coverage of candidates in this parameter space.

In addition, I divided the candidates into super-Earths, hot neptunes, and inflated and non-inflated giant planets and tried to select a sample as diverse as possible, still above observational thresholds described above, however.

The final selection is shown in the left panel of Figure 5.1. For the super-Earths and hot Neptunes, I only found four candidates in total, two for each class. In order to estimate the region usually occupied by these two classes of planets, I overplotted $\log(g)$–$T_{\rm equ}$ lines for

super-Earths and hot neptunes of varying mass and envelope fraction (taken from Lopez & Fortney 2014). I added two more hot, artificial candidates, one for the neptunes and one for the super-Earths, to increase the coverage in $\log(g)$–$T_{\rm equ}$ space. I cannot introduce even hotter artificial super-Earths or Neptunes, because their envelopes would likely be evaporated (Jin et al. 2014).

The giant planets were divided into inflated giant planets, non-inflated giant planets, and inflated giant planets associated to non-inflated giant planets. This association means that the inflated planets are lying close to the non-inflated ones in $\log(g)$–$T_{\rm equ}$ space, but are inflated. It is known that whether or not inflation occurs is correlated to irradiation strength and thus $T_{\rm equ}$ (see, e.g. Laughlin et al. 2011; Demory & Seager 2011, and Section 1.3.2). Therefore, such close neighbors in $\log(g)$–$T_{\rm equ}$ space, showing inflation or no inflation, may potentially shed light on the mechanisms driving inflation. To assess whether or not a giant planet is inflated, I show the density of all candidates as a function of their mass in the right panel of Figure 5.1. I also plot a synthetic planetary population, calculated using the planet formation and evolution code of Mordasini et al. (2012); Alibert et al. (2013); Jin et al. (2014), which does not include any inflation processes. All planets that have a density lower than the one shown for the synthetic giant planets were considered to be inflated.

5.2.2 List of selected candidates

The parameters of the exoplanet targets modeled in this paper are given in Table 5.1.

For the super-Earths I included an artificial planet with a mass of 5 $\rm M_\oplus$, placed at a distance of 0.1 AU around a sun-like star, which corresponds to a planetary equilibrium temperature of 880 K. I assumed an initial H–He envelope mass fraction of 1% of the planet's total mass. Calculations by Jin et al. (2014) indicate that such a planet loses approximately half of its envelope in the first 20 Myr of its lifetime, therefore we calculate the radius of the planet using the relation by Lopez & Fortney (2014) for a 5 $\rm M_\oplus$ planet with a 0.5 % envelope fraction at an age of 20 Myr. At later times, the envelope of such a planet will be evaporated even further, therefore the high enrichment I assume for its atmosphere (see Section 5.3) may also be seen as a proxy for a secondary atmosphere with a high mean molecular weight. Note that photo-evaporation is not included in the calculations of Lopez & Fortney (2014). I refrained from considering even hotter super-Earth planets, because more strongly irradiated planets will be more strongly affected by photo-evaporation such that the primordial planetary H–He envelope may not survive.

For the Neptunes, I considered an artificial object with a mass of 20 $\rm M_\oplus$, in orbit around a sun-like star, with a semi-major axis of 0.05 AU, corresponding to an effective temperature of 1250 K. The H–He envelope mass fraction was taken to be 15%. Again, I consulted Jin et al. (2014) and found that such a planet may retain a significant amount of its envelope up to 100 Myr and longer.

The parameters for the artificial planets listed in Table 5.1 were again obtained using Lopez & Fortney (2014).

Planet name	M_{Pl} ($\mathrm{M}_{♃}$)	M_{Pl} ($\mathrm{M}_{\oplus}$)	R_{Pl} ($\mathrm{R}_{♃}$)	$\log_{10}(g_{\mathrm{Pl}})$ (cgs)	$T^{\mathrm{f}}_{\mathrm{equ}}$ (K)	[Fe/H]$_*$	[Fe/H]$^{\mathrm{fid}}_{\mathrm{Pl}}$	Similar planets	Obs. References
Super-Earths									
GJ 1132b	0.01	1.62	0.1	3.1	579	-0.12	3$^{\mathrm{a}}$	–	–
GJ 1214b	0.02	6.36	0.24	2.96	547	0.39	3$^{\mathrm{a}}$	–	(1.1-7)
Artificial$^{\mathrm{b}}$	0.02	5	0.29$^{\mathrm{c}}$	2.67	880	0.00	3$^{\mathrm{a}}$	–	–
Neptunes									
GJ3470b	0.04	13.9	0.37	2.91	604	0.17	1.98	HATS-6b$^{\mathrm{d}}$	(2.1-6)
HAT-P-26b	0.06	18.59	0.56	2.68	1001	0.01	1.56	–	(3.1)
Artificial$^{\mathrm{b}}$	0.06	20	0.65$^{\mathrm{c}}$	2.45	1250	0.00	1.51	–	–
Gas giants									
WASP-80b	0.56	178.62	0.99	3.18	825	-0.14	0.60	HAT-P-17b	(4.1-3)
HAT-P-12b	0.21	66.74	0.94	2.79	960	-0.29	0.75	WASP-67b, HAT-P-18b	(5.1-5.4)
WASP-10b	3.14	997.98	1.04	3.88	972	0.05	0.27	WASP-8b$^{\mathrm{e}}$	(6.1)
HAT-P-20b	7.25	2302.98	0.87	4.4	970	0.35	0.32	–	(7.1)
Inflated giants									
TrES-4b	0.49	157.01	1.84	2.58	1795	0.28	1.1	WASP-17b, WASP-94b, WASP-79b	(8.1-5)
WASP-33b	2.16	686.51	1.68	3.3	2734	0.1	0.44	WASP-12b	(8.5), (9.1-5)
HAT-P-30b	0.71	225.98	1.34	3.01	1630	0.12	0.80	WASP-7b	(10.1)
Kepler-13Ab	6.0	1906.97	1.41	3.9	2180$^{\mathrm{f}}$	0.2	0.23	–	(11.1)
WASP-32b	3.6	1144.18	1.18	3.83	1560	-0.13	0.05	CoRoT-2b, WASP-43b	(12.1)
WASP-18b	10.52	3343.55	1.16	4.3	2411$^{\mathrm{f}}$	0.1	-0.04	–	(13.1)
XO-3b	11.83	3759.9	1.25	4.29	1729	-0.18	-0.35	HAT-P-2b	(14.1-2)
WASP-76b	0.92	292.4	1.83	2.85	2160	0.23	0.84	WASP-48b, KELT-7b, WASP-82b	–
HAT-P-19b	0.29	92.81	1.13	2.77	1010	0.23	1.22	WASP-69b	(6.1), (15.1)
WASP-39b	0.28	88.99	1.27	2.65	1116	-0.12	0.84	–	(5.4), (6.1), (16.1-2)

TABLE 5.1: High priority targets for which we simulate spectra in this study. Note that for the planets listed in the 'similar planet' column, the planetary masses usually agree relatively well with our target masses, therefore the enrichment (as estimated by Equation 5.1) may be similar. Note that the planetary enrichment is also linearly dependent on the host star's metallicity, however. Footnotes: (a): For these planets the metal mass fraction as estimated by Equation 5.1 was larger than 1, therefore we imposed a maximum metallicity value of 3. Additionally the calculations with enrichments ten times larger than the fiducial case, which would lead to a metallicity value of 4, have been neglected for these planets. (b): These planets are artificial candidates in order to fill in the T_{equ}–$\log(g)$ parameter space. (c): The artificial super-Earth and hot Neptune have relatively large radii because we assumed their ages to be 20 and 100 Myr for the super Earth and Neptune-like planet, respectively. At later ages they would be too strongly affected by envelope evaporation. (d): HATS-6b is much more massive than GJ 3470b. Therefore, only the metal depleted case ("FEH_m_1") of GJ3470b in our calculations is comparable to what we would estimate for HATS-6b. (e): WASP-8b is highly eccentric ($e = 0.31$). (f): The equilibrium temperatures given in this table correspond to the values derived from the stellar and orbital parameteres, i.e. $T_{\mathrm{equ}} = T_* \sqrt{R_*/2a}$, where T_* is the stellar effective temperature, R_* the stellar radius and a the planet's semi-major axis. Note that Kepler-13Ab and WASP-18b have emission brightness temperatures hotter than even the dayside averaged effective temperatures. For these planets calculations at even higher temperatures were carried out, see Section 5.3.5 for more information. References for observational data: (1.1): Bean et al. (2010), (1.2): Désert et al. (2011), (1.3): Bean et al. (2011), (1.4): Berta et al. (2012), (1.5): Fraine et al. (2013), (1.6): Kreidberg et al. (2014), (1.7): Cáceres et al. (2014), (2.1): Crossfield et al. (2013), (2.2): Demory et al. (2013b), (2.3): Nascimbeni et al. (2013), (2.4): Biddle et al. (2014), (2.5): Ehrenreich et al. (2014), (2.6): Dragomir et al. (2015), (3.1): Stevenson et al. (2016a), (4.1) Fukui et al. (2014), (4.2) Mancini et al. (2014), (4.3) Triaud et al. (2015), (5.1): Line et al. (2013a), (5.2): Todorov et al. (2013), (5.3): Mallonn et al. (2015a), (5.4): Sing et al. (2016), (6.1): Kammer et al. (2015), (7.1): Deming et al. (2015), (8.1): Knutson et al. (2009), (8.2): Chan et al. (2011), (8.3): Ranjan et al. (2014), (8.4): Sozzetti et al. (2015), (8.5): Turner et al. (2016), (9.1): Smith et al. (2011), (9.2): Deming et al. (2012), (9.3): de Mooij et al. (2013), (9.4): Haynes et al. (2015), (9.5): von Essen et al. (2015), (10.1) Foster et al. (2016), (11.1): Shporer et al. (2014), (12.1) Garland et al. (2016), (13.1): Nymeyer et al. (2011), (14.1): Wong et al. (2014), (14.2): Machalek et al. (2010), (15.1): Mallonn et al. (2015b), (16.1): Fischer et al. (2016), (16.2): Ricci et al. (2015)

5.3 Target parameter choice

For every target identified in Section 5.2.2, and modeled in Section 5.4, I calculated a fiducial model, and then varied five parameters within a parameter space, which I will describe in the following. The parameters that are studied are the atmospheric enrichment (see Section 5.3.1), clouds (Section 5.3.2), the C/O number ratio (Section 5.3.3), the inclusion of optical absorbers in the form of TiO/VO (Section 5.3.4), and the redistribution of the stellar irradiation energy (Section 5.3.5).

5.3.1 Atmospheric enrichment

The analysis of the radii of known, cool ($T_{\rm equ} < 1000$ K) exoplanets using planetary structure models suggests that the planets' enrichment in heavy elements, $Z_{\rm Pl}$, is proportional to the host stars' metal enrichment Z_*. The ratio $Z_{\rm Pl}/Z_*$ is a function of the planetary mass and decreases with increasing planetary mass (Miller & Fortney 2011; Thorngren et al. 2016). A fit of the function,

$$\frac{Z_{\rm Pl}}{Z_*} = \beta \left(\frac{M_{\rm Pl}}{\mathrm{M}_{\mathrm{Jup}}} \right)^{\alpha} , \tag{5.1}$$

to the sample of planets investigated in Miller & Fortney (2011) yields $\alpha = -0.71 \pm 0.10$ and $\beta = 6.3 \pm 1.0$ (Mordasini et al. 2014). In the same paper, (Mordasini et al. 2014) fit the results of a synthetic population of planets formed via the core accretion paradigm and find $\alpha = -0.68$ and $\beta = 7.2$, which fits the observational data, and the Solar System ice and gas giants. A comprehensive summary of observational evidence further backing the finding that lower-mass planets are more heavily enriched than more massive planets can be found in Mordasini et al. (2016).

An important question asks to what extent the metal content of the planet is mixed into its envelope and atmosphere. It is suggested that for Saturn, nearly all metals are locked into the central core, whereas for Jupiter the metals appear to be fully mixed into the envelope (Fortney & Nettelmann 2010). In my fiducial models, I assume planets where half of the metal enrichment is mixed into the planet's envelope and atmosphere.

For the fiducial models of the planets whose atmospheres I simulated, I thus used Equation 5.1 to describe the atmospheric enrichment, taking into account an additional factor 1/2 to relate the atmospheric enrichment to the planetary bulk enrichment. I take the host star's [Fe/H] as a proxy for the stellar enrichment.

Additionally, I consider models with ten times more or less metal enrichment than in the fiducial model.

5.3.2 Clouds

For every planet I consider nine different cloud model parameter setups in order to test a broad range of possible cloud properties. These setups are listed in Table 5.2.

Models 1 and 2 use the Ackerman & Marley (2001) cloud model to couple the effect of clouds self-consistently with the atmospheric temperature iteration (see my description and derivation of the Ackerman & Marley (2001) model in Section 3.5.1). The values for

Model	Shape	$f_{\rm sed}$	σ	$X_{\rm max}$ ($Z_{\rm Pl}$)	a (μm)	Fe	SCC
1	DHS	3	2	–	–	yes	yes
2	DHS	1	2	–	–	yes	yes
3	DHS	0.3	2	–	–	yes	yes/no
4	DHS	0.01	2	–	–	yes	yes/no
5	DHS	–	–	10^{-2}	0.08	no	yes
6	DHS	–	–	3×10^{-4}	0.08	no	yes
7	DHS	–	–	3×10^{-5}	0.08	no	yes
8	DHS	–	–	3×10^{-4}	0.08	yes	yes
9	Mie	–	–	3×10^{-4}	0.08	no	yes

TABLE 5.2: Cloud models studied for all planetary candidates listed in Table 5.1. The "shape" column describes whether the grain opacities are described assuming irregular grains (using DHS) or as homogeneous, spherical grains (using Mie theory). $f_{\rm sed}$ is the standard settling parameter from the Ackerman & Marley (2001) cloud model and σ is the width of the log-normal particle size distribution function in this model. Note that the value of $\sigma = 1$ formally corresponds to a Dirac delta function. For the parametrized cloud model $X_{\rm max}$ describes the maximum cloud mass fraction within the atmosphere, while a denotes the mono-disperse particle size. "Fe" denotes whether iron clouds have been included. The column "SCC" ("self-consistent coupling") denotes whether the cloud opacities have been coupled to the atmospheric temperature iteration or whether the converged, cloud-free atmospheric temperature structure has been used to obtain spectra including clouds. Note that for GJ 1214b, for example, models 3 and 4 converged with self-consistent coupling.

the settling parameter $f_{\rm sed}$, which is the ratio of the mass averaged grain settling velocity and the atmospheric mixing velocity, have been adopted covering the lower range of what is typically being used for brown dwarfs ($f_{\rm sed}$ = 1-5, see Saumon & Marley 2008; Morley et al. 2012), and I use $f_{\rm sed} = 1, 3$ here. Further, I account for the fact that Earth's high altitude clouds are well described using small $f_{\rm sed} < 1$ values, i.e. more vertically extended clouds, and that the flat transmission spectrum of GJ 1214b is best described using $f_{\rm sed} \ll 1$ (Ackerman & Marley 2001; Morley et al. 2013, 2015). I therefore use such small $f_{\rm sed}$ value cloud setups in models 3 and 4, namely $f_{\rm sed}$ = 0.3 and 0.01. Similar to Morley et al. (2015), I find that for the cases with small $f_{\rm sed} < 1$, with the planets often being quite strongly enriched, it can be challenging to obtain converged results when self-consistently coupling the cloud model to the radiative-convective temperature iteration. Thus, for cloud model setups 3 and 4, I follow a two-pronged approach: first, I attempt to calculate the atmospheric structures self-consistently, and if this does not succeed I follow Morley et al. (2015) and calculate cloudy spectra for these two model setups using the temperature structure of the fiducial, cloud-free model.

For the cases where the cloud models 3 and 4 converged, and for all other cloud models considered here, the clouds are coupled to the atmospheric structure iteration self-consistently. For, GJ 1214b, for example, which has an enrichment of 1000 $\times$ solar in my fiducial setup, the structures for cloud models 3 and 4, with self-consistent coupling, converged. I look at this planet in greater detail in Section 5.5.1. For cases for which the self-consistent coupling between cloud models 3 and 4 and the temperature iteration converged, I compared the resulting spectra to the calculations which applied models 3 and 4 to the cloud-free temperature structure. I found that the transmission spectra can agree quite well but may be offset due to different temperatures in the atmospheres. If the atmospheric temperatures are close to a chemically important temperature range (e.g. close to the temperature where carbon gets converted from methane (lower temperatures) to CO (larger temperatures)), the

transmission spectra can be quite different, with the cooler, not self-consistently coupled atmospheres exhibiting methane features which the self-consistent atmospheres lack. Analogously, emission spectra may share a similar spectral shape (not in all cases, due to the same reasons as outlined above for transmission spectra) but have a different flux normalization: The self-consistent models 3 and 4 conserve the flux, while the post-processed cloud calculations, simply applying clouds to the clear atmospheric structures for the spectra, do not.

My implementation of the Ackerman & Marley (2001) cloud model differs from the version described in the original paper in two ways: (i) I account for vertical mixing induced by insolation (see Appendix A.2.3). A similar approach was taken for GJ 1214b in the study by Morley et al. (2015). (ii): the mixing length in my cloud model implementation is equal to the atmospheric pressure scale height, while in the Ackerman & Marley (2001) model the mixing length in the radiative layers is up to ten times smaller than the atmospheric pressure scale height. This means that for a given $f_{\rm sed}$ value, the *petitCODE* clouds will be more extended, because the cloud density above the cloud deck is proportional to $P^{f_{\rm sed}/\lambda}$, where λ is the ratio of the mixing length $l_{\rm mix}$ divided by the pressure scale height H_P (cf. Equation 3.90). Further, the mixing velocity is equal to $K_{zz}/l_{\rm mix}$, where K_{zz} is the atmospheric eddy diffusion coefficient, meaning that for a given $f_{\rm sed}$ value, the *petitCODE* grains will be smaller. Both effects effectively lower the $f_{\rm sed}$ value in *petitCODE* when compared to the Ackerman & Marley (2001) value. When comparing my cloud model implementation with the Ackerman & Marley (2001) implementation in Appendix B.7 for verification purposes, I used the same $l_{\rm mix}$ choice as they did.

For models 5 to 9 in Table 5.2, I use my simple three-parameter cloud model as introduced in Section 3.5.2, which corresponds to vertically homogeneous clouds. Its cloud mass fractions per species are equal to the values derived from equilibrium chemistry, but not larger than $X_{\rm max} = 10^{-2} \cdot Z_{\rm Pl}$, $3 \times 10^{-4} \cdot Z_{\rm Pl}$ or $3 \times 10^{-5} \cdot Z_{\rm Pl}$, where $Z_{\rm Pl}$ is the atmospheric metal mass fraction. As said in Section 3.5.2, $X_{\rm max}$ can be thought of as a proxy for the settling strength, where smaller $X_{\rm max}$ values correspond to a stronger settling. The cloud particle radius for all grains in these models is fixed at 0.08 μm, with a mono-disperse size distribution. For the standard setup of these clouds the contribution of iron clouds was neglected. Only condensed species that can exist in thermochemical equilibrium within the atmospheric layers were considered, and only if the condensation-evaporation boundary was within the simulated domain. For every species, only a single cloud layer is allowed, implicitly assuming that the lowest possible cloud layer for a given species traps the cloud forming material.

I introduced the parametrized cloud model because I found that it is only possible to reproduce the steep Rayleigh slope observed for some hot Jupiters from the optical to the near IR (to $\sim$ 1.3 μm, see Sing et al. 2016) if one places small cloud particles within the radius range ($\sim$0.06 to 0.12 μm) in the high layers of the atmosphere. While the upper particle radius boundary results from the requirement of having a Rayleigh-like scattering opacity down to optical wavelengths, the lower radius boundary results from the requirement of

having a Rayleigh-like extinction out to the NIR. For Mg_2SiO_4, I found that the NIR extinction would become flatter for particles smaller than 0.06 μm, because of absorption and scattering. Similar ($\sim$ 0.1 μm) particle sizes have been found by Pont et al. (2013); Lee et al. (2014); Sing et al. (2015), who report that they need small cloud particles at high altitudes with sizes between 0.02 and 0.1 μm to reproduce the strong Rayleigh signal observed in the optical and UV of the planets HD 189733b and WASP-31b. The need for submicron-sized cloud particles in hot jupiters has recently also been pointed out by Barstow et al. (2017), at least in certain equilibrium temperature ranges. Pont et al. (2013) and Lee et al. (2014) find that this small particle cloud layer may be homogeneous over multiple scale heights in HD 189733b. Lee et al. (2014) analyzed HD189733b by retrieving the cloud properties (size and optical depth) and molecular abundances and found that the need for small (< 0.1 μm) cloud particles is a robust finding, independent from variations of the planet's radius, terminator temperature and cloud condensate species. Moreover, this small cloud particle size is consistent with the lower boundary of grain sizes derived in Parmentier et al. (2016) when studying the optical phase curve offsets of hot jupiters.

Iron clouds are neglected for the cloud models 5-7 and 9 because the strongly absorbing nature of iron in the optical does not allow for the dominance of Rayleigh scattering. For illustrative reasons, the case where iron opacities are included in the small particle regime has been studied in model 8.

For the cool super-Earths, Neptunes, and coolest planets in general (GJ 3470b, HAT-P-26b, GJ 1214b, GJ 1132b and WASP-80b), only Na_2S and KCl are considered as possible cloud species, because it is doubtful that higher temperature condensates can be mixed up from the deep locations of their cloud decks (Charnay et al. 2015a; Parmentier et al. 2016). For the planets that are only slightly hotter (WASP-39b, HAT-P-19b, HAT-P-12b, WASP-10b and HAT-P-20b), I considered both cases using either the full condensate or only the Na_2S and KCl condensate model, where the models including only Na_2S and KCl may be more appropriate in this temperature regime.

Spherical or irregularly shaped cloud particles?

As the standard scenario, the cloud particles are assumed to be irregularly shaped dust aggregates, which are described using the Distribution of Hollow Spheres method (DHS, also see the 'Cloud opacities' parts in sections 2.2.5 and 3.3.2). This is in contrast to the case of homogeneous spheres in Mie theory. I investigate the effect of Mie opacities as a non-standard scenario in cloud model 9. Only the small cloud particle case is studied with Mie theory, as only then may differences between DHS and Mie in the cloud resonance features be seen: for larger particles the cloud opacity is gray for both the DHS and Mie treatment, without any observable features.

As outlined in the 'Cloud opacities' part in Section 2.2.5, the use of Mie theory is a standard approach for cloud particles in brown dwarf / exoplanet atmospheres. This is a useful starting point to assess the first-order effect of clouds on planetary structures and spectra. However, in all cases where crystalline features of silicate grains have been observed in an

astrophysical context so far, it was found that the opacity of Mie grains poorly fits the observations and that methods such as DHS lead to a better agreement (see the 'Cloud opacities' part in Section 2.2.5). Given the observational evidence in different astrophysical scenarios, I therefore chose the DHS treatment of grains as the standard scenario. For brown dwarfs, an explicit detection of a cloud feature is still missing (although tentative evidence exists, see Cushing et al. 2006), and the transmission spectra of planets have so far only probed the (often cloudy/hazy) optical and NIR regions, which are devoid of cloud resonance features because these lie primarily in the MIR.

Crystalline or amorphous cloud particles?

For the planets studied in this work I assumed crystalline cloud particles, rather than amorphous ones, as long as the corresponding optical data are available. This is a very important difference because crystalline cloud particles will have quite sharply peaked resonance features in the MIR (resolvable at $R \sim 50$), while amorphous particles have much broader resonance features.

The assumption of amorphous cloud particles in exoplanets may be unphysical, because the high temperatures under which cloud formation occurs should lead to condensation in crystalline form and/or annealing (Fabian et al. 2000; Gail 2001; Harker & Desch 2002; Gail 2004). The cloud is always in contact with high-temperature regions close to the cloud base. Hence, even particles that may form in higher and cooler layers above the cloud base should experience annealing due to mixing and/or settling to hotter regions of the atmosphere, if they did not condense in crystalline form in the first place.

The fact that most silicates are present in amorphous form in the ISM is commonly attributed to the 'amorphization' of crystalline silicate grains by heavy ion bombardment, where the grains have been injected into the ISM by outflows of evolved stars in crystalline form (Kemper et al. 2004). Because such processes are unlikely to occur in planetary atmospheres, the assumption of crystalline particles may represent a better choice than amorphous particles.

Crystalline optical data were used for $MgAl_2O_4$, Mg_2SiO_4, Fe, and KCl (see Section 3.3.2 for the respective references).

Treatment of cloud self-feedback

The self-consistent coupling between the atmospheric temperature structure and the cloud model can, in certain cases, lead to oscillations and non-convergence in atmospheric layers where the presence of the cloud heats the layer enough to evaporate the cloud. If this occurred in the calculations, then the cloud base location was moving significantly in the atmosphere. A similar behavior has been found for water cloud modeling in Y-dwarfs (see Morley et al. 2014), using the same cloud model (Ackerman & Marley 2001) as one of the two that I adopted for the irradiated planets here.

In the *petitCODE* models, if the cloudy solution exhibited the unstable self-feedback behavior, I decreased the cloud density by multiplying it by 2/3 and waiting 100 iterations to

check if the solution would settle into a stable state. This was repeated until a stable state was found.

The motivation for this treatment is the following: a single temperature structure solution for an atmosphere with a cloud profile that leads to unstable cloud self-evaporation will, on average, have a lower cloud density. Physically, this can be thought of as an average over the planetary surface where the clouds are in a steady state between condensation and evaporation. Alternatively, if there exist regions of rising and sinking parcels of gas, a planet may develop a patchy cloud pattern (Morley et al. 2014), such that our treatment may also be thought of as an opacity-average over a patchy cloud model. In that sense my treatment is somewhat less sophisticated than the (Morley et al. 2014) approach for self-luminous planets/brown dwarfs, where a single atmospheric temperature structure was calculated as well, but the radiative transport and emerging flux from the planet was calculated for the clear and cloudy atmospheric patches separately, with less flux emerging from the cloudy and more flux emerging from the clear parts of the atmosphere. However, because for irradiated planets the majority of the flux does not stem from the cooling of the deep interior of the planet, but from the regions were the stellar flux is absorbed, the cloudy regions would have to re-radiate the same amount of energy as the cloud-free regions in the absence of advection of thermal energy. Thus, my treatment may be more appropriate. However, from phase-curve measurements, and the corresponding day-nightside emission contrasts, it is well known that the horizontal advection of thermal energy in irradiated planets is working relatively effectively, indicating that the advection timescale becomes comparable to the radiative timescale. This advection seems to be most effective for cool, low-mass planets (Perez-Becker & Showman 2013; Kammer et al. 2015; Komacek & Showman 2016). Therefore, for cool, low-mass planets, not all of the energy absorbed in a given region of the atmosphere is re-radiated immediately, which would in turn mean that the (Morley et al. 2014) treatment may still be valid.

I currently neglect the corresponding increase in the gas opacities due to the reduced cloud density because the condensates considered here do not significantly deplete the atmosphere's main opacity carriers (H_2O, CH_4, CO, CO_2, HCN, etc.): the atomic species such as Mg, Si, and Al are all naturally less abundant when considering solar abundance ratios. The corresponding decrease in the gas abundance ratios is of the range of $\sim$20 % for water if silicate condensation takes place. The only exception is Na_2S and KCl, which will deplete almost all Na and K from the gas phase if condensation occurs. However, because the unstable regions occur mostly at the location of the cloud bases, the evaporated Na and K gas is likely cold trapped to the cloud base regions such that the removal from the atmosphere's upper layers may still be valid. A more sophisticated treatment will have to be added in an upcoming version of the code.

5.3.3 C/O

In my calculations presented here the fiducial composition of all planets is always a scaled solar composition with C/O $\approx$ 0.56 (Asplund et al. 2009). For every planet, I also consider models with twice as many or half as many O atoms, leading to C/O ratios of 0.28 and

1.12, respectively. While the value of 1.12 may be slightly higher than can be reached from formation (which is $\mathrm{C/O} = 1$, see 'Open Question' 5 in Section 1.5), it obviously leads to the desired results, that is, carbon-dominated atmospheres: the transition value from water- to methane-dominated spectra occurs for C/O values between ∼0.7 and ∼0.9 (see Mollière et al. 2015, and Chapter 4), where the lower value for the transition is found in atmospheres that are cool enough to condense oxygen into silicates, increasing the gas phase C/O ratio. Even cooler planets can exhibit methane features without the need for an elevated C/O ratio (see Chapter 4).

As mentioned in Section 4.2, the observational evidence of planets with atmospheric C/O ratios > 1 is debated, and there have been numerous studies trying to theoretically assess whether the formation of C/O>1 or $\mathrm{C/O} \rightarrow 1$ planets is possible (Öberg et al. 2011; Ali-Dib et al. 2014; Thiabaud et al. 2014; Helling et al. 2014a; Marboeuf et al. 2014b,a; Madhusudhan et al. 2014a; Thiabaud et al. 2015; Öberg & Bergin 2016; Madhusudhan et al. 2016), while one of the most recent works on this topic indicates that hot jupiters (which usually have masses $\lesssim 3\mathrm{M}_{\mathrm{J}}$), and planets of lower mass, may never have $\mathrm{C/O} \gtrsim 1$ (Mordasini et al. 2016).

5.3.4 TiO/VO opacities

In cases where the target planets are hot enough for TiO and VO to exist in the gas phase at the terminator region, I calculate additional models, including TiO and VO opacities.

I repeat here that the existence of gaseous TiO and VO in planetary atmospheres is debated (Spiegel et al. 2009; Showman et al. 2009; Parmentier et al. 2013; Knutson et al. 2010). Recent evidence shows that this class of planets may exist nonetheless (Mancini et al. 2013; Haynes et al. 2015; Evans et al. 2016), therefore I include this possibility here.

5.3.5 Irradiation treatment

The properties of the circulation on planets, and the resulting energy transport, were discussed in Sections 2.1.1 and 4.2.1, an the methods available to approximate different regimes were summarized in Section 3.1.1, and Figure 3.1 therein, such that I here merely describe the assumptions made for the irradiation treatment in the Mollière et al. (2017) calculations:

For all planets I considered the cases of (a), globally averaged insolation, where the insolation flux is homogeneously spread over the full surface area of the planet and (b), day side averaged insolation, where the insolation flux is homogeneously spread over the dayside hemisphere of the planet.

For the the very hot planets WASP-18b and Kepler-13Ab a third treatment was carried out: for these planets, the brightness temperature of the dayside is higher than the temperature expected for both the dayside and the global average case (Nymeyer et al. 2011; Shporer et al. 2014). Here I used the 'no redistribution case' (c), as described in Section 3.1.1.

5.4 General characteristics of the results

In this section I summarize the effects of various parameters on the resulting atmospheric structures and spectra, where more emphasis is put on the models including clouds. For the sake of clarity, and in order to minimize redundancy, I concentrate on a selected subset of the candidates listed in Table 5.1 here, which I use to exemplify the effects of various parameters.

5.4.1 Atmospheric enrichment

Variations of the atmospheric enrichment affect the resulting atmospheric structures and spectra in at least three different ways.

First, an increase (or decrease) of the enrichment will result in an increased (or decreased) total opacity within the atmosphere. This is because the main carriers of the atmospheric opacities are the metals, rather than H_2 and He. The effect of scaling the planetary enrichment on the atmospheric temperature structure and emission spectra has been studied in Mollière et al. (2015, see Chapter 4): a higher enrichment moves the photosphere position to smaller pressures, leading to less pressure broadening of lines, and a decreased strength of the CIA opacity, because the strength of both these opacity sources scales linearly with pressure. Hence the opacity in the atmospheric windows decreases. This exposes deeper, hotter layers in the windows and leads to a larger contrast between emission minima and maxima in spectra. This effect, neglecting metallicity-dependent chemistry, is (inversely) degenerate with varying the planetary surface gravity as it holds that $d\tau_\nu = (\kappa_\nu / g) dP$, where τ_ν is the optical depth, κ_ν the opacity, g the surface gravity and P the pressure (see Chapter 4).

Second, atmospheric transmission spectra are affected by scaling the metallicity in two additional ways: Increasing the metallicity, and therefore the total opacity will result in an increased transit radius, while a significant increase in metallicity and the resulting increase of the atmospheric mean molecular weight will weaken the signal amplitude between maxima and minima in the transmission spectrum, because $R(\lambda) \propto [k_\mathrm{B} T/(\mu g)] \cdot \log(\kappa_\nu)$ (see Equation 1.12), where $R(\lambda)$ is the planetary transit radius, T the atmospheric temperature, μ the atmospheric mean molecular weight and g the planetary surface gravity.

Finally, an increased enrichment will affect the atmospheric abundances because of the metallicity-dependent chemistry: the CO_2 abundance, for example, is a strong function of metallicity (see, e.g. Moses et al. 2013, and references therein).

5.4.2 Clouds

The various cloud models investigated in this study are summarized in Section 5.3.2. Here I concentrate on the spectral characteristics of some of these cloud models. In Figure 5.2 I show the transmission spectra resulting from self-consistent atmospheric structure calculations of the planet HAT-P-12b, together with the observational data of the *HST* and *Spitzer* telescope (Sing et al. 2016). I look at the cases including only Na_2S and KCl clouds here. For these calculations, a planet-wide averaged insolation was assumed, because it was found

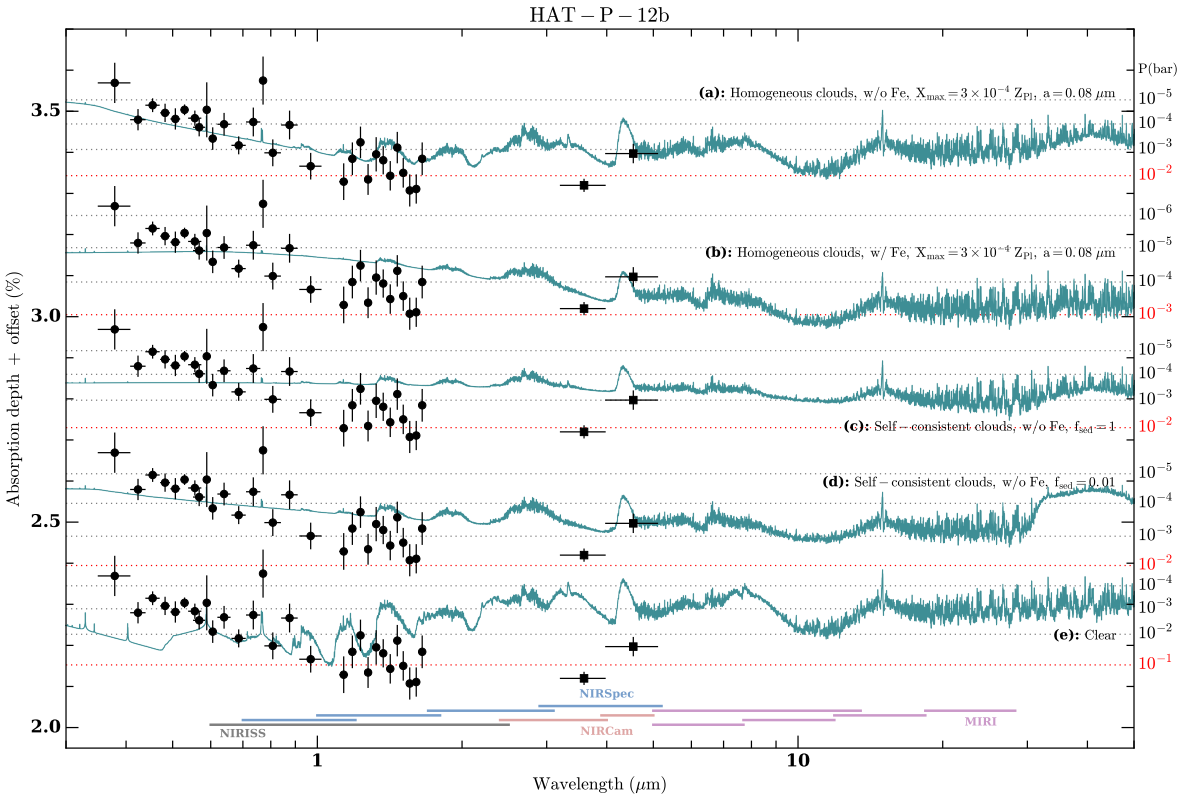

FIGURE 5.2: Transmission spectra for the warm Saturn HAT-P-12b, along with the observational data taken from Sing et al. (2016). For clarity, a vertical offset has been applied to the various models. The cloud species considered here are Na_2S and KCl only. From top to bottom, the following cases are plotted: (a) homogeneous clouds, with a maximum cloud mass fraction of $X_{\rm max} = 3 \times 10^{-4} \cdot Z_{\rm Pl}$ per species, and a single cloud particle size of 0.08 μm. Iron clouds have been neglected; (b) like (a), but including iron clouds; (c) self-consistent clouds using the Ackerman & Marley (2001) model with $f_{\rm sed} = 1$; (d) like (c), but using $f_{\rm sed} = 0.01$; (e) clear, fiducial atmospheric model. The colored bars at the bottom of the plot show the spectral range of the various *JWST* instrument modes. The dotted horizontal lines denote the pressure levels being probed by the transit spectra with the pressure values indicated on the right of the plot. Figure taken from Mollière et al. (2017).

that 3D GCM calculations lead to similar transmission spectra as the planet-wide averaged insolation 1D modes (but exceptions may exist; for more details see Fortney et al. 2010). The process of patchy clouds, which may mimic the signal of high-mean-molecular-weight atmospheres (Line & Parmentier 2016), cannot be reproduced with this approach.

The model spectra plotted in Figure 5.2 include the smaller and larger cloud particle ($f_{\rm sed}$=0.01 and 1, respectively) self-consistent clouds following the Ackerman & Marley (2001) cloud model, as well as the parametrized homogeneous clouds with small particles of size 0.08 μm. Models are shown with and without the consideration of iron clouds. Finally, the fiducial, cloud-free model is shown as well. The dotted horizontal lines drawn in the plot that indicate the pressure being probed by the various models, corresponding to the (wavelength-dependent) effective radius. The optimal y-offset value of the spectra with respect to the data was found by χ^2 minimization.

Before investigating the different cloudy models, I want to point out that the clear atmosphere (Model (e) in Figure 5.2) obviously represents a bad fit to the data: a simultaneous fit of the Rayleigh-like signature of the optical and NIR *HST* data and the *Spitzer* photometry at IR wavelengths is not possible. Both the *HST STIS* and *Spitzer* data are crucial for this claim of 'cloudiness', because the measurement of a Rayleigh signal in the optical alone is not sufficient: it could be simply caused by H_2 and He. Only a spectral slope less negative

than -4 in the optical may allow us to infer the presence of large particle clouds ($a \gtrsim \lambda/2\pi$, see the 'Cloud opacities' part of Section 2.2.5) from the spectrum alone, but this requires an accurate estimate of the atmospheric scale height (also see Heng 2016).

Studying the cloudy results in Figure 5.2 one sees that only the parametrized homogeneous clouds with a particle size of 0.08 μm (model (a) in Figure 5.2, correponding to Model 6 in Table 5.2) are able to produce Rayleigh scattering ranging from the optical (~ 0.4 μm) to the NIR as probed by the *HST* data. Further, this is only possible if iron clouds are neglected: Due to the high absorption cross-section of iron in the optical the Fe clouds clearly decrease the spectral slope such that it is less strong than expected for pure Rayleigh scattering (see Model (b) in Figure 5.2, correponding to Model 8 in Table 5.2).

The results for the Ackerman & Marley (2001) clouds are shown in the models (c) and (d) in Figure 5.2 for $f_{\rm sed}$=1 and 0.01, respectively. They correspond to models 2 and 4 in Table Table 5.2. Model (c) produces a flat slope in the optical and NIR and seems to mute the molecular features too strongly when compared to the data. For the self-consistent cloud with a small $f_{\rm sed}$=0.01 value (model d) we find that the slope in the optical is already relatively steep, approaching a Rayleigh scattering slope. However, although the average particle size is well below 0.08 μm, the slope is less steep than in the mono-disperse particle model (a) because the largest particles within the distribution dominate the opacity (Wakeford & Sing 2015). I thus do not find a good fit for HAT-P-12b when using the Ackerman & Marley (2001) model. The broad absorption feature starting at 30 μm in the transmission spectrum of model (d) is the Na_2S resonance feature.

To summarize, in the results presented here the Ackerman & Marley (2001) results correspond to clouds with broader particle size distributions, which tend to produce transmission spectra that are either flat or less strongly sloped than expected from small particle Rayleigh scattering. For the smallest $f_{\rm sed}$ values, I succeed in acquiring relatively steep scattering slopes, but at the same time the clouds are relatively optically thick, muting the molecular features more strongly. I want to stress that this does not mean that the (Ackerman & Marley 2001) model is not useful for fitting cloudy planetary spectra, but it is potentially more useful for transmission spectra that show a flat and gray cloud signature in the transmission spectrum, as is seen for GJ 1214b (see Morley et al. 2015, and our results for GJ 1214b using cloud model 4 in Section 5.5.1.)

Further, while model (a) in Figure 5.2 may fit the transmission results relatively well, I want to repeat that I used the same cloud setup for all candidate planets presented in this study, without trying to find the true best fit parameters. Therefore, a dedicated study for the individual planets may result in even better estimates of the atmospheric parameters. Moreover, it is not correct to assume that the homogeneous clouds used for model (a) represent a good description of the cloud mass fraction and particle sizes throughout the whole atmosphere. As can be read off in Figure 5.2, the maximum pressure being sensed by transmission in model (a) is approximately 10 mbar. Therefore, an equally good fit may be obtained using a cloud model that truncates the cloud at $P = 10$ mbar and sets the cloud density to zero at larger pressures. This may leave the transmission spectrum unchanged but will strongly affect the planet's emission spectrum: as mentioned previously, it is well

known that the emission spectra probe higher pressures than transmission spectra (see the 'Clouds' part of Section 4.2.1).

Due to the assumption of vertically homogeneous clouds, I obtain a Bond albedo[1] of 17 % for model (a) in Figure 5.2. Model (b), which has the same $X_{\rm max}$ value as model (a), only has an albedo of 5 %, because the iron cloud particles absorb light effectively. For the self-consistent clouds, I obtain 10 % for Model (c) and 8 % for Models (d). The clear model (e) has an albedo of 3 %. If clouds were truncated below the pressures probed by transmission, the albedos for the models would be lower.

In conclusion, it may well be the case, therefore , that the transmission spectrum of a planet is fit well by a cloudy atmosphere, while the planet's emission spectrum is described well by the corresponding clear atmosphere. For HAT-P-12b, this assessment is impossible because the *Spitzer* eclipse photometry for the dayside emission by Todorov et al. (2013) only gives upper limits at 3.6 and 4.5 μm. These limits are consistent with all the model calculations I carried out for this planet, for a planet-wide averaged insolation. The dayside averaged insolation case is excluded because all models have larger fluxes than allowed by the upper limits.

Cloud profiles

The cloud mass profiles used to obtain the results in Figure 5.2 are shown in the left panel of Figure 5.3. Only Na_2S condensed for the models considered here, because the atmosphere was too hot for KCl condensation to occur.

Grains which are small enough exhibit resonance features, while increasingly larger grains have flatter, more grayish opacities. Consequently, for model (d), which has $f_{\rm sed} = 0.01$, and thus small particle sizes, the Na_2S feature at 30 μm can be seen prominently in Figure 5.2, and the corresponding small particle size can be seen in the right panel of Figure 5.3. Due to the larger size of the cloud particles shown for the $f_{\rm sed} = 1$ model (Model (c) in Figure 5.2), the corresponding cloud resonance features in the MIR are hard to see. It can be seen clearly that the larger the $f_{\rm sed}$ value, the stronger the decrease of the cloud mass fraction above the cloud deck becomes, because it is then proportional to $P^{f_{\rm sed}}$ (also see Equation 3.90).

In addition to the Ackerman & Marley (2001) cloud profiles and particles sizes (solid lines), I also show the corresponding values of the three-parameter cloud model (see Section 3.5.2) used for the model calculations (a) and (b) in Figure 5.2. The particle radius was assumed to be fixed at 0.08 μm (vertical dotted line in the right panel of Figure 5.3). The vertical dotted lines in the left panel of Figure 5.3 show the three possible maximum cloud mass fraction values, where both models (a) and (b) used $X_{\rm max} = 3 \times 10^{-4} Z_{\rm Pl}$.

[1]The Bond albedo is defined as the ratio of the total flux reflected off the planet, and the stellar flux impinging on the planet.

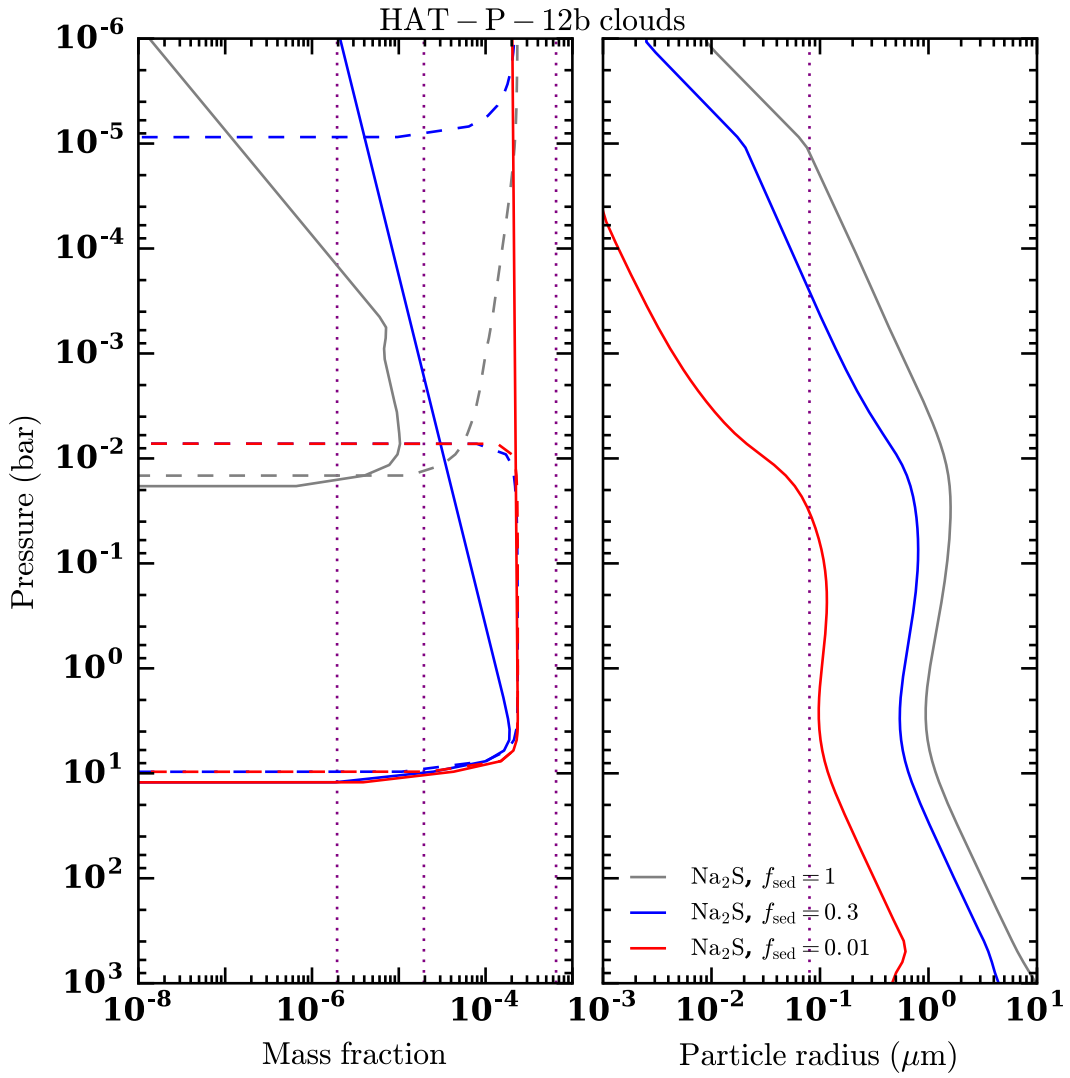

FIGURE 5.3: *Left panel*: the solid lines denote the Na_2S cloud-mass fractions as a function of pressure for the $f_{sed} = 0.01, 0.3$, and 1 models, shown in red, blue, and gray, respectively. The dashed lines denote the mass fractions derived from equilibrium chemistry, that is, in the absence of mixing and settling. For a comparison, the three dotted lines denote the three different X_{max} values used in the homogeneous cloud models. *Right panel*: mean cloud particle radii derived for the $f_{sed} = 0.01$, 0.3, and 1 cloud models. Again for comparison, the vertical dotted line denotes the particle size $a = 0.08$ μm adopted for the homogeneous cloud models. Figure taken from Mollière et al. (2017).

5.4.3 C/O

The importance of the C/O ratio for atmospheric chemistry and the effects arising from varying this parameter have been described in, e.g., Seager et al. (2005); Kopparapu et al. (2012); Madhusudhan (2012); Moses et al. (2013). Additionally, I studied the properties of planetary atmospheres upon the variation of the C/O ratio systematically in Mollière et al. (2015, see Chapter 4), such that I only give a short summary here.

In Figure 5.4, I show the emission spectra calculated for the warm Jupiter WASP-10b ($T_{equ} = 972$ K) and the hot Jupiter WASP-32b ($T_{equ} = 1560$ K), along with the *Spitzer* eclipse measurements by Kammer et al. (2015) and Garland et al. (2016), respectively. Both the synthetic spectra and data of WASP-32b have been multiplied by an offset factor of three in order to minimize the overlap between the spectra of WASP-10b and WASP-32b. I plot the spectra resulting from a dayside averaged insolation for both planets. For the hotter planet,

WASP-32b, the spectra exhibit a clear dichotomy, with the solar C/O spectrum ($C/O_{\odot} \sim 0.56$) dominated by water absorption and the spectrum with twice the solar C/O value (1.12) dominated by carbon absorption, such as the methane feature visible a 3.2 μm.

For the cooler planet, WASP-10b, the spectrum of the solar C/O case shows both water and methane absorption (again, see the telltale methane feature at 3.2 μm), while the C/O=1.12 case shows methane absorption, but no water absorption. The reason that lower-temperature atmospheres can show both water and methane absorption at the same time, regardless of the C/O ratio, has been described in detail in Section 4.7.1. However, depending on the vigor of vertical mixing, methane may not be visible in the spectrum of the solar C/O case until the planet is as cool as 500 K, due to chemical quenching (see, e.g., Zahnle & Marley 2014). I do not model such non-equilibrium chemistry effects in the calculations. However, the importance of non-equilibrium chemistry strongly depends on the values of the mixing strength, which is related to the planetary surface gravity. Both planets shown here have relatively high surface gravities, which tends to decrease the mixing strength (Zahnle & Marley 2014).

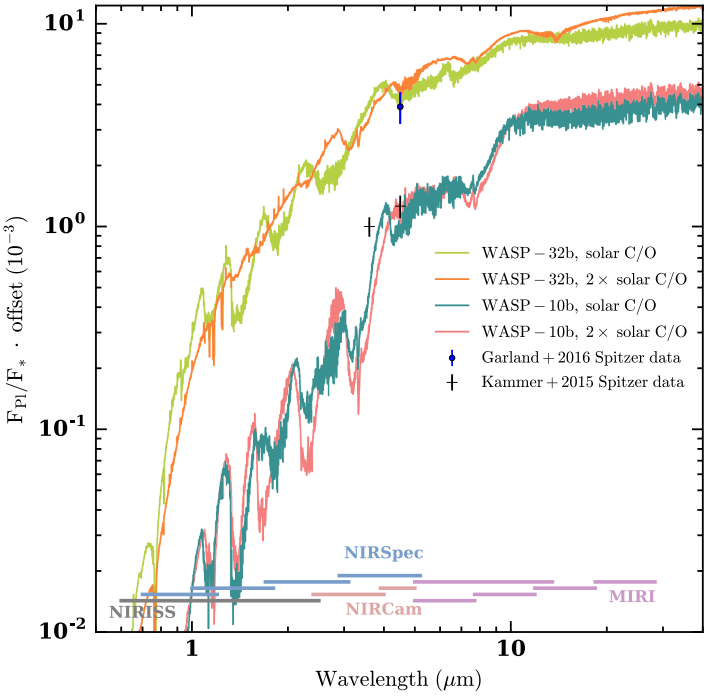

FIGURE 5.4: Synthetic emission spectra of the planets WASP-32b and WASP-10b for the clear fiducial models with solar C/O ratios and for the cases with C/O ratios twice as large as solar. We also plot existing *Spitzer* photometry for the targets by Garland et al. (2016) (WASP-32b) and Kammer et al. (2015) (WASP-10b). A dayside-averaged insolation was assumed for both planets. For clarity, both the synthetic spectra and data of WASP-32b have been multiplied by an offset factor of three.

5.4.4 TiO/VO opacities

In the cases where equilibrium chemistry allows for TiO and VO to exist in the gas phase, and for the calculations for which I specifically include TiO and VO opacities, I find that the converged atmospheric solutions exhibit inversions. For cases where the atmospheres are cool enough such that Ti and V have condensed out of the gas phase, I find that the results are identical to the clear, fiducial calculations, which do not include TiO/VO opacities.

In addition to emission features, atmospheres with TiO and VO inversions show emission spectra that are more isothermal than the corresponding fiducial cases, that is, the SED more closely resembles a blackbody. This is because the inversion decreases the overall temperature variation in the photospheric layers of the atmospheres. I want to stress that this does not mean that the atmospheres attain a globally more isothermal state. I still find strong inversions if the insolation and the TiO/VO abundances are high enough. The decreasing

temperature variability merely holds for the photospheric region, not for the whole atmosphere: inversions form if the opacity of the atmosphere in the visual wavelengths is larger than in the IR wavelengths (see Section 2.2.1). When entering the atmosphere from the top, the optical depth for the stellar light reaches unity before the location of the planetary photosphere is reached. Therefore, the higher atmospheric layers, in which a non-negligible amount of the stellar light is absorbed, need to heat up significantly in order to reach radiative equilibrium (i.e. absorbed energy equals radiated energy). These layers will cause the formation of emission features. On the other hand, the photosphere represents the region where the planet's atmosphere radiates most of its flux to space, because here the IR optical depth reaches unity. This region is below the inversion region. Below the photosphere, the atmospheric temperature will increase monotonously. Consequently, the photosphere is bracketed by two regions: a region where the temperature decreases, as one approaches the photosphere coming from the inversion above, and a region where the temperature increases again when moving on to larger pressures. Hence, the total temperate variation across the photospheric region, which is a region in which the atmospheric temperature gradient transitions from being negative to being positive, is small. Therefore, the spectral energy distribution escaping from this region is closer to an isothermal blackbody than in an atmosphere without an inversion.

In transmission, these atmospheres exhibit TiO/VO resonance features in the optical and NIR, which are well known from theoretical calculations of atmospheric spectra (see, e.g. Fortney et al. 2008, 2010) but have not yet been conclusively detected in observations.

If I include TiO/VO opacities, all atmospheres with equilibrium temperatures higher than 1500 K show inversions in their atmospheres for the dayside averaged insolation calculations. In planet-wide averaged insolation calculations these planets showed inversions as well, but the planets with equilibrium temperatures below 1750 K had inversions that were relatively high in the atmospheres, such that either none or only weak emission features were seen. The transmission signatures of TiO/VO were seen in all cases that exhibited an inversion.

5.5 Simulated observations

In this section I show the characteristics of the simulated observations carried out for all targets defined in Table 5.1. Similar to Section 5.4, I concentrate on a few, exemplary objects. Here I investigate how the simulated observations appear as a function of the number of transits/eclipses, and which wavelength ranges have the most diagnostic power for characterizing the planets.

The instrument parameters adopted to describe the performance of *JWST* are listed in Table 5.3. The values for the full well capacity and readout noise of the *NIRSpec* instrument were taken from Ferruit et al. (2014), and we adopted the same full well capacity for *NIRISS*, due to the similarity of the detectors. The noise floor for *NIRSpec* is expected to be below 100 ppm (Ferruit et al. 2014), and we adopted a value of 75 ppm here. Following Rocchetto et al. (2016) one may assume a noise floor value of 20 ppm for *NIRISS*. Further, we set the

	NIRISS SOSS I	*NIRSpec G395M*	*MIRI LRS*
λ range	0.8-2.8 μm	2.9-5.0 μm	5.5-13.5 μm
QE	0.8	0.8	0.6
FWC	77 000 e-	77 000 e-	250 000 e-
$N_{\rm read}$	23 e-	18 e-	14 e-
DC	0.02 e- s^{-1}	0.01 e- s^{-1}	0.2 e- s^{-1}
$T_{\rm tot}$	0.15	0.54	0.35
$N_{\rm floor}$	20 ppm	75 ppm	40 ppm

TABLE 5.3: Instrument parameter values used for the synthetic *JWST* observations. The collecting area of *JWST* is assumed to be 24 m^2, with a 'warm' mirror temperature of 35 K. The abbreviations in the first column stand for the *quantum efficiency* (QE), the *full well capacity* (FWC), the *readout noise* ($N_{\rm read}$), the *dark current* (DC), the *total system transmission* ($T_{\rm tot}$), and the *systematics noise floor* $N_{\rm floor}$.

MIRI noise floor value to 40 ppm, because the values adopted in the existing literature range from 30 to 50 (see Beichman et al. 2014; Greene et al. 2016, respectively). The remaining instrument characteristics for *MIRI* were taken from (Ressler et al. 2015).

Note that for every instrument, a separate observation needs to be carried out. In regions where the wavelength binning of *petitCODE* was coarser than the intrinsic resolution, I interpolated the spectra of *petitCODE* to this higher resolution. The synthetic observations yield the single observation errors, but multiple transit/eclipse observations can be obtained by sampling the noiseless spectra, using errors normalized with $N_{\rm transit}^{1/2}$, where $N_{\rm transit}$ is the number of observations.

5.5.1 Molecular features on extremely cloudy super-Earths: the case of GJ 1214b

The observational data for GJ 1214b, as well as synthetic spectra and observations, are shown in the left panel of Figure 5.5. For clarity, the synthetic observations have been rebinned to a resolution of 50. The noise of the measurements increases with wavelength as less light is coming from the star at longer wavelengths. In addition to the cloudy $f_{\rm sed} = 0.3$ model (Model 3 in Table 5.2) shown in the plot, I also show a clear atmosphere for comparison. For this planet, cloud models 3 and 4 converged with the cloud feedback included. I therefore present self-consistent calculations for cloud model 3 for GJ 1214b.

It is evident that the clear spectrum is inconsistent with the *HST* data by Kreidberg et al. (2014), whereas cloudy models provide a better fit. The need for clouds has been studied in detail in Morley et al. (2013); Kreidberg et al. (2014); Morley et al. (2015), where Morley et al. (2013, 2015) found that high atmospheric enrichments are necessary to fit the data. They also put forward the possibility that the flat transmission spectrum of GJ 1214b could be caused by hydrocarbon hazes, and suggested pathways of how to distinguish between mineral clouds and hydrocarbon hazes using emission spectroscopy or by analyzing the reflected light from these planets.

The *petitCODE* cloudy spectrum is mostly flat from the optical to the NIR, but some molecular features can be made out clearly, especially in the MIR region, including the methane features at 2.3, 3.2, and 7.5 μm, and the CO_2 features at 2.7, 4.3, and 15 μm. The CO_2 feature at 15 μm is not within the spectral range of the *MIRI LRS* instrument. Due to the

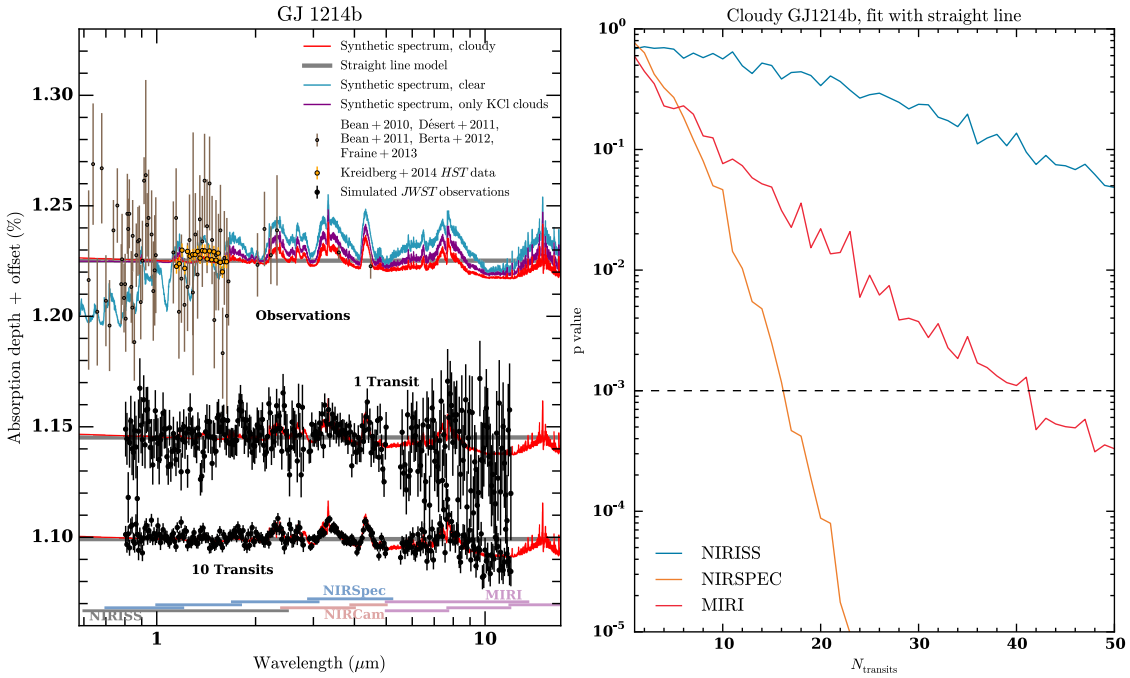

FIGURE 5.5: *Left panel:* synthetic transit spectra, observations, and synthetic observations for the planet GJ 1214b. The orange points denote the observational data by Kreidberg et al. (2014), while brown points denote the observational data by Bean et al. (2010); Désert et al. (2011); Bean et al. (2011); Berta et al. (2012); Fraine et al. (2013). Synthetic spectra for the cloudy $f_{\rm sed} = 0.3$ model (Model 3 in Table 5.2) are shown as red or purple solid lines for the case including Na_2S+KCl clouds or KCl clouds only. The clear model is shown as a teal line. A straight line model is shown as a thick gray solid line. The black dots show the synthetic observations derived for one (top) and ten (bottom) transits, re-binned to a resolution of 50. Vertical offsets have been applied for the sake of clarity. *Right panel:* p values of the Kolmogorov-Smirnov test for the residuals between the synthetic observation of the Na_2S+KCl cloud model and the straight line model fitted to the these observations. The p value is shown as a function of $N_{\rm transit}$ for the three different instruments of Table 5.3. For every (instrument, $N_{\rm transit}$) setup, a new straight line model is fitted to the observations. The black dashed line denotes our threshold value of 10^{-3}. Figure taken from (Mollière et al. 2017).

high metallicity, CO_2 is the most spectrally active carbon- and oxygen-bearing molecule and more abundant than CH_4, CO, or H_2O at the pressures being probed by the transmission spectrum. For a cloudy, highly enriched atmosphere, as presented here, I therefore predict the existence of CO_2 and CH_4 features in the otherwise flat transmission spectrum.

Because GJ 1214b is the coolest planet considered in our sample, I only include KCl and Na_2S clouds in its atmosphere (see Section 5.3.2). However, even Na_2S clouds may form too deep in this atmosphere for them to be mixed up into the region probed in transmission Morley et al. (2013); Charnay et al. (2015a). Both approaches, excluding Na_2S or including it, have been studied in the literature (Morley et al. 2013; Charnay et al. 2015b; Morley et al. 2015). I thus also show a comparison to a model solely including KCl clouds in Figure 5.5. One sees that as the cloud opacity decreases, the molecular features can be seen more clearly.

The highest quality spectrum currently available for GJ 1214b is consistent with a straight line (Kreidberg et al. 2014). I therefore want to assess how well *JWST* observations could distinguish the high metallicity cloudy model from a flat, featureless spectrum, as a function of the number of transits observed. As an example, I show a comparison model (a straight line spectrum) as a gray line in Figure 5.5. The transit radius of the straight line model was chosen by fitting a synthetic single transit observation of the KCl+Na_2S cloud model in all instruments with a straight line by means of χ^2 minimization.

First I tested which instrument, that is, which wavelength range, is best suited for the

task, and how many transits are needed to conclusively rule out the straight line case. In order to avoid ruling out a straight line scenario because of an offset of the global (fitted for all three instruments) straight line model to a single instrument spectrum, I fitted straight line models to the synthetic observation within each instrument separately. For this, I generated synthetic observations $T_\lambda(\mathrm{instrument}, N_{\mathrm{transit}})$, where the $T_\lambda(\mathrm{instrument})$ denotes the observed wavelength-dependent transmission using one of the instruments listed in Table 5.3, and N_{transit} is the number of transits accumulated to obtain the observation. For every (instrument,N_{transit}) pair, I then fitted a straight line to the observations and calculated the residuals of the straight line to the cloudy observation, taking into account the appropriate errors when stacking N_{transit} transits in the instrument of interest. The residuals were then compared to a Gaussian normal distribution using a Kolmogorov-Smirnov test[2]. To rule out the straight line model, given the observation of the cloudy model, I adopted a conservative threshold p value of 10^{-3}. This means that the probability of observing a straight line model and finding the above distribution of residuals, or one that is even less consistent with a normal distribution, is 10^{-3}. Alternatively to fitting a straight line model to the synthetic observations, it is also possible to adopt an arbitrary offset between the model and the observations and then shift the distribution of residuals between the straight line model and the cloudy model such that is has a mean value of zero. For this case I obtained identical results.

I show the resulting p values as a function of N_{transit} in the right panel of Figure 5.5, for the three different instruments. To minimize the Monte Carlo noise resulting from the generation of the synthetic observations, I took the median p value of 100 realizations for every (instrument,N_{transit}) point. I find that *NIRISS* would not be able to rule out a straight line spectrum even if 50 spectra were stacked. This is due to the fact that the cloudy model is relatively flat in this wavelength region. With *NIRSpec*, on the other hand, the distinction may be possible by stacking 16 observations. For *MIRI*, a refutal of the straight line model is possible after $\sim$40 transits. Thus, using the conservative p value threshold, it seems quite hard to refute the straight line case, although the *NIRSpec* observations look different from a straight line when inspected by eye already after less than ten transits in Figure 5.5. Therefore, if one carries out the same test once more, but compares the observations with the cloudy model itself, one finds p values with a median of $1/2$, independent of the number of transits. Hence, one may say that a cloudy model is more likely to describe the data than the straight line model, already after less than $\sim$10 transits, if one uses the *NIRSpec* band and carries out a retrieval analysis. Note, however, that the p value is subject to statistical noise, due to the limited number of spectral points.

The reason for the Kolmogorov-Smirnov test to require a relatively large number of transits for the distinguishability analysis presented here is that the triangularly shaped molecular features will lead to relatively symmetric residual distributions when compared to the straight line model. In this sense, it becomes harder for the Kolmogorov-Smirnov test to distinguish between the resulting residual distribution and a Gauss distribution, because

[2] I used the kstest() function of the Scipy library for this task, see http://docs.scipy.org.

this test is insensitive to the wavelength correlation of the residuals. For a conclusive statement, rather than an upper limit, regarding the number of transits needed for constraining GJ 1214b's atmosphere, one therefore needs more sophisticated statistical tools, such as retrieval analyses (see Section 1.4.2 and Chapter 6). However, the Kolmogorov-Smirnov test may still be used to assess which instrument, and thus wavelength range, may be best suited for distinguishing the cloudy GJ 1214b observation from a straight line, and my analysis indicates that *NIRSpec* will be best suited for this task, followed by *MIRI*. *NIRISS* was found to be the least well suited.

Finally, I find that our KCl+Na_2S cloud model presented for GJ 1214b in the left panel of Figure 5.5 results in a p value of 0.45 if compared to the existing observational data. It is therefore consistent with these data.

5.5.2 Cloud resonance features in hot jupiters: the case of TrES-4b

In the left panel of Figure 5.6, I show the simulated transmission observations of TrES-4b. TrES-4b is a strongly inflated (1.84 $R_{\downarrow_+}$) hot jupiter that circles its F-type host star ($T_* = 6200\ K$) once every 3.6 days (Chan et al. 2011). The dayside emission of this planet seems to be consistent with a temperature inversion (Knutson et al. 2009), and the dayside for this planet may therefore be too hot to have a significant silicate cloud coverage. However, the limbs may be much cooler than the bulk dayside, allowing for such clouds to exist (see, e.g. Wakeford et al. 2017). To account for this effect, I model the transmission spectra for the planets assuming a global redistribution of the stellar irradiation energy (also see Section 5.4.2). The theoretical global equilibrium temperature of this planet is 1795 K. It is therefore within the temperature range where mineral clouds such as Mg_2SiO_4 and $MgAl_2O_4$ can be expected.

For this case I will now consider the synthetic observations of the cloud models 6 and 9 in Table 5.2, that is, homogeneously distributed clouds of small particles assuming either irregular (DHS) or spherically homogeneous (Mie) particles. For comparison I also show the clear model for this planet.

The feature at 10 μm in the cloudy models, which is highlighted by the dashed-line box in Figure 5.6, arises from resonances of the crystalline Mg_2SiO_4 particles. The differences in the location and relative strength of the Mg_2SiO_4 resonance peaks, arising from the different particle shapes (irregular vs. spherically-homogeneous), are evident.

By carrying out a Kolmogorov-Smirnov analysis of the residuals between the clear model and the synthetic DHS cloud model observations, I find that a single transit in *MIRI* will be enough to discriminate between the clear and cloudy model. This implies that a single transit is sufficient for finding evidence for silicate cloud particles in such an atmosphere. Before carrying out the Kolmogorov-Smirnov analysis I corrected the offset between the two models in the MIR part short-ward of 9 μm, which is fully determined by molecular features. This was done in order to prevent a model discrimination based purely on global model offsets.

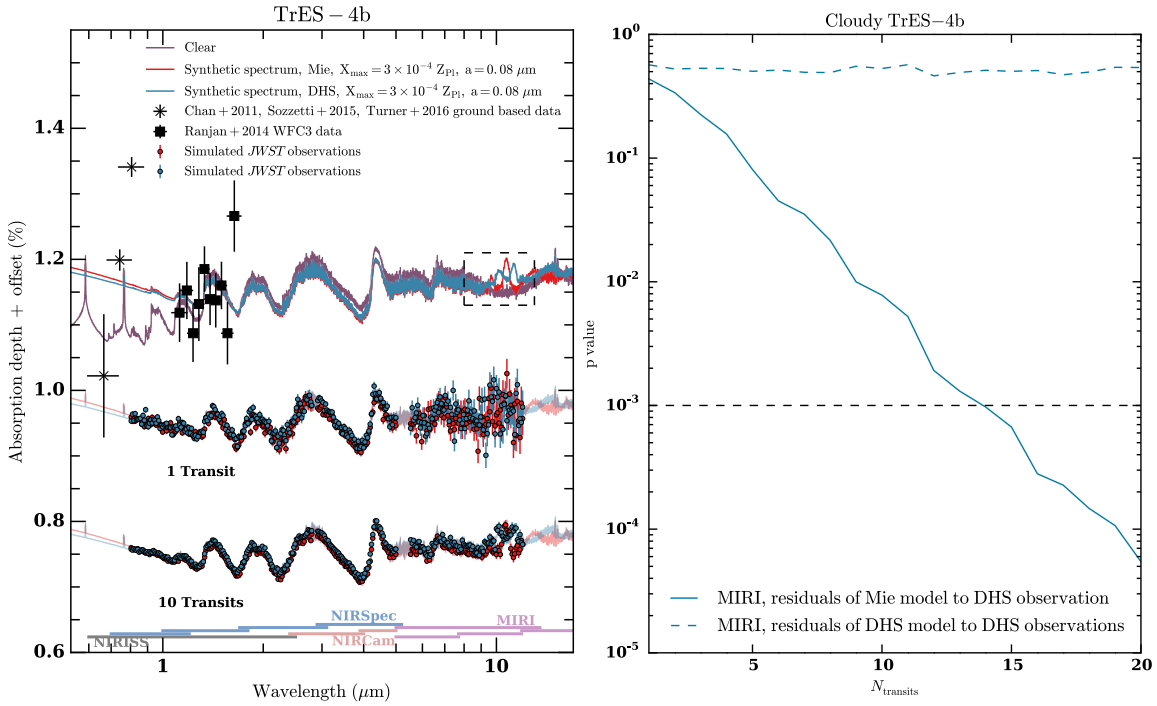

FIGURE 5.6: *Left panel:* synthetic transit spectra, observations, and synthetic observations for the planet TrES-4b. Black crosses denote the ground-based observational data by Chan et al. (2011); Sozzetti et al. (2015); Turner et al. (2016). Black squares denote the *HST WFC3* data by Ranjan et al. (2014). Synthetic spectra for the homogeneously cloudy models with $X_{\rm max} = 3 \times 10^{-4}\ Z_{\rm Pl}$ are shown as teal and red solid lines for the DHS and Mie opacity, respectively. The dashed box at ∼10 μm highlights the silicates features due to Mg_2SiO_4 resonances.The teal and red dots show the corresponding synthetic observations derived for one and ten transits, re-binned to a resolution of 50. Vertical offsets have been applied for the sake of clarity. *Right panel:* p values of the Kolmogorov-Smirnov test of the residuals between the synthetic observation of the TrES-4b DHS model and the Mie model (solid teal line). The p value is shown as a function of $N_{\rm transit}$ for data taken with *MIRI LRS* considering only the wavelength range of the silicate feature (9-13 μm) and correcting for global model offsets. The dashed teal line shows the p value obtained when analyzing the residuals of the DHS model to its own observation. The black dashed line denotes our threshold value of 10^{-3}. Figure taken from Mollière et al. (2017)

While the existence of an extinction feature at 10 μm, spanning the wavelength range from ∼8 to ∼12 μm, would hint at the presence of silicate absorbers in the planet's atmosphere, a single transit will not be enough to discriminate between all possible silicate absorbers: the resolution needed to resolve individual crystalline dust features is in the range of 50. Thus the number of stacked transits needs to guarantee a high enough SNR for a single point at this resolution. Juhász et al. (2009) have shown that for protoplanetary disks, the SNR required to characterize the silicate dust properties well (crystallinity and size) is between 10 and 100 per spectral point. Additionally, the zoo of silicate species which could possibly exist in planetary atmospheres is much more diverse than considered here: In the example shown here I considered crystalline Mg_2SiO_4 for the silicates. But also silicates such as $MgSiO_3$, iron-enriched olivines and pyroxenes, or species such as SiO_2, $FeSiO_3$ and Fe_2SiO_4 are possible (see Wakeford & Sing 2015). Another complication arises from the wavelength-dependent shape and position of the absorption features for particles larger than ~ 1 μm, but note that a strong Rayleigh signal observed in the optical and NIR transmission spectrum would suggest particles that are smaller than 0.1 μm. Unfortunately, the currently available ground-based data for this planet exhibit a large spread such that conclusive statements regarding the optical and NIR part of the planet's spectrum appear difficult.

In summary, this means that a single transit is not enough to fully characterize silicate dust based on the 10 μm feature in transmission spectra. However, if the need for small particle clouds is evident from the transmission spectrum, due to a strong Rayleigh signal in the optical and NIR, then the observation of a 10 μm feature presents strong evidence for the presence of silicate grains in the atmospheres, while the lack of such a feature means that the strong Rayleigh slope in the optical and NIR cannot be caused by silicates. In that sense *JWST* will shed light on the nature of small grain clouds by allowing us to find whether silicates are responsible or not, potentially using a single transit observation with *MIRI*.

In the idealized example shown here, where the only considered silicate species are crystalline Mg_2SiO_4 particles of either irregular or spherically-homogeneous shape, one can now asses how many transits would be needed to conclusively distinguish between both models. Similar to the Kolmogorov-Smirnov test carried out before for the clear and cloudy model, one can analyze the residuals of the Mie cloud model with respect to the observations of the DHS cloud model. The results are shown in the right panel of Figure 5.6. Again, because the silicate features only occur in the *MIRI* wavelength regime, I concentrate on this instrument only for the analysis, and only on the silicate feature, considering a wavelength range from 9 to 13 μm. In order to analyze only the difference in the cloud features I again corrected the cloud models for the offset that can be seen in the *MIRI* wavelength regime, outside of the silicate feature.

I find that the Mie cloud model is inconsistent with DHS observations if $\sim$13-14 transits are stacked for this planet. Because I only considered two possible cloud models here, and not the full parameter space, the number of transits needed to characterize the state of the clouds may likely be higher, however. Again, looking at the ten transit observations in Figure 5.6, a discrimination between the two cases seems to already be possible at a smaller number or transits. Therefore, similar to the analysis carried out for GJ 1214b in Section 5.5.1, I expect that statistical tools more powerful than the ones used here should be able to retrieve this difference for a smaller number of transits.

The two cloudy models shown in Figure 6 are consistent with the observational *HST* and *Spitzer* data, resulting in p values of 0.20 an.d 0.25 for the DHS and Mie cases, respectively.

5.5.3 Origin of isothermal emission on the hottest hot jupiters

In this section I will investigate simulated eclipse observations of our targets using *JWST*. I concentrate on a very interesting class of emission targets, namely the hottest hot Jupiters in my target selection: WASP-33b, Kepler-13Ab, and WASP-18b. Along with their high equilibrium temperatures, these planets share an additional similarity: their spectra can all be approximated well by blackbody emission, yet all of them are best fit by inversions in their atmospheres, see Haynes et al. (2015), Shporer et al. (2014) and Nymeyer et al. (2011) for WASP-33b, Kepler-13Ab, and WASP-18b respectively. Further examples for such planets in the literature are TrES-3b (Croll et al. 2010) and WASP-24b (Smith et al. 2012).

The case of WASP-18b is especially intriguing. Based on the orbital and stellar parameters, the planet's theoretical equilibrium temperature (i.e., assuming a planet-wide average of the insolation) is $T_{\rm equ} = 2410$ K. If one assumes a dayside averaging of the insolation

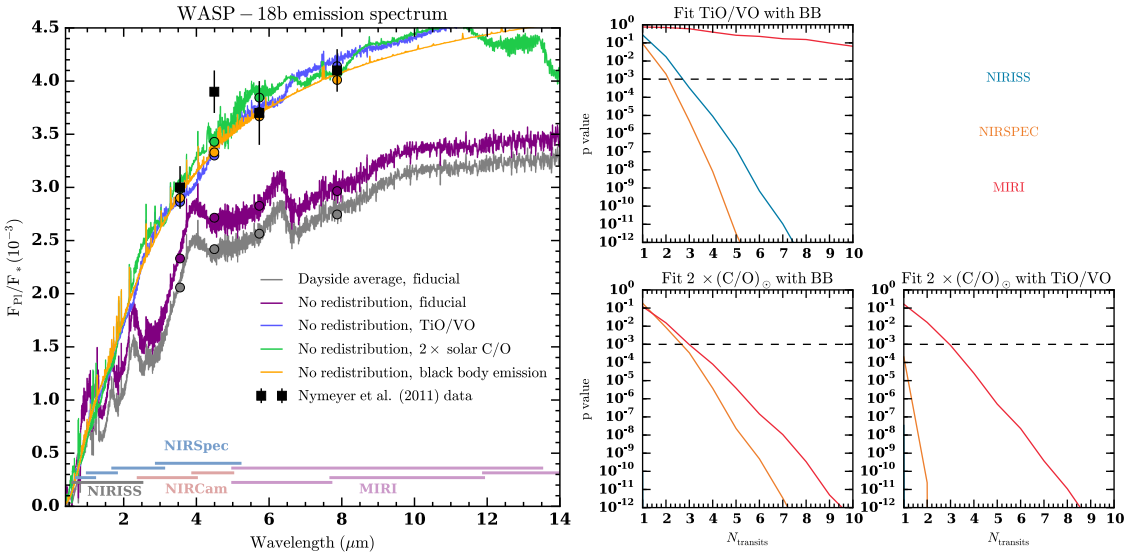

FIGURE 5.7: *Left panel:* Synthetic spectra and observational data of the emission spectrum of WASP-18b. A description of the different lines is shown in the legend. The observational data by Nymeyer et al. (2011) are shown as black errorbars. The 'emission' lines, which can be made out in the blackbody $F_{\rm Pl}/F_*$ spectrum, are absorption lines of the stellar spectrum. The colored circles show the corresponding *Spitzer* channel values for the synthetic spectra. *Right panel:* p values of the Kolmogorov-Smirnov test of the residuals between the synthetic observation of the three WASP-18b models and the two respective remaining models. The p value is shown as a function of $N_{\rm transit}$ for data taken with the three different instruments listed in Table 5.3. In order to avoid distinguishing between the models based on offsets, the residual distributions were shifted to have a mean value of 0. The black dashed line denotes our threshold value of 10^{-3}. If an instrument is not shown in one of the three sub-panels then it has a p value lower than 10^{-12} already after one observation. Figure taken from Mollière et al. (2017).

flux then the dayside effective temperature $T_{\rm day}$ would be 2870 K. Yet, the measured dayside emission flux of this planet is consistent with brightness temperatures between 3100 and 3300 K, and the spectrum can be fit reasonably well by a blackbody at 3200 K (although an inversion fits better, see Nymeyer et al. 2011). Theoretically, the maximum flux that can be measured for an irradiated planet when observed during transit geometry, and when assuming blackbody emission, is equal to the flux emitted by a blackbody of temperature $T_{\rm max} = T_* \sqrt{R_*/a}$, where T_* is the stellar effective temperature, R_* the stellar radius and a the planet's semi-major axis (see Appendix A.4.1 for a derivation). Note that the shape of the SED of such a planet would correspond to an even higher temperature, because the planet must emit all flux close to the substellar point, and into the direction of the observer: if the planet truly had a global temperature of $T_{\rm max} = T_* \sqrt{R_*/a}$, it would violate energy conservation, emitting more flux than it receives from the star.

For WASP-18b, $T_{\rm max} = 3410$ K, such that the planet's corresponding blackbody temperature of 3200 K is still below this theoretical limit. Nonetheless, this suggests that a non-negligible fraction of the planetary flux must be emitted close to the location of the substellar point and thus into the direction of the observer during eclipse geometry. One can also see this by considering the insolation flux received by each circular planetary annulus at an angle ϑ away from the substellar point, which is $F(\vartheta) = T_*^4 (R_*/a)^2 \cos(\vartheta)$. If one neglects any energy redistribution due to winds, then the planetary surface at angle ϑ away from the substellar point has to re-emit exactly $F(\vartheta)$. Assuming blackbody emission, one finds that the flux measured during transit geometry is the same as if the planet had a global temperature of $T_{\rm rad} = (2/3)^{1/4} T_* \sqrt{R_*/a}$ (see Appendix A.4.2 for a derivation), which

corresponds to 3080 K for WASP-18b. This is less than the stated blackbody temperature of 3200 K, suggesting that for this planet, energy redistribution may not only be limited, but fully absent.

The same situation seems to be the case for Kepler-13Ab, which is best fit by an inversion in its atmosphere, yet also reasonably well described by a blackbody at 2750 K (Shporer et al. 2014). For this planet, the theoretical upper limit on the observable effective temperature, as seen during eclipse geometry, is $T_{\rm max}$=3085 K, the temperature derived for the case fully neglecting energy redistribution is $T_{\rm rad}$=2790 K, the dayside averaged effective temperature is $T_{\rm day}$=2590 K, if nightside emission is neglected, and the global equilibrium temperature would be $T_{\rm equ}$=2180 K. The measured effective temperature of the planet is closest to $T_{\rm rad}$, suggesting that wind redistribution of stellar insolation energy may be neglected for this planet as well. Interestingly, and quite paradoxically, Shporer et al. (2014) derive a geometric albedo of $0.33^{+0.44}_{-0.06}$ for this planet, corresponding to a bond albedo of 0.5, if a matte, that is, perfectly Lambertian[3], scattering process is assumed. This albedo value arises from the fact that the optical eclipse depth for this planet shows an excess, which cannot be explained by 1D model calculations investigated in Shporer et al. (2014). The effective blackbody temperature derived from emission observations in the infrared (2750 K) is inconsistent with a bond albedo of 0.5, for which $T_{\rm max}$ would be only 2590 K. Note, however, that the derivation of the geometric albedo in Shporer et al. (2014) assumed that the brightness temperature as well as the geometric albedo are constant within the three different bands used in their analysis, which is not necessarily the case. Further, the presence of scattering aerosols in the planet's atmosphere in this high albedo case requires particles that are stable even at the high temperatures found for this planet, which is challenging. The measured excess of the optical eclipse depth may therefore be the emission feature of an unknown opacity source.

The planet WASP-33b is less extreme, because its theoretical dayside averaged effective temperature is $T_{\rm day}$ = 3250 K, that is, still above the value derived when a blackbody is fitted to the emission observations (2950 K, see Haynes et al. 2015). Note that this planet is also fit better by an inversion than by a blackbody.

Given the fact that WASP-18b and Kepler-13Ab seem to have only limited, or no redistribution of the stellar insolation energy at all, I decided to calculate spectra for these planets, fully neglecting the redistribution, using Scenario (c) described in Section 5.3.5.

I show the resulting spectra in the left panel of Figure 5.7, together with the data by Nymeyer et al. (2011). No offset or scaling factor was applied to the synthetic spectra. As one can see, the fiducial case (no clouds, solar C/O ratio, and no TiO/VO opacities) is least capable to fit the data, being multiple sigmas away from all the measured points. For comparison, I also plot the fiducial case when assuming a dayside averaged insolation. In this case, the synthetic spectrum is even further away from the data.

Only three scenarios provide a good fit to the data, namely the case where I included TiO/VO opacities, which lead to an inversion, the case where I consider a C/O ratio that is twice the solar value, leading to C/O = 1.12, and the case where I assume the planetary

[3]Lambertian scattering denotes the process of isotropic scattering, when all information on the direction of the incoming light is lost.

annuli to emit as isothermal blackbodies. It was crucial to neglect redistribution for these cases. The corresponding dayside-averaged cases resulted in fluxes that were too low. The 'emission' lines, which can be made out in the blackbody $F_{\rm Pl}/F_*$ spectrum, are absorption lines of the stellar spectrum.

Note that the *Spitzer* point at 4.5 μm does not seem to be fitted by the models. However, a good fit to data is not about the model perfectly describing every data point. In fact, if the error bars of a measurement are estimated accurately, then one expects that one third of all measured points are further than 1 σ away from the prediction of the 'correct' model. To assess the goodness of fit of the models to the data I will again make use of the Kolmogorov Smirnov test. Note that χ^2 may be used to compare the various models against each other, but not to assess the overall goodness of fit of a given model: For a linear model, the expected value of a model correctly describing the data is $\chi^2 = \#\mathrm{dgf}$, where $\#\mathrm{dgf}$ is the number of degrees of freedom, such that $\chi^2_{\rm red} = 1$. However, the spectral models we use here are non-linear, with the exact number of the degrees of freedom unknown. The expected χ^2 value of a model consistent with the data can therefore not be calculated, and the use of the χ^2 to assess the goodness of fit is not allowed (also see Andrae et al. 2010). The p value of the Kolmogorov Smirnov test applied on the residuals between the WASP-18b *Spitzer* measurements and the data, on the other hand, represents a valid method for assessing the goodness of fit. The p values for the TiO/VO, C/O=2$\times$(C/O)$_\odot$ and blackbody model are 0.38, 0.82 and 0.13, respectively. All models are therefore consistent with the data, with the best fit being provided by the C/O=2$\times$(C/O)$_\odot$ model.

For the high temperatures considered here, gaseous SiO may become important because the dayside of the planet is too hot to form any silicate clouds. I neglect the opacity of SiO, but this molecule is a strong UV absorber for $\lambda < 0.3$ μm (see, e.g., Sharp & Burrows 2007), and may therefore lead to even stronger inversions. In future calculations, an inclusion of the SiO opacities for these hottest planets is therefore necessary.

The C/O = 1.12 case fits the data well because C/O ratios close to 1 may cause inversions, see Mollière et al. (2015, and Chapter 4). Such inversions form because for C/O ratios close to 1, oxygen and carbon are predominantly locked up in CO, decreasing the abundance of water if approached from C/O < 1, or that of methane and HCN if approached from C/O > 1. Because water, methane and HCN have large IR opacities, they are the atmosphere's most effective coolant. Therefore, for C/O ~ 1, the cooling ability of the atmospheres is decreased, while the heating due to the alkali absorption of stellar light stays strong (note that I include the equilibrium ionization for sodium and potassium).

Given the fact that the blackbody emission case fits the data well, one can also understand why the inversion cases provide a good fit to the data: the inversion stops the monotonous decrease of temperature within the atmosphere, leading to smaller temperature variations across the photosphere. The photosphere therefore becomes more isothermal (also see Section 5.4.4).

Similar to the analyses carried out for the transiting planets, I now look into the number of transits needed to distinguish between the three models which fit the observational data best. Applying an offset to the spectra for the emission spectra presented here would violate

energy conservation, therefore I first carried out the analysis without applying an offset at first. In this case the spectra of the three models can be distinguished from each other using only a single eclipse observation, in either of the three instruments considered here.

However, in order to assess how well the models may be distinguished because of differences in their spectral shape, I next applied an offset to the models before carrying out the Kolmogorov-Smirnov test. This was done by shifting the mean value of the residual distribution to zero. The corresponding plots are shown in the right panel of Figure 5.7. Physically, such an offset may be motivated by a non-negligible redistribution of the stellar insolation, decreasing the planetary flux measured during an eclipse observation. It has to be kept in mind, however, that a simple offset as carried out here is only an approximation, because the spectral shape may change under such conditions.

In general, the results follow the expectations: *JWST* is less capable of distinguishing between the TiO/VO and the blackbody case because the TiO/VO case does not have many features and is mostly simply offset in comparison to the blackbody model. This is especially true in the *MIRI* wavelength range, such that ten transits are not enough to distinguish between the two models at high confidence, because I do not allow for the distinction between two models based simply on an offset in this test: this is why I applied the aforementioned shift of the residual distribution. The instrument best suited for distinguishing both models is *NIRSpec*, achieving this goal in just two transits.

JWST's capability of distinguishing the CO = 1.12 and the blackbody case is much better, due to features visible in the spectrum of the CO=1.12 case: The features at 3 μm, 6.5 to 8.5 μm and from 11 μm onward all stem from HCN absorption (not emission), whereas the feature at 4.5 μm is caused by CO absorption. These are typical absorbers expected for a hot, carbon-rich atmosphere. The largest diagnostic power is provided by using *NIRISS* observations (one eclipse measurement), while *MIRI* and *NIRSpec* can discriminate between the models after three eclipse measurements.

The easiest case to distinguish is the case when comparing the C/O = 1.12 to the TiO/VO model because both these cases show molecular features. Again, *NIRISS* (and also *NIRSpec*) is best at achieving this goal, using just a single transit, whereas *MIRI* needs three transits. In conclusion, one can therefore say that if one of our self-consistent models was the true state of the atmosphere, then *JWST* could determine its state by taking between one and three transits in *NIRISS*. Of course I do not prove that the three models here are the only possible ones, but the example illustrates the foreseen diagnostic power of *JWST* for such atmospheres.

5.6 Summary

In this study I present a set of self-consistent atmospheric calculations for prime transiting exoplanet targets to be observed with *JWST*, based on the work published in Mollière et al. (2017). The grid of models presented here is available online, including the atmospheric

structures, abundances, and transmission and emission spectra. For the spectra, I additionally published wavelength dependent uncertainties for *JWST* observations, derived from radiometric modeling.

The exoplanet targets have been chosen because they have a high expected signal-to-noise, cover the $T_{\rm equ}$–$\log(g)$ space homogeneously, and include planet types ranging from super-Earths to hot Jupiters. This diverse set of targets may therefore allow the study of the the full breadth of transiting exoplanets at high SNR.

Because the data currently available for these planets is often limited, both in its spectral coverage and SNR, it is crucial to explore different atmospheric scenarios in order to assess the width of possible observational results that may be seen once *JWST* becomes available. To this end, I explored a wide range of scenarios, by varying the planets' enrichment and composition (C/O ratio), and optionally included absorbers in the optical (TiO/VO). Additionally, I put a large emphasis on studying the effects of different cloud properties. Furthermore, I apply different assumptions for the heat-redistribution; and mimic them by changing the irradiation, assuming either a planet-wide or dayside average of the irradiation. For some selected, very hot planets I also studied the case of fully neglecting the redistribution of stellar irradiation.

Given the large uncertainties when trying to model clouds self-consistently, I use two different cloud models, applying either my implementation of the (Ackerman & Marley 2001) cloud model (see Section 3.5.1), or by applying the simple three-parameter cloud model, see Section 3.5.2. Because cloud particles in planetary atmospheres are expected to be crystalline, rather than amorphous, I use optical constants for crystalline material whenever available. Additionally, all direct detections of crystalline silicate grains in different astrophysical contexts suggest that the grains should be irregularly shaped dust agglomerates, such that this is my standard assumption. The case of spherically-homogeneous cloud particles, with opacities derived from standard Mie theory, is studied as an optional case.

All calculations I presented here are compared to observational data whenever available. For a selected subset of the targets, I study and compare different models that are consistent with the available data, and investigate how well *JWST* may be at distinguishing them, and which instrument is best used for this task. The method I use for this subset study may be applied to any models within our grid. I summarize the main findings of this study below.

- *Super-Earths with thick cloud cover* were studied by investigating our models for GJ 1214b. I find that if one assumes a heavy enrichment (1000 $\times$ solar) and a thick cloud deck, then the models are consistent with current observational data. While the current data are consistent with a completely flat, featureless spectrum, I find that $<$10 transits with the *NIRSpec* instrument may be sufficient to unambiguously reveal CO_2 and CH_4 features in the atmosphere of this planet. For a more conclusive statement on the number of transits needed to characterize this planet, given my models, more sophisticated statistical tools, such as retrieval analyses, are required. I have already started to implement a fast radiative transfer solver and first retrieval code, see Chapter 6 and plan to carry out such analyses as a next step.

- **Gas giants** were studied by investigating the models calculated for HAT-P-12b and TrES-4b. In concordance with previous studies, I find that vertically homogeneous, small particle (< 0.1 μm) clouds are best at producing strong Rayleigh scattering signatures, but only if iron-bearing cloud species are neglected. For TrES-4b, I expect a feature at 10 μm in the transmission spectrum if it harbors clouds that are made up from such small silicate particles. I find that one transit with *MIRI* may be sufficient to reveal the 10 μm feature, while less than ten transits may be enough to distinguish between irregularly shaped or spherically-homogeneous cloud particles, if the silicate species is known. Similarly, more sophisticated statistical tools will improve the analysis of the minimum number of transits required. A full characterization of silicate cloud particles (species, size distribution, vertical extent, particle shape, etc.) will likely require more transits.

- **Extremely hot transiting planets** are often well fitted by isothermal emission when comparing to the data from eclipse measurements. I study the planet WASP-18b as an example and find that self-consistent models can explain the observations of this planet if energy redistribution by winds is fully neglected. The model setups which fit current observational data best are models featuring inversions either because of TiO/VO absorption or because of C/O number ratios close to 1. In this latter scenario, the main coolants (water or methane and HCN) are significantly depleted in favor of CO, such that inversions form. I find that a single eclipse observation with *NIRSpec* is enough to distinguish between these cases.

By investigating these three example cases, I show that *JWST* will be able to shed light on many intriguing puzzles of atmospheric studies that are difficult to solve using today's observational facilities. Further, by publishing my atmospheric model calculations, along with synthetic observational uncertainties for *JWST*, I allow for the study of different possible scenarios and how well they can be observed and distinguished.

It has to be kept in mind that pitting given models against each other does not answer how conclusively we will be able to characterize a given atmosphere using *JWST* data. For such assertions, retrieval studies for the synthetic models would have to be carried out, and the results compared to the input model, as was done in Greene et al. (2016), but even then the conclusions depend on the input models. Nonetheless, studying the atmospheric models for the target planets as presented here enabled me to evaluate the power of *JWST* at constraining the atmospheric state given various likely, self-consistent solutions for the investigated planets, which are consistent with the data available today.

Finally, because the full models are published, including temperature and abundance structures, retrieval models may be tested on the grid, allowing for the study of the retrievability of the expected *JWST* observations when considering self-consistent atmospheric models.

6 Atmospheric parameter retrieval from spectral observations

6.1 How to characterize an exo-atmosphere from observations

The state-of-the-art approach to characterize exoplanet atmospheres from observations is to carry out retrievals. In general, the term 'retrieval' describes processes which seek to answer the question *"what are the values of the parameters describing the atmospheric structure, such that they give rise to the observations, within the uncertainties?"*. In Section 1.4.2, I gave a detailed introduction to atmospheric characterization techniques, such that only a short summary will be given here. For more information, the reader is referred to Section 1.4.2.

There exist multiple approaches to go about answering the above question, with different advantages and disadvantages. In general, one usually constructs an atmospheric model, with input parameters $\mathbf{x} \in \mathbb{R}^n$, which gives rise to synthetic observables. These can then be compared with the data $\mathbf{d} \in \mathbb{R}^m$. Such models can be divided into self-consistent and parametrized models.

In the former the parameters $\mathbf{x}$ contain physically meaningful quantities, such as the atmospheric metallicity, surface gravity, equilibrium temperature, etc. The models then proceed to find the atmospheric state in a physically self-consistent way, such as in *petitCODE*. The main problem with such models is that they are computationally expensive. If the dimensionality of the parameter space is not too high, this problem may be circumvented by precalculating a grid of model atmospheres. Nonetheless, there is no guarantee that the solution is to be found within the boundaries of the grid. In such cases an optimal estimation fitting approach may be used to find the best-fit parameters, but there is the danger of only finding a local minimum in the solution space, and the parameter uncertainties cannot be well constrained, especially if the data quality is low. Moreover, there is no guarantee that the self-consistent models contain all necessary physics, such that the retrieval approach may not be able to find the correct, physical solution, because it is not contained in the model's solution space. Moreover, the model may allow to find a good fit to the data, but with incorrect choices of the atmospheric model parameters $\mathbf{x}$, in order to make up for the missing physics.

The second possibility is to more or less fully parametrize the atmospheric model, such that the abundances, and temperature profiles do not need to be consistent with any physical constraints. Such 'free retrievals' will then find the parameter choice that best describes

the data, regardless of being physically plausible or not. While this is an disadvantage, the clear advantage is that such models can be computed much faster, because no iteration, in order to satisfy physical constraints, is necessary. In addition, physical constraints can be imposed by using parametrization functions which are based on physical considerations, or by placing penalties on, or downright reject, parameter combinations which clearly violate physical constraints. While the model flexibility in free retrievals can be dangerous, it can also be beneficial, by possibly correctly constraining the atmospheric state, and uncovering missing physics in the self-consistent model approaches at the same time. Moreover, because they can be calculated quickly, they allow for a full determination of the posterior parameter distribution function, and hence uncertainties. Moreover, they allow for the direct comparison between two given models, e.g. by using nested sampling, and thus to find the more likely one, see Section 1.4.2.

In what follows below, I will describe how I constructed a free retrieval tool, using my own implementation of a fast radiative transfer solver, and an open-source, publicly available, and highly efficient implementation of the Markov Chain Monte Carlo (MCMC) method. The radiative transfer solver used for this purpose differs from the one used in *petitCODE* in that it is trimmed for speed. The method is described in Section 6.3.1. It currently neglects scattering processes for the computation of emission spectra, and is verified by comparing to *petitCODE* spectra (with scattering turned off) in Section 6.3.4. Like all Bayesian atmospheric retrieval tools currently in use (for their description, and examples of their application, see, e.g., Irwin et al. 2008; Madhusudhan & Seager 2009; Benneke & Seager 2012; Line et al. 2012; Lee et al. 2012; Line et al. 2013b; Benneke 2015; Waldmann et al. 2015a; Greene et al. 2016; Feng et al. 2016; Brogi et al. 2017; Rocchetto et al. 2016; MacDonald & Madhusudhan 2017), my retrieval implementation currently neglects scattering for the calculation of the emission spectra. In addition, because this is a code for free retrieval, the atmospheric structure is fully parametrized.

A general introduction to MCMC is given in Section 6.2. The fast radiative transfer model is described in Section 6.3, and the parametrized atmospheric model in Section 6.4. I show first tests of the retrieval method in Section 6.5. I give an outlook, and how I want to expand the code in the future, in Section 6.6.

6.2 The Markov Chain Monte Carlo (MCMC) method

As stated above, the goal of a Bayesian atmospheric retrieval code is to find the distribution of values $\mathbf{x}$ of the n parameters, where $\mathbf{x} \in \mathbb{R}^n$, which describe the data $\mathbf{d} \in \mathbb{R}^m$, which could be a vector with, e.g., measured fluxes in m different wavelengths. As lined out in Section 1.4.2, Bayes' theorem states that the probability distribution of $\mathbf{x}$ can be written as

$$P(\mathbf{x}|\mathbf{d}) = \frac{P(\mathbf{d}|\mathbf{x})P(\mathbf{x})}{P(\mathbf{d})} \,, \tag{6.1}$$

where the prior $P(\mathbf{x})$ encapsulates any knowledge that we have, e.g., from physical considerations, or other measurements. $P(\mathbf{d}|\mathbf{x})$ can, e.g., be expressed as $e^{-\chi^2/2}$, i.e. be calculated

from the χ^2 between a model realization and the data. While all quantities on the RHS of the above equation are straightforward to calculate, it is often numerically unfeasible to do so, especially because the model evidence

$$P(\mathbf{d}) = \int P(\mathbf{d}|\mathbf{x})P(\mathbf{x})d^n\mathbf{x}\,, \tag{6.2}$$

requires to carry out an integral over n dimensions, and the evaluation of $P(\mathbf{d}|\mathbf{x})$ can be very expensive. Here the MCMC method helps: it allows to efficiently draw samples from the target distribution of $P(\mathbf{x}|\mathbf{d})$, rather than carrying out the integral of Equation 6.2.

In the following, I will quickly outline how MCMC works, based on the very good introduction given in Springel (2014). The basis of MCMC is the so-called 'Markov process' f, which transforms a state vector $\mathbf{x}$, describing a certain choice of parameter values of the model, to a state vector $\mathbf{x}'$, with a probability distribution $W_f(\mathbf{x}'|\mathbf{x})$, such that $\int W_f(\mathbf{x}'|\mathbf{x})d^n\mathbf{x}' = 1$ and $W_f(\mathbf{x}'|\mathbf{x}) \geq 0$. $W_f(\mathbf{x}'|\mathbf{x})$ does only depend on $\mathbf{x}$, and not on any previous states of $\mathbf{x}$. If a sufficiently large set of states $\mathbf{x}$ is drawn from an arbitrary probability distribution $\mathcal{P}(\mathbf{x})$, then the application of f on all states of the set will give rise to states $\mathbf{x}'$ following the probability distribution

$$\mathcal{P}'(\mathbf{x}') = \int W_f(\mathbf{x}'|\mathbf{x})\mathcal{P}(\mathbf{x})d^n\mathbf{x}\,. \tag{6.3}$$

Note that I write $\mathcal{P}(\mathbf{x})$ instead of $P(\mathbf{x})$ here, to prevent a confusion of $\mathcal{P}(\mathbf{x})$ with the prior $P(\mathbf{x})$. It now holds that if there exists an equilibrium distribution $\mathcal{P}_{\rm equ}$ with

$$\mathcal{P}_{\rm equ}(\mathbf{x}') = \int W_f(\mathbf{x}'|\mathbf{x})\mathcal{P}_{\rm equ}(\mathbf{x})d^n\mathbf{x}\,, \tag{6.4}$$

and if f can reach any state $\mathbf{x}'$ starting from any state $\mathbf{x}$ (if f is applied a sufficient number of times), then the distribution of an ensemble of states $\mathbf{x}$ will approach $\mathcal{P}_{\rm equ}$ if f is applied to them often enough (Springel 2014). It furthermore holds that there can exist only one equilibrium distribution $\mathcal{P}_{\rm equ}$ for a Markov process f, such that the function $\mathcal{P}_{\rm equ}$, towards which the ensemble distribution $\mathcal{P}$ converges, is unique. Moreover, it holds that not only the distribution of an ensemble of states will approach $\mathcal{P}_{\rm equ}$, also the distribution of all values of a single state $\mathbf{x}$, to which f was applied sufficiently often, will approach $\mathcal{P}_{\rm equ}$ (Springel 2014). Such a sequence of states, arising from the successive application of f, is called 'Markov Chain'.

The goal of a Markov Chain Monte Carlo method in Bayesian atmospheric retrieval therefore is to create a Markov process f which has $P(\mathbf{x}|\mathbf{d})$ as its equilibrium distribution. Moreover, f should be chosen in a way such that it transforms any $\mathcal{P}(\mathbf{x})$ to $\mathcal{P}_{\rm equ}(\mathbf{x})$ with as few Markov steps as possible, such that any successively sampled state positions can be regarded as being sampled from $\mathcal{P}_{\rm equ}$. I describe one such choice of f below, as well as give a summary of the actual method being used in my retrieval implementation.

6.2.1 Detailed balance and the Metropolis-Hastings algorithm

Again, the explanations here are based on the steps outlined in Springel (2014).
A Markov process will converge the distribution of state ensembles to $\mathcal{P}_{\mathrm{equ}}$ if f is chosen such that

$$\mathcal{P}_{\mathrm{equ}}(\mathbf{x}) W_f(\mathbf{x}'|\mathbf{x}) = \mathcal{P}_{\mathrm{equ}}(\mathbf{x}') W_f(\mathbf{x}|\mathbf{x}') \,, \tag{6.5}$$

which is called the 'detailed balance' condition. This follows from using Equation 6.5 for calculating

$$\int W_f(\mathbf{x}'|\mathbf{x}) \mathcal{P}_{\mathrm{equ}}(\mathbf{x}) d^n\mathbf{x} = \int W_f(\mathbf{x}|\mathbf{x}') \mathcal{P}_{\mathrm{equ}}(\mathbf{x}') d^n\mathbf{x} = \mathcal{P}_{\mathrm{equ}}(\mathbf{x}') \,, \tag{6.6}$$

which is equal to Equation 6.4.

Now, one such Markov process, satisfying detailed balance, is the Metropolis-Hastings algorithm. For a given state $\mathbf{x}$ one starts by proposing to change to a new state $\mathbf{x}'$, where the proposal state $\mathbf{x}'$ is drawn from a probability distribution $q(\mathbf{x}'|\mathbf{x})$. The proposal state is now accepted with the probability r, where r is the so-called 'Hastings ratio'

$$r = \min\left(1, \frac{\mathcal{P}_{\mathrm{equ}}(\mathbf{x}') q(\mathbf{x}|\mathbf{x}')}{\mathcal{P}_{\mathrm{equ}}(\mathbf{x}) q(\mathbf{x}'|\mathbf{x})}\right) \,. \tag{6.7}$$

This is done by drawing a random number u, uniformly distributed between 0 and 1, and accepting the change of $\mathbf{x}$ to $\mathbf{x}'$ if $u \leq r$. If it is not accepted, then the updated state is $\mathbf{x}' = \mathbf{x}$. Proposing an $\mathbf{x}'$ drawn from $q(\mathbf{x}'|\mathbf{x})$, together with accepting it with a probability r, then corresponds to a step of the Markov process. If, without loss of generality, $r < 1$, it then holds that

$$W_f(\mathbf{x}'|\mathbf{x}) = r \cdot q(\mathbf{x}'|\mathbf{x}) = \frac{\mathcal{P}_{\mathrm{equ}}(\mathbf{x}') q(\mathbf{x}|\mathbf{x}')}{\mathcal{P}_{\mathrm{equ}}(\mathbf{x})} \,, \tag{6.8}$$

while $W_f(\mathbf{x}|\mathbf{x}') = q(\mathbf{x}|\mathbf{x}')$, because the r of the inverse transition must be 1. Together with Equation 6.8 this thus means that this Markov process satisfies detailed balance.

The algorithm outlined above is also called 'Metropolis-Hastings' algorithm. In a Bayesian atmospheric retrieval one can now sample $P(\mathbf{x}|\mathbf{d})$ by setting $\mathcal{P}_{\mathrm{equ}}(\mathbf{x}) = P(\mathbf{x}|\mathbf{d})$, such that the Hastings ratio becomes, using Bayes' theorem,

$$r = \min\left(1, \frac{P(\mathbf{x}'|\mathbf{d}) q(\mathbf{x}|\mathbf{x}')}{P(\mathbf{x}|\mathbf{d}) q(\mathbf{x}'|\mathbf{x})}\right) = \min\left(1, \frac{P(\mathbf{d}|\mathbf{x}')}{P(\mathbf{d}|\mathbf{x})} \cdot \frac{P(\mathbf{x}')}{P(\mathbf{x})} \cdot \frac{q(\mathbf{x}|\mathbf{x}')}{q(\mathbf{x}'|\mathbf{x})}\right) \,, \tag{6.9}$$

which shows that the Metropolis-Hastings algorithm is independent of the model evidence. The last missing ingredient would be to decide on a specific shape $q(\mathbf{x}'|\mathbf{x})$, which could correspond to, e.g., $\mathbf{x}' = \mathbf{x} + \mathbf{u}$, with u being drawn from a multidimensional normal distribution, hence q would be a normal distribution.

6.2.2 Affine-invariant ensemble samplers and the `emcee` package

I gave a very simple example for the proposal distribution q in the Metropolis-Hastings algorithm above. If the shape of $P(\mathbf{x}|\mathbf{d})$ is unknown, it can be inherently difficult to find a

proposal distribution q which efficiently produces a representative sample of $P(\mathbf{x}|\mathbf{d})$. As an example, consider a case where the distribution to be sampled is

$$\mathcal{P}(x_1, x_2) \propto \exp\left(-\frac{x_1^2}{2\sigma^2} - \frac{x_2^2}{20000\sigma^2}\right) . \tag{6.10}$$

In this case, if q was an isotropic, 2-dimensional normal distribution, we would probably define it with a width of $\sigma/100$ in order to be able to resolve the smaller spread of x_2 well. In that case we would have to sample for a long time for an ensemble state to traverse a distance of σ in the x_1 direction, such that the MCMC sampling would be very inefficient. In general, classical MCMC schemes need to be set up very carefully, and if they use a multi-dimensional normal distribution for q, they should ideally include the full covariance matrix, such that one ends up with $N(N+1)/2$ tunable parameters before the MCMC chain is even started. This is necessary to account for non-isotropic, skewed or even multimodal target distributions P. For the example distribution above there exists a so-called 'affine' (meaning linear) coordinate transformation, however, which makes P isotropic, and thus easy to sample, namely $x_1' = x_1$ and $x_2' = x_2/100$. An affine transformation can therefore greatly improve the sampling efficiency, but it can also make it worse, if it is not chosen appropriately.

In my retrieval implementation I use the MCMC sampler called `emcee`, which is a freely available Python version of the 'affine-invariant' MCMC ensemble sampler introduced by Goodman & Weare (2010). `emcee` was written by Foreman-Mackey et al. (2013). Affine-invariance means that the performance of `emcee` is completely unaffected by any affine transformations, such that no matter how "unfortunate" the choice of the parameter coordinates, it will always converge with the same speed. This is facilitated by advancing a set of N so-called 'walkers' $\mathbf{x}_k$, i.e. a set of states $\mathbf{x}_k$ with $k \in [1, \ldots, N]$. Once all ensemble states have been updated by the Markov process, a new Markov step begins. For this `emcee` randomly draws, for every walker $\mathbf{x}_i$, another walker $\mathbf{x}_j$ with $i \neq j$ from the ensemble. $\mathbf{x}_i$ is then updated to $\mathbf{x}_i' = \mathbf{x}_j + z(\mathbf{x}_i - \mathbf{x}_j)$ with a probability r, given by the Hastings ratio. z is drawn from a probability distribution $g(z) = 1/\sqrt{z}$ for $z \in [1/a, a]$, with $a > 1$. The Markov process will thus shift the state $\mathbf{x}_i$ along the line defined by $\mathbf{x}_i - \mathbf{x}_j$ to yield $\mathbf{x}_i'$, and accept the shift with a probability r. z values placing $\mathbf{x}_i'$ closer to $\mathbf{x}_j$ than $\mathbf{x}_i$ was to $\mathbf{x}_j$ before are more likely, but note that the shift will likely not be accepted if the corresponding Hastings ratio is small, i.e. if $\mathbf{x}_j$ is much less likely than $\mathbf{x}_i$. Moreover, the interval of possible $z > 1$ values is larger than the interval of possible $z < 1$ values. The only free parameter of `emcee` is a, i.e. no twiddling with a multitude of hyperparameters of q is necessary.

It can be intuitively understood why the Markov process used in `emcee` is affine-invariant: the shift of a walker is always by a fraction of the distance to another walker. This means that if the target distribution $\mathcal{P}$ is narrow along a given direction, then the walkers will, in general, not take too big steps along this direction. This assumes that the walkers already occupy the region defined as most likely by the target distribution. This is of course not the case for the first ensemble steps, but the walkers will likely move closer to the positions of the ones with the highest likelihood $P(\mathbf{d}, \mathbf{x})$, due to the probability r defined by the hastings

ratio.

When drawing samples from $P(\mathbf{x}, \mathbf{d})$, `emcee` will thus propose shifts for all the walkers based on the ensemble's current position, and then calculate the likelihood $P(\mathbf{d}, \mathbf{x})$ at the proposed positions to assess whether the walkers should move or not. After this the process is restarted. Hence, the likelihood calculation of every Markov step can be parallelized, making `emcee` the ideal tool to use on clusters, when drawing a large number of samples with computationally expensive likelihood estimations.

6.3 Fast forward model development

While correlated-k (see Section 3.2.2) greatly speeds up the radiative transfer calculation, deriving the total opacity from a large number of individual line species (see Appendix A.1) is still costly in computational terms. For retrieval applications millions to hundreds of millions of spectra need to be generated at high enough spectral resolution, such that even if parallelization is used the amount of time spent on the computation of a single spectrum should not exceed a couple of seconds. It would thus be favorable to be able to calculate spectra without having to calculate the total opacity $\kappa_{\rm tot}(g)$, and to use the $\kappa_i(g)$ of the individual species i directly. I will outline how to do this below.

6.3.1 Emission spectra

For the calculation of the emission spectra one has to solve the formal radiative transfer equation

$$\frac{dI(\tau)}{d\tau} = S(\tau) - I(\tau) \,, \tag{6.11}$$

where, as usual, I is the specific intensity, S the source function and τ the optical depth. Wavelength dependencies have been neglected in this notation. Next I use that, if S is known, the solution to this first order differential equation can be written as

$$I(\tau) = I(0)e^{-\tau} + \int_0^\tau S(\tau')e^{\tau'-\tau}d\tau' \,, \tag{6.12}$$

which is easily verified by inserting this expression into the above equation of radiative transfer. For the outgoing intensity $I^{\rm top}$ at the top of the atmosphere one can thus write

$$I^{\rm top} = I^{\rm bot}\mathcal{T}^{\rm atmo} + \int_{\mathcal{T}^{\rm atmo}}^1 S(\mathcal{T})d\mathcal{T} \,, \tag{6.13}$$

where $I^{\rm bot}$ is the upward pointing intensity at the bottom of the atmosphere, $\mathcal{T}(\tau) = e^{-\tau}$ is the transmission from a given point in the atmosphere to the top, with $\mathcal{T}^{\rm atmo} = \mathcal{T}(\tau^{\rm atmo})$ being the transmission from the bottom of the atmosphere to the top. For the emission-only case, when assuming local thermal equilibrium (LTE) for the atmospheric gas, one can set $S = B$, where B is the Planck function evaluated at the frequency and temperature of interest. In a numerical, discrete-layer representation, the arising intensity in the atmosphere

can thus be written as

$$\bar{I}^{\mathrm{top}} = \bar{B}(T_{\mathrm{bot}})\bar{\mathcal{T}}^{\mathrm{atmo}} + \frac{1}{2}\sum_{i=1}^{N_{\mathrm{L}}-1}\left[\bar{B}(T^i) + \bar{B}(T^{i+1})\right]\left(\bar{\mathcal{T}}^i - \bar{\mathcal{T}}^{i+1}\right) \,, \tag{6.14}$$

where N_{L} is the number of atmospheric layers and the symbol $\bar{Q}$ denotes the wavelength average of a quantity Q within the correlated-k spectral bin of interest. Here I used the fact that the Planck function is roughly constant across one of these bins, and replaced it with its mean value within the bin, before calculating the average of I_{top}. This equation has the advantage that it only depends on the wavelength averaged transmission, which can be obtained without knowing $\kappa_{\mathrm{tot}}(g)$, see below. This makes the evaluation of Equation 6.14 fast, and is the reason why it is used in the correlated-k retrieval code *NEMESIS*. Equation 6.14 is equivalent to their Equation 13 in Irwin et al. (2008). I thus follow their example for the retrieval radiative transport.

Using the correlated-k assumption, and further making the standard assumption that the opacity distribution functions of given molecular species are uncorrelated (see Section 3.2.2), one can write the transmission from a layer i, at pressure P_i, to the top of the atmosphere, at pressure $P = 0$, as

$$\bar{\mathcal{T}}^i = \prod_{j=1}^{N_{\mathrm{species}}}\left[\sum_{l=1}^{N_g}\exp\left(-\int_0^{P_i}\frac{X_j\kappa_{lj}}{a}dP\right)\Delta g_l\right] \,, \tag{6.15}$$

where N_{species} is the number of species, N_g the number of the Gaussian quadrature points in g-space, X the mass fraction of a given species in a given atmospheric layer, a the gravitational acceleration within the atmosphere, and κ_{lj} the opacity of species j at $g = g_l$, see Appendix A.5 for the derivation. In particular one sees that if only the intensity arising from atmospheric emission is of interest, only the atmospheric transmissions needs to be computed, which are themselves the products of the transmissions of the atmosphere's opacity species. This means that the numerically expensive computation of the combined opacity table of all species is not necessary, which allows for a fast correlated-k application in retrieval calculations.

Note that the technique outlined in this section cannot be used for the *petitCODE* calculations. For the *petitCODE* temperature iteration we need to calculate terms such as (see Section 3.6)

$$\kappa_J = \frac{1}{J}\sum_{i=1}^{N_{\Delta\nu}}\left[\int_0^1 \kappa_i(g)J_i(g)dg\right]\Delta\nu_i \,, \tag{6.16}$$

where $N_{\Delta\nu}$ is the number of spectral bins, and $J = \sum_{i=1}^{N_{\Delta\nu}}\left[\int_0^1 J_i(g)dg\right]\Delta\nu_i$. This quantity cannot be expressed using the atmospheric transmission functions alone. Hence $\kappa_{\mathrm{tot}}(g)$ has to be calculated in *petitCODE*, such that the functions $Q(g)$ of radiative quantities Q can be computed.

6.3.2 Transmission spectra

As can be seen from Equation 3.123 in Section 3.8, the planet's transmission radius depends only on the atmospheric transmission, such that also transmission spectra can be calculated quickly, i.e. without calculating $\kappa_{\rm tot}(g)$.

6.3.3 Implementation

I implemented a fast radiative transfer scheme for the calculation of transmission and emission spectra, based on the theory outlined above. For the comparison between the model results and observations the statistical tools publicly available for Python are very useful, such that Python is an ideal language to carry out the retrieval. However, because Python is a script language, it is rather slow, and the numerically expensive part of calculating the planetary model spectra should not be carried out in Python itself. Hence I implemented the methods outlined in sections 6.3.1 and 6.3.2 in FORTRAN, and made them available for use in Python using the *F2PY* package.[1]

For all molecular line opacities I use the same wavelength and pressure–temperature grid as used for *petitCODE*, see Section 3.3. Identically to the treatment in *petitCODE*, I use a wavelength binning such that $\lambda/\Delta\lambda = 1000$ at all wavelengths. The g-grid for the $\kappa(g)$ opacities is set up to be a 16-point Gaussian quadrature grid, separated in an 8-point grid ranging from $g = 0$ to $g = 0.9$ and another 8-point grid ranging from $g = 0.9$ to $g = 1$. Additionally, I solve the radiative transport on a 3-point Gaussian grid for the radiation angle $\mu = \cos\vartheta$, rather than the 20-point Gaussian grid used in *petitCODE*. A comparison of the retrieval code results to *petitCODE* spectra yielded negligible differences, see Section 6.3.4.

6.3.4 Verification

In order to verify my radiative transport implementation for the retrieval code, I compared its spectral calculations to the solutions obtained with *petitCODE*. To that end I took a P–T structure for the fiducial, globally-averaged insolation case of TrES-4b from Mollière et al. (2017). For this test I only considered H_2O, CH_4, CO, and CO_2 line opacities, as well as H_2–H_2 and H_2–He CIA opacities. Nominally, the correlated-k radiative transfer code for retrieval is set up to consider vertically constant molecular abundances, hence I adopted such an abundance model for the test case here. Note, however, that the retrieval correlated-k code can in principle use any arbitrary vertical abundance profile. The adopted mass fractions were $X_{\rm H_2O} = 10^{-2.5}$, $X_{\rm CH_4} = 10^{-5}$, $X_{\rm CO} = 10^{-2}$, and $X_{\rm CO_2} = 10^{-4}$. For the hydrogen and helium abundances I adopted $X_{\rm H_2} = 0.75 \times X_{\rm H/He}$ and $X_{\rm He} = 0.25 \times X_{\rm H/He}$, where $X_{\rm H/He} = 1 - X_{\rm H_2O} - X_{\rm CO} - X_{\rm CO_2} - X_{\rm CH_4}$. The comparison model, regarded as the "truth", were spectra calculated with the *petitCODE* radiative transfer modules, using the same atmospheric setup. The *petitCODE* radiative transfer treatment was verified in Section 3.2.3.

[1] See https://docs.scipy.org/doc/numpy/f2py/.

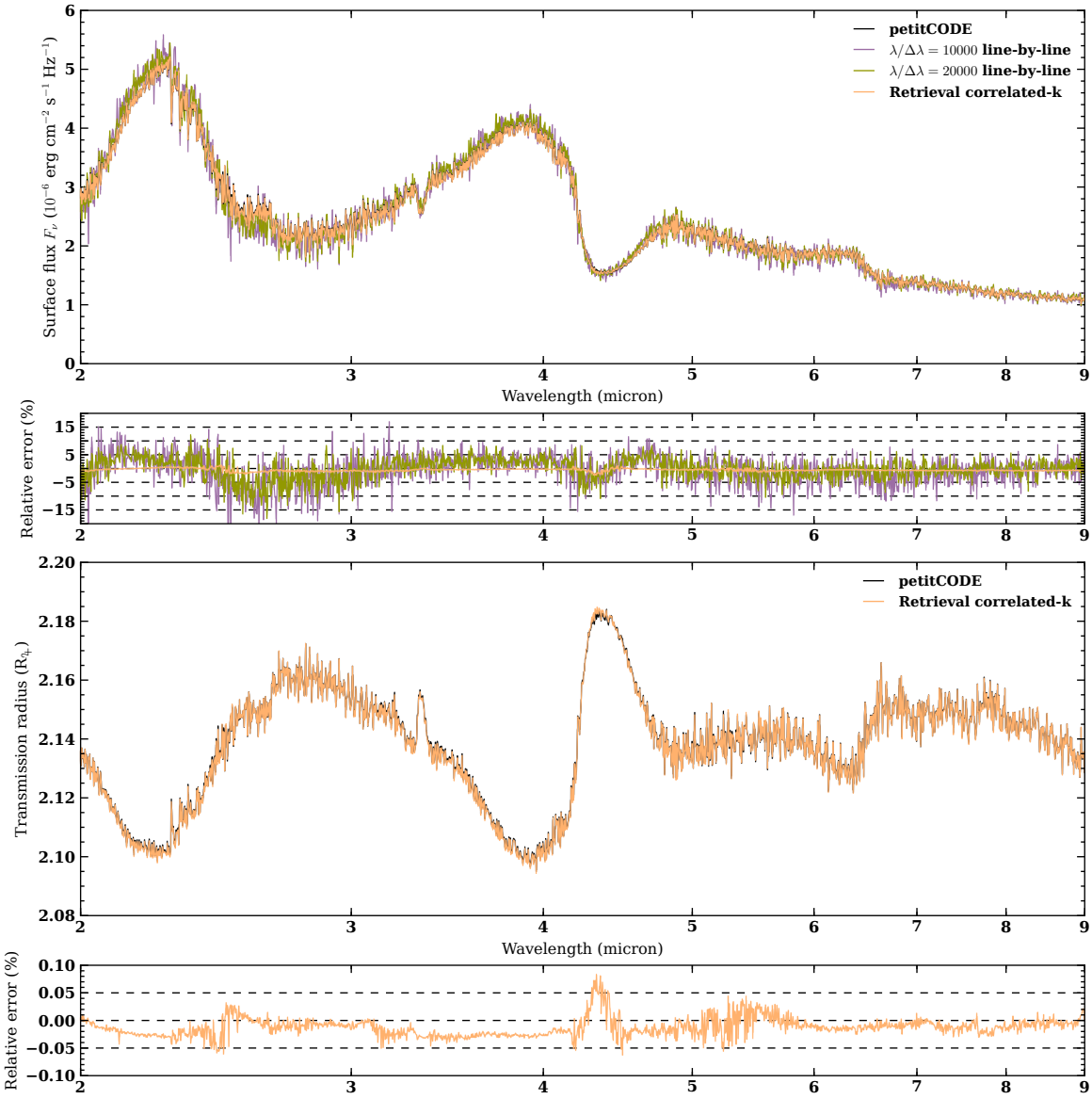

FIGURE 6.1: *Uppermost panel:* emission spectrum using the temperature structure of the fiducial, globally-averaged insolation case of TrES-4b from Mollière et al. (2017), using only H_2O, CH_4, CO, and CO_2 line opacities with vertically constant abundances, as well as H_2–H_2 and H_2–He CIA opacities. Scattering has been neglected. The different lines denote the *petitCODE* radiative transfer (black spectrum), verified in Section 3.2.3, and the retrieval correlated-k implementation (orange line). Liny-by-line calculations for the resolutions $\lambda/\Delta\lambda = 10000$ (purple line) and $\lambda/\Delta\lambda = 20000$ (olive line) are shown as well, having been re-binned to the correlated-k resolution. *Upper middle panel:* relative deviation of the three cases to the *petitCODE* solution. *Lower middle panel:* transmission spectrum for the same case as shown above. Only the *petitCODE* and retrieval correlated-k model are compared here. The corresponding relative deviation of the retrieval correlated-k calculation to the *petitCODE* result is given in the *lowermost panel*.

When starting the implementation of the retrieval scheme I also implemented a line-by-line radiative transfer scheme, i.e. solving the radiative transfer equation with the frequency as the spectral coordinate, rather than the cumulative opacity distribution function g. To remain in the same order of magnitude for the numerical costs and memory used by the correlated-k as well as line-by-line methods, I implemented the line-by-line versions at wavelength binnings of $\lambda/\Delta\lambda = 10000$ and 20000. In order to obtain the opacity grid for the line-by-line case, I randomly sampled my fiducial opacity grid, which has a resolution of $\lambda/\Delta\lambda = 10^6$, as described as a possible method in Section 3.2.2. Only the calculation of

emission spectra was implemented for the line-by-line method, such that I do not show it in the comparison of transmission spectra.

I show the results of the comparison and verification study in Figure 6.1. For the emission spectra, one can see that the relative flux deviation of the correlated-k implementation of the retrieval model is always below 2% when compared to the *petitCODE* solution, and usually smaller. As described in Section 3.2.3, the randomly sampled line-by-line opacity cases have much larger errors, with a larger scatter.The scattering range is in the 5 to 10% regime. As expected, the scatter seems to become smaller at larger resolution. The systematic offsets of the line-by-line case may be due to the line distribution in a given spectral bin, and the average error introduced when randomly sampling an opacity value from that bin. Furthermore, a given P-T opacity grid point was sampled only once, when generating the reduced resolution line-by-line opacities. The sampling error is thus frozen, and affects the opacity error in the temperature range in which the grid point is used for the P–T interpolation. It would be a cleaner way to sample the line-by-line opacities at high-resolution (10^6) for every interpolation step, but loading these opacities into memory is computationally unfeasible.

The transmission spectra are compared in the lower two panels of Figure 6.1. As stated above, only the two correlated-k implementations, of the retrieval code and of *petitCODE*, are compared. Again, the two implementations compare very well, and the transmission radius error is below 0.05 %. However, most of the radius contribution stems from the deep regions of the planet with zero transmission, a value which would be obtained independently from the radiative transfer implementation, because then the exact value of the (large) opacity is not important. It is thus better to normalize the deviation with the transmission signal amplitude, which is roughly 0.06 R_{J}, for a planet size of about 2.1 R_{J}.[2] The relative deviation between the two correlated-k implementations, when measured relative to the amplitude is thus always below ~ 2 %.

6.4 Retrieval model parameters

In the current form of the retrieval code an atmospheric model, and the spectra arising from it, are fully set by the following parameters:

- The atmospheric abundance values X_i, denoting the vertically constant mass fractions of species i with non-negligible opacity.
- The atmospheric mean molecular weight (MMW) μ.
- The planet's surface gravity g and radius R_{Pl}.
- The reference pressure P_0, chosen such that for the planet's pressure-dependent radius it holds that $r(P_0) = R_{\mathrm{Pl}}$.

[2] This radius value of the planet seems very large. This value is obtained because TrES-4b is an inflated hot jupiter, with a measured transit radius of $1.84^{+0.08}_{-0.09}$ R_{J} (Sozzetti et al. 2015). Furthermore, I arbitrarily fixed this radius to an atmospheric pressure value of 10 bar, and hydrostatic equilibrium leads to the large radii obtained from the transmission spectral calculation. Choosing a smaller reference pressure value would shift the planet's transmission radius to smaller values.

- The free parameters ξ_i of the temperature structure model, where $i = 1, \ldots, N_{\rm params}$, with $N_{\rm params}$ being the number of free temperature structure parameters.

I so far only applied the retrieval code on examples of transiting planets, such that I kept the $R_{\rm Pl}$ and g values fixed, because these can be measured from transmission spectra and RV measurements (see Section 1.2).

6.4.1 Abundance model

In the case of hydrogen helium dominated atmospheres, I only specify the mass fractions X_i of the molecular and atomic species other than H_2 and He (i.e. the metals), and only for the species with non-negligible opacity. I then set

$$X_{\rm H/He} = 1 - \sum_{i=1}^{N_{\rm metals}} X_i \,, \tag{6.17}$$

where $N_{\rm metals}$ is the number of metal species, and calculate the hydrogen and helium mass fractions as

$$X_{\rm H_2} = 0.75 \times X_{\rm H/He} \,, \text{and } X_{\rm He} = 0.25 \times X_{\rm H/He} \,, \tag{6.18}$$

assuming a gas of approximately primordial composition. Note that molecules treated as belonging to the metal species, such as H_2O, can also contain hydrogen atoms. However, I currently do not subtract the hydrogen contribution from the masses of the corresponding metal species. I calculate the atmosphere's total MMW μ using the formula

$$\frac{1}{\mu} = \sum_{i=1}^{N_{\rm species}} \frac{X_i}{\mu_i} \,. \tag{6.19}$$

This treatment is correct if the majority of the metal mass is carried by species with non-negligible opacities. If there are spectrally invisible atmospheric species of significant abundance, then it may make sense to add the contribution of their combined mass fraction $X_{\rm invisible}$ and MMW $\mu_{\rm invisible}$ to the above equations. For the current retrieval implementation I use vertically constant abundances.

6.4.2 Temperature structure parametrization

For the temperature structure parametrization I use the following model

$$T(P) = \left\langle T_{\rm Guillot}(P) \cdot \left(1 + \frac{\alpha}{1 + P/P_{\rm trans}}\right) \right\rangle_P \,, \tag{6.20}$$

with

$$T_{\rm Guillot}(P) = \frac{3T_{\rm int}^4}{4}\left(\frac{2}{3} + \delta P\right) + \frac{3T_{\rm equ}^4}{4}\left[\frac{2}{3} + \frac{1}{\gamma\sqrt{3}} + \left(\frac{\gamma}{\sqrt{3}} - \frac{1}{\gamma\sqrt{3}}\right) e^{-\gamma\delta\sqrt{3}P}\right] \,, \tag{6.21}$$

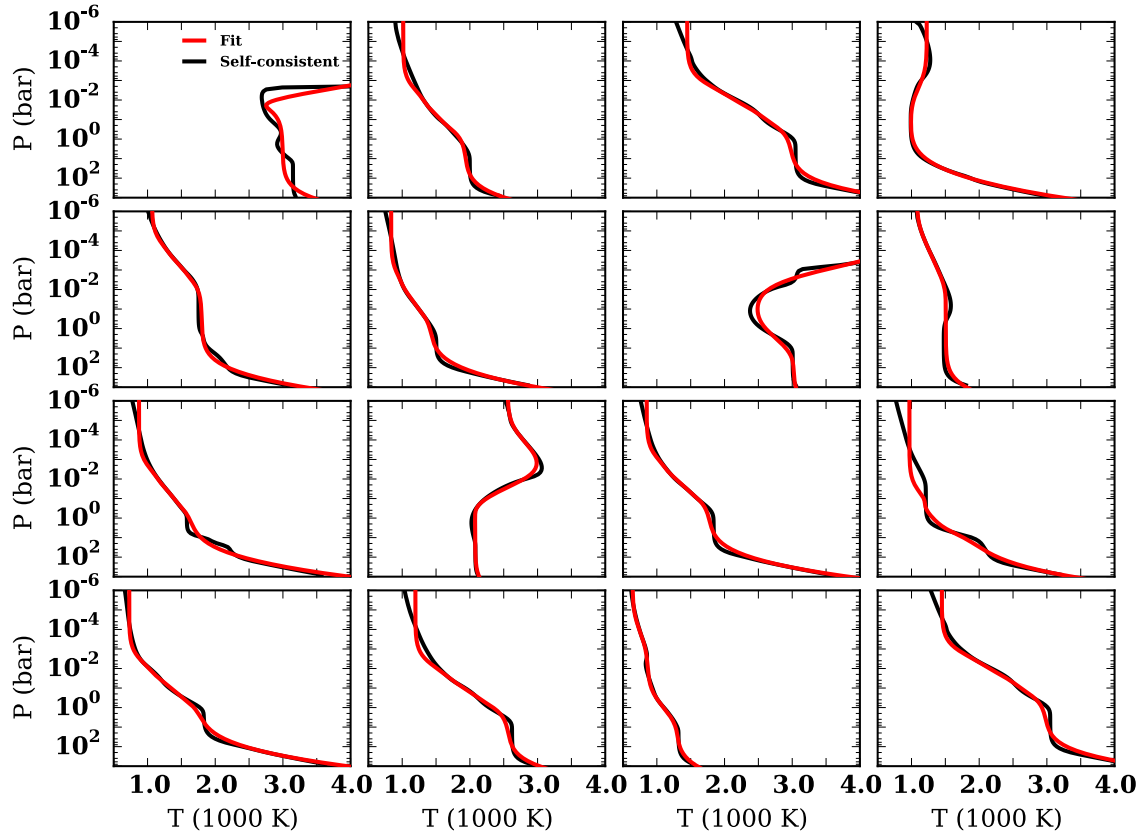

FIGURE 6.2: 6-parameter fit of the retrieval temperature model (see Equation 6.20) to atmospheric temperature structures randomly drawn from the grid of atmospheres presented in Mollière et al. (2017) (also see Chapter 5). The self-consistent pressure–temperature structures are shown as black solid lines, while the fitted parametrized models are shown as red solid lines.

which is the Guillot (2010) temperature model, introduced in Equation 2.26, for which I replaced $\tau = P\kappa_{\rm IR}/g = \delta P$, such that $\delta = \kappa_{\rm IR}/g$. The $\langle\rangle_P$ denotes a boxcar smoothing, carried out over a $\log(P)$-width of 1 dex. The temperature model thus has six free parameters, namely α, $P_{\rm trans}$, γ, δ, $T_{\rm int}$, and $T_{\rm equ}$.

The second term on the RHS of Equation 6.20 was introduced to allow the upper part of the atmosphere do develop a non-isothermal behavior at high altitudes, i.e. low pressures: the Guillot (2010) temperature model assumes a double-gray opacity, i.e. two opacity values, constant with respect to wavelength in the optical and IR wavelengths, see Section 2.2. At high altitudes the atmosphere is optically thin, such that its effect on the incoming stellar, and outgoing planetary radiation field is negligible. The atmospheric gas then sees the same radiation field, independent of its position, resulting in isothermal upper atmospheres. This can be seen in figures 2.2 and 2.3 where the atmospheres become isothermal for pressures smaller than $\sim 10^{-3}$ bar. For non-gray atmospheric solutions such an isothermal structure does not exist, however, which can be seen, e.g., in the self-consistent temperature structures calculated with *petitCODE*, shown in Figure 4.1 in Chapter 4. Because *petitCODE* solves for the temperature structure by taking the wavelength dependency of the opacity and radiation field into account, the high altitude temperature decrease arises from the self-shielding of the atmospheric gas. This means that even though the optically thin, high-altitude atmosphere

has little impact on the wavelength integrated radiation field, it can still be optically thick in the molecular line cores. Hence, at increasingly higher altitudes the emission of the deep hot layers in the wavelength region of the line cores has been absorbed more and more, leading to a decreased heating of the gas.

In order to show that this model is flexible enough to adapt to various atmospheric scenarios I present a fit of the parametrized temperature model to self-consistent temperature structures drawn from the atmospheric grid presented in Mollière et al. (2017) (described in Chapter 5) in Figure 6.2. The parametrized model seems to be versatile enough to adapt to atmospheres without inversions, but also to cases with weak or strong inversions. Moreover, also the non-isothermal upper atmospheres seem to be described reasonably well by this model. The parametrized model could potentially be further improved by adding another free parameter β, which controls the width of the transition caused by the second term on the RHS of Equation 6.20, such that it would read $1 + \alpha/[1 + (P/P_{\rm trans})^{\beta}]$. The ability of my model to parametrize atmospheric temperature profiles seems to be comparable to the one used in the retrieval study by Madhusudhan & Seager (2009), where a similar test was carried out (their Figure 2).

6.5 Retrieval tests with mock observational data

In order to test my retrieval implementation, I retrieved simulated *JWST* observations for two different cases.

For calculating the noise of the first test case I assumed that the planet was "TrRES-4b"-like, using the same planetary radius, host star parameters, and distance to Earth as assumed for this planet in Chapter 5, Table 5.1, namely $R_{\rm Pl} = 1.84$ R$_{\rm J}$, $T_* = 6295$ K, $R_* = 1.831$ R$_\odot$, and a distance of 479 pc. I used the same JWST instrument setup as described in Chapter 5, Table 5.3. The simulated observations were obtained with the *EclipseSim* tool (van Boekel et al. 2012). I then retrieved the atmospheric parameters of an input spectrum that was generated with the retrieval radiative transfer model itself: this served to validate the overall implementation of the retrieval scheme. This test is described in Section 6.5.1.

For the second test, I retrieved an atmospheric structure calculated with *petitCODE*, using the full set of molecular line opacities available within *petitCODE*, and including scattering also for the emission case. This simulates the retrieval code's performance when retrieving atmospheric structures from actual observations, as the relevant atmospheric physics is modeled when constructing the synthetic input observation of this test. It will hence allow to estimate the inaccuracies due to the retrieval model assumptions, and such a tests have received little attention in the retrieval community so far. Only Rocchetto et al. (2016) carried out similar tests, in order to show the importance of using non-isothermal atmospheric models for retrieval, but they used a parametrized temperature profile, and only considered transmission spectra. This test differs from the first test in multiple ways: first, there exists no exact representation of the input P-T profile with the temperature profile of the retrieval model. Second, the molecular abundances for *petitCODE* results are derived from equilibrium chemistry, and are thus vertically varying, whereas the retrieval code assumes constant

abundances. Moreover, as of now I only retrieve the abundances of H_2O, CH_4, CO, CO_2, Na, and K. Hence these are the only opacity species which I currently include[3], in addition to H_2-H_2 and H_2-He CIA, as well as Rayleigh scattering for the transmission spectra. The *petitCODE* calculation includes all line opacity species listed in Table 3.1, except for TiO, VO and O_3. Finally, the input emission spectrum of *petitCODE* includes scattering, whereas the retrieval model does not. The test is described in Section 6.5.2.

6.5.1 Input models generated by retrieval code

As said above, the input spectra in this section were calculated with the retrieval code itself, and I assumed vertically constant abundances when calculating the spectrum, i.e. I used the same abundance model as within the retrieval code (see Section 6.4.1). For the abundances I assumed the following mass fractions: $\log_{10}(X_{\mathrm{H_2O}}) = -2.5$, $\log_{10}(X_{\mathrm{CH_4}}) = -5$, $\log_{10}(X_{\mathrm{CO_2}}) = -4$, $\log_{10}(X_{\mathrm{CO}}) = -2$, $\log_{10}(X_{\mathrm{Na}}) = -5$, and $\log_{10}(X_{\mathrm{K}}) = -5$. The P–T profile was defined using Equation 6.20, and making the following parameter choices: $\log_{10}(\delta) = -5$, $\log_{10}(\gamma) = -0.4$, $T_{\mathrm{int}} = 600$ K, $T_{\mathrm{equ}} = 2300$ K, $P_{\mathrm{trans}} = 0.01$ bar, and $\alpha = 0.5$. I assumed $P_0 = 0.01$ bar for calculating the transmission spectra. The synthetic observation was carried out by assuming one eclipse in each of the three *JWST* instruments listed in Table 5.3.

The retrieval was run by drawing 200000 so-called 'pre burn-in' samples to find the global minimum, plus 10^6 samples centered around that minimum, to derive a reliable posterior distribution. The latter part is the main MCMC run, and it was set up by sampling the initial walker positions from a Gaussian, centered around the best-fit value of the pre burn-in run. The spread of the Gaussian was set up to be about half to the mean variation of the pre burn-in run. The number of ensemble walkers was 800, such that the total number of samples drawn (10^6) required 1250 steps. After the 10^6 samples had been drawn I discarded the first 160000 to leave out the 'burn-in', i.e. the phase where the walkers relax from the initial Gauss to the actual posterior distribution.

The result of the retrieval run, based on the emission spectrum, is shown in Figure 6.3. The noise-less input spectrum, the observed input spectrum, as well as the best-fit result of the main $10^6 - 160000$ MCMC samples is shown in Panel (a). It can be seen that the spectrum fits the input spectrum very well, and the residuals, shown in in the lower sub panel of Panel (a), do not exhibit any discernible features and scatter symmetrically about zero.

The input P–T profile, together with the best-fit profile, and the 5-95 % and 15-85 % envelopes of the cumulative temperature profile distribution is shown in Panel (b) of Figure 6.3. I concentrate on these envelopes because the 15 to 85 % envelope, in particular, approximately corresponds to the 1 σ envelope if the posterior distribution were to be well represented by a Gauss profile (with envelope boundaries at 15.87 and 84.24 %). One can see that between 10^{-6} and 1 bar the best-fit P–T profile and the input P–T profile agree very

[3]More species are straightforward to include. However, the computational time is ∼linear in the number of species, and I expect the molecular species listed here to be the most important ones for warm to hot gaseous planets, such that I want to test how valid this assumption is. For carbon-rich hot jupiters (with a C/O ratio > 1), also HCN (ans possibly C_2H_2) would have to be included.

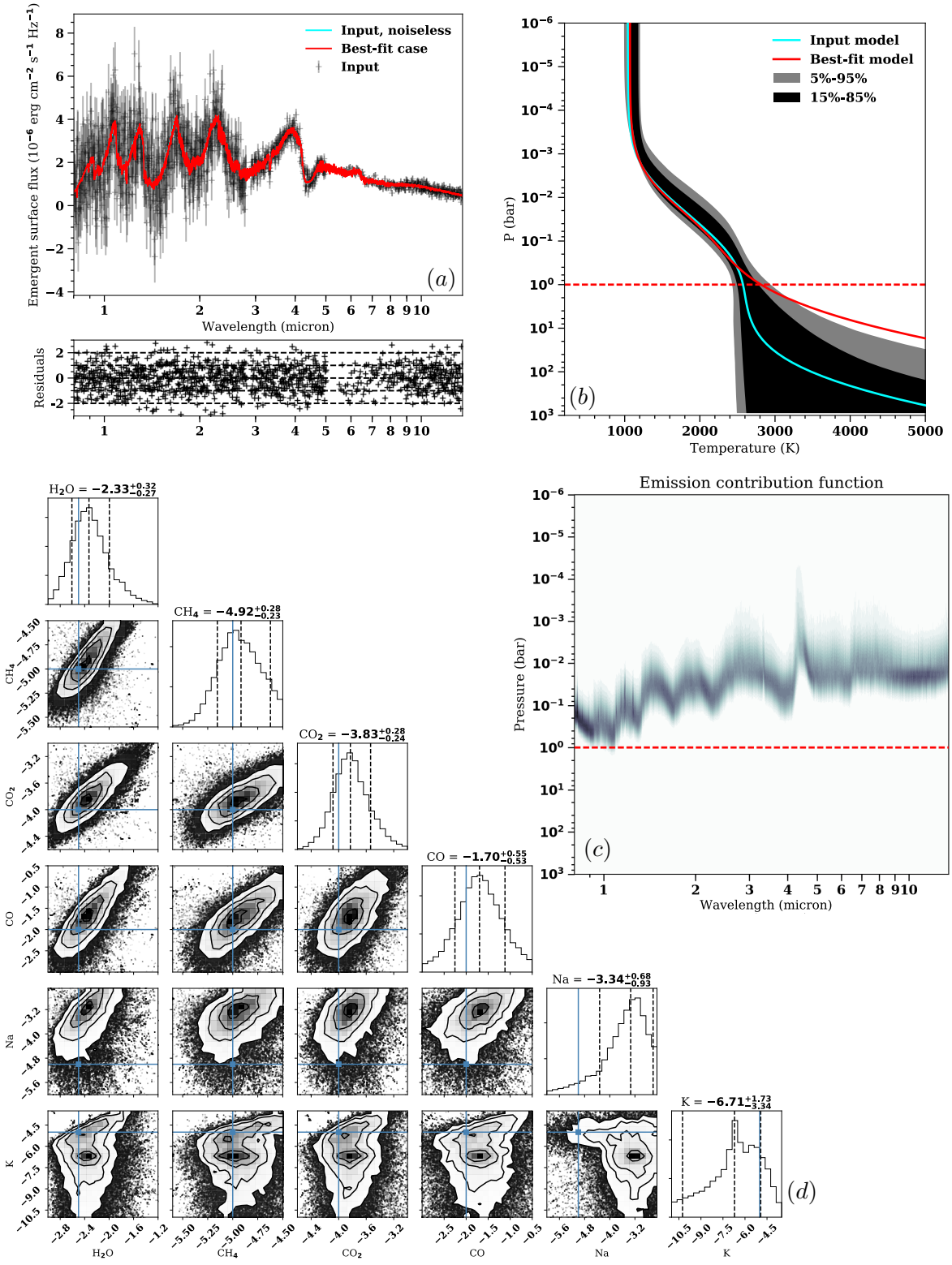

FIGURE 6.3: Retrieval results of the constant abundance input emission spectrum generated by the retrieval model. *Panel (a), top:* emission spectrum of the input model (cyan line), and its synthetic observation (black crosses with error bars). The best-fit retrieved spectrum is shown as a red line, with its residuals to the synthetic observation shown in the *bottom sub panel*. *Panel (b):* atmospheric temperature profiles: the input profile is shown as a cyan line, the best-fit retrieved profile is shown as a red line, and the 5-95 % and 15-85 % envelopes of the cumulative temperature profile distribution are shown in gray and black, respectively. The red dashed line denotes the maximum pressure that can be probed in the wavelength range of the spectra shown in *Panel (a)*. *Panel (c)*: emission contribution function of the best-fit retrieved atmosphere. The red dashed line means the same as in Panel (b). *Panel (d):* posterior distribution of the $\log_{10}$(molecular mass fraction)s. The true input mass fraction is denoted by the blue lines, whereas the three dashed lines denote the values corresponding to 15, 50, and 85 % of the cumulative distribution of the values.

well, but start to deviate significantly for pressures larger than 1 bar. For pressures lower than $\sim 2 \times 10^{-3}$ bar the input temperature lies outside the 15 to 85 %, but within the 5 to 95 % envelope. For all pressures larger than $\sim 2 \times 10^{-3}$ bar the input temperature profile lies within the 15 to 85 % envelope. Hence I regard the input temperature profile as having been successfully retrieved. The reason for a decreased agreement between the input temperature profile and the 15 to 85 % envelope at pressures $\lesssim 2 \times 10^{-3}$, as well as the difference between the input and the best-fit P–T profile at pressures > 1 bar, can be understood from looking at Panel (c) of Figure 6.3.

Panel (c) of Figure 6.3 shows the so-called 'emission contribution function' of the best-fit atmospheric parameters, which is a measure for how strongly the emission of a layer contributes to the atmosphere's emerging spectrum at the top. It depends on the temperature, and on the optical thickness of a given layer, because the latter determines how strongly it will be able to emit light into a ray passing through it. The contribution of a layer is not only decided by these tho factors, however, but also by the optical depth of the atmosphere above the layer: if the overlying atmosphere is optically thick, then the light emitted by the layer will be absorbed before it leaves the planet, and hence the layer's contribution to the total emission will become zero. From the sum on the RHS of Equation 6.14 one can see that the contribution of the region between layer i and $i+1$, i.e. of layer $i+1/2$, to a ray passing through it is given by $(1/2)\left[\bar{B}(T^i) + \bar{B}(T^{i+1})\right]\left(\bar{\mathcal{T}}^i - \bar{\mathcal{T}}^{i+1}\right)$. This means that the total contribution of a layer to the arising spectrum at the top of the atmosphere is

$$C_{\mathrm{em}}^{i+1/2} = \frac{\sum_{j=1}^{N_\mu}\left[\bar{B}(T^i) + \bar{B}(T^{i+1})\right]\left(\bar{\mathcal{T}}_j^i - \bar{\mathcal{T}}_j^{i+1}\right)\mu_j \Delta\mu_j}{\sum_{j=1}^{N_\mu}\left\{2\bar{B}(T_{\mathrm{bot}})\bar{\mathcal{T}}^{\mathrm{atmo}} + \sum_{k=1}^{N_{\mathrm{L}}-1}\left[\bar{B}(T^k) + \bar{B}(T^{k+1})\right]\left(\bar{\mathcal{T}}_j^k - \bar{\mathcal{T}}_j^{k+1}\right)\right\}\mu_j \Delta\mu_j}\,, \tag{6.22}$$

where $\mu = \cos(\vartheta)$, ϑ being the angle between the ray and the atmospheric normal. N_μ is the number of angle grid points. This can be derived from noticing that the emission flux F is $2\pi \int_0^1 \mu I(\mu) d\mu$ (see Equation 3.36).

From Panel (c) in Figure 6.3 one now sees that most of the emission stems from regions between 2×10^{-3} and 1 bar. Consequently, this is the region within which the retrieved atmospheric P–T structure agrees best with the input structure. Moreover, as no radiation emitted a pressures larger than 1 bar is able to leave the planet, the 15-85 % temperature envelope at $P > 1$ bar is fully determined from the parametrized temperature model. For a real planet the atmospheric physics may give rise to deep retrieved temperature profiles which are different from what the parametrized P–T profile predicts. It may then be incorrect to assume that the retrieved temperature profile below the regions probed by observations, > 1 bar in the case presented here, are representing the actual temperature profile of the atmosphere. Because we cannot know the actual deep atmospheric physics with definite certainty, except for theoretical expectations, this has to be critically kept in mind when drawing inferences derived from the deep temperature profile.

This also explains why the best-fit P–T structure can exhibit temperatures very different from the input profile at $P > 1$ bar. Additionally, from Panel (c) one sees that the only wavelength region which samples the high atmospheric region at $P < 2 \times 10^{-3}$ bar is the

CO_2 feature at 4.2 to 4.6 μm. When I checked the mean flux of the synthetic observation across the 4.5 μm region I found that the observations, by chance, let to a slightly too large flux (also compare red and cyan lines in Panel (a)). Hence the retrieved temperatures there are slightly too high, when compared to the input model.

Finally, the posterior distribution of the retrieved abundances is given in Panel (d) of Figure 6.3. While the full atmospheric model is determined by 12 parameters (6 abundances and 6 temperature structure parameters), and the full posterior distribution is 12-dimensional, I only show the posteriors for the abundances of the line absorbers in Panel (d). This is because one is, in general, not interested in the parameters which describe the parametrized P–T structure; rather the distribution of temperature profiles they give rise to is of interest, which is given in Panel (b) of Figure 6.3. The parameter values for the P–T profiles do not carry any physical meaning, they merely help to generate different temperature profiles. Hence, such parameters are often called 'nuisance parameters'. The sampled abundance distributions are shown in 2-d and 1-d marginalized spaces, i.e. projected onto the planes defined of the $\log_{10}(X_i)$ and $\log_{10}(X_j)$ axes for species i and j in the 2-d case, and on the $\log_{10}(X_i)$ axis of species i in the 1-d case. One sees that, within the 15-85 % envelopes of the sampled values (which are given as the error values on top of the columns in Panel (d)), all molecular abundances agree with the input value. Only the sodium and potassium abundances cannot be successfully retrieved: the strong sodium and potassium resonance lines lie at ~589 nm and ~768 nm (see Section 3.3.1), and therefore outside the *JWST* spectral range. However, they can affect the *JWST* spectra because their broad line wings extend out to 0.9 and 1.15 μm, respectively. This means that their spectral influence reaches out to 0.9 μm, beyond which their opacity contribution is overwhelmed by H_2O absorption, which starts at 0.9 μm. Hence it seems that the quite noisy emission spectral data between 0.8 and 0.9 μm is degenerate with respect to the sodium and potassium abundances, and favored an increased sodium, and decreased potassium abundance for the observation presented here.

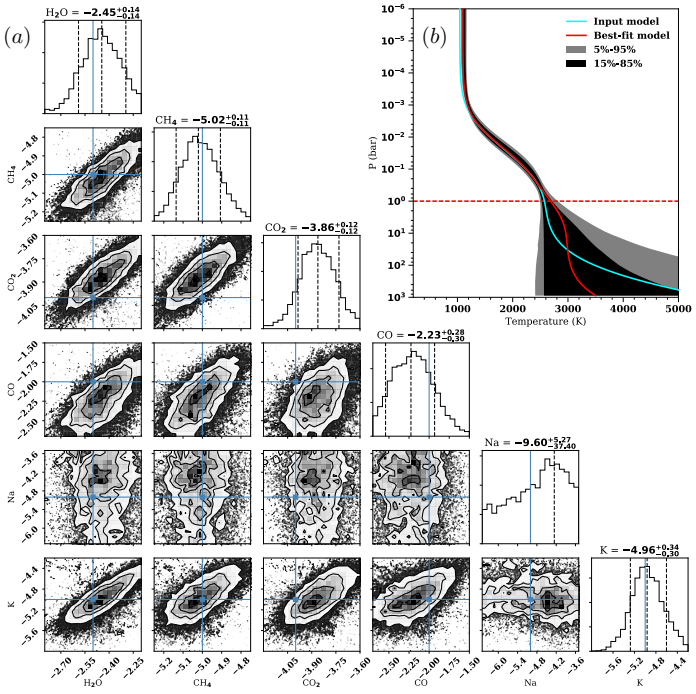

FIGURE 6.4: *Panel (a)*: retrieved abundance posterior distribution of a case with observational errors half as large as in the case considered in Figure 6.3. *Panel (b)*: retrieved temperature envelope for the case shown in *Panel (a)*.

For comparison, in Figure 6.4, I show the posterior abundances (and temperature envelopes) retrieved for a case where the observational error was only half as large, corresponding to four eclipse observations in each instrument, or a planet which is at half the distance of TrES-4b, i.e. 240 pc. In this case the K input abundance is correctly retrieved, whereas the extent of the uncertainty envelope of the sodium abundance ($\log_{10}(X_{\rm Na}) = 9.60^{+5.27}_{-37.40}$) indicates an unconstrained abundance. This test shows that the retrieved results may depend quite strongly on the by-chance sampling of the spectrum during the observation process, at least when parameters are determined by only a narrow spectral range, and affected by non-negligible noise.

In conclusion, emission part of the first retrieval test was successful: Within the 15 to 85 % envelopes, I correctly retrieved the atmospheric abundances, and the temperature profile in the region which generates the spectrum. And, as mentioned above: the distribution of the residuals between the input and best-fit spectrum does not show any systematic features and scatters about zero (see Panel (a)). One property of the retrieved results, which may look worrisome, is that the mean values of the retrieved abundances in Panel (d) in Figure 6.3 all appear to have a positive systematic offset with respect to the input value. In that sense it is reassuring that this is not the case for the retrieved abundances shown in Figure 6.4, such that the particular result for the abundances in Panel (d) of Figure 6.3 may be caused by an 'unfortunate' sampling of the noiseless spectra when generating the synthetic observation. While a detailed test of this is clearly needed, it was beyond the current scope of this work, but will have to be investigated in greater detail in the future.

The result from retrieving the atmospheric transmission spectrum for the constant abundance case is shown in Figure 6.5. Like for the emission retrieval case in Figure 6.3, I show the input and best-fit retrieved spectra and temperature structures, along with the retrieved abundances and the transmission contribution function.

The transmission contribution function of layer i at a given wavelength is calculated from

$$C^i_{\rm tr} = \frac{R_0^2 - R^2(\kappa_i = 0)}{\sum_{j=1}^{N_{\rm L}} \left[R_0^2 - R^2(\kappa_j = 0)\right]} \,, \tag{6.23}$$

where R_0 is the planet's transmission radius at a given wavelength, and $R(\kappa_i = 0)$ is the transmission radius one obtains when setting the opacity in the ith layer to zero. I use squared radii here, because transmission spectra measure the flux decrease of the star as it is transited by its planet, which is proportional to the planet's area.

From Panel (a) in Figure 6.5 one can see that the transmission spectrum is correctly retrieved, with a residual distribution which scatters about zero, with no noticeable features. From Panel (b) one sees that the atmospheric temperature structure is successfully retrieved within the regions which are probed by transmission (see Panel (c)). Likewise, the abundances of H_2O, CH_4, CO_2 and K are all retrieved, with the true input values falling within the 15 to 85 % envelopes.

In the lowest row of Panel (d) in Figure 6.5 one can see that there exists a correlation between the reference pressure P_0 and the molecular abundances of the spectrally active species. This can be understood from the fact that the transmission spectrum is less sensitive

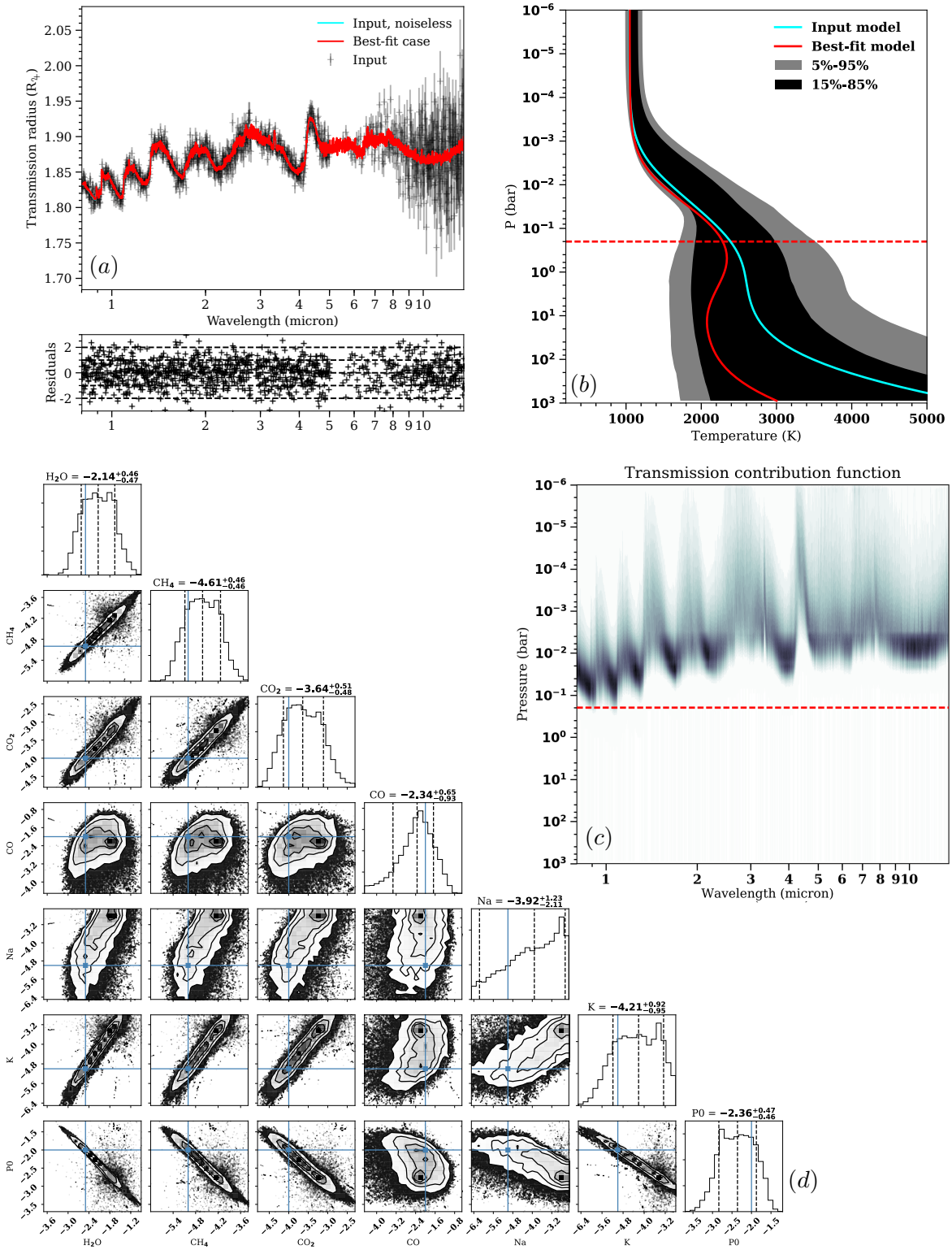

FIGURE 6.5: Retrieval results of the constant abundance input transmission spectrum generated by the retrieval model. *Panel (a), top:* transmission spectrum of the input model (cyan line), and its synthetic observation (black crosses with error bars). The best-fit retrieved spectrum is shown as a red line, with its residuals to the synthetic observation shown in the *bottom sub panel*. *Panel (b):* atmospheric temperature profiles: the input profile is shown as a cyan line, the best-fit retrieved profile is shown as a red line, and the 5-95 % and 15-85 % envelopes of the sampled structures are shown in gray and black, respectively. The red dashed line denotes the maximum pressure that can be probed in the wavelength range of the spectra shown in *Panel (a)*. *Panel (c)*: transmission contribution function of the best-fit retrieved atmosphere. The red dashed line means the same as in Panel (b). *Panel (d):* posterior distribution of the $\log_{10}$(molecular mass fraction)s. The true input mass fraction is denoted by the blue lines, whereas the three dashed lines denote the values corresponding to 15, 50, and 85 % of the cumulative distribution of the values.

to pressure than it is to the temperature of the atmospheric regions being probed. Within the retrieval model, if larger P_0 pressure values are assumed, such that $r(P = P_0) = R_{\rm Pl}$, then a given pressure value will correspond to a larger radius, which follows directly from integrating the hydrostatic equilibrium equation (see Equation 2.3). Hence, if too large P_0 values are put into the model, at correct molecular abundances, then the transmission radii of the planet will become too large. In such cases, reducing the molecular abundances improves the fit, as one can then probe deeper into the atmosphere, which decreases the planetary transmission radii. This effect is well known, and has been described in, e.g., Lecavelier des Etangs et al. (2008); Benneke & Seager (2012); Griffith (2014); Heng & Kitzmann (2017).

The marginalized abundance distributions in Panel (d) of Figure 6.5 show that there seems not only to be a correlation, but actually a clear degeneracy, because the retrieved abundances for H_2O, CH_4, CO_2 and K, and the reference pressure P_0, exhibit a plateau in their posterior distributions. The respective plateaus include the true input values. Again, the quite broad distribution of the sodium abundance uncertainties, $\log_{10}(X_{\rm Na}) = 3.92^{+1.23}_{-2.11}$, indicate that the sodium abundance is not well constrained in the *JWST* wavelength range. Interestingly, the CO posterior does not exhibit a clear plateau.

6.5.2 Input models generated by *petitCODE*

With the retrieval method itself having been verified, I proceeded to test its performance when retrieving input spectra which are more complex, and self-consistent with regard to the physical processes that appear necessary for describing the atmospheric state. Such tests are necessary to assess how well the idealized retrieval model assumptions (constant abundances, limited set of absorbers, no scattering in emission) allow to infer atmospheric properties, or whether more complex assumptions for the retrieval model are necessary. To carry out this test I considered the spectra of the the clear, globally averaged insolation case of TrES-4b, calculated self-consistently as described in Chapter 5, also see Mollière et al. (2017). This spectral calculation included scattering, and used the full set of molecular opacities available within the *petitCODE* framework (except for TiO, VO and O_3, see Table 3.1). Moreover, because the molecular abundances are determined from assuming chemical equilibrium, the input spectrum will arise from vertically varying molecular abundances.

I show the result for the retrieval of TrES-4b's synthetic emission spectrum in Figure 6.6. In addition to the plots shown for the previous test cases (see figures 6.3 and 6.5), there now is a Panel (e) in the figure, which shows the vertically varying molecular abundances of the input model, as well as the fully marginalized posterior distributions of the retrieved, vertically constant abundances.

The results indicate that the retrieval code can correctly estimate the atmospheric structure and abundances, at least for the input test case shown here. The retrieved temperature structure (see Panel (b)) contains the input temperature profile within its 5 to 95 % envelope, and within its 15 to 85 % envelope in the atmospheric region where most of the flux is stemming from, see Panel (c). The residual distribution between the model and input spectrum does not show any systematic features, and scatters symmetrically about zero. The fact that the best-fit and noiseless input spectrum exhibit an offset in the region around

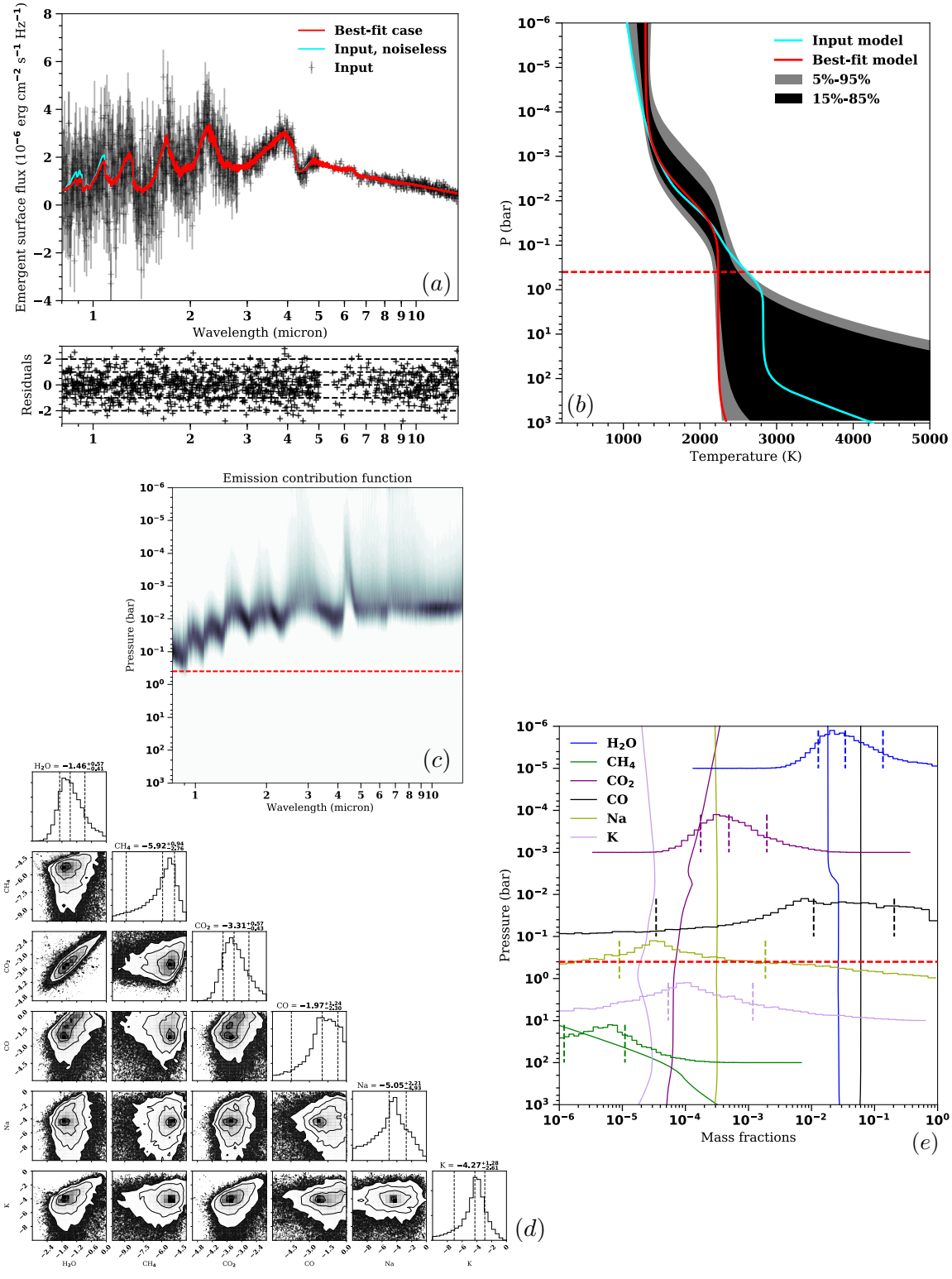

FIGURE 6.6: Retrieval results of the full self-consistent *petitCODE* emission spectrum generated by the retrieval model. *Panel (a), top:* emission spectrum of the input model (cyan line), and its synthetic observation (black crosses with error bars). The best-fit retrieved spectrum is shown as a red line, with its residuals to the synthetic observation shown in the *bottom sub panel*. *Panel (b):* atmospheric temperature profiles: the input profile is shown as a cyan line, the best-fit retrieved profile is shown as a red line, and the 5-95 % and 15-85 % envelopes of the sampled structures are shown in gray and black, respectively. The red dashed line denotes the maximum pressure that can be probed in the wavelength range of the spectra shown in *Panel (a)*. *Panel (c)*: emission contribution function of the best-fit retrieved atmosphere. The red dashed line means the same as in Panel (b). *Panel (d):* posterior distribution of the $\log_{10}$(molecular mass fraction)s. The three dashed lines denote the values corresponding to 15, 50, and 85 % of the cumulative distribution of the values. *Panel (e):* colored solid lines: vertically varying abundances of the self-consistent *petitCODE* input model. Different colors denote different species, as indicated in the legend. The red dashed line means the same as in Panel (b). The colored histograms show the fully marginalized abundance posteriors of the respective species, assuming vertically constant abundance profiles. The distributions have been offset and rescaled for clarity. The vertical dashed lines indicate the abundances at 15, 50, and 85 % of the cumulative abundance distributions.

1 μm must therefore stem from 'bad luck' when sampling the noiseless spectrum for the synthetic observation. The retrieved vertically constant abundances of the molecules correlates well with the input profiles, see Panel (e). All molecular abundances, except for CH_4, are retrieved within the 15 to 85 % abundance envelopes.

From the test shown here I conclude that my retrieval implementation, in its current form, may be used to retrieve the emission spectra of hot jupiters, at least in the *JWST* wavelength regime. If the data were to also contain the shorter, optical wavelength regime, then the contribution of reflected stellar light may be problematic for the retrieval algorithm, because I do not currently include scattering (and no other retrieval code currently does). The second limitation arises from the fact that I currently neglect clouds, which can modify the emission spectrum both due to absorption and scattering. While taking care of clouds in the retrieval tests presented here was beyond the scope of this work, I plan to include a parametrized cloud model as one of the next steps (also see Section 6.6.1). Additionally, as discussed in the 'Clouds' part of Section 4.2.1, and Section 5.4.2, hot jupiter emission may still be described well by cloud-free spectra, even when their transmission spectra show evidence for clouds.

The retrieval result based on the transmission spectrum is shown in Figure 6.7. Panel (a) shows the synthetic observation, the noiseless input spectrum, the best-fit retrieved transmission spectrum, as well as ten spectra generated from sampling the posterior parameter distribution. As can be seen from the lower sub-panel of Panel (a), the posterior distribution exhibits no systematic features and scatters symmetrically about zero, indicating a good fit to the synthetic observation. While Panel (a) looks promising, it can be seen from panels (b) that the idealized retrieval model has problems to correctly constrain the atmospheric state for a fully self-consistent input spectrum: only between 10^{-3} and 4×10^{-2} bar does the input temperature profile fall within the retrieved 5 to 95 % envelope, and only between 4×10^{-3} and 10^{-2} bar within the 15 to 85 % envelope. In addition, the whole posterior temperature envelope seems to be offset to larger pressures, when compared to the input profile. This can also be seen from Panel (d): the default value for P_0 in Mollière et al. (2017) was 10 bar, but the retrieval constrains it to be 66 bar. As discussed in the transmission spectrum results in Section 6.5.1, too large P_0 values will result in too small abundances, such that H_2O, CO, and K are less abundant than in the input model. The CO_2 and Na abundances are retrieved within the 15 to 85 % envelope. It is interesting to see that the deep atmosphere is too cool when compared to the input profile, which counteracts the effect of the too large P_0 somewhat (because the density enters in the hydrostatic equilibrium equation, see Equation 2.3). Apparently, however, this effect is not strong enough to lead to the correct abundances in the part of the atmosphere which is probed by observations. Note that the best-fit temperature profile falls somewhat outside of 5 to 95 % temperature envelope, at least between 4×10^{-4} and 4×10^{-2} bar. To ensure that other likely solutions, with P–T structures within the retrieved uncertainty envelope, also provide a good fit to the input spectrum, I sampled ten additional atmospheric structures from the full parameter posterior distribution, which give rise to the aforementioned ten sampled spectra in Panel (a), which are shown as yellow solid lines. As can be seen these spectra do indeed provide a good fit to the spectrum. Hence, for

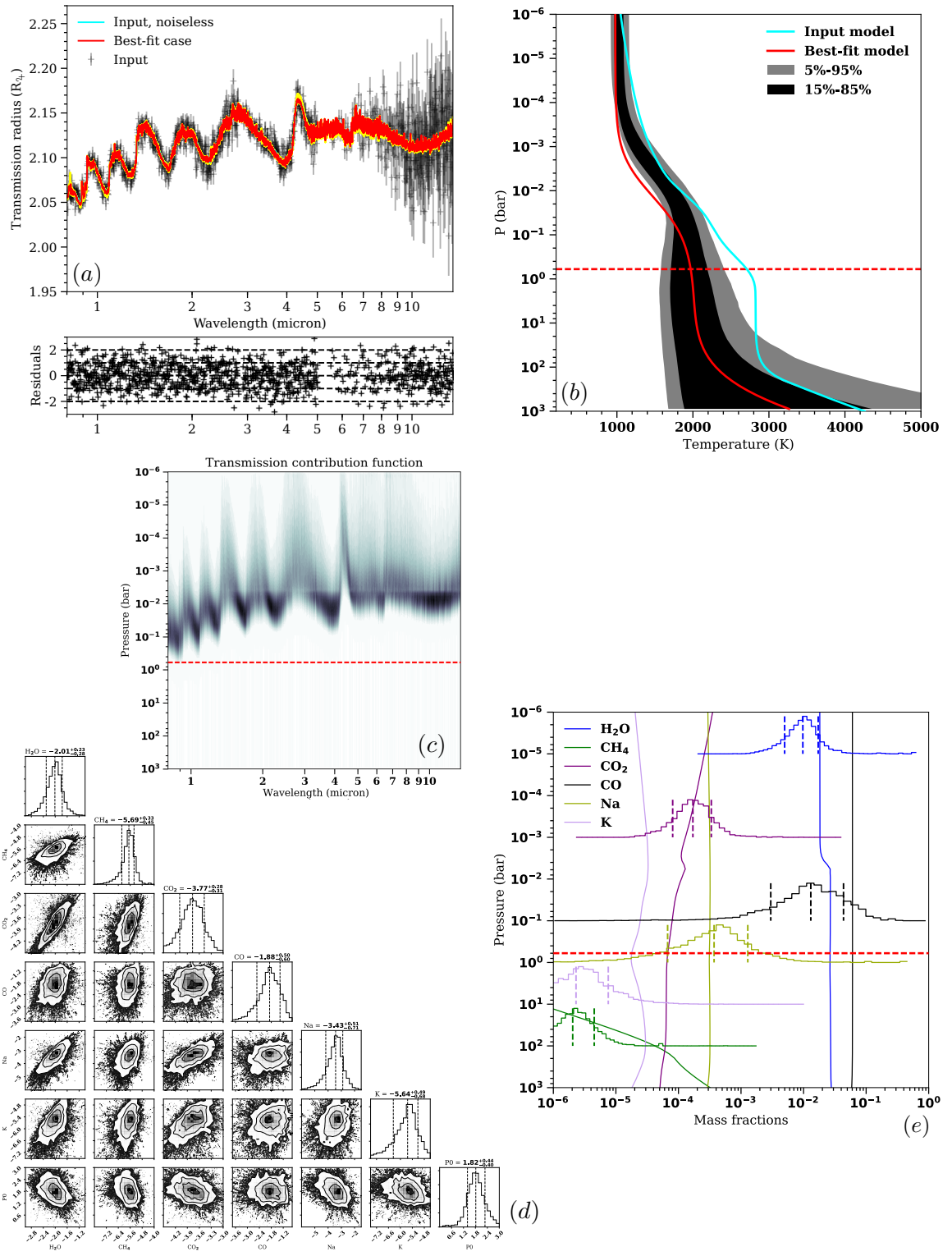

FIGURE 6.7: Same as Figure 6.6 but for the transmission case. The yellow lines in Panel (a) are ten spectra derived from randomly sampling the posterior parameter distribution.

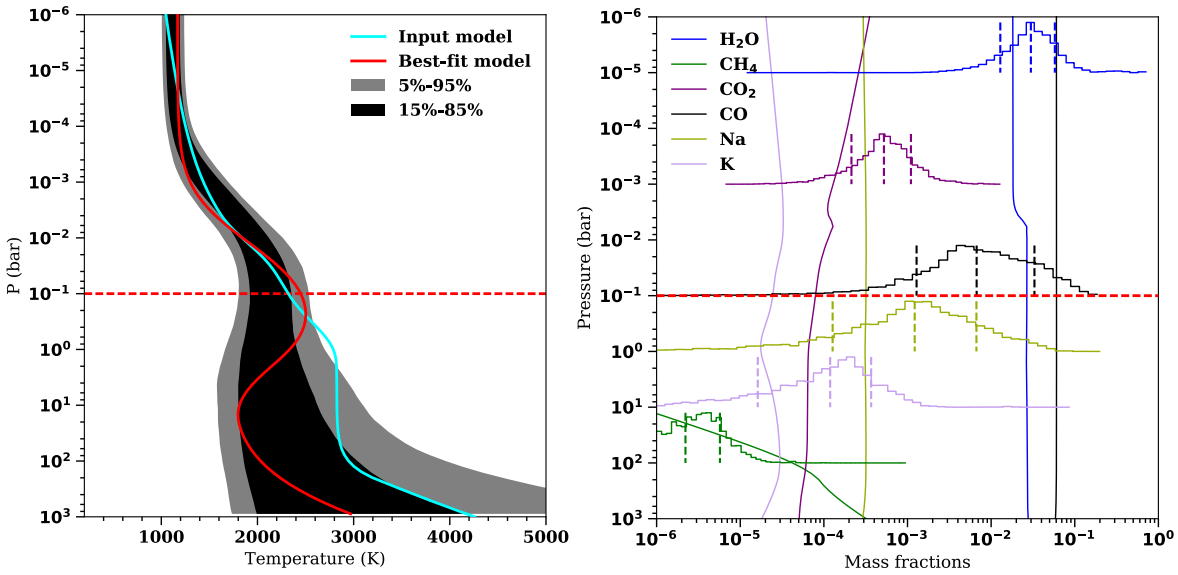

FIGURE 6.8: *Left panel:* retrieved temperature envelope for the same case as discussed in Figure 6.7, but with the set of opacities restricted to only contain the retrieval model opacity species. *Right panel:* retrieved abundances for the case shown in the *left panel*. Lines mean the same as in Panel (e) of Figure 6.6.

transmission spectra, the idealized approach of vertically constant molecular abundances, and potentially not including all necessary absorber species, starts to break down in the case presented here: the retrieval code is still finding a good fit, but it does so by finding atmospheric parameters which are offset from the true values, thus trying to make up for its lack of flexibility in the retrieval abundance model. Moreover, it is interesting to see that the retrieved temperature envelope is much narrower than the one retrieved in the constant abundance case (compare figures 6.5 and 6.7), indicating that the P_0–abundance degeneracy is broken, and that the P_0 and abundance values are 'better' constrained by the increased input model complexity.

Note that vertically constant abundances are a standard assumption in most retrieval codes in the literature, except from the self-consistent retrieval code by Benneke (2015). Apart from Rocchetto et al. (2016), no such tests as presented here seem to have been carried out before. While Rocchetto et al. (2016), who only studied transmission spectra, show that the use of non-isothermal temperature profiles helps to better constrain abundances, their results, using vertically constant abundances, indicate similar difficulties when retrieving the atmospheric state from transmission spectra. Additionally, they show that whether or not the retrieval yields good results depends on factors like the C/O ratio of the atmosphere being studied. For C/O$\sim$1 the atmospheric opacity is minimal (also see Section 4.4) and one probes deep into the atmosphere, in regions were the abundances vary strongly. For these cases, the quality of the retrieval results degrades strongly, because vertically constant abundances represent an even worse approximation. Both their and my results thus indicate that transmission spectral retrieval models need to be improved in the future.

Finally, I carried out the same test once more, using the same restricted set of line opacity species for the input spectrum as included in the retrieval model (i.e. CH_4, H_2O, CO, CO_2, Na, K, H_2 and He). For this case the results on the retrieved temperature structures improved, see the left panel of Figure 6.8, and so did the retrieved abundance values, see the

right panel of Figure 6.8, although CO is still not retrieved within the 15 to 85 % envelope. This result is somewhat puzzling, because no major absorbers have been left out when using only the restricted set of atmospheric absorbers. For obtaining a clear picture on the influence of specific retrieval model assumptions, it is thus necessary to carry out more detailed tests in the future. Unfortunately, this was beyond the scope of this work, and requires more investigation in the future.

6.5.3 Summary

To summarize, my tests show that the retrieval implementation is working well, and that synthetic observations generated with the input model can be retrieved correctly. If the input model spectrum arises from a more complicated atmospheric treatment (I used input spectra generated with *petitCODE*), then, within the *JWST* wavelength range, the abundances and temperature structures of cloud-free hot jupiters seem to be well retrievable using emission spectroscopy. Even atmospheric structures of hot jupiters appearing cloudy in transmission may be well retrievable with the current emission spectrum implementation, see the 'Clouds' part of Section 4.2.1, and Section 5.4.2.

Note that *petitCODE* additionally includes scattering, variable abundances, and additional atmospheric absorbers, when compared to the retrieval atmospheric model. However, a more systematic suite of tests will need to be carried out in the future, to identify pathological cases in which the retrieval code assumptions may break down. The reason for being able to retrieve the atmospheric emission spectra well, while neglecting scattering, is that the largest scattering contribution of cloud-free hot jupiters stems from Rayleigh scattering. Rayleigh scattering only becomes dominant in the optical wavelengths, and is thus largely outside the *JWST* range.

If such a complicated model is used to generate transmission spectra, then the results of the retrieved atmospheric abundances and temperature structure are to be treated with caution: the influence of the free parameters of the (possibly too simple) retrieval model may be misused to account for the larger complexity of the input model. Here tests will have to show what the best retrieval approach is (e.g. allowing for vertically varying abundance profiles, as well as including more atmospheric absorbers).

6.6 Outlook

6.6.1 Useful model extensions

One of the next immediate steps will be to introduce a parametrized cloud model into the retrieval scheme, as well as adding vertically varying abundances, parametrized, e.g., by a power-law profile.

For transmission spectra a first, very simplified cloud modeling scheme has already been included, but retrieval tests with it still need to be carried out: I model large particle clouds, with almost flat extinction spectra, by defining a pressure $P_{\rm cloud}$, below which (in terms of altitude) the opacity goes to infinity. Conceptually, this corresponds to an optically thick

cloud deck. Similar approaches have been taken by, e.g. Benneke & Seager (2012); Sing et al. (2016). Additionally, the presence of small-particle hazes, which can lead to scattering slopes in the optical and NIR, are approximated by scaling the Rayleigh opacities of the gas by a given factor, which is based on the cloud/haze treatment used in Sing et al. (2016). This is only an approximate haze treatment, and it does not allow for hazes arising from larger particles, which would lead to an extinction slope somewhat shallower than Rayleigh scattering (also see the discussion in the 'Cloud opacities' part of Section 2.2.5). In addition, the current haze model assumes a vertically homogeneous distribution of haze particles, while the $P_{\rm cloud}$-model assumes a step function for the cloud density profile. The reasons for the cloud treatment to be often very simple in past publications, when fitting observations, is that clouds have, so far, only affected the spectra by introducing gray opacities and scattering slopes. Any cloud features, which would reside in the MIR, are currently inaccessible to observations. Hence, an increased complexity in the parametrized cloud models was largely unwarranted. With *JWST* this may change, however, because cloud features in the MIR may start to become observable (see Section 5.5.2). For such observations it may make sense to include individual cloud species in the retrievals, just as it is done for the gas species, and to define a cloud base position, a cloud base density, as well as a power-law decrease of the density, and a mean particle size, based on the parameters which describe the clouds in the Ackerman & Marley (2001) cloud model (see Section 3.5.1).

6.6.2 Model complexity and nested sampling retrieval

Another useful next step for my retrieval code is to assess the posterior probabilities with a nested sampling algorithm, rather than with the MCMC method. As outlined in Section 1.4.2, if one can think of various different models to generate synthetic spectra, then nested sampling (Skilling 2004) retrieval allows to find the most likely one, based on a pairwise comparison of their model evidences. Possible questions which can be answered with nested sampling retrieval are, e.g., which atmospheric absorbers to include, and whether the consideration of clouds, or a partial cloud coverage, are justified to describe the data (Benneke & Seager 2013; MacDonald & Madhusudhan 2017). Another example is to ask whether or not the data warrants models with more than one temperature profile (Feng et al. 2016), which may be necessary if the flux originates from regions on the planet's surface with very different temperatures. Once high SNR data from *JWST* becomes available, the use of such more complex models may become more justified, but this will have to be tested with nested sampling retrieval on a case-by-case basis.

For implementing nested retrieval I will most likely make use of the *MultiNest* algorithm by Feroz et al. (2009), and its corresponding Python wrapper *PyMultiNest*[4] by Buchner et al. (2014). Like affine-invariant MCMC, nested sampling retrieval can be parallelized.

[4] https://johannesbuchner.github.io/PyMultiNest/pymultinest.html

6.6.3 Application

With the additions proposed above, it will be possible to apply my retrieval code to spectral and photometric data for transiting and directly imageable planets. To that end I plan to publish my retrieval radiative transfer code (with the parametrized atmospheric model) as part of a software called *BACON* (**B**ayesian **A**tmospheric **C**haracterizati**ON**), which I am currently developing together with Matthias Samland. *BACON* will be publicly available, and contain the observational data and model grid handling tools developed by Matthias Samland for his characterization of 51 Eri b (Samland et al. 2017, also see the 'Direct imaging spectroscopy' part of Section 1.4.1). *BACON* is planned to be very flexible in terms of what kind of data (photometry or spectroscopy), and how many different data sets are used, and to allow to retrieve the spectral covariance of the data in addition to the atmospheric parameters. Furthermore, the user will be able to easily chose what kind of retrieval is to be carried out, either by interpolating in atmospheric model grids, provided by the user, or by using my 'free' retrieval radiative transfer code, described in this chapter. In addition, *BACON* will offer a straightforward way for the user to include priors. The analysis in Samland et al. (2017), as well as the retrieval tests shown in this chapter, make use of the MCMC tool `emcee`, but we plan to also include nested retrieval as an option for the statistical analysis within *BACON*. We have already started first test retrievals with our preliminary *BACON* framework: we used the new *Spitzer IRS* reduction of HD 189733b's emission spectrum by Jeroen Bouwman and find promising first results, indicating that we can fit the spectrum well, as well as constrain this planet's dayside temperature structure.

7 Summary and Outlook

7.1 Summary

My thesis is concerned with the modeling of exoplanet atmospheres. In it, I describe how I built my code for the numerical modeling of atmospheric structures and observable spectra, called *petitCODE*, as well as the results I obtained by applying this code, which have been published in *The Astrophysical Journal* (Mollière et al. 2015) and in *Astronomy & Astrophysics* (Mollière et al. 2017). In addition, using *petitCODE*, I was able to contribute to multiple studies as a co-author (Mancini et al. 2016a; Mordasini et al. 2016; Mancini et al. 2016b; Southworth et al. 2017; Mancini et al. 2017; Samland et al. 2017). I have recently started to also construct tools for the evaluation of observational data, by implementing a fast radiative transfer solver, and coupling it to a Markov Chain Monte Carlo (MCMC) code, in order to assess the posterior distributions of the parameters which describe the state of the atmosphere. I will summarize the contents of the chapters below.

In Chapter 2 I describe the underlying theory of the atmospheric modeling of exoplanets, which touches upon their dynamics, and the resulting dynamic redistribution of insolation energy, as well as the atmospheres' vertical temperature structures, arising from radiative or convective energy transport. I discuss the sources of energy flux affecting the atmosphere (internal and irradiation), and their effect and evolution. I further summarize the sources of opacity within the atmosphere, arising from atoms, molecules, and clouds, and how the chemistry within such atmospheres can be modeled, which is essential for obtaining the total opacity.

Chapter 3 summarizes how I set up *petitCODE*, by describing the methods for solving the radiative transfer equation, while efficiently treating the molecular line opacities, and gives the references for the line lists I used for calculating these, and for the molecular and cloud continuum opacities. In addition I describe how I model equilibrium chemistry, using a self-written Gibbs minimizer, and which cloud model assumptions I make. Finally, I explain how *petitCODE* solves for the atmospheric temperature structure.

In Chapter 4 I describe the first application of *petitCODE*, which was published in Mollière et al. (2015), and which systematically studied the properties of hot jupiter atmospheres as a function of their effective temperature, surface gravity, composition (modeled by varying their metallicity [Fe/H] and C/O number ratio), and host star spectral type. To this end, I calculated 10,640 self-consistent atmospheric models. I could confirm previously known effects, such as that of a planet's surface gravity on its emission spectrum, or the appearance

of oxygen or carbon-dominated atmospheres. In addition, I showed for the first time that a C/O number ratio close to unity can lead to inversions in irradiated atmospheres, by chemically depleting it in its coolants. Moreover, I found that the spectral type of the host star can have a profound impact on atmospheric temperature structures, with planets circling later-type host stars attaining a more isothermal structure.

In Chapter 5, published in Mollière et al. (2017), I describe how *petitCODE* was used to make detailed predictions for exoplanets which we expect to be excellent targets for observation with *JWST*. The targets were initially selected by requiring them to have a SNR > 5 in the MIR (around 7 μm), using a simplified atmospheric model. I then calculated dedicated, self-consistent atmospheric models for all targets, varying the atmospheric composition, and whether, and how, clouds were included in the models. I obtained synthetic observations using the *EclipseSim* code (van Boekel et al. 2012). I found that *JWST* may be able to uncover molecular features in the atmospheres of notoriously cloudy super-Earths, such as GJ 1214b (Kreidberg et al. 2014), using less than 10 transits in the NIR. Cloud features arising from small silicate cloud particles in hot jupiter atmospheres may be seen using just a single transit in the *MIRI* instrument, which would correspond to the first conclusive identification of a cloud species in the atmosphere of an extrasolar planet. Finally, I found that a few ($\lesssim 3$) eclipse measurements with *JWST* may be sufficient to constrain the reason for the seemingly isothermal emission spectra (due to inversions?) seen in some of the hottest hot jupiters known today.

Chapter 6 describes the first steps I have taken towards constructing a retrieval code for the observation of planetary atmospheres. In it, I describe my fast radiative transfer implementation, as well as verifications thereof. I then explain the parametrized atmospheric temperature and abundance model to be used for the retrievals. I furthermore carry out retrieval tests, using, for the input, emission and transmission spectra obtained from modeling a hot jupiter with my parametrized retrieval model, and from self-consistent *petitCODE* calculations. Mock observations for *JWST* were obtained using the *EclipseSim* code, and I successfully retrieved the posterior distributions of the atmospheric temperature structures and abundances, using the open-source MCMC framework `emcee` (Foreman-Mackey et al. 2013). Only if self-consistent transmission spectra were retrieved was the retrieval result affected by biases, which may likely be resolved by introducing vertically varying abundance profiles, and including additional opacities in the retrieval code.

7.2 Outlook

With the development of *petitCODE* I have constructed a robust numerical framework to make self-consistent calculations of exoplanet atmospheres and their spectra. As I have shown in this thesis, *petitCODE* allows to study atmospheres over a large parameter space. Moreover, I can not only make such theoretical predictions, I am now also starting to move into the field of atmospheric retrieval, both of which skills are highly useful already now, but will be even more useful once *JWST*, and telescopes and instruments further in the future (such as *METIS* at the *E-ELT*, or the space telescope *ARIEL*) will become available.

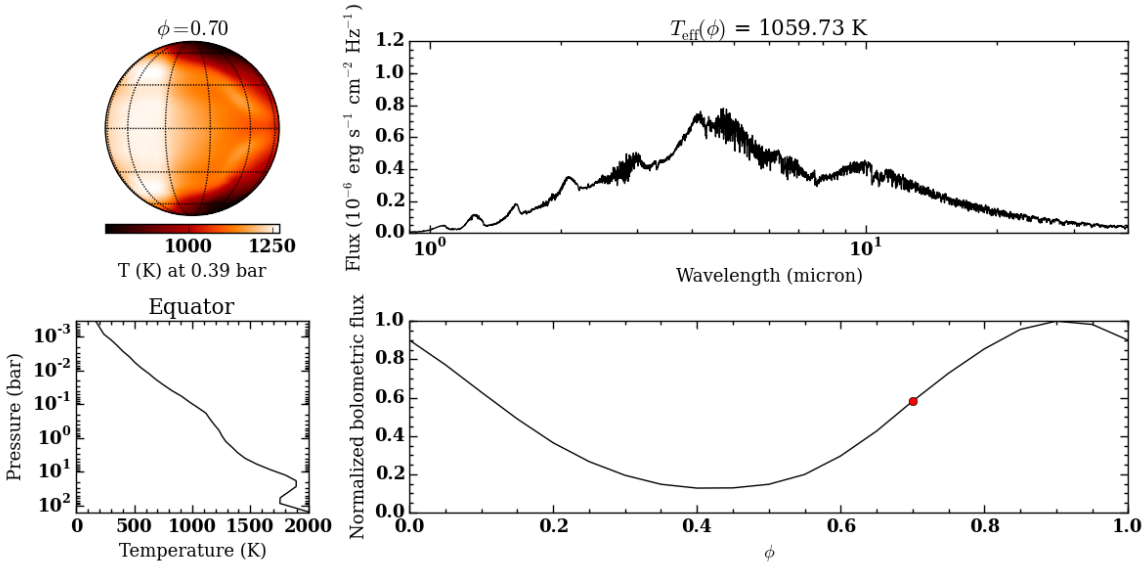

FIGURE 7.1: First result of coupling *MITgcm* with *petitCODE*, using a Newtonian cooling scheme to estimate the 3d temperature structure of a hot Jupiter. The plots show the resulting temperature map at 0.39 bar (*upper left*), the planet's emission spectrum (*upper right*) and the equatorial temperature structure (*lower left*), all derived from *MITgcm* at a phase of $\phi = 0.70$, i.e. shortly before seeing the planet's evening limb face-on . The *lower right panel* shows the planet's bolometric emission as a function of phase. For the phase-dependent spectra all points on the visible planetary disk were considered.

In addition, and as discussed in Section 6.6.2, the increased data quality to be expected from future missions may warrant for more complex models to be considered for exoplanet modeling, and both *petitCODE* and the retrieval code can, and will be updated and expanded to contain more physics and flexibility.

For the retrieval code, as outlined in Section 6.6.2, useful additions will be to include vertically varying abundance profiles, multiple temperature profiles, patchy cloud models, as well as including clouds of different species specifically into the retrieval model, especially as *JWST* may allow for the direct detection of cloud resonance features in the MIR. Next, moving from an MCMC framework to a nested sampling retrieval will be highly useful, as it allows for a direct comparison between different possible atmospheric models. As summarized in Section 6.6.2, various groups have already started tackling some of these tasks. In addition, publishing my retrieval code as part of the open-source *BACON* framework (see Section 6.6.3) will supply the exoplanet community with an easy-to-use tool for atmospheric retrieval, just in time for the revolution in exoplanet spectral data quality and coverage, to be expected from *JWST*.

In addition, while retrieval models of increased complexity may allow us to constrain the states of atmospheres better and better, it will be the task of more complex, and physically self-consistent atmospheric codes to interpret the results. For example, once a given molecular abundance has been retrieved for a certain region of the atmosphere, what does this tell us about the underlying elemental abundances in the atmosphere? To that end, the inclusion of processes such as non-equilibrium chemistry is paramount, as well as an improved understanding of condensation and cloud formation, in addition to describing planets, and

their atmospheres, as three-dimensional, dynamical systems. Here, likewise, already various groups have started to work towards building more complete models, looking at vertical non-equilibrium chemistry of isolated objects, as well what happens when winds in irradiated planets transport abundances horizontally around the planet, or if non-gray (i.e. wavelength-dependent) radiative transfer treatments are combined with 3-d hydrodynamical simulations of irradiated planets (see, e.g., Showman et al. 2009; Agúndez et al. 2014; Charnay et al. 2015a). Concrete plans for using the tools I developed in this thesis for such tasks already exist, such as building in a (reduced) non-equilibrium chemistry network into *petitCODE*, as well as coupling the radiative transfer schemes of *petitCODE* to the 3-d, hydrodynamical modeling of Ludmila Carone's version of the *MITgcm*[1] code (Carone et al. 2014, 2015, 2016). GCM stands for 'General Circulation Model' and is a general term for hydrodynamical atmospheric models. For achieving this coupling, as a first test, I calculated atmospheric temperature structures as a function of their angle off the substellar point. We then used the resulting structures in the GCM calculations by implementing a Newtonian cooling scheme and using a predefined profile for the radiative timescale. The resulting 3-d temperature structure was then fed back into *petitCODE* to calculate phase-dependent emission spectra. Figure 7.1 shows the resulting temperature map and emission spectrum at phase $\phi = 0.70$, i.e. just before viewing the planet's evening limb face-on. In the final coupling between *petitCODE* and *MITgcm* the radiative transfer will be called within *MITgcm*, and directly calculate the corresponding radiative heating terms. This fully couples the non-gray radiative transfer self-consistently to the 3-d hydrodynamics of the atmosphere.

The steps to be taken next by the exoplanet modeling community appear to be clear. Nonetheless, connecting all relevant processes in a numerical affordable way, as well as filling in gaps in our knowledge, will certainly be an inherently difficult endeavor, especially as observations will drive the modeling community to come up with new approaches, and theories. Nonetheless, we will be rewarded with exciting insights into the atmospheres and composition of far-away worlds, which may even allow us make inferences about their formation. There could be no better time to be a member of the exoplanet science community.

[1] http://mitgcm.org

A Derivations and methods

In parts based on Mollière et al. (2015, 2017).

A.1 A fast k-table combination method for correlated-k

Algorithm used at a spectral bin size of $\lambda/\Delta\lambda = 1000$ (R1000 method)

In order to combine the species' individual k-tables to obtain the total k-table of an atmospheric layer I use method that is faster than the classical method. Similarly to the classical approach, however, the method makes use of the assumption that the opacities are not correlated. The main idea is to iteratively combine the opacities of two species: The opacity of a real species and the effective opacity of a "help"-species. If the opacities of all species are uncorrelated, then the combined opacity of two species is not correlated with the opacity of any other remaining species. Furthermore, the combined opacity of the two combined species can be treated as belonging to a new single species, which is the "help"-species.

I then proceed in the following way: For every species, within every $\Delta\nu$ bin, I save the opacity distribution $\kappa(g)$ on a grid of 30 points. The 30-point grid consists of two 15-point Gaussian grids ranging from 0 to 0.9 and from 0.9 to 1, respectively.[1] When starting to construct the total opacity, the first two species 1 and 2 get combined according to equations (3.73) and (3.74). This results in $30 \times 30 = 900$ new values $\kappa_{12,ij}$ which need to be sorted by size. Using the cumulative sum of their associated weights $\Delta g_i \Delta g_j$, where Δg_i and Δg_j are the respective Gauss-grid weights, I interpolate the result back to the original 30-point Gauss-grid. This newly obtained opacity κ_{12} is then iteratively combined with the remaining species' opacities and results in the final opacity distribution $\kappa_{\mathrm{tot}}(g)$. In a procedural notation the method can thus be described as (where X_i are the respective species' mass fractions)

```
Total opacity = X_1 * kappa(g) of species 1

For all remaining species (i = 2 to N_sp) {

  Total opacity =   combine(Total opacity,
       X_i*kappa(g) of species i)

  re-bin Total opacity to nominal g-grid

}
```

For notational convenience the method for combining the opacities as introduced in this section will be called "R1000 method" in the following section. The number of points used

[1] This is not the same grid on which the radiative transport will be carried out. The radiative transport grid consists of 20 points, see Section 3.2.3. The 30-point Gaussian grid is only used for the combination of the k-tables.

for combining two species' opacities will be called N_{R1e3}. As explained above, the nominal value of N_{R1e3}, when working at a resolution of $\lambda/\Delta\lambda = 1000$, is $N_{\mathrm{R1e3}} = 30$.

Algorithm used at a bin size of $\lambda/\Delta\lambda = 10$ and 50

In order to correctly describe the opacity distributions at small $\lambda/\Delta\lambda$ many g-grid points would need to be used, as especially at low pressures the opacity tables $\kappa(g)$ tend to be very sharply peaked at g values very close to 1. Therefore the R1000 method would become numerically inefficient and cannot be used.

However, once more the idea is to combine two species iteratively in order to obtain the total opacity. Moreover, I make use of the assumption that the opacities are not correlated again. In the $\lambda/\Delta\lambda = 10$ and 50 cases the spectral bins are 100 or 20 times broader than in the $\lambda/\Delta\lambda = 1000$ case. They therefore include many lines, and the assumption of uncorrelatedness should be valid to an even higher degree than in the $\lambda/\Delta\lambda = 1000$ case.

The idea to obtain the total opacity is the following: In principle the combination of two species could be accomplished by randomly sampling the two individual opacity distributions, and taking the sum of the sampled values as a sample of the combined opacity. In a numerically simplified version one could discretize the opacity distributions by providing a pre-sampled set of N opacity values and their corresponding weights Δg. The random sampling could then be approximated by randomly drawing values from the opacity sets of each species, and adding them, taking the product of their weights as the new weight. If one would sample continuous values from a distribution, it is possible to sample values from within a given interval multiple times. Thus, if a discretized opacity value has been drawn from the opacity set it must in principle not be excluded from being drawn in any of the next sampling steps.

The discretization is carried out in the following way in my method: for every species, I divide the $\kappa(g)$ table into two sets. The first set contains $\kappa(g)$ values with $g < g_{\mathrm{bord}}$. Their g-coordinates are located at the centers of grid cells defined by $N_p + 1$ grid borders, spaced equidistantly between $g = 0$ and $g = g_{\mathrm{bord}}$. The second set contains $\kappa(g)$ values with $g \geq g_{\mathrm{bord}}$. Their g values are located at the centers of N_p grid cells, defined by N_p+1 grid borders spaced equidistantly between $g = g_{\mathrm{bord}}$ and $g = 1$. I chose $g_{\mathrm{bord}} = 0.985$ and $N_p = 128$. The N_p values of a species with $g < g_{\mathrm{bord}}$ will in the following be called κ_{low}, and the N_p values with $g \geq g_{\mathrm{bord}}$ will be called κ_{high}. Additionally, for every species, I save the lowest and highest opacity value within the frequency bin, corresponding to the $g = 0$ and $g = 1$ opacity values. κ_{low} describes the low g, continuum properties of the species' opacity, while κ_{high} describes the high g, line core properties of the species' opacity.

Returning to sampling values from 2 species, the probability of sampling and combining two values stemming from the respective $g < g_{\mathrm{bord}}$-regions is g_{bord}^2. The probability for combining two values, one from the $g < g_{\mathrm{bord}}$-region of species 1, and one from the $g > g_{\mathrm{bord}}$-region of species 2, is $g_{\mathrm{bord}} \cdot (1 - g_{\mathrm{bord}})$ etc...

To speed up sampling, I assume that once an opacity value of a given species has been drawn, it cannot be drawn again (I will return to the validity of this approach below).

In order to approximate the sampling process of the combined opacity distribution function of two species, I then construct a $4N_p \times 2$ matrix K, containing the various possible combinations of κ_{low} and κ_{high} of both species in the first column, weighted by how common these combinations would be in a random sampling process of both species' opacities in the second column. When sampling points from species 1 and combining them with sampled points from species 2, the assumption that a given value can not be redrawn allows for

a simple shuffling in the sampling process:

$$K = \begin{pmatrix} X_1 \cdot \text{shuffle}(\kappa_{1,\text{low}}) + X_2 \cdot \text{shuffle}(\kappa_{2,\text{low}}) & \frac{g_{\text{bord}}^2}{N_p} \\ X_1 \cdot \text{shuffle}(\kappa_{1,\text{low}}) + X_2 \cdot \text{shuffle}(\kappa_{2,\text{high}}) & \frac{g_{\text{bord}}(1-g_{\text{bord}})}{N_p} \\ X_1 \cdot \text{shuffle}(\kappa_{1,\text{high}}) + X_2 \cdot \text{shuffle}(\kappa_{2,\text{low}}) & \frac{g_{\text{bord}}(1-g_{\text{bord}})}{N_p} \\ X_1 \cdot \text{shuffle}(\kappa_{1,\text{high}}) + X_2 \cdot \text{shuffle}(\kappa_{2,\text{high}}) & \frac{(1-g_{\text{bord}})^2}{N_p} \end{pmatrix}. \tag{A.1}$$

The first column of K represents the sampled values of the new combined opacity, the second column gives the weight of each sampled value, similar to the $\Delta g_1 \Delta g_2$ weights in the classical method described in Section 3.2.2. I then sort the lines of the matrix K by the values in the first column. After this I construct a vector y of length $4N_p$ with the entries (starting at $m = 2$)

$$y_m = y_{m-1} + \frac{k_{(m-1),2} + k_{m,2}}{2} \tag{A.2}$$

and $y_1 = k_{1,2}/2$. The second column of K is then replaced with y. After this, the first column of K contains the newly sampled $\kappa_{\text{tot}}(g)$ values of the combined opacity of species 1 and 2, the second column contains the corresponding g values. Using $\kappa_{\text{tot}}(0) = X_1\kappa_1(0) + X_2\kappa_2(0)$, and $\kappa_{\text{tot}}(1) = X_1\kappa_1(1) + X_2\kappa_2(1)$, the total opacity can then be interpolated to the N_p low-g and N_p high-g values to yield the final result. The resulting opacity is then ready for being combined with the opacity of the next species. In order to shuffle the opacities I use the Knuth-shuffle algorithm, which is of order $\mathcal{O}(N_p)$.

The assumption of not being able to draw a given opacity value more than once is not correct. However, I found this to not affect the quality of the results. From the above one sees that in every combination step one needs to sort $4N_p$ values. The R1000 method would have the same computational costs when storing $N_{\text{R1e3}} = 2\sqrt{N_p}$ opacity points per species, losing resolution when comparing to the $2N_p$ points used in the method introduced here. Furthermore, the results of the R1000 method, at the same computational cost, turn out to be worse, both when comparing to the actual shape of the wanted total opacity distribution as well as when comparing

$$\frac{1}{\Delta\nu} \int_{\nu}^{\nu+\Delta\nu} \kappa_{\nu'} \mathrm{d}\nu' \approx \sum_i \kappa_i \Delta g_i \tag{A.3}$$

for both methods.[2] The error of the method introduced here is in the range of %, whereas the error of the R1000 method, at these low $\lambda/\Delta\lambda$ resolutions, and at the same computational cost, is in the range of tens of %. Comparing the results of the new method with results of the R1000 method, when taking $N_{\text{R1e3}} = 2N_p$, i.e. the same number of points in both cases, yields slightly better results for the R1000 method. However, the numerical cost for the R1000 method is $\mathcal{O}(4N_p^2)$, while it is $\mathcal{O}(4N_p)$ in the new method presented here. The reason for the R1000 method, at the fiducial resolution $N_{\text{R1e3}} = 30$, to fail here is that I consider 20-100 more points per wavelength bin. This requires a higher resolution when trying to resolve the actual opacity distribution function.

In Figure A.1 I show an example calculation from combining the opacities of water, methane and ammonia in the wavelength range going from 6.64 to 7.34 μm. The $\kappa(g)$ distributions of the individual species are shown in the plot. All species are contributing approximately equally strongly to the total opacity in this example, and have lines in the wavelength region of interest. Therefore, this case represents something like a worst-case scenario, as

[2] I will need to evaluate Equation A.3 when computing the Planck mean opacity in the temperature calculation.

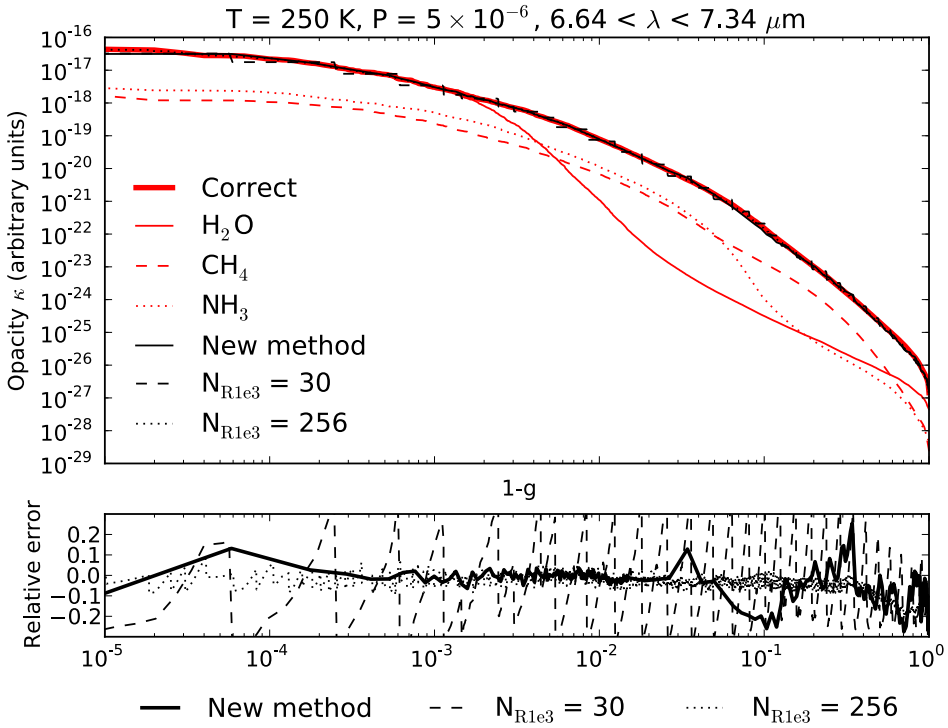

FIGURE A.1: Comparison of the different methods to combine the $\kappa(g)$ tables of different species. *Upper panel:* Opacity of water (red solid line), methane (red dashed line) and ammonia (red dotted line) as a function of g. The total $\kappa(g)$ obtained from adding the opacities in frequency space is shown as a red thick solid line. The results when using the R1000 method with N_{R1e3} = 30 points and N_{R1e3} = 256 points are shown as black dashed and dotted lines, respectively. The result when using the new method introduced in this section is shown as a black solid line. *Lower panel:* Relative error of the three methods compared to the correct solution: N_{R1e3} = 30 points (dashed line), N_{R1e3} = 256 points (dotted line), new method (thick solid line). Figure taken from Mollière et al. (2015).

the method is the most accurate when one species dominates, or the other species only contribute via a their line wing continua. I plot the correct total $\kappa(g)$ distribution, obtained when adding the opacities in frequency space first, as well as the results obtained from using the R1000 method, and the result from using the new method introduced in this section. One sees that the new method is never worse in accuracy than the R1000 method, and usually has an relative error which is an order of magnitude smaller. The error of the $N_{R1e3} = 256$ results is an order of magnitude smaller than the $N_{R1e3} = 30$ result.

Spectral calculations with *petitCODE*, using the above efficient method at $\lambda/\Delta\lambda = 10$ do not deviate by more than 5 % (and usually less) in wavelength regions of appreciable flux, when comparing to the rebinned $\lambda/\Delta\lambda = 10^6$ line-by-line calculations (see Section 3.2.3, Figure 3.4). This is a accuracy commonly stated for correlated-k (see, e.g., Fu & Liou 1992; Lacis & Oinas 1991). The strength of the new method reported here is to be numerically efficient, while conserving the opacity information at a high level of detail.

A.2 Cloud particle size and atmospheric mixing properties

A.2.1 Cloud particle size distribution

Motivated by clouds and precipitation measurements on earth the particle density in Ackerman & Marley (2001) is approximated by a broad lognormal distribution

$$\frac{dn}{dr} = \frac{N}{r\sqrt{2\pi}\log\sigma_g}\exp\left[-\frac{\log^2(r/r_g)}{2\log^2\sigma_g}\right], \tag{A.4}$$

where n is the cumulative number of particles per volume up to a certain size r (and its full value, integrated over all radii is N), $r_{\rm g}$ is the mean geometric radius of the particles, and $\sigma_{\rm g}$ is the standard deviation. The fiducial value for $\sigma_{\rm g}$ used in Ackerman & Marley (2001) is

$$\sigma_{\rm g}^{\rm fiducial} = 2\,. \tag{A.5}$$

Following Ackerman & Marley (2001), I will parametrize the particle settling velocity as

$$v_f = v_{\rm mix}\left(\frac{r}{r_w}\right)^{\alpha}\,. \tag{A.6}$$

Further, as said in Section 3.5.1, $f_{\rm sed}$ is the mass-averaged ratio of the settling velocity to the atmospheric mixing velocity, i.e.

$$f_{\rm sed} = \frac{\int_0^\infty r^{3+\alpha}(dn/dr)dr}{r_w^\alpha \int_0^\infty r^3(dn/dr)dr}\,. \tag{A.7}$$

Using

$$\int_0^\infty r^\beta \frac{dn}{dr}dr = N r_{\rm g}^\beta {\rm exp}\left(\frac{1}{2}\beta^2 {\rm log}^2\sigma_{\rm g}\right) \tag{A.8}$$

one finds

$$r_{\rm g} = r_w f_{\rm sed}^{1/\alpha}{\rm exp}\left(-\frac{\alpha+6}{2}{\rm log}^2\sigma_{\rm g}\right)\,. \tag{A.9}$$

If we know the total local cloud density $\rho_{\rm c}$, then it must hold for the mass distribution per unit volume dm/dr that

$$\rho_{\rm c} = \int_0^\infty \frac{dm}{dr}dr = \int_0^\infty \frac{4\pi}{3}r^3\rho_{\rm p}\frac{dn}{dr}dr = \frac{4\pi}{3}r_g^3\rho_{\rm p}N{\rm exp}\left(\frac{9}{2}{\rm log}^2\sigma_{\rm g}\right)\,, \tag{A.10}$$

where $\rho_{\rm p}$ is the material density of an individual cloud particle. Here it was assumed that the cloud particles are spherical. Therefore we get

$$N = \frac{3\rho_c}{4\pi\rho_{\rm p}r_{\rm g}^3}{\rm exp}\left(-\frac{9}{2}{\rm log}^2\sigma_{\rm g}\right)\,. \tag{A.11}$$

Hence, if α and r_w are known, one can calculate r_g, N and thus dn/dr. For this we need to obtain $v_{\rm mix}$ from the atmospheric mixing properties, as well as the size-dependent particle settling speeds, which can then be fit with the parametrized formula given in Equation A.6. I will summarize how the size-dependent settling speeds are calculated in Section A.2.2, followed by how $v_{\rm mix}$ is calculated in Section A.2.3.

A.2.2 Size-dependent settling speeds

The first ingredient for calculating the particle settling speed v_f is the dynamic viscosity, and the expression used in Ackerman & Marley (2001) is from Rosner (2012):

$$\eta = \frac{15}{16}\frac{\sqrt{\pi m k_{\rm B}T}}{\pi d^2}\frac{(k_{\rm B}T/\epsilon)^{0.16}}{1.22}\,. \tag{A.12}$$

For an H_2 atmosphere the atmospheric molecular diameter is $d = 2.827\times10^{-8}$ cm and the depth of the Lennard-Jones potential ϵ is $59.7\ k_{\rm B}$ K. The symbol m denotes the mass of the H_2 molecule.

In the laminar flow regime one can use the formula which is given in Ackerman & Marley (2001), and also in a similar form in Podolak (2003) (except that Podolak (2003)'s is larger by a factor π):

$$v_f = \frac{2r^2(\rho_\mathrm{p} - \rho)\psi g}{9\eta} \,, \tag{A.13}$$

where

$$\psi = 1 + N_\mathrm{Kn}(1.249 + 0.42e^{-0.87/N_\mathrm{Kn}}) \tag{A.14}$$

smoothly connects the regimes of Stokes and Epstein drag, corresponding to small or large Knudsen numbers N_Kn, respectively. I use ψ from Podolak (2003), instead of the corresponding β from Ackerman & Marley (2001), which ignores the exponential second term in the bracket in ψ. The Knudsen number N_Kn is the ratio between the molecular mean free path and droplet radius, and can be evaluated by

$$N_\mathrm{Kn} = \frac{\mu m_\mathrm{p}}{\pi\rho d^2 r} \,, \tag{A.15}$$

with m_p being a proton mass and μ being the atmospheric mean molecular weight in amu.

In order to obtain r_w and α one can then fit the result of Equation A.13 by choosing r_w and α such that

$$\frac{2\pi r^2(\rho_\mathrm{p} - \rho)\psi g}{9\eta} \approx v_\mathrm{mix}\left(\frac{r}{r_w}\right)^\alpha \,. \tag{A.16}$$

The relation for v_f is fit for radii between r_w/σ_g and r_w for $f_\mathrm{sed} > 1$, and between r_w and $\sigma_g r_w$ for $f_\mathrm{sed} \leq 1$.

In the turbulent flow regime Ackerman & Marley (2001) solve for the settling velocity using a fitted function, relating the drag coefficient and the Reynolds number: They fit $y = \log(N_\mathrm{Re})$ as a function of $x = \log(C_\mathrm{d}N_\mathrm{Re}^2)$ and obtain

$$y = 0.8x - 0.01x^2 \,. \tag{A.17}$$

This allows to solve for C_d if $C_\mathrm{d}N_\mathrm{Re}^2$ is given. This quantity, i.e. the drag coefficient C_d multiplied with the squared Reynolds number N_Re is given by

$$C_\mathrm{d}N_\mathrm{Re}^2 = \frac{32\rho g r^3(\rho_\mathrm{p} - \rho)}{3\eta^2} \,. \tag{A.18}$$

Using this equation together with Equation A.17 allows to solve for C_d. The settling speed of a particle of radius r is then finally given as

$$v_f = \psi\sqrt{\frac{8gr(\rho_\mathrm{p} - \rho)}{3C_\mathrm{d}\rho}} \,. \tag{A.19}$$

However, the fit given in A.17 does *not* reproduce the boundary values stated in Ackerman & Marley (2001), namely that $C_\mathrm{d} = 24$ for $N_\mathrm{Re} = 1$ and $C_\mathrm{d} = 0.45$ for $N_\mathrm{Re} = 1000$ and does also not reproduce the values referenced from Pruppacher & Klett (1979), Table 10-1, regardless of wether the natural logarithm (log) or the logarithm base 10 is used ($\log_{10}$). I thus fitted the data myself, allowing for a constant y-intercept value and obtained

$$y = -2.7905 + 0.9209x - 0.0135x^2 \,. \tag{A.20}$$

This relation fitted all referenced $(N_\mathrm{Re}, C_\mathrm{d})$ pairs very well. Further, the coefficients in front of x and x^2 are almost identical (modulo small differences from the fit) to the values given in Equation A.17, so I assume the y-intercept value was simply forgotten in the Ackerman

& Marley (2001) paper. In the final implementation I will only use Equation A.19 and fit r_w and α at the same time, such that

$$v_{\rm mix}\left(\frac{r}{r_w}\right)^{\alpha} \approx \psi\sqrt{\frac{8gr(\rho_{\rm p}-\rho)}{3C_{\rm d}\rho}} \,. \tag{A.21}$$

A.2.3 Atmospheric mixing speed

In order to fit the parameters in Equation A.21 one needs to know the atmospheric mixing speed $v_{\rm mix}$. I will first summarize how to obtain it for the convective region, using MLT, and then how to obtain it above the convective region.

MLT mixing speed

The mixing velocity in the convective zone can be expressed as

$$v_{\rm mix} = \frac{K}{H_P} \,, \tag{A.22}$$

where the eddy diffusion coefficient used in Ackerman & Marley (2001) is stemming from Gierasch & Conrath (1985) and taken to be

$$K = \frac{H_P}{3}\left(\frac{RF_{\rm conv}}{\mu\rho c_P}\right)^{1/3} \,, \tag{A.23}$$

with R being the universal gas constant, μ the molecular weight in units of g per mol, c_P the specific heat and $F_{\rm conv}$ the flux in the atmosphere transported by convection, as defined in Equation 2.15. This quantity can to be taken from the mixing length model introduced in Section 2.1.2. If $F_{\rm conv}$ is known one then finds

$$v_{\rm mix} = \frac{1}{3}\left(\frac{RF_{\rm conv}}{\mu\rho c_P}\right)^{1/3} \,. \tag{A.24}$$

Using the equations introduced for MLT in Section 2.1.2, I will show how to solve for $F_{\rm conv}$ in the following. Combining equations 2.15, 2.17, and 2.19, one sees that the convective flux in the framework of mixing length theory can be expressed as

$$F_{\rm conv} = \rho c_P T\sqrt{g\delta}\frac{l_{\rm mix}^2}{4\sqrt{2}}H_P^{-3/2}(\nabla_{\rm atmo}-\nabla_{\rm blob})^{3/2} \,, \tag{A.25}$$

where c_P is the specific heat capacity at constant pressure and

$$\delta = -\left(\frac{\partial \log\rho}{\partial \log T}\right) \,, \tag{A.26}$$

which is equal to $\delta = 1$ for an ideal gas.

This means that we know everything except for $(\nabla_{\rm atmo}-\nabla_{\rm blob})^{3/2}$. Now one defines

$$U = \frac{3acT^3}{c_P\rho^2\kappa_{\rm R}L^2}\sqrt{\frac{8H_P}{g\delta}} \,, \tag{A.27}$$

where a is the radiation energy density constant, c the speed of light and $\kappa_{\rm R}$ the Rosseland mean opacity. One can then also define

$$W = \nabla_{\rm rad} - \nabla_{\rm ad} \tag{A.28}$$

and

$$\xi = \sqrt{\nabla_{\rm atmo} - \nabla_{\rm ad} + U^2}\,. \tag{A.29}$$

One finally finds that the following equation must be solved:

$$(\xi - U)^3 + \frac{8U}{9}\left(\xi^2 - U^2 - W\right) = 0\,, \tag{A.30}$$

which yields

$$\xi = \frac{19}{27}U - \frac{184}{27}2^{1/3}\frac{U^2}{A} + \frac{2^{2/3}}{27}A\,, \tag{A.31}$$

where

$$A = \left(1168U^3 + 2187UW + 27\sqrt{3}\sqrt{2048U^6 + 2336U^4W + 2187U^2W^2}\right)^{1/3}\,. \tag{A.32}$$

This gives the value of $\nabla_{\rm atmo}$.

An easy to evaluate expression for $\nabla_{\rm blob}$ is found from using various equations defined in Kippenhahn & Weigert (1990), which results in

$$\nabla_{\rm blob} = \nabla_{\rm ad} + 2U\xi - 2U^2\,. \tag{A.33}$$

The solution for the convective flux can then be plugged into Equation A.24, yielding the convective mixing velocity.

One more 'subtlety' needs to be mentioned here: Mixing length theory is only defined if the Schwarzschild criterion is fulfilled, i.e. if $W > 0$. This is quite easy to see: the quantity Γ defined in Section 2.1.2 can be expressed as

$$\Gamma = \frac{\text{energy transported by convective blob}}{\text{radiative losses of convective blob}} = \frac{\sqrt{\nabla_{\rm atmo} - \nabla_{\rm blob}}}{2U}\,. \tag{A.34}$$

After restructuring the equations in Kippenhahn & Weigert (1990) one finds that

$$W = U^2\left[4\Gamma^2 + 4\Gamma + \frac{9}{8}\left(\sqrt{4\Gamma^2 + 4\Gamma + 1} - 1\right)^3\right]\,, \tag{A.35}$$

which shows that W is always ≥ 0 in mixing length theory. The lowest value can be reached for $\Gamma \to 0$ which yields $W \to 0$, i.e. $W < 0$ can never lead to convection in the framework of the above theory.

In order to obtain the atmospheric mixing above the convective region a different approach must be taken, and I summarize this below.

Parametrized mixing speed

On top of the convective region I assumed that there is a minimum $K_{\rm min} = 10^5$ cm^2 s^{-1} stemming from the breaking of gravitational waves in the atmosphere, follwing Ackerman & Marley (2001). Additionally, I include two more contributions:

In the deep atmospheric layers, just above the convectively unstable region, I account for the motion arising from convective overshoot. To arrive at a simple description for the overshoot eddy diffusion coefficient, I considered the fit reported in Ludwig et al. (2002);

Helling et al. (2008), namely

$$K_{\rm overshoot}(P) = K_{\rm MLT}\left[\frac{H_P}{H_{\rm MLT}}\right]^2\left(\frac{P}{P_{\rm MLT}}\right)^{\alpha g_5^{1/2}}\,, \tag{A.36}$$

where $K_{\rm MLT}$ is the eddy diffusion coefficient found in the last deep convective layer, that is, just before the atmosphere becomes stable against convection further above. $P_{\rm MLT}$ is the pressure in the last (uppermost) convectively unstable atmospheric layer, and $P < P_{\rm MLT}$. The exponent terms are defined as $g_5 = g/(10^5\ {\rm cm\ s^{-2}})$, where g is the gravitational acceleration in the atmosphere. The α factor is a linear function of the internal temperature and varies between 1 and 3 for $T_{\rm int}$ ranging from 1500 to 300 K, following Helling et al. (2008).

However, I found that for many planets a self-consistent coupling of the overshoot, mixing, and the atmospheric temperature iteration leads to non-convergence. The reason is that in cases where clouds form deep in the atmosphere, just above the convective region, they can make the atmosphere sufficiently optically thick to trigger convection. This moves $P_{\rm MLT}$ to lower values. In the regions that then switch to being convective, the increased mixing strength results in larger cloud particle radii (for a fixed $f_{\rm sed}$), which lead to a smaller cloud opacity, which causes the culprit layers to become stable against convection again. These layers therefore oscillate between being convectively stable or unstable, impeding convergence. To circumvent this problem, I decided to impose the overshoot mixing coefficient and thus set

$$K_{\rm overshoot}(P) = 10^9\cdot\left(\frac{P}{1000\ {\rm bar}}\right)\ {\rm cm^2\ s^{-1}}\,, \tag{A.37}$$

which I found to be broadly consistent with the self-consistent values obtained for the various planets I considered in Mollière et al. (2017). Note that this treatment is only valid for irradiated planets with atmospheric structures dominated by insolation as, for self-luminous planets, the radiative convective boundary moves to smaller pressures.

In the upper regions of irradiated planets, one finds an increase of the eddy diffusion coefficient, as the insolation drives vertical motion in the atmosphere, and because there is more stellar flux in the upper regions of the atmosphere. Parmentier et al. (2013) found in GCMs that the corresponding eddy diffusion coefficient behaves approximately as $K_{\rm irrad} \propto P^{-1/2}$ and two GCMs modeling HD 189733b and HD 209458b yielded

$$K_{\rm 209458b} = 5\times10^8\cdot\left(\frac{P}{1\ {\rm bar}}\right)^{-0.5}\ {\rm cm^2\ s^{-1}}\,, \tag{A.38}$$

$$K_{\rm 189733b} = 10^7\cdot\left(\frac{P}{1\ {\rm bar}}\right)^{-0.65}\ {\rm cm^2\ s^{-1}}\,, \tag{A.39}$$

see Agúndez et al. (2014). I adopted an irradiation contribution to K which is proportional to $P^{-1/2}$, where the reference value at 1 bar for HD 189733b was used. The difference between the mixing strength of HD 189733b and HD 209458b originated in the inclusion of TiO/VO opacities for HD 209458b, and similar values were obtained for HD 209458b if these opacities were neglected (private communication with V. Parmentier). For pressures smaller than 10^{-5} bar, I held the $K_{\rm irrad}$ value constant to the value at 10^{-5} bar, because this is where the GCM calculations stopped.

The full eddy diffusion coefficient is thus found as

$$K = \max\left(K_{\rm min}, K_{\rm overshoot} + K_{\rm irrad}\right)\,. \tag{A.40}$$

Additionally, I make the same assumption as above, namely that $v_{\rm mix} = K/H_P$.

A.3 Derivation of the Guillot (2010) temperature profiles

Because it appears twice within this thesis, I will here derive the Guillot (2010) temperature formula, because it can be obtained as a byproduct of the VEF temperature derivation in Section 3.6. I neglect all scattering processes here, such that $F_* = F_*^{\rm ini}$. Further, the plane-parallel assumption is made.

One additional ingredient is needed for this: from the steps used when deriving Equation 3.66 one can easily show that for the first moment of the stellar radiation field, impinging at an angle ϑ_*, with $\cos(\vartheta_*)$, it holds that

$$H_{*,\nu} = \frac{F_{*,\nu}}{4\pi} = \frac{F_{*,\nu}(0)}{4\pi} e^{-\tau_{{\rm vert},\nu}/\mu_*} \tag{A.41}$$

From Equation 3.117 we obtain, assuming $f = 1/3$, that

$$\frac{dJ}{dP} = \frac{3}{g}\kappa_H H \ . \tag{A.42}$$

$f = 1/3$ corresponds to the case of diffuse, i.e. ∼isotropic radiation, as it then holds that $J = I$ and

$$K = \frac{I}{2}\int_{-1}^{1} \mu^2 d\mu = \frac{I}{3} = \frac{J}{3} \ , \tag{A.43}$$

where the isotropy of I and Equation 3.105 were used.

Additionally, following Guillot (2010), I will now define the 'irradiation temperature' $T_{\rm irr}$ by

$$\frac{\sigma T_*^4 R_*^2}{d^2} = \sigma T_{\rm irr}^4 \ , \tag{A.44}$$

where T_* and R_* are the stellar effective temperature and radius, and d is the planet–star distance. The stellar flux entering the planetary atmosphere parallel to the atmospheric normal then is

$$F_*(0) = \sigma \mu_* T_{\rm irr}^4 \ . \tag{A.45}$$

Using flux conservation (see Equation 3.114), and assuming the opacity for the stellar absorption to be gray, one then finds for the planet's first moment of the radiation field that

$$H(P) = \frac{\sigma T_{\rm int}^4}{4\pi} + \frac{\sigma \mu_* T_{\rm irr}^4}{4\pi} e^{-\tau_{{\rm vert},*}/\mu_*} \ . \tag{A.46}$$

I next make the assumption that the optical depth of the stellar irradiation is $\tau_{{\rm vert},*} = \gamma \tau_{\rm vert}$, where $\tau_{\rm vert}$ is the optical depth of the planetary radiation field.

One then obtains from equations A.42 and A.46 that

$$\frac{dJ}{d\tau_{\rm vert}} = 3\left(\frac{\sigma T_{\rm int}^4}{4\pi} + \frac{\sigma \mu_* T_{\rm irr}^4}{4\pi} e^{-\gamma\tau_{\rm vert}/\mu_*}\right) \ , \tag{A.47}$$

where $\kappa_{\rm H} = \kappa$ (gray atmosphere), and $d\tau = \kappa dP/g$ was used. Using $J(0) = H(0)/\psi$ one then obtains that

$$J(\tau) = 3\frac{\sigma T_{\rm int}^4}{4\pi}\tau_{\rm vert} - 3\frac{\sigma \mu_*^2 T_{\rm irr}^4}{4\pi\gamma}\left(e^{-\gamma\tau_{\rm vert}/\mu_*} - 1\right) + \frac{1}{\psi}\left(\frac{\sigma T_{\rm int}^4}{4\pi} + \frac{\sigma \mu_* T_{\rm irr}^4}{4\pi}\right) \ . \tag{A.48}$$

Next, for the planetary radiation field, at the top of the atmosphere, if one assumes it to be ∼isotropic, but only non-zero for positive μ values, it holds that $J = I/2$ and $H = I/4$, such

that it holds that $\psi = 1/2$ (see Equation 3.105). One then finds that

$$J(\tau) = \frac{3\sigma T_{\rm int}^4}{4\pi}\left(\tau_{\rm vert} + \frac{2}{3}\right) + 3\frac{\sigma\mu_* T_{\rm irr}^4}{4\pi}\left(\frac{2}{3} + \frac{\mu_*}{\gamma} - \frac{\mu_*}{\gamma}e^{-\gamma\tau_{\rm vert}/\mu_*}\right) \tag{A.49}$$

Assuming radiative equilibrium (see Equation 3.97) one then gets

$$T^4 = \frac{3T_{\rm int}^4}{4}\left(\tau_{\rm vert} + \frac{2}{3}\right) + 3\frac{\mu_* T_{\rm irr}^4}{4}\left[\frac{2}{3} + \frac{\mu_*}{\gamma} + \left(\frac{\gamma}{3\mu_*} - \frac{\mu_*}{\gamma}\right)e^{-\gamma\tau_{\rm vert}/\mu_*}\right] \tag{A.50}$$

where Equation 3.66 was used to obtain J_*. This is identical to equation 27 in Guillot (2010), and to Equation B.1 used in the next Appendix, because $T_{\rm irr}^4 = 4T_{\rm equ}^4$ (see Equation 1.1). Equation 2.26 in Section 2.2 can be obtained from realizing that the stellar flux for a planet-wide average is equal to $\sigma T_{\rm irr}^4/4$, instead of $\mu_*\sigma T_{\rm irr}^4$, and by assuming that the mean angle μ_* used within the square brackets on the RHS of Equation A.50 is $\mu_* = 1/\sqrt{3}$. If this angle is assumed then the stellar radiation behaves like an isotropic irradiation field (see Guillot 2010).

A.4 Derivation of $T_{\rm rad}$ and $T_{\rm max}$

Here I derive the effective temperature corresponding to the maximum bolometric flux which an observer can receive from an irradiated planet ($T_{\rm max}$) when viewing the planetary dayside face-on. Furthermore, I derive the effective temperature corresponding to the case when the redistribution of the stellar irradiation on the planetary surface (by winds) can be neglected ($T_{\rm rad}$), likewise when viewing the planetary dayside face-on. For both cases I will assume blackbody emission.

A.4.1 Derivation of $T_{\rm max}$

At the orbital position of the planet, at a distance a to the star, the stellar flux measured at the location of the planet is

$$F_* = \frac{\sigma T_*^4 R_*^2}{a^2}\,, \tag{A.51}$$

where σ is the Stefan-Boltzmann constant, T_* the stellar effective temperature, and R_* the stellar radius. The planet intercepts this flux with a cross-section $\pi R_{\rm Pl}^2$, where $R_{\rm Pl}^2$ is the planetary radius, such that the total energy received by the planet per unit time is

$$L_* = \frac{\sigma T_*^4 R_*^2}{a^2}\pi R_{\rm Pl}^2\,. \tag{A.52}$$

The maximum flux an observer, who sees the planetary dayside face-on, will measure, is if the planet succeeds in emitting as much light in the direction of the observer as possible. Assuming isotropic blackbody emission, this is achieved if the planet transports all the energy it receives to the substellar point, and emits it from there, because the planetary normal vector of the substellar point, when viewing the dayside face-on, is parallel to the observer's line of sight. Assuming that the emitting area has a size ΔA, then the flux measured by the observer will be

$$F_{\rm meas} = \underbrace{\frac{\sigma T_{\rm subs}^4}{\pi}}_{\int B_\nu(T_{\rm subs})d\nu} \times \underbrace{(\mathbf{n}_{\rm Pl}\cdot\mathbf{n}_{\rm sight})}_{1} \times \underbrace{\frac{\Delta A}{d^2}}_{\Delta\Omega}\,, \tag{A.53}$$

where d is the observer's distance to the star and $T^4_{\rm subs}$ is the effective temperature of the planet's substellar region of size ΔA, and it was used that the angle between the detector normal $n_{\rm sight}$ and the planetary light $n_{\rm Pl}$ is zero. For the definition of the flux I used Equation 3.5. The emission of the substellar point must radiate away the energy L_*, such that one finds that

$$\sigma T^4_{\rm subs}\Delta A = \frac{\sigma T^4_* R^2_*}{a^2}\pi R^2_{\rm Pl}\,, \tag{A.54}$$

and hence

$$\frac{\sigma T^4_{\rm subs}}{\pi} = \frac{\sigma T^4_* R^2_*}{a^2 \Delta A} R^2_{\rm Pl}\,. \tag{A.55}$$

Plugging Equation A.55 into Equation A.53 yields

$$F_{\rm meas} = \sigma \frac{T^4_* R^2_*}{a^2}\frac{R^2_{\rm Pl}}{d^2}\,. \tag{A.56}$$

From this it follows that the global equilibrium temperature, which an observer would associate the planetary surface with, is equal to

$$T_{\rm max} = T_*\sqrt{\frac{R_*}{a}}\,, \tag{A.57}$$

as the measured planetary flux would then be $\sigma T^4_{\rm max}(R_{\rm Pl}/d)^2$. Note that the the substellar point's real effective temperature must be much higher, as $T_{\rm subs} \propto (1/\Delta A)^{1/4}$, where ΔA may be chosen arbitrarily small.

A.4.2 Derivation of $T_{\rm rad}$

The flux recorded by the observer, when viewing the dayside of the planet face on, is equal to

$$F_{\rm meas} = \int I_{\rm day}(\Omega)\underbrace{(\mathbf{n}_{\rm Pl}\cdot\mathbf{n}_{\rm sight})}_{1} d\Omega\,, \tag{A.58}$$

where again $n_{\rm sight}$ is the normal vector of the detector, and $n_{\rm Pl}$ is the direction of propagation of the planetary light, which moves into the direction of the observer. The angle between these vectors is ∼equal to 0, due to the large distance of the observer to the planet. If there is no redistribution of the insolation energy by winds, and the planet emits like a blackbody, then the temperature of the planetary surface at an angle ϑ away from the substellar point must satisfy

$$\frac{\sigma T^4_* R^2_*}{a^2}\cos(\vartheta) = \sigma T^4(\vartheta) \tag{A.59}$$

such that

$$I_{\rm day} = \frac{\sigma}{\pi}\frac{T^4_* R^2_*}{a^2}\cos(\vartheta)\,, \tag{A.60}$$

where the symbols have the same meaning as in Appendix A.4.1 above. The area of a planetary annulus at an angle ϑ away from the substellar point is

$$\Delta A = 2\pi R_{\rm Pl}\sin(\vartheta) R_{\rm Pl}\Delta\vartheta\,, \tag{A.61}$$

and the effective area seen by the observer is equal to $\cos(\vartheta)\Delta A$, such that one finally gets, using $\Delta\Omega = \cos(\vartheta)\Delta A/d^2$, where d is the distance between planet and observer, that

$$\begin{aligned} F_{\rm meas} &= 2\sigma\frac{T_*^4 R_*^2}{a^2 d^2} R_{\rm Pl}^2 \int_0^{\pi/2} \cos^2(\vartheta)\sin(\vartheta) d\vartheta \\ &= 2\sigma\frac{T_*^4 R_*^2}{a^2 d^2} R_{\rm Pl}^2 \int_0^1 \mu^2 d\mu \\ &= \sigma\frac{2}{3}\frac{T_*^4 R_*^2}{a^2}\frac{R_{\rm Pl}^2}{d^2} \,. \end{aligned} \tag{A.62}$$

From this it follows that the global equilibrium temperature, which an observer would associate the planetary surface with, is equal to

$$T_{\rm rad} = T_* \left(\frac{2}{3}\right)^{1/4} \sqrt{\frac{R_*}{a}} \,, \tag{A.63}$$

as the measured planetary flux would then be $\sigma T_{\rm rad}^4 (R_{\rm Pl}/d)^2$.

A.5 Calculating the mean atmospheric transmission using k-tables

In frequency space, the mean atmospheric transmission is defined as

$$\bar{\mathcal{T}}^i = \frac{1}{\Delta\nu}\int_{\nu_0-\Delta\nu/2}^{\nu_0+\Delta\nu/2} \exp\left[-\int_0^{P_i}\frac{1}{a}\left(\sum_{j=1}^{N_{\rm species}} X_j \kappa_\nu^j\right) dP\right] d\nu \,, \tag{A.64}$$

where κ_ν^j is the atmospheric opacity in units of area per mass of the absorbing species j with mass fraction X_j, a is the atmospheric gravitational acceleration and P is the atmospheric pressure. This transforms to

$$\bar{\mathcal{T}}^i = \frac{1}{\Delta\nu}\int_{\nu_0-\Delta\nu/2}^{\nu_0+\Delta\nu/2} \prod_{j=1}^{N_{\rm species}} \exp\left(-\int_0^{P_i}\frac{X_j\kappa_\nu^j}{a} dP\right) d\nu \,. \tag{A.65}$$

Now we make the correlated-k assumption, namely that the same cumulative probability values of the opacity distribution function map to the same frequencies in different layers of the atmosphere, which results in

$$\bar{\mathcal{T}}^i = \int_0^\infty \cdots \int_0^\infty \left[\prod_{j=1}^{N_{\rm species}} \exp\left(-\int_0^{P_i}\frac{X_j\kappa^j}{a} dP\right)\right] f(\kappa^1,\ldots,\kappa^{N_{\rm species}}) d\kappa^1 \cdots d\kappa^{N_{\rm species}} \,, \tag{A.66}$$

where f is the (non-cumulative) opacity distribution function. Furthermore, as usually done for correlated-k, we will assume the individual molecular species' opacities to be uncorrelated in frequency space, i.e.,

$$f(\kappa^1,\ldots,\kappa^{N_{\rm species}}) = f_1(\kappa^1)\cdots f_{N_{\rm species}}(\kappa^{N_{\rm species}}) \,. \tag{A.67}$$

This results in

$$\bar{\mathcal{T}}^i = \prod_{j=1}^{N_{\rm species}} \left[\int_0^1 \exp\left(-\int_0^{P_i}\frac{X_j\kappa_g^j}{a} dP\right) dg\right] \,, \tag{A.68}$$

with $g = f(\kappa)d\kappa$ being the values of the cumulative opacity distribution functions. Replacing the integral over g by a numerical approximation we get

$$\bar{\mathcal{T}}^i = \prod_{j=1}^{N_{\text{species}}} \left[\sum_{l=0}^{N_g} \exp\left(- \int_0^{P_i} \frac{X_j \kappa_{lj}}{a} dP \right) \Delta g_l \right] . \tag{A.69}$$

B Code testing

In parts based on Mollière et al. (2015, 2017).

Whenever a new module was implemented into *petitCODE*, I aimed at verifying it by comparing to other codes, analytical results, and carrying out simple sanity checks. Tests for the correlated-k radiative transport, and for the correlated-k opacity combination method, were already presented in Section 3.2.3, Figure 3.4, as well as Section A.1, Figure A.1, repectively.

B.1 Temperature iteration method

In order to verify that my code solved for the temperature structures correctly, I set it up in an idealized fashion, in order to reproduce the analytical solution presented in Guillot (2010): scattering was neglected, and the stellar light was assumed to be absorbed with a vertically constant, gray opacity which was smaller than the constant planetary radiation field opacity, $\kappa_* = \gamma\kappa_{\rm Pl}$. Further, as in Guillot (2010), I forced the Eddington coefficients, $f = K/J$ and $\psi = H(P = 0)/J(P = 0)$, to be constant at $f = 3$ and $\psi = 1/2$, thereby reproducing the choice made in Guillot (2010). The angle-dependent temperature solution corresponding to this setup, presented in Guillot (2010) is (also see Section A.3)

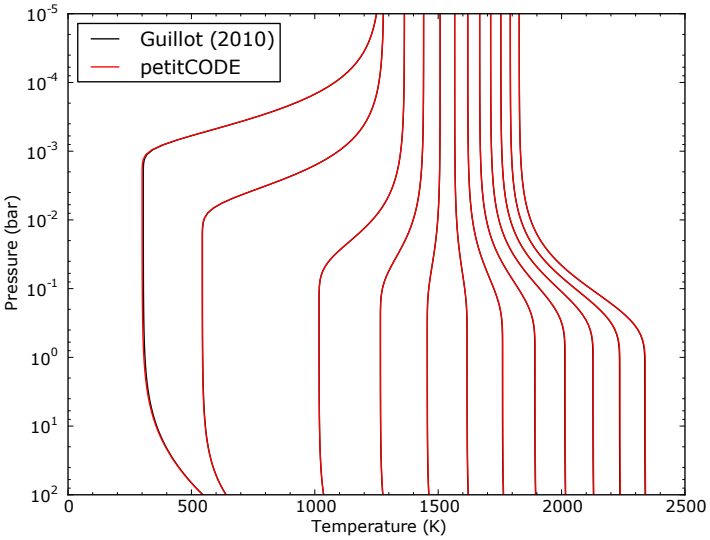

FIGURE B.1: P–T structures calculated with *petitCODE* under idealized Guillot (2010)-like conditions in comparison to the Guillot (2010) model. The Guillot (2010) solutions are shown as black solid lines, while the *petitCODE* solutions are shown as red solid lines. From left to right: μ_* = 0.001, 0.01, 0.1, 0.2, 0.3, 0.4, 0.5, 0.6, 0.7, 0.8, 0.9, 1.0.

$$T^4 = \frac{3T_{\rm int}^4}{4}\left(\frac{2}{3} + \tau\right) + 3\mu_* T_{\rm equ}^4 \left[\frac{2}{3} + \frac{\mu_*}{\gamma} + \left(\frac{\gamma}{3\mu_*} - \frac{\mu_*}{\gamma}\right) e^{-\gamma\tau/\mu_*}\right] , \tag{B.1}$$

with $\mu_* = \cos(\vartheta)$ being the angle between the incident stellar light and the atmospheric normal. As one can see in Figure B.1, the code correctly reproduces the analytical solution for this idealized scenario.

B.2 Flux conservation

I tested whether the converged solution is consistent with the input parameters. This was done by checking whether a final PT-structure, together with the molecular abundances and their corresponding opacities, gives rise to the correct total emergent flux. For a day-side averaged PT-spectrum, in the absence of scattering, the total emergent flux should be

$$F_{\rm imposed} = \sigma \left[T_{\rm int}^4 + \frac{T_*^4}{2} \left(\frac{R_*}{d} \right)^2 \right] . \tag{B.2}$$

Furthermore, deep within the atmosphere, but at lower pressure than the radiative-convective boundary $P_{\rm conv}$, the radiation field only needs to carry the internal flux of the planet. The reason for this is that all the stellar flux has been absorbed. One thus finds that

$$F_{\rm deep}(P < P_{\rm conv}) = \sigma T_{\rm int}^4 . \tag{B.3}$$

Even further down the PT-structure will eventually become convective such that the radiative flux becomes negligible when compared to the convective flux. In Figure B.2 one can see the result obtained from integrating the angle and frequency dependent radiation field of the $\lambda/\Delta\lambda = 10$ correlated-k structure calculation. The radiation field was integrated to yield the bolometric flux in the atmosphere (as a function of pressure). It can be seen that the surface flux converges to $F_{\rm imposed}$. Furthermore, at approximately 3 bar, the stellar flux has been fully absorbed and the radiative flux is equal to $\sigma T_{\rm int}^4$. At even higher pressures ($P \sim 70$ bar) the atmosphere becomes convective and the flux transported by radiation starts to dwindle. The radiation field thus behaves as expected and the converged solution indeed fulfills the input parameters of the problem.

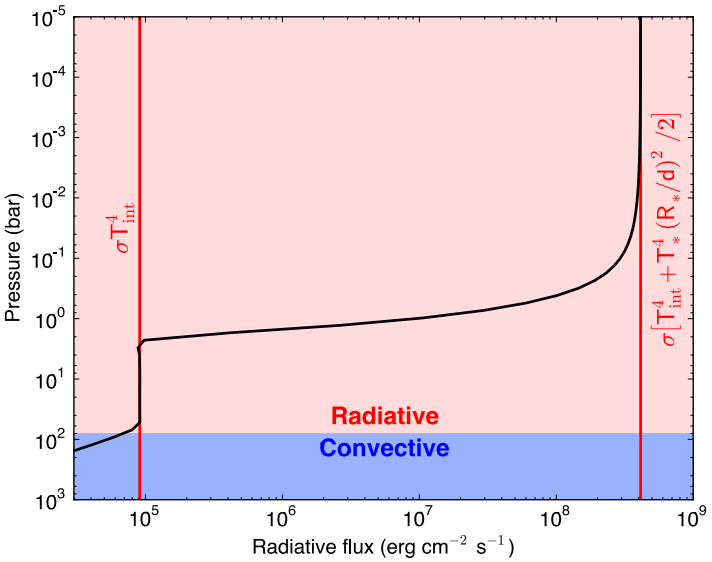

FIGURE B.2: Bolometric flux of the converged atmospheric structure calculated from the $\lambda/\Delta\lambda = 10$ correlated-k radiation field integrated over angle and frequency space. The bolometric flux is shown as a black solid line. The two red solid vertical lines denote the imposed total and internal fluxes of the planet. The red shaded area denotes the radiative region of the atmosphere, whereas the blue shaded region shows the convective region. Figure taken from Mollière et al. (2015)

B.3 Scattering implementation

To test my scattering implementation, I compared the atmospheric bond albedo[1] as a function of the incidence angle of the stellar light, μ_*, to the values predicted by Chandrasekhar's H-functions (Chandrasekhar 1950) and found excellent agreement.

In order to carry out this test I adopted gray absorption and scattering opacities, with the scattering albedo defined as $\eta = \kappa^{\rm scat}/(\kappa^{\rm abs} + \kappa^{\rm scat})$. I compared my results to the test

[1] Defined as the flux ratio $F_{\rm reflected}/F_*$.

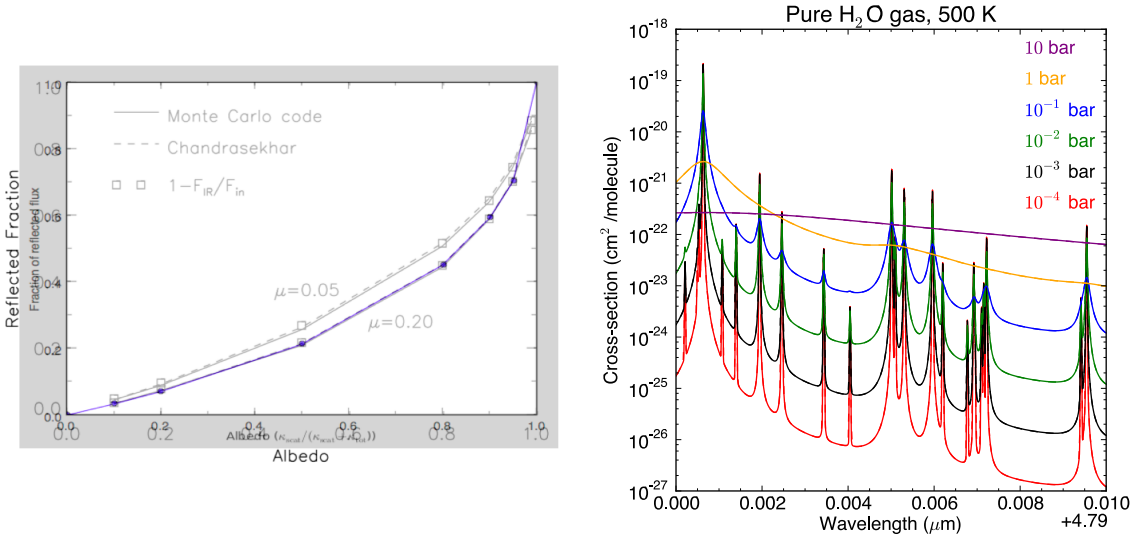

FIGURE B.3: *Left panel:* Atmospheric bond albedo as a function of the albedo η. The background Figure is a screenshot taken from Dullemond & Natta (2003). The overlayed blue line is the results obtained from *petitCODE*, assuming an incidence angle of $\mu_* = 0.2$. *Right panel:* Absorption cross-section per molecule as a function of wavelength for pure $^1H_2^{16}O$ gas for the bands that lie between 4.79 and 4.8 μm for a temperature of 500 K and a pressure of 10^{-4} (red), 10^{-3} (black), 10^{-2} (green), 10^{-1} (blue), 1 (yellow) and 10 bar (purple). Own results are plotted as solid lines, while "HITRAN on the web" results are plotted as dashed lines.

presented in Dullemond & Natta (2003) and show an overlay to their test figure in the left panel of Figure B.3, where I increased the albedo η of the atmosphere at a constant incidence angle of $\mu_* = 0.2$.

B.4 Opacity calculation

In order to test my implementation for the opacity calculation I compared to values available from the HITRAN line list database (Rothman et al. 2013). There exists an online absorption coefficient calculator, which can calculate the inverse mean free path

$$\alpha(\nu) = \frac{P}{k_\mathrm{B} T} \sigma(\nu) \,, \tag{B.4}$$

taking into account certain bands of an isotopologue of a molecule, and assuming a pure gas of the isotoplogue under consideration.[2]

I compared my and their opacity to the main water isotopologue, taking into account bands that lie between 4.79 and 4.8 μm. I set $T = 500$ K and varied the pressure between 10^{-4} and 10 bars, equally spaced apart in log-space. The comparison plots can be seen in the right panel of Figure B.3. The agreement between my own (solid lines) and their "HITRAN on the web" results (dashed lines) is very good. The differences are less than 1 %, and usually much less.

B.5 Transmission spectra

To test my transmission spectral calculation, I carried out dedicated comparison calculations with the transmission spectra published in Fortney et al. (2010). To this end, I assumed

[2] see `http://hitran.iao.ru/`. Note that this online tool only calculates opacities for specific bands, in small wavelength ranges.

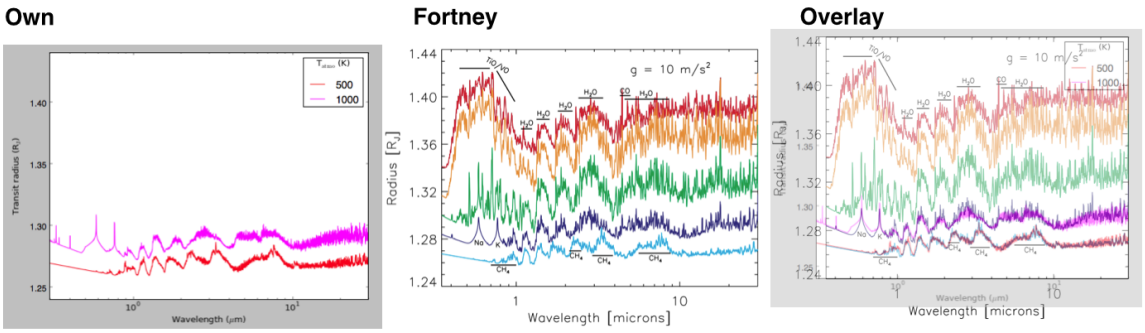

FIGURE B.4: Comparison of transmission spectra for isothermal atmospheres between *petitCODE* and the Fortney et al. (2010) model, for the case presented in Figure 2 in the Fortney et al. (2010) paper. The isothermal atmospheric temperature increase from top to bottom, showing spectra at 500 to 1500 K, in 500 K steps. I only compared to the 500 and 1000 K cases, see text.

isothermal atmospheres at 500 and 1000 K, solar abundances, and a planetary reference ratio of $R_{\rm Pl}(10\,{\rm bar}) = 1.25\,{\rm R}_{\rm 4}$. The results agree well, see Figure B.4. Note the different alkali line shape in the *petitCODE* results, because I use the alkali wings by N. Allard (see Table 3.1 in Section 3.3.1). When I carried out this test, I did not compare to temperatures above 1000 K, because I did not have included the TiO and VO opacities in my database yet.

B.6 Emission spectra and self-consistent temperature structures

I am part of a code benchmarking study, where the three self-consistent codes *Exo-REM* (Baudino et al. 2015), *ATMO* (Tremblin et al. 2015) and *petitCODE* are compared. The study is to appear in Baudino et al. (in prep.), and is currently in an advanced stage of writing. As one of the tests we have calculated the self-consistent atmospheric structures and emission spectra of the two self-luminous planets GJ504 b and VHS 1256-1257 b. For GJ504 b we

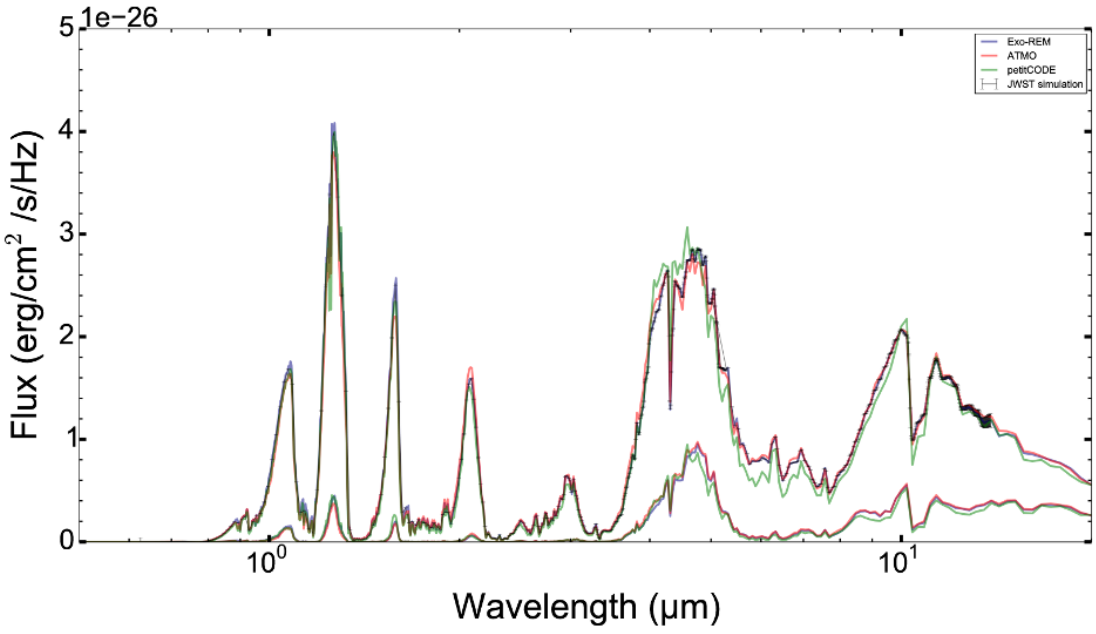

FIGURE B.5: Comparison of the self-consistent spectra of the self-luminous planets GJ504 b (lower spectrum) and VHS 1256-1257 b (upper spectrum), calculated with *Exo-REM* (Baudino et al. 2015), *ATMO* (Tremblin et al. 2015) and *petitCODE*. Figure taken from Baudino et al. (in prep.).

assumed $T_{\rm eff} = 510$ K, $\log(g) = 3.9$ (cgs units) and $[{\rm Fe/H}] = 0.28$. For VHS 1256-1257 b we took $T_{\rm eff} = 880$ K, $\log(g) = 4.24$ and $[{\rm Fe/H}] = 0.21$.

Hence, this test does not only investigate the calculation of the emission spectra, but also the solution of the atmospheric structure. I show the spectra for both planets, obtained with the three different codes, in Figure B.5. This figure was taken from Baudino et al. (in prep.). As can be seen from the figure, we reach a fair agreement, with most differences arising from the fact that *petitCODE* uses different line lists for NH_3, PH_3, and CO.

B.7 Cloud model implementation

In Figure (B.6) I show the cloud densities obtained with my implementation of the Ackerman & Marley (2001) cloud model, and compare to the case the authors studied in their paper. The test was carried out for a self-luminous object with $f_{\rm sed} = 3$, $T_{\rm eff} = 500$K, $g = 100$ m s^{-2} and [Fe/H] = 0.0, i.e. for the exact same parameters as in Ackerman & Marley (2001), except for the metallicity, for which no information was given in their paper. Qualitatively the results agree very well. The cloud base for the enstatite clouds is approximately at the same pressure and peak density. The pressure dependent decrease in cloud densities agrees very well.

The water cloud is somewhat higher in the *petitCODE* atmosphere, and therefore at a lower cloud density (because the total atmospheric density is lower). I have compared the P–T structure of my code and of the Ackerman & Marley (2001) solution by rescaling the two plots shown in Figure (B.6) and overlaying them. The two temperature structures agree very well. The issue of having two different cloud base pressures may be explained by the fact that the two different equilibrium chemistry treatments (i.e. their's and mine) may have slightly different condensation temperatures for a given pressure. In atmospheric regions where temperature varies strongly with varying (log)pressure the two cloud bases will lie closely together in pressure space, because the difference in condensation temperature corresponds only to a small atmospheric pressure change. The two water clouds lie in a region of the atmosphere which is more or less isothermal, however. Thus, a much larger log(P) difference in the atmosphere between the two water cloud bases is found. Therefore my implementation of the Ackerman & Marley (2001) cloud model may work just as well for

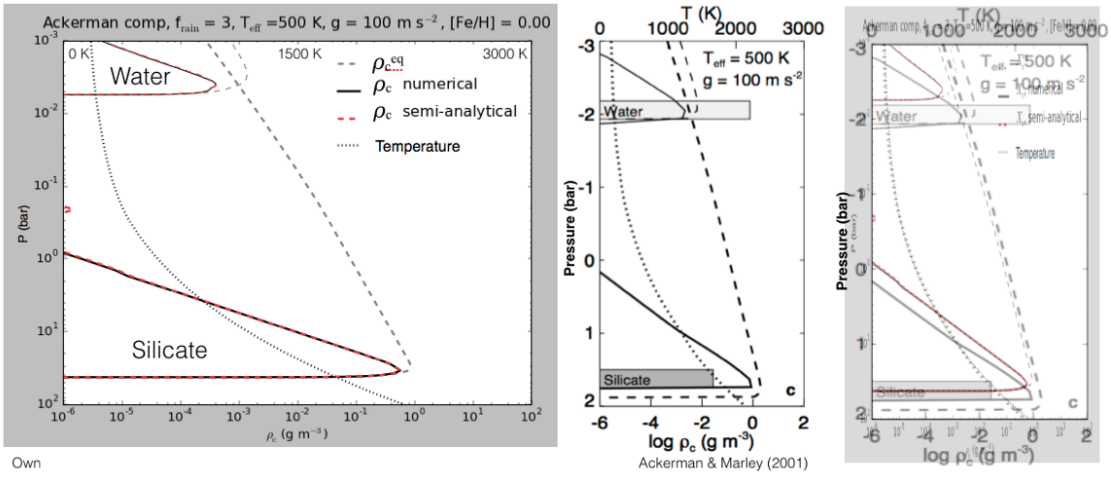

FIGURE B.6: *petitCODE* enstatite and water clouds (*left panel*) in comparison with a plot taken from Ackerman & Marley (2001) (*middle panel*) and the two plots' superposition (*right panel*). The following quantities are shown, as a function of pressure: atmospheric temperature (dotted black line), cloud condensate densities (solid black lines), approximative cloud condensate densities from using a semi-analytical solution (red dashed lines), and the equilibrium chemistry condensate densities (gray dashed black lines).

water as in the enstatite case. It is small differences in the equilibrium chemistry treatment which may account for the water cloud differences seen here.

B.8 Gibbs minimizer for chemical equilibrium

In order to obtain the chemical abundances I used NASA's *CEA* code (Gordon & McBride 1994; McBride & Gordon 1996) in Mollière et al. (2015) at first, see Chapter 4. While this code often worked reliably, it was prone to crashes or wrong results when low atmospheric temperatures as well as condensates were considered. In order to overcome this problem I wrote a Gibbs minimizer myself (see Section 3.4.1, and Section 2.3.1 for the underlying theory), following the theoretical concepts and conventions outlined for the *CEA* code in detail in Gordon & McBride (1994). This code was used in Mollière et al. (2017), see Chapter 5, and is now the standard method for obtaining equilibrium abundances within *petitCODE*. While my chemistry code, which I called *easyCHEM*, uses the same equations and thermodynamical data as *CEA*, it was found to converge stably in all cases where *CEA* had previously crashed or lead to wrong results.

A comparison between *easyCHEM* and *CEA* is given in Figure B.7, which shows the HCN abundance as a function of P and T for a gas of scaled solar composition (at $[\mathrm{Fe/H}] = 0.3$). As one can see, there is an exact agreement between *easyCHEM* and *CEA*.

An example for cases where *CEA* breaks down is shown in Figure B.8. Here I show the mass fractions of gaseous methane and condensed iron for the same gas as considered before. I find that the *CEA* solutions break down for many (also gaseous) molecules at temperatures below 300 to 400 K, such as for CH_4 and iron. Additionally, between 500 and

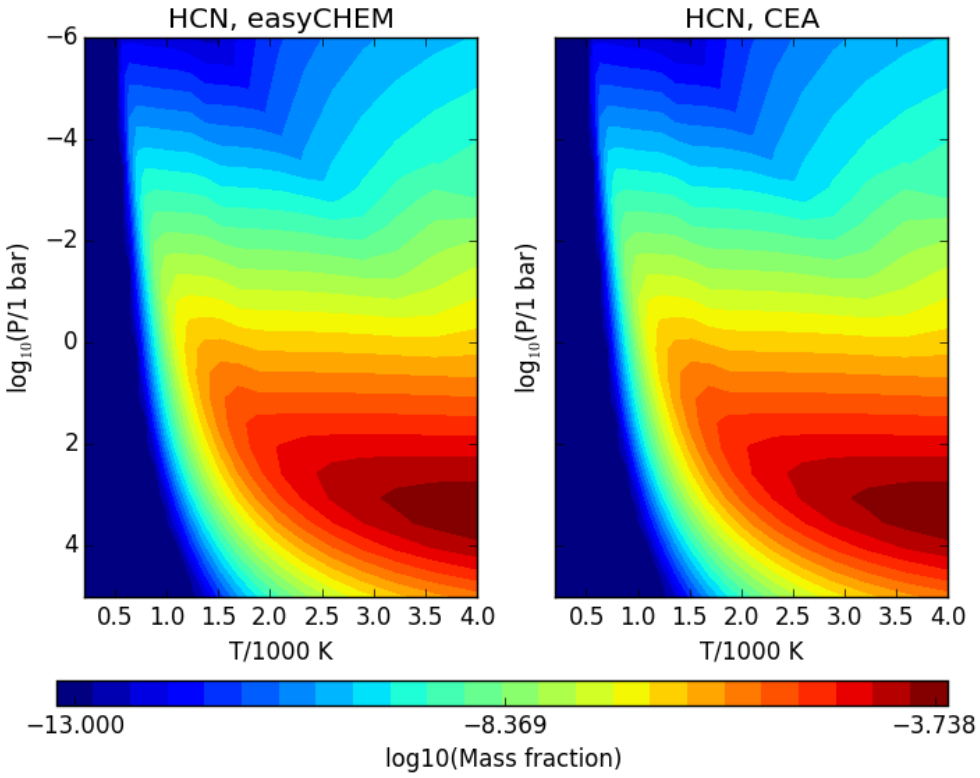

FIGURE B.7: HCN mass fraction in a gas of scaled solar composition (at $[\mathrm{Fe/H}] = 0.3$), as a function of the atmospheric temperature and pressure. The left panel shows the abundances obtained withe my own code, *easyCHEM*, while the right panel shows the abundance obtained with NASA's *CEA* code.

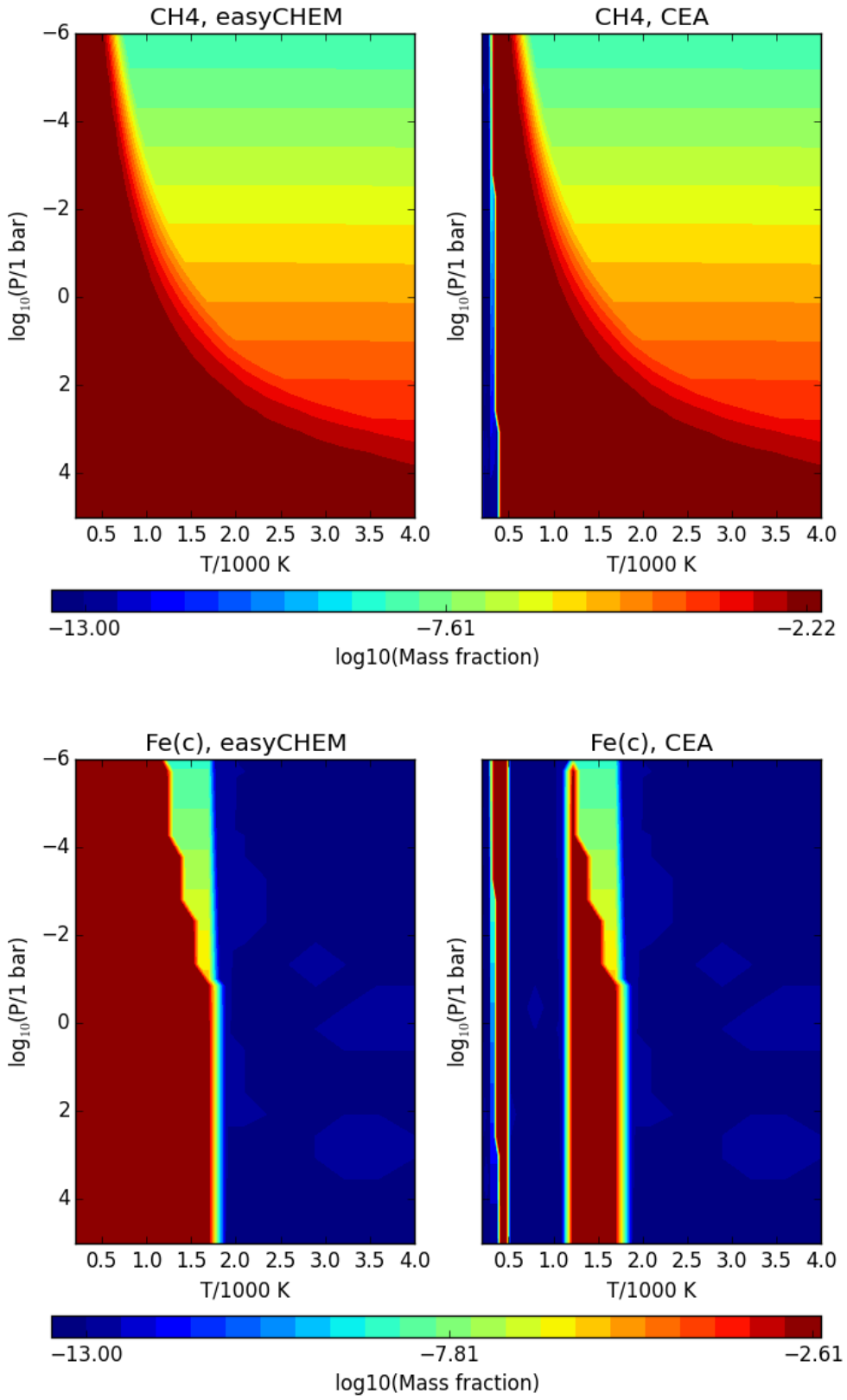

FIGURE B.8: Mass fractions for CH_4 (*upper panel*) and condensed iron (*lower panel*) in a gas of scaled solar composition (at $[Fe/H] = 0.3$), as a function of the atmospheric temperature and pressure. The left panel shows the abundances obtained withe my own code, *easyCHEM*, while the right panel shows the abundance obtained with NASA's *CEA* code.

1200 K, the condensed iron mass fraction is found to be zero with *CEA*, although the corresponding thermodynamic data within this temperature range are specifically included. Both *easyCHEM* and *CEA* used the exact same inputs and thermodynamic data for the comparison plots shown here.

List of Abbreviations

ALI	**A**ccelerated **L**ambda **I**teration
CIA	**C**ollision **I**nduced **A**bsorption
DHS	**D**istribution of **H**ollow **S**pheres
GCM	**G**eneral **C**irculation **M**odel
GI	**G**ravitational **I**nstability
HWHM	**H**alf **W**idth at **H**alf **M**aximum
IR	**I**nfra**r**ed
JWST	**J**ames **W**ebb **S**pace **T**elescope
LHS	**L**eft **H**and **S**ide
LTE	**L**ocal **T**hermal **E**quilibrium
MCMC	**M**arkov **C**hain **M**onte **C**arlo
MIR	**M**id **I**nfra**r**ed
MLT	**M**ixing **L**ength **T**heory
MMW	**M**ean **M**olecular **W**eight
NIR	**N**ear **I**nfra**r**ed
RHS	**R**ight **H**and **S**ide
RV	**R**adial **V**elocity
SED	**S**pectral **E**nergy **D**istribution
SNR	**S**ignal-to-**N**oise **R**atio
wt-%	**W**eight **P**ercentage

Bibliography of own publications

Here I list my first and co-author papers, as per requirement of the *HGSFP*.

Bibliography of first-author papers used in this thesis:
Mollière, P., van Boekel, R., Dullemond, C., Henning, T., & Mordasini, C. 2015, ApJ, 813, 47
Mollière, P., van Boekel, R., Bouwman, J., et al. 2017, A&A, 600, A10

Bibliography of first-author papers cited in this thesis:
Mollière, P. & Mordasini, C. 2012, A&A, 547, A105

Bibliography of co-author papers cited in this thesis:
Baruteau, C., Bai, X., Mordasini, C., & Mollière, P. 2016, Space Sci.Rev.
Mancini, L., Giordano, M., Mollière, P., et al. 2016a, MNRAS, 461, 1053
Mancini, L., Kemmer, J., Southworth, J., et al. 2016b, MNRAS, 459, 1393
Mancini, L., Southworth, J., Raia, G., et al. 2017, MNRAS, 465, 843
Mordasini, C., van Boekel, R., Mollière, P., Henning, T., & Benneke, B. 2016, ApJ, 832, 41
Samland, M., Mollière, P., Bonnefoy, M., et al. 2017, A&A, in press
Southworth, J., Mancini, L., Madhusudhan, N., et al. 2017, AJ, 153, 191

Bibliography of co-author papers not cited in this thesis (as not mentioned/necessary):
Mordasini, C., Mollière, P., Dittkrist, K.-M., Jin, S., & Alibert, Y. 2015, International Journal of Astrobiology, 14, 201

Bibliography

Ackerman, A. S. & Marley, M. S. 2001, ApJ, 556, 872

Agol, E., Cowan, N. B., Knutson, H. A., et al. 2010, ApJ, 721, 1861

Agúndez, M., Parmentier, V., Venot, O., Hersant, F., & Selsis, F. 2014, A&A, 564, A73

Ali-Dib, M., Mousis, O., Petit, J.-M., & Lunine, J. I. 2014, ApJ, 785, 125

Alibert, Y., Carron, F., Fortier, A., et al. 2013, A&A, 558, A109

Allard, F., Guillot, T., Ludwig, H.-G., et al. 2003a, in IAU Symposium, Vol. 211, Brown Dwarfs, ed. E. Martín, 325

Allard, F., Hauschildt, P. H., Alexander, D. R., Tamanai, A., & Schweitzer, A. 2001, ApJ, 556, 357

Allard, N. F., Allard, F., Hauschildt, P. H., Kielkopf, J. F., & Machin, L. 2003b, A&A, 411, L473

Allard, N. F., Kielkopf, J. F., Spiegelman, F., Tinetti, G., & Beaulieu, J. P. 2012, A&A, 543, A159

Anderson, D. R., Hellier, C., Gillon, M., et al. 2010, ApJ, 709, 159

Andrae, R., Schulze-Hartung, T., & Melchior, P. 2010, ArXiv e-prints

Anglada-Escudé, G., Amado, P. J., Barnes, J., et al. 2016, Nature, 536, 437

Arras, P. & Bildsten, L. 2006, ApJ, 650, 394

Asplund, M., Grevesse, N., Sauval, A. J., & Scott, P. 2009, ARA&A, 47, 481

Baines, E. K., McAlister, H. A., ten Brummelaar, T. A., et al. 2009, ApJ, 701, 154

Ballard, S. & Johnson, J. A. 2016, ApJ, 816, 66

Baraffe, I., Chabrier, G., Allard, F., & Hauschildt, P. H. 1998, A&A, 337, 403

Barber, R. J., Strange, J. K., Hill, C., et al. 2014, MNRAS, 437, 1828

Barman, T. S., Hauschildt, P. H., & Allard, F. 2001, ApJ, 556, 885

Barstow, J. K., Aigrain, S., Irwin, P. G. J., et al. 2013, MNRAS, 430, 1188

Barstow, J. K., Aigrain, S., Irwin, P. G. J., et al. 2014, ApJ, 786, 154

Barstow, J. K., Aigrain, S., Irwin, P. G. J., Kendrew, S., & Fletcher, L. N. 2015, MNRAS, 448, 2546

Barstow, J. K., Aigrain, S., Irwin, P. G. J., & Sing, D. K. 2017, ApJ, 834, 50

Barstow, J. K. & Irwin, P. G. J. 2016, MNRAS, 461, L92

Baruteau, C., Bai, X., Mordasini, C., & Mollière, P. 2016, Space Sci.Rev.

Batalha, N., Kalirai, J., Lunine, J., Clampin, M., & Lindler, D. 2015, ArXiv e-prints

Batalha, N. M. 2014, Proceedings of the National Academy of Science, 111, 12647

Batygin, K., Stanley, S., & Stevenson, D. J. 2013, ApJ, 776, 53

Baudino, J.-L., Bézard, B., Boccaletti, A., et al. 2015, A&A, 582, A83

Baudino, J.-L., Mollière, P., Venot, O., et al. in prep.

Bean, J. L., Désert, J.-M., Kabath, P., et al. 2011, ApJ, 743, 92

Bean, J. L., Miller-Ricci Kempton, E., & Homeier, D. 2010, Nature, 468, 669

Beaulieu, J.-P., Bennett, D. P., Fouqué, P., et al. 2006, Nature, 439, 437

Beichman, C., Benneke, B., Knutson, H., et al. 2014, PASP, 126, 1134

Benneke, B. 2015, ArXiv e-prints

Benneke, B. & Seager, S. 2012, ApJ, 753, 100

Benneke, B. & Seager, S. 2013, ApJ, 778, 153

Berta, Z. K., Charbonneau, D., Désert, J.-M., et al. 2012, ApJ, 747, 35

Bétrémieux, Y. & Kaltenegger, L. 2014, ApJ, 791, 7

Biddle, L. I., Pearson, K. A., Crossfield, I. J. M., et al. 2014, MNRAS, 443, 1810

Birkby, J. L., de Kok, R. J., Brogi, M., et al. 2013, MNRAS, 436, L35

Birkby, J. L., de Kok, R. J., Brogi, M., Schwarz, H., & Snellen, I. A. G. 2017, AJ, 153, 138

Birnbaum, G., Chu, S.-I., Dalgarno, A., Frommhold, L., & Wright, E. L. 1984, Phys.Rev.A, 29, 595

Bitsch, B., Crida, A., Morbidelli, A., Kley, W., & Dobbs-Dixon, I. 2013, A&A, 549, A124

Bobis, L. & Lequeux, J. 2008, Journal of Astronomical History and Heritage, 11, 97

Bodenheimer, P. & Pollack, J. B. 1986, Icarus, 67, 391

Bohren, C. F. & Huffman, D. R. 1998, Absorption and Scattering of Light by Small Particles, 544

Boley, A. C., Hayfield, T., Mayer, L., & Durisen, R. H. 2010, Icarus, 207, 509

Bonnefoy, M., Boccaletti, A., Lagrange, A.-M., et al. 2013, A&A, 555, A107

Bonnefoy, M., Zurlo, A., Baudino, J. L., et al. 2016, A&A, 587, A58

Borucki, W. J., Koch, D., Jenkins, J., et al. 2009, Science, 325, 709

Borysow, A. 2002, A&A, 390, 779

Borysow, A. & Frommhold, L. 1989, ApJ, 341, 549

Borysow, A., Frommhold, L., & Moraldi, M. 1989, ApJ, 336, 495

Borysow, A., Jorgensen, U. G., & Fu, Y. 2001, J. Quant. Spec. Radiat. Transf., 68, 235

Borysow, J., Frommhold, L., & Birnbaum, G. 1988, ApJ, 326, 509

Bouwman, J., Meeus, G., de Koter, A., et al. 2001, A&A, 375, 950

Brogi, M., de Kok, R. J., Birkby, J. L., Schwarz, H., & Snellen, I. A. G. 2014, A&A, 565, A124

Brogi, M., Line, M., Bean, J., Désert, J.-M., & Schwarz, H. 2017, ApJ, 839, L2

Brogi, M., Snellen, I. A. G., de Kok, R. J., et al. 2012, Nature, 486, 502

Buchner, J., Georgakakis, A., Nandra, K., et al. 2014, A&A, 564, A125

Burch, D. E., Gryvnak, D. A., Patty, R. R., & Bartky, C. E. 1969, J. Opt. Soc. Am., 59, 267

Burke, B. F. & Franklin, K. L. 1955, Journal of Geophys. Res., 60, 213

Burrows, A., Guillot, T., Hubbard, W. B., et al. 2000, ApJ, 534, L97

Burrows, A., Hubeny, I., Budaj, J., Knutson, H. A., & Charbonneau, D. 2007, ApJ, 668, L171

Burrows, A., Hubeny, I., & Sudarsky, D. 2005, ApJ, 625, L135

Burrows, A., Marley, M., Hubbard, W. B., et al. 1997, ApJ, 491, 856

Burrows, A., Sudarsky, D., & Hubeny, I. 2006, ApJ, 650, 1140

Burrows, A. & Volobuyev, M. 2003, ApJ, 583, 985

Cáceres, C., Kabath, P., Hoyer, S., et al. 2014, A&A, 565, A7

Carone, L., Keppens, R., & Decin, L. 2014, MNRAS, 445, 930

Carone, L., Keppens, R., & Decin, L. 2015, MNRAS, 453, 2412

Carone, L., Keppens, R., & Decin, L. 2016, MNRAS, 461, 1981

Cassan, A., Kubas, D., Beaulieu, J.-P., et al. 2012, Nature, 481, 167

Chan, T., Ingemyr, M., Winn, J. N., et al. 2011, AJ, 141, 179

Chan, Y. M. & Dalgarno, A. 1965, Proceedings of the Physical Society, 85, 227

Chandrasekhar, S. 1950, Radiative transfer.

Charbonneau, D., Berta, Z. K., Irwin, J., et al. 2009, Nature, 462, 891

Charbonneau, D., Brown, T. M., Noyes, R. W., & Gilliland, R. L. 2002, ApJ, 568, 377

Charbonneau, D., Knutson, H. A., Barman, T., et al. 2008, ApJ, 686, 1341

Charnay, B., Meadows, V., & Leconte, J. 2015a, ApJ, 813, 15

Charnay, B., Meadows, V., Misra, A., Leconte, J., & Arney, G. 2015b, ApJ, 813, L1

Cowan, N. B. & Agol, E. 2011, ApJ, 729, 54

Crida, A., Morbidelli, A., & Masset, F. 2006, Icarus, 181, 587

Cridland, A. J., Pudritz, R. E., & Alessi, M. 2016, MNRAS, 461, 3274

Croll, B., Jayawardhana, R., Fortney, J. J., Lafrenière, D., & Albert, L. 2010, ApJ, 718, 920

Crossfield, I. J. M. 2015, PASP, 127, 941

Crossfield, I. J. M., Barman, T., Hansen, B. M. S., & Howard, A. W. 2013, A&A, 559, A33

Crossfield, I. J. M., Barman, T., Hansen, B. M. S., Tanaka, I., & Kodama, T. 2012, ApJ, 760, 140

Cumming, A., Butler, R. P., Marcy, G. W., et al. 2008, PASP, 120, 531

Currie, T., Burrows, A., Madhusudhan, N., et al. 2013, ApJ, 776, 15

Cushing, M. C., Roellig, T. L., Marley, M. S., et al. 2006, ApJ, 648, 614

Dalgarno, A. & Williams, D. A. 1962, ApJ, 136, 690

D'Angelo, G., Durisen, R. H., & Lissauer, J. J. 2010, Giant Planet Formation, ed. S. Seager, 319–346

de Kok, R. J., Brogi, M., Snellen, I. A. G., et al. 2013, A&A, 554, A82

de Mooij, E. J. W., Brogi, M., de Kok, R. J., et al. 2013, A&A, 550, A54

Demarque, P., Woo, J.-H., Kim, Y.-C., & Yi, S. K. 2004, ApJS, 155, 667

Deming, D., Fraine, J. D., Sada, P. V., et al. 2012, ApJ, 754, 106

Deming, D., Knutson, H., Kammer, J., et al. 2015, ApJ, 805, 132

Deming, D., Seager, S., Winn, J., et al. 2009, PASP, 121, 952

Deming, D., Wilkins, A., McCullough, P., et al. 2013, ApJ, 774, 95

Demory, B.-O., de Wit, J., Lewis, N., et al. 2013a, ApJ, 776, L25

Demory, B.-O., Gillon, M., de Wit, J., et al. 2016, Nature, 532, 207

Demory, B.-O. & Seager, S. 2011, ApJS, 197, 12

Demory, B.-O., Seager, S., Madhusudhan, N., et al. 2011, ApJ, 735, L12

Demory, B.-O., Torres, G., Neves, V., et al. 2013b, ApJ, 768, 154

Demtröder, W. 2010, Experimentalphysik 3

Désert, J.-M., Bean, J., Miller-Ricci Kempton, E., et al. 2011, ApJ, 731, L40

Diamond-Lowe, H., Stevenson, K. B., Bean, J. L., Line, M. R., & Fortney, J. J. 2014, ApJ, 796, 66

Doyon, R., Hutchings, J. B., Beaulieu, M., et al. 2012, in Society of Photo-Optical Instrumentation Engineers (SPIE) Conference Series, Vol. 8442, Society of Photo-Optical Instrumentation Engineers (SPIE) Conference Series, 2

Dragomir, D., Benneke, B., Pearson, K. A., et al. 2015, The Astrophysical Journal, 814, 102

Dressing, C. D. & Charbonneau, D. 2013, ApJ, 767, 95

Duffell, P. C. 2015, ApJ, 807, L11

Dullemond, C. P. 2012, Lecture Notes on Radiative transfer in astrophysics

Dullemond, C. P. & Natta, A. 2003, A&A, 408, 161

Dullemond, C. P., van Zadelhoff, G. J., & Natta, A. 2002, A&A, 389, 464

Dunham, Jr., T. 1933, PASP, 45, 42

Dürmann, C. & Kley, W. 2015, A&A, 574, A52

Ehrenreich, D., Bonfils, X., Lovis, C., et al. 2014, A&A, 570, A89

Espinoza, N., Fortney, J. J., Miguel, Y., Thorngren, D., & Murray-Clay, R. 2017, ApJ, 838, L9

Esteves, L. J., De Mooij, E. J. W., & Jayawardhana, R. 2015, ApJ, 804, 150

Evans, T. M., Sing, D. K., Wakeford, H. R., et al. 2016, ApJ, 822, L4

Fabian, D., Jäger, C., Henning, T., Dorschner, J., & Mutschke, H. 2000, A&A, 364, 282

Fabrycky, D. & Tremaine, S. 2007, ApJ, 669, 1298

Feng, Y. K., Line, M. R., Fortney, J. J., et al. 2016, ApJ, 829, 52

Feroz, F., Hobson, M. P., & Bridges, M. 2009, MNRAS, 398, 1601

Ferruit, P., Bagnasco, G., Barho, R., et al. 2012, in Society of Photo-Optical Instrumentation Engineers (SPIE) Conference Series, Vol. 8442, Society of Photo-Optical Instrumentation Engineers (SPIE) Conference Series, 2

Ferruit, P., Birkmann, S., Böker, T., et al. 2014, in Proceedings of the SPIE, Vol. 9143, Space Telescopes and Instrumentation 2014: Optical, Infrared, and Millimeter Wave, 91430A

Fischer, D. A., Marcy, G. W., Butler, R. P., et al. 2008, ApJ, 675, 790

Fischer, D. A. & Valenti, J. 2005, ApJ, 622, 1102

Fischer, J., Gamache, R. R., Goldman, A., Rothman, L. S., & Perrin, A. 2003, J. Quant. Spec. Radiat. Transf., 82, 401

Fischer, P. D., Knutson, H. A., Sing, D. K., et al. 2016, ApJ, 827, 19

Foreman-Mackey, D., Hogg, D. W., Lang, D., & Goodman, J. 2013, PASP, 125, 306

Forgan, D. & Rice, K. 2013, MNRAS, 432, 3168

Fortney, J. J. 2005, MNRAS, 364, 649

Fortney, J. J. 2012, ApJ, 747, L27

Fortney, J. J., Ikoma, M., Nettelmann, N., Guillot, T., & Marley, M. S. 2011, ApJ, 729, 32

Fortney, J. J., Lodders, K., Marley, M. S., & Freedman, R. S. 2008, ApJ, 678, 1419

Fortney, J. J., Marley, M. S., Lodders, K., Saumon, D., & Freedman, R. 2005, ApJ, 627, L69

Fortney, J. J., Mordasini, C., Nettelmann, N., et al. 2013, ApJ, 775, 80

Fortney, J. J. & Nettelmann, N. 2010, Space Sci.Rev., 152, 423

Fortney, J. J., Saumon, D., Marley, M. S., Lodders, K., & Freedman, R. S. 2006, ApJ, 642, 495

Fortney, J. J., Shabram, M., Showman, A. P., et al. 2010, ApJ, 709, 1396

Foster, A. S., Harrington, J., Cubillos, P., et al. 2016, in American Astronomical Society Meeting Abstracts, Vol. 227, American Astronomical Society Meeting Abstracts, 212.05

Fraine, J. D., Deming, D., Gillon, M., et al. 2013, ApJ, 765, 127

Franklin, K. L. & Burke, B. F. 1956, AJ, 61, 177

Freedman, R. S., Marley, M. S., & Lodders, K. 2008, ApJS, 174, 504

Fressin, F., Torres, G., Charbonneau, D., et al. 2013, ApJ, 766, 81

Fu, Q. & Liou, K. N. 1992, Journal of Atmospheric Sciences, 49, 2139

Fuhrmann, K., Pfeiffer, M. J., & Bernkopf, J. 1997, A&A, 326, 1081

Fukui, A., Kawashima, Y., Ikoma, M., et al. 2014, ApJ, 790, 108

Gail, H.-P. 2001, A&A, 378, 192

Gail, H.-P. 2004, A&A, 413, 571

Gammie, C. F. 2001, ApJ, 553, 174

Garland, J., Harrington, J., Cubillos, P., et al. 2016, in American Astronomical Society Meeting Abstracts, Vol. 227, American Astronomical Society Meeting Abstracts, 212.06

Gehren, T., Liang, Y. C., Shi, J. R., Zhang, H. W., & Zhao, G. 2004, A&A, 413, 1045

Gierasch, P. J. & Conrath, B. J. 1985, Energy conversion processes in the outer planets, ed. G. E. Hunt, 121–146

Goodman, J. & Weare, J. 2010, Communications in Applied Mathematics and Computational Science, 5, 65

Goody, R., West, R., Chen, L., & Crisp, D. 1989, J. Quant. Spec. Radiat. Transf., 42, 539

Gordon, S. & McBride, B. J. 1994, Computer Program for Calculation of Complex Chemical Equilibrium Compositions and Applications. Part 1: Analysis (National Aeronautics and Space Administration, Washington, D.C. 20546-0001, USA: NASA)

Goukenleuque, C., Bézard, B., Joguet, B., Lellouch, E., & Freedman, R. 2000, Icarus, 143, 308

Greene, T. P., Line, M. R., Montero, C., et al. 2016, ApJ, 817, 17

Griffith, C. A. 2014, Philosophical Transactions of the Royal Society of London Series A, 372, 20130086

Grillmair, C. J., Burrows, A., Charbonneau, D., et al. 2008, Nature, 456, 767

Grimm, S. L. & Heng, K. 2015, ApJ, 808, 182

Guillot, T. 2010, A&A, 520, A27

Guillot, T., Burrows, A., Hubbard, W. B., Lunine, J. I., & Saumon, D. 1996, ApJ, 459, L35

Guillot, T. & Showman, A. P. 2002, A&A, 385, 156

Gustafsson, B., Bell, R. A., Eriksson, K., & Nordlund, A. 1975, A&A, 42, 407

Guyon, O., Martinache, F., Cady, E. J., et al. 2012, in Proceedings of the SPIE, Vol. 8447, Adaptive Optics Systems III, 84471X

Hadden, S. & Lithwick, Y. 2014, ApJ, 787, 80

Hansen, B. M. S. 2008, ApJS, 179, 484

Hansen, C. J., Kawaler, S. D., & Trimble, V. 2004, Stellar interiors : physical principles, structure, and evolution

Harker, D. E. & Desch, S. J. 2002, ApJ, 565, L109

Harris, G. J., Tennyson, J., Kaminsky, B. M., Pavlenko, Y. V., & Jones, H. R. A. 2006, MNRAS, 367, 400

Hartmann, J.-M., Boulet, C., Brodbeck, C., et al. 2002, J. Quant. Spec. Radiat. Transf., 72, 117

Harvey, A. H., Gallagher, J. S., & Levelt Sengers, J. M. H. 1998, Journal of Physical and Chemical Reference Data, 27, 761

Haswell, C. A. 2010, Transiting Exoplanets

Hauschildt, P. H. & Baron, E. 1999, Journal of Computational and Applied Mathematics, 109, 41

Haynes, K., Mandell, A. M., Madhusudhan, N., Deming, D., & Knutson, H. 2015, ApJ, 806, 146

Helled, R., Bodenheimer, P., Podolak, M., et al. 2014, Protostars and Planets VI, 643

Helling, C., Ackerman, A., Allard, F., et al. 2008, MNRAS, 391, 1854

Helling, C., Woitke, P., Rimmer, P. B., et al. 2014a, Life, volume 4, issue 2, pages 142-173, 4, 142

Helling, C., Woitke, P., Rimmer, P. B., et al. 2014b, Life, 4, 142

Heng, K. 2016, ApJ, 826, L16

Heng, K. & Kitzmann, D. 2017, ArXiv e-prints

Heng, K. & Showman, A. P. 2015, Annual Review of Earth and Planetary Sciences, 43, 509

Heng, K., Wyttenbach, A., Lavie, B., et al. 2015, ApJ, 803, L9

Henning, T. & Stognienko, R. 1996, A&A, 311, 291

Hofmeister, A. M. & Criss, R. E. 2005, Tectonophysics, 395, 159

Howard, A. W., Marcy, G. W., Bryson, S. T., et al. 2012, ApJS, 201, 15

Hubbard, W. B., Fortney, J. J., Lunine, J. I., et al. 2001, ApJ, 560, 413

Hubeny, I. 2017, ArXiv e-prints

Hubeny, I., Burrows, A., & Sudarsky, D. 2003, ApJ, 594, 1011

Humlícek, J. 1982, J. Quant. Spec. Radiat. Transf., 27, 437

Ingersoll, A. P. 1969, Journal of Atmospheric Sciences, 26, 1191

Iro, N., Bézard, B., & Guillot, T. 2005, A&A, 436, 719

Irwin, P. G. J., Teanby, N. A., de Kok, R., et al. 2008, J. Quant. Spec. Radiat. Transf., 109, 1136

Iyer, A. R., Swain, M. R., Zellem, R. T., et al. 2016, ApJ, 823, 109

Jaeger, C., Molster, F. J., Dorschner, J., et al. 1998, A&A, 339, 904

Jin, S., Mordasini, C., Parmentier, V., et al. 2014, ApJ, 795, 65

Johansen, A. & Lacerda, P. 2010, MNRAS, 404, 475

Jordán, A., Espinoza, N., Rabus, M., et al. 2013, ApJ, 778, 184

Juhász, A., Bouwman, J., Henning, T., et al. 2010, ApJ, 721, 431

Juhász, A., Henning, T., Bouwman, J., et al. 2009, ApJ, 695, 1024

Kamland Collaboration, Gando, A., Gando, Y., et al. 2011, Nature Geoscience, 4, 647

Kammer, J. A., Knutson, H. A., Line, M. R., et al. 2015, ApJ, 810, 118

Karkoschka, E. & Tomasko, M. G. 2011, Icarus, 211, 780

Kasting, J. F. 1993, Science, 259, 920

Kemper, F., Vriend, W. J., & Tielens, A. G. G. M. 2004, ApJ, 609, 826

Kim, Y.-C., Demarque, P., Yi, S. K., & Alexander, D. R. 2002, ApJS, 143, 499

Kippenhahn, R. & Weigert, A. 1990, Stellar Structure and Evolution, 192

Kliore, A., Cain, D. L., Levy, G. S., et al. 1965, Science, 149, 1243

Knutson, H. A., Benneke, B., Deming, D., & Homeier, D. 2014, Nature, 505, 66

Knutson, H. A., Charbonneau, D., Allen, L. E., et al. 2007, Nature, 447, 183

Knutson, H. A., Charbonneau, D., Burrows, A., O'Donovan, F. T., & Mandushev, G. 2009, The Astrophysical Journal, 691, 866

Knutson, H. A., Howard, A. W., & Isaacson, H. 2010, ApJ, 720, 1569

Knutson, H. A., Lewis, N., Fortney, J. J., et al. 2012a, ApJ, 754, 22

Knutson, H. A., Lewis, N., Fortney, J. J., et al. 2012b, ApJ, 754, 22

Komacek, T. D. & Showman, A. P. 2016, ApJ, 821, 16

Komacek, T. D., Showman, A. P., & Tan, X. 2017, ApJ, 835, 198

Kombayashi, M. 1967, J. Meteor. Soc. Japan, 45, 137–138

Konopacky, Q. M., Barman, T. S., Macintosh, B. A., & Marois, C. 2013, Science, 339, 1398

Kopparapu, R. k., Kasting, J. F., & Zahnle, K. J. 2012, ApJ, 745, 77

Kozai, Y. 1962, AJ, 67, 591

Kratter, K. & Lodato, G. 2016, ARA&A, 54, 271

Kreidberg, L., Bean, J. L., Désert, J.-M., et al. 2014, Nature, 505, 69

Kreidberg, L., Line, M. R., Bean, J. L., et al. 2015, ApJ, 814, 66

Kurucz, R. 1993, SYNTHE Spectrum Synthesis Programs and Line Data. Kurucz CD-ROM No. 18. Cambridge, Mass.: Smithsonian Astrophysical Observatory, 1993., 18

Lacis, A. A. & Oinas, V. 1991, Journal of Geophys. Res., 96, 9027

Lambrechts, M. & Johansen, A. 2014, A&A, 572, A107

Laughlin, G., Crismani, M., & Adams, F. C. 2011, ApJ, 729, L7

Lavie, B., Mendonça, J. M., Mordasini, C., et al. 2016, ArXiv e-prints

Lecavelier des Etangs, A., Pont, F., Vidal-Madjar, A., & Sing, D. 2008, A&A, 481, L83

Lee, E. J. & Chiang, E. 2016, ApJ, 817, 90

Lee, J.-M., Fletcher, L. N., & Irwin, P. G. J. 2012, MNRAS, 420, 170

Lee, J.-M., Heng, K., & Irwin, P. G. J. 2013, ApJ, 778, 97

Lee, J.-M., Irwin, P. G. J., Fletcher, L. N., Heng, K., & Barstow, J. K. 2014, ApJ, 789, 14

Lega, E., Crida, A., Bitsch, B., & Morbidelli, A. 2014, MNRAS, 440, 683

Liang, M.-C., Seager, S., Parkinson, C. D., Lee, A. Y.-T., & Yung, Y. L. 2004, ApJ, 605, L61

Lidov, M. L. 1962, Planetary and Space Science, 9, 719

Lin, D. N. C. & Ida, S. 1997, ApJ, 477, 781

Lin, D. N. C. & Papaloizou, J. 1986, ApJ, 309, 846

Lindal, G. F. 1992, AJ, 103, 967

Lindal, G. F., Lyons, J. R., Sweetnam, D. N., Eshleman, V. R., & Hinson, D. P. 1987, Journal of Geophys. Res., 92, 14987

Lindal, G. F., Sweetnam, D. N., & Eshleman, V. R. 1985, AJ, 90, 1136

Line, M. R., Knutson, H., Deming, D., Wilkins, A., & Desert, J.-M. 2013a, ApJ, 778, 183

Line, M. R., Knutson, H., Wolf, A. S., & Yung, Y. L. 2014, ApJ, 783, 70

Line, M. R., Marley, M. S., Liu, M. C., et al. 2016a, ArXiv e-prints

Line, M. R. & Parmentier, V. 2016, ApJ, 820, 78

Line, M. R., Stevenson, K. B., Bean, J., et al. 2016b, AJ, 152, 203

Line, M. R., Wolf, A. S., Zhang, X., et al. 2013b, ApJ, 775, 137

Line, M. R. & Yung, Y. L. 2013, ApJ, 779, 3

Line, M. R., Zhang, X., Vasisht, G., et al. 2012, ApJ, 749, 93

Lissauer, J. J. 1993, ARA&A, 31, 129

Lodders, K. 2010, Exoplanet Chemistry, ed. R. Barnes, 157

Lomonosov, M. 1762, Erscheinung der Venus vor der Sonne beobachtet bey der Kayserlichen Academie der Wissenschafften in St. Petersburg, den 26. May 1761

Lopez, E. D. & Fortney, J. J. 2014, ApJ, 792, 1

Ludwig, H.-G., Allard, F., & Hauschildt, P. H. 2002, A&A, 395, 99

Lynden-Bell, D. & Pringle, J. E. 1974, MNRAS, 168, 603

MacDonald, R. J. & Madhusudhan, N. 2017, ArXiv e-prints

Machalek, P., Greene, T., McCullough, P. R., et al. 2010, ApJ, 711, 111

Macintosh, B., Graham, J. R., Barman, T., et al. 2015, Science, 350, 64

Madhusudhan, N. 2012, ApJ, 758, 36

Madhusudhan, N., Amin, M. A., & Kennedy, G. M. 2014a, ApJ, 794, L12

Madhusudhan, N., Bitsch, B., Johansen, A., & Eriksson, L. 2016, ArXiv e-prints

Madhusudhan, N., Burrows, A., & Currie, T. 2011a, ApJ, 737, 34

Madhusudhan, N., Crouzet, N., McCullough, P. R., Deming, D., & Hedges, C. 2014b, ApJ, 791, L9

Madhusudhan, N., Harrington, J., Stevenson, K. B., et al. 2011b, Nature, 469, 64

Madhusudhan, N., Knutson, H., Fortney, J. J., & Barman, T. 2014c, Protostars and Planets VI, 739

Madhusudhan, N. & Seager, S. 2009, ApJ, 707, 24

Madhusudhan, N. & Seager, S. 2011, ApJ, 729, 41

Makarov, V. V., Beichman, C. A., Catanzarite, J. H., et al. 2009, ApJ, 707, L73

Malik, M., Grosheintz, L., Mendonça, J. M., et al. 2017, AJ, 153, 56

Mallonn, M., Nascimbeni, V., Weingrill, J., et al. 2015a, A&A, 583, A138

Mallonn, M., von Essen, C., Weingrill, J., et al. 2015b, A&A, 580, A60

Mancini, L., Giordano, M., Mollière, P., et al. 2016a, MNRAS, 461, 1053

Mancini, L., Kemmer, J., Southworth, J., et al. 2016b, MNRAS, 459, 1393

Mancini, L., Southworth, J., Ciceri, S., et al. 2014, A&A, 562, A126

Mancini, L., Southworth, J., Ciceri, S., et al. 2013, A&A, 551, A11

Mancini, L., Southworth, J., Raia, G., et al. 2017, MNRAS, 465, 843

Mandell, A. M., Drake Deming, L., Blake, G. A., et al. 2011, ApJ, 728, 18

Marboeuf, U., Thiabaud, A., Alibert, Y., Cabral, N., & Benz, W. 2014a, A&A, 570, A36

Marboeuf, U., Thiabaud, A., Alibert, Y., Cabral, N., & Benz, W. 2014b, A&A, 570, A35

Marcy, G. W., Butler, R. P., Vogt, S. S., et al. 2008, Physica Scripta Volume T, 130, 014001

Marleau, G.-D. & Cumming, A. 2014, MNRAS, 437, 1378

Marley, M. S. & Robinson, T. D. 2015, ARA&A, 53, 279

Marley, M. S., Saumon, D., Guillot, T., et al. 1996, Science, 272, 1919

Marois, C., Lafrenière, D., Doyon, R., Macintosh, B., & Nadeau, D. 2006a, ApJ, 641, 556

Marois, C., Phillion, D. W., & Macintosh, B. 2006b, in Proceedings of the SPIE, Vol. 6269, Society of Photo-Optical Instrumentation Engineers (SPIE) Conference Series, 62693M

Marois, C., Zuckerman, B., Konopacky, Q. M., Macintosh, B., & Barman, T. 2010, Nature, 468, 1080

Masset, F. S. 2011, Celestial Mechanics and Dynamical Astronomy, 111, 131

Masset, F. S. & Benítez-Llambay, P. 2016, ApJ, 817, 19

Masset, F. S. & Casoli, J. 2010, ApJ, 723, 1393

Mayer, C. H., McCullough, T. P., & Sloanaker, R. M. 1958, ApJ, 127, 1

Mayor, M., Marmier, M., Lovis, C., et al. 2011, ArXiv e-prints

Mayor, M. & Queloz, D. 1995, Nature, 378, 355

McBride, B. J. & Gordon, S. 1996, Computer Program for Calculation of Complex Chemical Equilibrium Compositions and Applications II. User's Manual and Program Description (National Aeronautics and Space Administration, Washington, D.C. 20546-0001, USA: NASA)

McKay, C. P., Pollack, J. B., & Courtin, R. 1989, Icarus, 80, 23

Menzel, D. H. 1926, ApJ, 63, 48

Menzel, D. H. & Whipple, F. L. 1955, PASP, 67, 161

Miguel, Y. & Kaltenegger, L. 2014, ApJ, 780, 166

Miller, N. & Fortney, J. J. 2011, ApJ, 736, L29

Min, M., Hovenier, J. W., & de Koter, A. 2003, A&A, 404, 35

Min, M., Hovenier, J. W., & de Koter, A. 2005, A&A, 432, 909

Mitchell, J. L. & Lora, J. M. 2016, Annual Review of Earth and Planetary Sciences, 44, 353

Mizuno, H., Nakazawa, K., & Hayashi, C. 1978, Progress of Theoretical Physics, 60, 699

Mollière, P. & Mordasini, C. 2012, A&A, 547, A105

Mollière, P., van Boekel, R., Bouwman, J., et al. 2017, A&A, 600, A10

Mollière, P., van Boekel, R., Dullemond, C., Henning, T., & Mordasini, C. 2015, ApJ, 813, 47

Molster, F. J., Waters, L. B. F. M., & Tielens, A. G. G. M. 2002, A&A, 382, 222

Moorhead, A. V., Ford, E. B., Morehead, R. C., et al. 2011, ApJS, 197, 1

Morbidelli, A. & Nesvorny, D. 2012, A&A, 546, A18

Mordasini, C., Alibert, Y., Benz, W., Klahr, H., & Henning, T. 2012, A&A, 541, 97

Mordasini, C., Alibert, Y., Benz, W., & Naef, D. 2009, A&A, 501, 1161

Mordasini, C., Alibert, Y., Georgy, C., et al. 2012, A&A, 547, A112

Mordasini, C., Klahr, H., Alibert, Y., Miller, N., & Henning, T. 2014, A&A, 566, A141

Mordasini, C., van Boekel, R., Mollière, P., Henning, T., & Benneke, B. 2016, ApJ, 832, 41

Morley, C. V., Fortney, J. J., Kempton, E. M.-R., et al. 2013, ApJ, 775, 33

Morley, C. V., Fortney, J. J., Marley, M. S., et al. 2012, ApJ, 756, 172

Morley, C. V., Fortney, J. J., Marley, M. S., et al. 2015, ApJ, 815, 110

Morley, C. V., Marley, M. S., Fortney, J. J., et al. 2014, ApJ, 787, 78

Moses, J. I., Madhusudhan, N., Visscher, C., & Freedman, R. S. 2013, ApJ, 763, 25

Nascimbeni, V., Piotto, G., Pagano, I., et al. 2013, A&A, 559, A32

Natta, A., Testi, L., Calvet, N., et al. 2007, Protostars and Planets V, 767

Nayakshin, S. 2010a, MNRAS, 408, L36

Nayakshin, S. 2010b, MNRAS, 408, 2381

Ng, K.-C. 1974, J. Chem. Phys., 61, 2680

Niemann, H. B., Atreya, S. K., Bauer, S. J., et al. 2005, Nature, 438, 779

Niemann, H. B., Atreya, S. K., Carignan, G. R., et al. 1998, Journal of Geophys. Res., 103, 22831

Nier, A. O., Hanson, W. B., Seiff, A., et al. 1976, Science, 193, 786

Nymeyer, S., Harrington, J., Hardy, R. A., et al. 2011, ApJ, 742, 35

Öberg, K. I. & Bergin, E. A. 2016, ApJ, 831, L19

Öberg, K. I., Murray-Clay, R. A., & Bergin, E. A. 2011, ApJ letters, 743, L16

Olson, G. L., Auer, L. H., & Buchler, J. R. 1986, J. Quant. Spec. Radiat. Transf., 35, 431

Ormel, C. W. & Klahr, H. H. 2010, A&A, 520, A43

Paardekooper, S.-J., Baruteau, C., Crida, A., & Kley, W. 2010, MNRAS, 401, 1950

Paardekooper, S.-J., Baruteau, C., & Kley, W. 2011, MNRAS, 410, 293

Palik, E. 2012, Handbook of Optical Constants of Solids No. Bd. 1 (Elsevier Science)

Papaloizou, J. C. B. & Nelson, R. P. 2005, A&A, 433, 247

Papaloizou, J. C. B., Nelson, R. P., & Snellgrove, M. D. 2004, MNRAS, 350, 829

Parmentier, V., Fortney, J. J., Showman, A. P., Morley, C., & Marley, M. S. 2016, ApJ, 828, 22

Parmentier, V., Showman, A. P., & Lian, Y. 2013, A&A, 558, A91

Perets, H. B. & Murray-Clay, R. A. 2011, ApJ, 733, 56

Perez-Becker, D. & Showman, A. P. 2013, ApJ, 776, 134

Perri, F. & Cameron, A. G. W. 1974, Icarus, 22, 416

Pettit, E. & Nicholson, S. B. 1955, PASP, 67, 293

Piskunov, N. E., Kupka, F., Ryabchikova, T. A., Weiss, W. W., & Jeffery, C. S. 1995, A&AS, 112, 525

Podolak, M. 2003, Icarus, 165, 428

Podolak, M., Podolak, J. I., & Marley, M. S. 2000, Planetary and Space Science, 48, 143

Podolak, M., Weizman, A., & Marley, M. 1995, Planetary and Space Science, 43, 1517

Pont, F., Sing, D. K., Gibson, N. P., et al. 2013, MNRAS, 432, 2917

Press, W. H., Teukolsky, S. A., Vetterling, W. T., & Flannery, B. P. 1992, Numerical recipes in FORTRAN. The art of scientific computing

Pruppacher, H. R. & Klett. 1979, Microphysics of Atmospheric Clouds and Precipitation (Springer Science & Business Media)

Rafikov, R. R. 2005, ApJ, 621, L69

Ranjan, S., Charbonneau, D., Désert, J.-M., et al. 2014, ApJ, 785, 148

Rasio, F. A. & Ford, E. B. 1996, Science, 274, 954

Ressler, M. E., Sukhatme, K. G., Franklin, B. R., et al. 2015, PASP, 127, 675

Ricci, D., Ramón-Fox, F. G., Ayala-Loera, C., et al. 2015, PASP, 127, 143

Ricci, L., Testi, L., Natta, A., et al. 2010, A&A, 512, A15

Richard, C., Gordon, I. E., Rothman, L. S., et al. 2012, J. Quant. Spec. Radiat. Transf., 113, 1276

Robie, R. A., Hemingway, B. S., & Fisher, J. R. 1978, Thermodynamic properties of minerals and related substances at 298.15 K and 1 bar (105 pascals) pressure and at higher temperatures, Tech. rep., report

Robinson, T. D. & Catling, D. C. 2014, Nature Geoscience, 7, 12

Rocchetto, M., Waldmann, I. P., Venot, O., Lagage, P.-O., & Tinetti, G. 2016, ApJ, 833, 120

Rodler, F., Kürster, M., & Barnes, J. R. 2013, MNRAS, 432, 1980

Rodler, F., Lopez-Morales, M., & Ribas, I. 2012, ApJ, 753, L25

Rodmann, J., Henning, T., Chandler, C. J., Mundy, L. G., & Wilner, D. J. 2006, A&A, 446, 211

Rosner, D. E. 2012, Transport processes in chemically reacting flow systems (Courier Corporation)

Rossow, W. B. 1978, Icarus, 36, 1

Rothman, L. S., Gordon, I. E., Babikov, Y., et al. 2013, J. Quant. Spec. Radiat. Transf., 130, 4

Rothman, L. S., Gordon, I. E., Barber, R. J., et al. 2010, J. Quant. Spec. Radiat. Transf., 111, 2139

Rugheimer, S., Kaltenegger, L., Zsom, A., Segura, A., & Sasselov, D. 2013, Astrobiology, 13, 251

Rybicki, G. B. & Lightman, A. P. 1986, Radiative Processes in Astrophysics, 400

Saar, S. H. & Donahue, R. A. 1997, ApJ, 485, 319

Safronov, V. S. 1972, Evolution of the protoplanetary cloud and formation of the earth and planets.

Sagan, C. 1960, AJ, 65, 352

Sagan, C. 1962, AJ, 67, 281

Samland, M., Mollière, P., Bonnefoy, M., et al. 2017, ArXiv e-prints

Saumon, D. & Marley, M. S. 2008, ApJ, 689, 1327

Sauval, A. J. & Tatum, J. B. 1984, ApJS, 56, 193

Schwabl, F. 2006, Statistical Mechanics

Schweitzer, A., Hauschildt, P. H., Allard, F., & Basri, G. 1996, MNRAS, 283, 821

Scott, A. & Duley, W. W. 1996, ApJS, 105, 401

Seager, S., Richardson, L. J., Hansen, B. M. S., et al. 2005, ApJ, 632, 1122

Seager, S. & Sasselov, D. D. 2000, ApJ, 537, 916

Seager, S., Whitney, B. A., & Sasselov, D. D. 2000, ApJ, 540, 504

Servoin, J. L. & Piriou, B. 1973, Physica Status Solidi B Basic Research, 55, 677

Shaklan, S. B., Marchen, L. F., Zhao, F., et al. 2004, in Proceedings of the SPIE, Vol. 5528, Space Systems Engineering and Optical Alignment Mechanisms, ed. L. D. Peterson & R. C. Guyer, 22–31

Sharp, C. M. & Burrows, A. 2007, ApJS, 168, 140

Showman, A. P., Fortney, J. J., Lian, Y., et al. 2009, ApJ, 699, 564

Showman, A. P. & Polvani, L. M. 2011, ApJ, 738, 71

Shporer, A. & Hu, R. 2015, AJ, 150, 112

Shporer, A., O'Rourke, J. G., Knutson, H. A., et al. 2014, ApJ, 788, 92

Sing, D. K., Fortney, J. J., Nikolov, N., et al. 2016, Nature, 529, 59

Sing, D. K., Lecavelier des Etangs, A., Fortney, J. J., et al. 2013, MNRAS, 436, 2956

Sing, D. K., Pont, F., Aigrain, S., et al. 2011, MNRAS, 416, 1443

Sing, D. K., Wakeford, H. R., Showman, A. P., et al. 2015, MNRAS, 446, 2428

Skemer, A. J., Morley, C. V., Zimmerman, N. T., et al. 2016, ApJ, 817, 166

Skilling, J. 2004, in American Institute of Physics Conference Series, Vol. 735, American Institute of Physics Conference Series, ed. R. Fischer, R. Preuss, & U. V. Toussaint, 395–405

Smith, A. M. S., Anderson, D. R., Madhusudhan, N., et al. 2012, A&A, 545, A93

Smith, A. M. S., Anderson, D. R., Skillen, I., Collier Cameron, A., & Smalley, B. 2011, MNRAS, 416, 2096

Sneep, M. & Ubachs, W. 2005, J. Quant. Spec. Radiat. Transf., 92, 293

Snellen, I., de Kok, R., Birkby, J. L., et al. 2015, A&A, 576, A59

Snellen, I. A. G., Brandl, B. R., de Kok, R. J., et al. 2014, Nature, 509, 63

Snellen, I. A. G., de Kok, R. J., de Mooij, E. J. W., & Albrecht, S. 2010, Nature, 465, 1049

Southworth, J., Mancini, L., Madhusudhan, N., et al. 2017, AJ, 153, 191

Sozzetti, A., Bonomo, A. S., Biazzo, K., et al. 2015, A&A, 575, L15

Spiegel, D. S., Silverio, K., & Burrows, A. 2009, ApJ, 699, 1487

Springel, V. 2014, Lecture Notes on the Fundamentals of Simulation Methods

Sromovsky, L. A., Fry, P. M., & Kim, J. H. 2011, Icarus, 215, 292

Stamatellos, D. & Whitworth, A. P. 2009, MNRAS, 392, 413

Stevenson, D. J. & Salpeter, E. E. 1977, ApJS, 35, 221

Stevenson, K. B. 2016, ApJ, 817, L16

Stevenson, K. B., Bean, J. L., Madhusudhan, N., & Harrington, J. 2014a, ApJ, 791, 36

Stevenson, K. B., Bean, J. L., Seifahrt, A., et al. 2016a, ApJ, 817, 141

Stevenson, K. B., Désert, J.-M., Line, M. R., et al. 2014b, Science, 346, 838

Stevenson, K. B., Harrington, J., Nymeyer, S., et al. 2010, Nature, 464, 1161

Stevenson, K. B., Lewis, N. K., Bean, J. L., et al. 2016b, ArXiv e-prints

Stofan, E. R., Elachi, C., Lunine, J. I., et al. 2007, Nature, 445, 61

Sudarsky, D., Burrows, A., & Hubeny, I. 2003, ApJ, 588, 1121

Swain, M., Deroo, P., Tinetti, G., et al. 2013, Icarus, 225, 432

Swain, M. R., Deroo, P., Griffith, C. A., et al. 2010, Nature, 463, 637

Takeda, Y., Kang, D.-I., Han, I., et al. 2012, PASJ, 64

Tanaka, H., Takeuchi, T., & Ward, W. R. 2002, ApJ, 565, 1257

Testi, L., Natta, A., Shepherd, D. S., & Wilner, D. J. 2003, A&A, 403, 323

Thiabaud, A., Marboeuf, U., Alibert, Y., et al. 2014, A&A, 562, A27

Thiabaud, A., Marboeuf, U., Alibert, Y., Leya, I., & Mezger, K. 2015, A&A, 574, A138

Thomas, G. E. & Stamnes, K. 2002, Radiative Transfer in the Atmosphere and Ocean, 546

Thorngren, D. P., Fortney, J. J., Murray-Clay, R. A., & Lopez, E. D. 2016, ApJ, 831, 64

Todorov, K. O., Deming, D., Knutson, H. A., et al. 2013, ApJ, 770, 102

Toomre, A. 1981, In: The structure and evolution of normal galaxies; Proceedings of the Advanced Study Institute, 111

Toon, O. B. & Ackerman, T. P. 1981, Appl.Optics, 20, 3657

Tremblin, P., Amundsen, D. S., Chabrier, G., et al. 2016, ApJ, 817, L19

Tremblin, P., Amundsen, D. S., Mourier, P., et al. 2015, ApJ, 804, L17

Triaud, A. H. M. J., Gillon, M., Ehrenreich, D., et al. 2015, Monthly Notices of the Royal Astronomical Society, 450, 2279

Tsiaras, A., Rocchetto, M., Waldmann, I. P., et al. 2016, ApJ, 820, 99

Tsuji, T., Ohnaka, K., & Aoki, W. 1996, A&A, 305, L1

Turbet, M., Leconte, J., Selsis, F., et al. 2016, A&A, 596, A112

Turner, J. D., Pearson, K. A., Biddle, L. I., et al. 2016, MNRAS, 459, 789

Tyler, G. L., Eshleman, V. R., Hinson, D. P., et al. 1986, Science, 233, 79

Udry, S. & Santos, N. C. 2007, ARA&A, 45, 397

Urey, H. C. 1955, Proceedings of the National Academy of Science, 41, 127

van Boekel, R., Benneke, B., Heng, K., et al. 2012, in Society of Photo-Optical Instrumentation Engineers (SPIE) Conference Series, Vol. 8442, Society of Photo-Optical Instrumentation Engineers (SPIE) Conference Series, 1

Venot, O., Hébrard, E., Agúndez, M., Decin, L., & Bounaceur, R. 2015, A&A, 577, A33

Venot, O., Hébrard, E., Agúndez, M., et al. 2012, A&A, 546, A43

Venot, O., Rocchetto, M., Carl, S., Roshni Hashim, A., & Decin, L. 2016, ApJ, 830, 77

von Essen, C., Mallonn, M., Albrecht, S., et al. 2015, A&A, 584, A75

Waite, J. H., Young, D. T., Cravens, T. E., et al. 2007, Science, 316, 870

Wakeford, H. R. & Sing, D. K. 2015, A&A, 573, A122

Wakeford, H. R., Visscher, C., Lewis, N. K., et al. 2017, MNRAS, 464, 4247

Waldmann, I. P., Rocchetto, M., Tinetti, G., et al. 2015a, ApJ, 813, 13

Waldmann, I. P., Tinetti, G., Rocchetto, M., et al. 2015b, ApJ, 802, 107

Wang, L. & Wu, H. 2007, Biomedical Optics: Principles and Imaging (Wiley)

Weidenschilling, S. J. & Marzari, F. 1996, Nature, 384, 619

Weiss, L. M. & Marcy, G. W. 2014, ApJ, 783, L6

Wilner, D. J., D'Alessio, P., Calvet, N., Claussen, M. J., & Hartmann, L. 2005, ApJ, 626, L109

Winn, J. N., Matthews, J. M., Dawson, R. I., et al. 2011, ApJ, 737, L18

Woitke, P., Min, M., Pinte, C., et al. 2016, A&A, 586, A103

Wolszczan, A. 1994, Science, 264, 538

Wolszczan, A. & Frail, D. A. 1992, Nature, 355, 145

Wong, I., Knutson, H. A., Cowan, N. B., et al. 2014, ApJ, 794, 134

Wong, M. H., Mahaffy, P. R., Atreya, S. K., Niemann, H. B., & Owen, T. C. 2004, Icarus, 171, 153

Wright, G. S., Rieke, G., Boeker, T., et al. 2010, in Society of Photo-Optical Instrumentation Engineers (SPIE) Conference Series, Vol. 7731, Society of Photo-Optical Instrumentation Engineers (SPIE) Conference Series, 0

Wright, J. T., Marcy, G. W., Howard, A. W., et al. 2012, ApJ, 753, 160

Wright, W. H. 1925, Lick Observatory Bulletin, 12, 48

Wu, Y. & Murray, N. 2003, ApJ, 589, 605

Yi, S., Demarque, P., Kim, Y.-C., et al. 2001, ApJS, 136, 417

Yi, S. K., Kim, Y.-C., & Demarque, P. 2003, ApJS, 144, 259

Yurchenko, S. N. & Tennyson, J. 2014, MNRAS, 440, 1649

Zahnle, K., Marley, M. S., Morley, C. V., & Moses, J. I. 2016, ApJ, 824, 137

Zahnle, K. J. & Marley, M. S. 2014, ApJ, 797, 41

Zellem, R. T., Lewis, N. K., Knutson, H. A., et al. 2014, ApJ, 790, 53

Zhang, H. W., Gehren, T., Butler, K., Shi, J. R., & Zhao, G. 2006, A&A, 457, 645

Zhu, C., Babb, J. F., & Dalgarno, A. 2006, Phys.Rev.A, 73, 012506

Zhu, Z., Stone, J. M., & Rafikov, R. R. 2013, ApJ, 768, 143

Zsom, A., Kaltenegger, L., & Goldblatt, C. 2012, Icarus, 221, 603

Zurlo, A., Vigan, A., Galicher, R., et al. 2016, A&A, 587, A57

Acknowledgements

This thesis has been made possible by the support and help of many people. First, I want to thank my supervisors, Roy van Boekel and Thomas Henning. Roy for giving insightful suggestions whenever I got stuck somewhere, and for always taking time for me. Thanks also for organizing the trip to API and SRON, which I really enjoyed. Finally, for his helpful comments which have improved the content of this thesis. I want to thank Thomas for keeping the big picture in mind, making ambitious plans for next steps, taking time to comment on my projects and drafts, and for sending me around the world to attend conferences, and meet exiting people.

Next there is Kees Dullemond, without whom this thesis would not have been possible. It is from attending his lectures that I received my radiative transfer 101, and his excellent lecture notes contain easy-to-apply descriptions of many methods, which I used at several points in *petitCODE*. In addition, he provided me with a version of his disk structure code, with which I could play around, and the underlying principles of which became the theoretical foundation of *petitCODE*. Discussing radiative transfer problems with him is great fun and brought clarity into seemingly complicated problems for me multiple times. Thanks Kees!

Additionally, I want to thank the members of our *JWST* model (benchmarking) group (especially Pascal Tremblin, Jean-Loup Baudino, Bruno Bezard, and Michiel Min, as well as Pierre-Olivier Lagage for the coordination). I learned a lot from the model comparisons and the current state of *petitCODE* certainly benefitted strongly from the benchmarking project.

I would also like to thank the members of the PSF Theory group, for taking me in, and for providing distractions such as Theory Lunch and nerd discussions. Especially, I want to thank Andreas, Kai, Matthäus and Adriana, which sometimes successfully convinced me to take work less seriously, and to do something else. In addition, I would like to thank Gabriel for interesting discussions "über Gott und die Welt", as one would say in German, and for constantly correcting my (German) grammar.

I would like to thank IMPRS (and Christian Fend in particular) for financially supporting trips to conferences and funding the retreats of my IMPRS generation, which were very enjoyable!

I want to thank Ludmila Carone for plowing through this thesis, and giving many comments which improved upon its text. I also thank Matthias Samland, who read parts of this thesis.

Moreover, I need to thank "The Three Christophs" which had a big influence on bringing me here: my high school teacher Christoph Holtwiesche, whose matter-of-fact statement that I would study physics turned out to be true, and who set me on this path. Christoph Brand, my Statistical Physics tutor, who (unknowingly?) motivated me to apply for the astrophysics master's course in Cambridge. And last, but certainly not least, Christoph Mordasini, thanks to whom I actually started to work in astrophysics in the first place, and whose enthusiasm and help resulted in my first serious scientific work, and additional collaborations since then. Here's to many more!

Most importantly, I want to thank Laura, for always being there, and for being patient with me. Thanks for making me happy, and for reminding me that work is not the most important thing.

Finally, I want to thank my family. My parents for their lifelong (!) support, and for always letting me pursue whatever I wanted, and for being there if I needed help. My brothers, for being my brothers, and great friends at the same time. Lastly, I want to thank my grandparents, especially my grandmother, who consistently asked how I am doing with my thesis, and when I would finally be done, every time I saw her. I would have been very happy had I been able to tell her that now I finished.

"Plus grand est l'obstacle, et plus grande est la gloire de le surmonter."

Molière